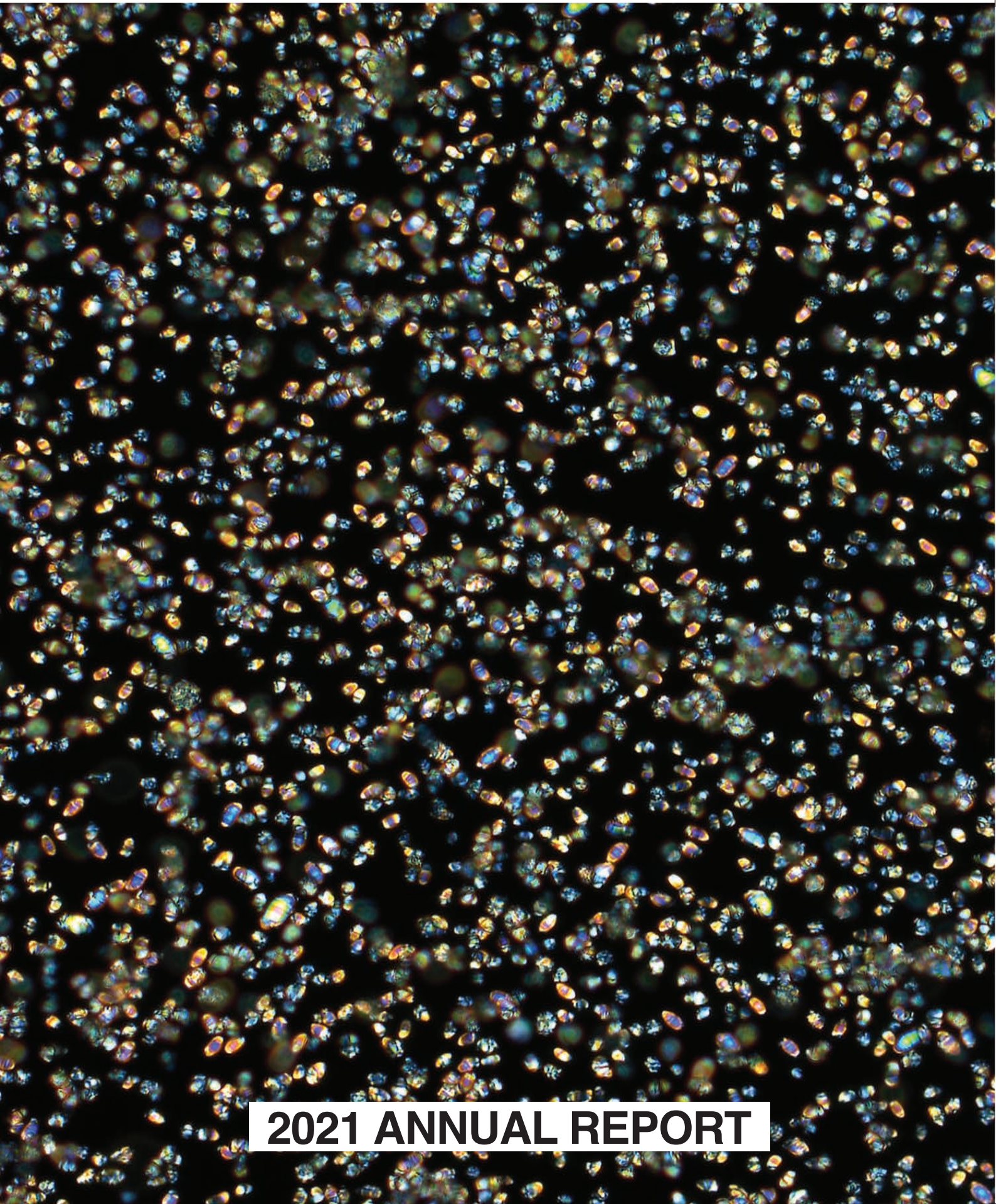


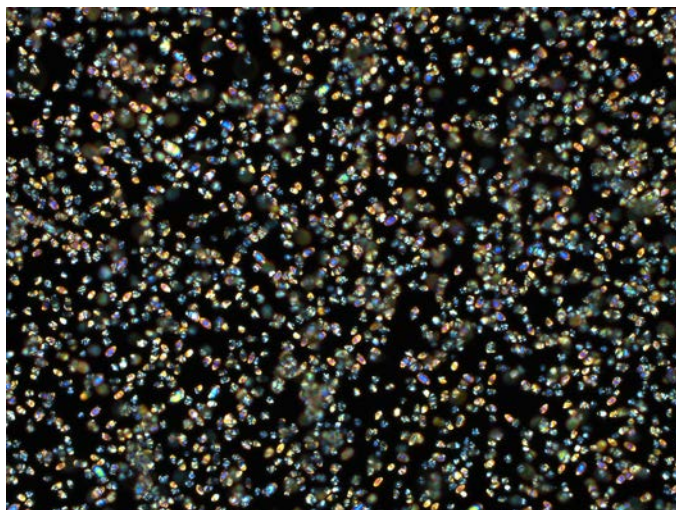
# CHIMaD

Center for  
Hierarchical  
Materials Design



**2021 ANNUAL REPORT**

**On the cover:** Elongated liquid crystal elastomer particles as viewed by polarized optical microscopy (University of Chicago, *Rowan Group*)



**Editor**

E. Begum Gulsoy, Ph.D.  
*CHiMaD Associate Director*

**CHiMaD Headquarters**

Northwestern University, O.T. Hogan Biological Sciences Building, Suite 1160  
2205 Tech Drive, Evanston, IL, USA 60208  
Ph: (847) 467-6287 [chimad.northwestern.edu](http://chimad.northwestern.edu) | [chimad@northwestern.edu](mailto:chimad@northwestern.edu)

This work was performed under the following financial assistance award 70NANB19H005 from U.S. Department of Commerce, National Institute of Standards and Technology as part of the Center for Hierarchical Materials Design (CHiMaD).

The template used for this report was downloaded from: <http://www.LaTeXTemplates.com>, was created by Mathias Legrand ([legrand.mathias@gmail.com](mailto:legrand.mathias@gmail.com)) with modifications by Vel ([vel@latextemplates.com](mailto:vel@latextemplates.com)). Further modifications were applied by the editor. This template is licensed under CC BY-NC-SA 3.0 (<http://creativecommons.org/licenses/by-nc-sa/3.0/>).

*CHiMaD 2021*



## Contents

<b>I</b>	<b>Center for Hierarchical Materials Design</b>	
<b>1</b>	<b>Center for Hierarchical Materials Design</b>	<b>7</b>
<b>II</b>	<b>Accomplishments</b>	
<b>2</b>	<b>Major Goals and Objectives</b>	<b>11</b>
<b>3</b>	<b>2D Electronic Materials Inks</b>	<b>13</b>
<b>3.1</b>	<b>Design Goals</b>	<b>13</b>
<b>3.2</b>	<b>Research Accomplishments</b>	<b>15</b>
3.2.1	Graphene Inks for Printed Electrochemical Biosensors	15
3.2.2	Hexagonal Boron Nitride Ionogel Inks for Printed Sensors, Batteries, and Supercapacitors	16
3.2.3	2D Semiconductor Inks for Printed Photodetectors	17
3.2.4	Enhancing Semiconducting 2D Ink Performance by Scanning Probe-Informed Modeling	19
3.2.5	Designing Edge-Selective Functionalization to Improve Printed 2D Transistor Performance	22
3.2.6	Diazonium Functionalization of 2D Indium Monoselenide	23
3.2.7	Trifluoromethylation Based Passivation of 2D Semiconductors	24
3.2.8	Computational Design of Heterostructure Materials for Printed 2D Semiconductor Photodetectors	25
<b>4</b>	<b>Grain Boundary and Interface Engineering in Thermoelectrics</b>	<b>27</b>
<b>4.1</b>	<b>Design Goals</b>	<b>27</b>

<b>4.2</b>	<b>Research Accomplishments</b>	<b>28</b>
4.2.1	Phase Boundary Mapping . . . . .	28
4.2.2	Mechanical Properties of Thermoelectric Materials . . . . .	29
4.2.3	Thermal Transport . . . . .	29
4.2.4	Investigation of Weak-bonding Elements' Influence on Thermoelectric Transport	31
4.2.5	Rapid Screening of Low Thermal Conductivity Materials using Chemical Bonding Principles . . . . .	32
<b>5</b>	<b>Design of Properties of Polyelectrolyte Complexes . . . . .</b>	<b>35</b>
<b>5.1</b>	<b>Design Goals</b>	<b>35</b>
<b>5.2</b>	<b>Research Accomplishments</b>	<b>36</b>
5.2.1	Processing polyelectrolyte complexes with deep eutectic solvents . . . . .	36
5.2.2	Diffusion in dense polyelectrolyte systems . . . . .	36
5.2.3	Modeling-based design to engineering protein hydrogels with random copolymers	38
5.2.4	Probing the size-dependent polarizability of mesoscopic ionic clusters and their induced-dipole interactions . . . . .	39
5.2.5	A perspective on the design of ion-containing polymers for polymer electrolyte applications . . . . .	40
5.2.6	Polyelectrolyte complex phase behavior . . . . .	41
5.2.7	Polyelectrolyte complex micelle design . . . . .	42
<b>6</b>	<b>Directed Self-Assembly of Soft Matter Systems . . . . .</b>	<b>45</b>
<b>6.1</b>	<b>Design Goals</b>	<b>45</b>
<b>6.2</b>	<b>Research Accomplishments</b>	<b>45</b>
6.2.1	Resonant Soft X-ray Reflectivity Measurements of A-b-(B-r-C) Copolymers . . .	45
6.2.2	Impact of Structural Isomerism On the Self-Assembly of Diblock Copolymers .	46
6.2.3	Surface energy and density measurements . . . . .	47
<b>7</b>	<b>Materials for High-Performance Impact Mitigation . . . . .</b>	<b>49</b>
<b>7.1</b>	<b>Design Goals</b>	<b>49</b>
<b>7.2</b>	<b>Research Accomplishments</b>	<b>50</b>
7.2.1	Harnessing the polymer glass transition for stress-adaptive shear response . . .	50
7.2.2	Tuning dynamic bond exchange and morphology for impact applications . .	51
7.2.3	A new class of dynamic covalent suspensions with switchable response . . . . .	53
7.2.4	Direct detection of frictional contact network formation in dense piezoelectric suspensions . . . . .	54
7.2.5	Rigid cluster analysis of dense frictional suspensions . . . . .	54
7.2.6	Stress activated constraints in dense suspensions . . . . .	55
7.2.7	Impact mitigation with network-based meta-materials . . . . .	56
<b>8</b>	<b>Alloy Design for Additive Manufacturing . . . . .</b>	<b>59</b>
<b>8.1</b>	<b>Design Goals</b>	<b>59</b>
<b>8.2</b>	<b>Research Accomplishments</b>	<b>61</b>
8.2.1	Printable Cobalt Superalloy, Olson Group . . . . .	61
8.2.2	Design of Printable TRIP Steel, Olson Group . . . . .	62
8.2.3	Optimization of Printable 17-4PH Stainless Steel, Olson Group & QuesTek . . . .	62
8.2.4	Printable Titanium Alloys, Olson Group . . . . .	63
8.2.5	SRG Design Consortium Projects and Design Class Interactions, Olson Group .	63

8.2.6	X-ray Diffraction Analysis of QuesTek Co Alloy Prototypes, QuesTek . . . . .	63
8.2.7	Printable Cobalt Alloy Thermodynamic Database Development, QuesTek . . .	64
8.2.8	Latest Printable Cobalt Alloy Design Cross-plots with Updated Thermodynamic Database, QuesTek . . . . .	65
8.2.9	Solidification During Additive Manufacturing, Voorhees Group . . . . .	65
8.2.10	AM-CFD development for porosity prediction, Liu Group . . . . .	66
8.2.11	Dimensionless Learning, Liu Group . . . . .	67
8.2.12	Simulation-guided Process Design, Cao Group . . . . .	68
<b>9</b>	<b>Cobalt-based Superalloys for High-Temperature Use . . . . .</b>	<b>75</b>
<b>9.1</b>	<b>Design Goals . . . . .</b>	<b>75</b>
<b>9.2</b>	<b>Research accomplishments . . . . .</b>	<b>75</b>
9.2.1	Co Database Development . . . . .	75
9.2.2	Computationally Designed Alloys . . . . .	76
9.2.3	W-Free Cobalt-based Superalloys . . . . .	78
9.2.4	Machine learning model for creep life . . . . .	83
9.2.5	Predicting Phase Stability Using Machine Learning . . . . .	85
9.2.6	Machine learning in phase-field sensitivity analysis . . . . .	85
9.2.7	Phase Field Modeling of Co-based superalloys . . . . .	86
<b>10</b>	<b>High-Performance Composite Design for Extreme Environments . . . . .</b>	<b>89</b>
<b>10.1</b>	<b>Design Goals . . . . .</b>	<b>89</b>
<b>10.2</b>	<b>Research Accomplishments . . . . .</b>	<b>90</b>
10.2.1	Modeling the Single Fiber Fragmentation Test . . . . .	90
10.2.2	Glassy Polymer Dynamics in the Megahertz Frequency Regime . . . . .	90
10.2.3	Development of Coarse-graining Methodologies for Computational Investigations of Polymer Deformation . . . . .	92
10.2.4	Effective potential for polymer-grafted nanoparticles . . . . .	92
10.2.5	Data Centric Materials Design via Mixed-Variable Bayesian Optimization . . . . .	93
<b>11</b>	<b>Phase Field Methods . . . . .</b>	<b>95</b>
<b>11.1</b>	<b>Design Goals . . . . .</b>	<b>95</b>
<b>11.2</b>	<b>Research Accomplishments . . . . .</b>	<b>95</b>
11.2.1	Benchmark Problems . . . . .	95
11.2.2	Phase Field modeling of Additive Manufacturing . . . . .	96
11.2.3	Orientation-field model for grain growth . . . . .	97
11.2.4	PFHub Website . . . . .	97
11.2.5	CHiMaD Phase Field Workshop Series . . . . .	98
<b>12</b>	<b>Uncertainty Quantification of Phase Equilibria and Thermodynamics . . . . .</b>	<b>101</b>
<b>12.1</b>	<b>Design Goals . . . . .</b>	<b>101</b>
<b>12.2</b>	<b>Research Accomplishments . . . . .</b>	<b>101</b>
12.2.1	Bayesian automated weighting of simulated and experimental data . . . . .	101
12.2.2	Propagation of uncertainty from unary to binary phase diagram . . . . .	105
12.2.3	Community workshop report on uncertainty quantification for thermodynamic properties . . . . .	107

<b>13</b>	<b>Artificial Intelligence and High-Performance Data Mining</b>	<b>109</b>
<b>13.1</b>	<b>Design Goals</b>	<b>109</b>
<b>13.2</b>	<b>Research Accomplishments</b>	<b>109</b>
13.2.1	Cross-property Deep Transfer Learning Framework for Enhanced Predictive Analytics on Small Materials Data	109
13.2.2	Enabling Deeper Learning on Big Data for Materials Informatics Applications	110
13.2.3	Data Centric Materials Design via Mixed-Variable Bayesian Optimization	111
13.2.4	Data-Driven and Topological Design of Structural Materials for Fracture Resistance	112
13.2.5	Steel Fatigue Data Mining for Design of Improved Steels	113
13.2.6	Enhancing Phase Mapping for High-throughput X-ray Diffraction Experiments using Fuzzy Clustering	113
13.2.7	Data-Driven Multi-Scale Modeling and Optimization for Elastic Properties of Cubic Microstructures	114
13.2.8	Semi-Parametric Functional Calibration and Uncertainty Quantification	115
13.2.9	Improving Scalability of Parallel CNN Training by Adaptively Adjusting Parameter Update Frequency	115
<b>14</b>	<b>Materials Data Facility</b>	<b>117</b>
<b>14.1</b>	<b>Design Goals</b>	<b>117</b>
<b>14.2</b>	<b>Research Accomplishments</b>	<b>117</b>
14.2.1	Data Publication and Discovery	118
14.2.2	Automating Materials-Aware Metadata Extraction	120
14.2.3	Natural Language Processing	122
<b>14.3</b>	<b>Community Support and Other Collaborations</b>	<b>125</b>
<b>15</b>	<b>CHiMaD Outreach: Training and Professional Development</b>	<b>129</b>
<b>15.1</b>	<b>Goals</b>	<b>129</b>
<b>15.2</b>	<b>Accomplishments: Outreach and Training</b>	<b>129</b>
15.2.1	CHiMaD Materials Design Training	129
15.2.2	<i>CHiMaD Focus Workshop</i> Uncertainty Quantification of Phase Equilibria and Thermodynamics	132
15.2.3	<i>CHiMaD Focus Workshop</i> CHiMaD Phase Field Methods Workshop Series	132
15.2.4	CHiMaD Professional Development Workshops	135
15.2.5	SRG Annual Meeting	135
15.2.6	CHiMaD Annual Meeting	136
15.2.7	Materials Genome Toolkit Program	136
15.2.8	Undergraduate Education in Materials Design	136
15.2.9	CHiMaD-ASM Materials Genome Camp for K-12 STEM Educators	138
<b>15.3</b>	<b>Accomplishments: Data Outreach</b>	<b>140</b>
15.3.1	Data-focused Events to which CHiMaD was invited to participate	140
15.3.2	CHiMaD/NIST Office of Data Informatics Monthly Seminar Series	141

<b>16</b>	<b>Products .....</b>	<b>145</b>
16.1	Publications	145
16.2	Presentations	154
16.3	Technologies and Techniques	162
16.4	Inventions, Patent Applications and/or Licenses	165
16.5	Data	166
16.6	CHiMaD Databases	167







# Center for Hierarchical Materials Design





## 1. Center for Hierarchical Materials Design

### Foreword

The classical industrial materials development paradigm rests on a make-and-test strategy that results in unacceptably long times and increased costs before new materials can be inserted into applications. By contrast, materials design strategies offer the potential to radically transform U.S. manufacturing and cut costs dramatically by changing the way in which new products are deployed or inserted into production lines. The Center for Hierarchical Materials Design (CHiMaD) was founded to enable this transformation of U.S. manufacturing. Our mission is to demonstrate, advance, and disseminate the power of the materials design approach by providing opportunities to train scientists and engineers in materials design, by fostering the development of synergistic computational, experimental tools and, most importantly, the data that enable design, and by discovering new materials. CHiMaD has become a forum where multidisciplinary and multi-sector communities convene for in-depth discussions on all topics related to Materials Genome Initiative (MGI). A close partnership with the National Institute of Standards and Technology (NIST) has been central to the Center's success on all fronts.

We are pleased to present the 2021 annual report of the Center for Hierarchical Materials Design (CHiMaD), NIST Center of Excellence in Advanced Materials. Near the beginning of the second year of our new cycle a world-wide pandemic led to a change in the manner in which the CHiMaD performed its research, outreach, and educational missions. Given this, the great progress described in this report is again a credit to the creativity and perseverance of the CHiMaD PIs and collaborators at NIST. We are designing revolutionary materials from cobalt superalloys to thermoelectrics and polymer blends. The data created is shared with the community and drives the machine learning algorithms used in materials design and discovery.

2022 promises a return to in-person meetings and training sessions, as well as fully staffed laboratories. It will be a truly exciting year to push forward the field of materials genomics.

**Peter Voorhees, Juan de Pablo**, CHiMaD Directors  
**Greg Olson**, Chief Designer





# Accomplishments

2	Major Goals and Objectives .....	11
3	2D Electronic Materials Inks .....	13
4	Grain Boundary and Interface Engineering in Thermoelectrics .....	27
5	Design of Properties of Polyelectrolyte Complexes .....	35
6	Directed Self-Assembly of Soft Matter Systems .....	45
7	Materials for High-Performance Impact Mitigation .....	49
8	Alloy Design for Additive Manufacturing .....	59
9	Cobalt-based Superalloys for High-Temperature Use .....	75
10	High-Performance Composite Design for Extreme Environments .....	89
11	Phase Field Methods .....	95
12	Uncertainty Quantification of Phase Equilibria and Thermodynamics .	101
13	Artificial Intelligence and High-Performance Data Mining .....	109
14	Materials Data Facility .....	117
15	CHiMaD Outreach: Training and Professional Development .....	129





## 2. Major Goals and Objectives

### Mission and Vision

*Accelerating materials discovery and commercialization by design and development of hierarchical methods and materials and enabling the complete integration of computation, experimentation and databases by building a strong community of current and future researchers*

Designing novel materials of specific properties for a particular application requires simultaneously utilizing physical theory, advanced computational methods and models, materials properties databases and complex calculations. This approach stands in contrast to the traditional trial-and-error method of materials discovery. CHiMaD aims to focus this approach on the creation of novel *hierarchical materials* which exploit distinct structural details at various scales, from the atomic on up, to obtain enhanced properties. The center's research focuses on both organic and inorganic advanced materials in fields as diverse as self-assembled biomaterials, smart materials for self-assembled circuit designs and, advanced metal alloys.

### Objectives

- **Create** a collaborative environment and concentration of scientific and technical capability to accelerate materials discovery and development
- **Provide opportunities** to transition new breakthroughs in advanced materials to industry
- **Convene** multidisciplinary and multi-sector communities for in-depth discussions
- **Provide training** opportunities for scientists and engineers in materials metrology
- **Foster** the development of artificial intelligence fueled materials design
- **Foster** the development of integrated computation, modeling and data-driven tools
- **Foster** the discovery of new materials
- **Establish opportunities** for extended collaborations with NIST

### Major Goals

CHiMaD is demonstrating the power and potential of bringing together data science, computational approaches and state-of-art experiments to design materials ranging from alloys for additive manufacturing to polymers for impact protection. Our research efforts compass eight active use-case groups, and four tool development efforts along with

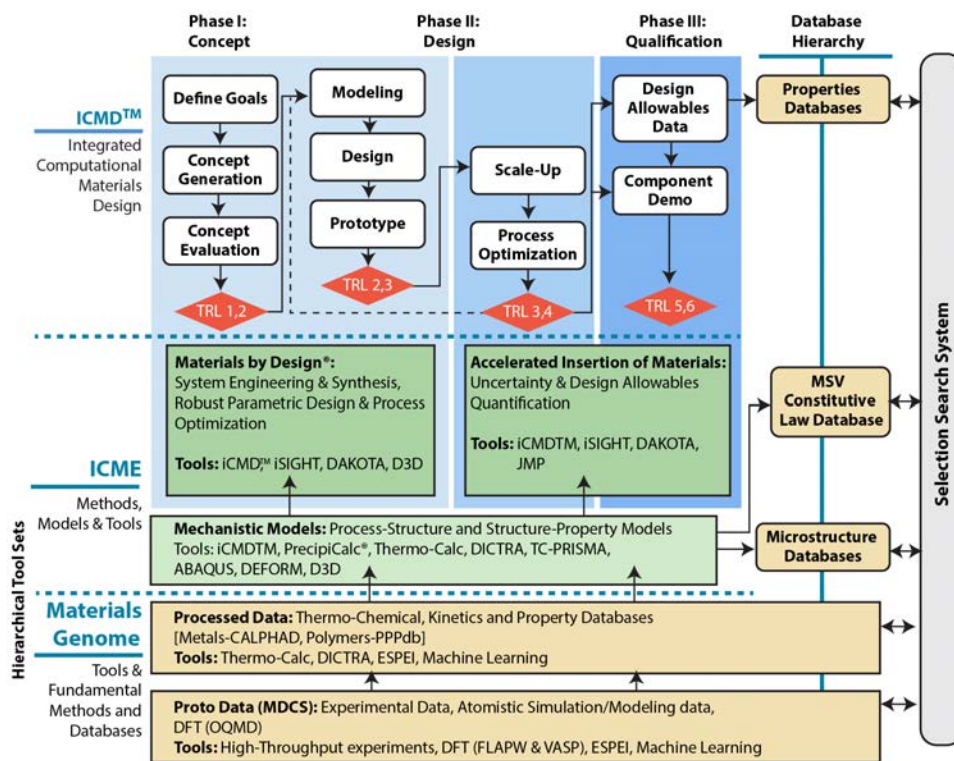


Figure 2.1: Hierarchical architecture of methods, tools (green), and databases (tan) for next-generation materials design and accelerated qualification.

databases and outreach. The design goals and accomplishments of each group is stated in the next chapters.





## 3. 2D Electronic Materials Inks

**Mark Hersam (NU)**, Lincoln Lauhon (NU), Tobin Marks (NU), Chris Wolverton (NU), Guilia Galli (UC)

**Albert Davydov (NIST)**, **Dean Delongchamp (NIST)**, **Lee Richter (NIST)**

### 3.1 Design Goals

Two-dimensional (2D) materials have emerged as promising candidates for next-generation electronics. With properties ranging from insulating (e.g., hexagonal boron nitride (hBN)) to semiconducting (e.g., transition metal dichalcogenides) to conducting (e.g., graphene), nearly any electronic device can be fabricated by properly assembling 2D materials into heterostructures. While device prototypes have been demonstrated on idealized research-scale samples, scalable manufacturing remains an unresolved challenge for 2D electronic materials. In parallel, the field of printed electronics has made significant progress towards roll-to-roll additive manufacturing based on organic and nanoparticle inks. The 2D Electronic Material Inks Use-Case Group aims to unite these efforts by designing electronic inks that combine the superlative electronic properties of 2D materials with the scalable manufacturing of printed electronics. Importantly, the diverse range of properties provided by 2D materials imply that printed 2D electronic material inks will not only enable printed electronics but also other flexible and wearable technologies including printed sensors, batteries, and supercapacitors.

To achieve the ultimate goal of developing libraries of printed 2D electronic material inks, multiple design considerations will be concurrently optimized.

*Exfoliation:* Design goals include optimizing exfoliation yield, throughput, and flake size, while minimizing structural and chemical defects in the resulting 2D materials.

*Ink formulation:* Design goals include engineering solvents and stabilizing surfactants and polymers with tailored rheological properties for additive manufacturing (e.g., aerosol, inkjet, gravure, and screen printing), while maintaining substrate adhesion and mechanical flexibility for roll-to-roll processing.

*Printed structure morphology:* Design goals include controlling film morphology and microstructure following printing via solvent evaporation, solvent additives, surface hy-

drophilicity, and novel substrates and coatings, including those based on 2D materials.

*Control of interfacial properties:* Design goals include minimizing interfacial resistance in conductive inks, maximizing porosity for low- $\kappa$  dielectric inks, minimizing thickness and leakage current for high- $\kappa$  dielectric inks, and maximizing mobility for semiconductor inks. For example, in the case of conductive graphene inks, quantitative design targets include charge carrier mobilities greater than  $100 \text{ cm}^2/\text{V-s}$  and electrical conductivities in excess of  $10^4 \text{ S/m}$ , which will enable corresponding reductions in the contact resistance to printed semiconductors that currently limit the performance of heterostructure diodes and transistors.

The system design chart in Figure 3.1 delineates the processing-structure-properties-performance work flow for the 2D Electronic Material Inks Use-Case Group.

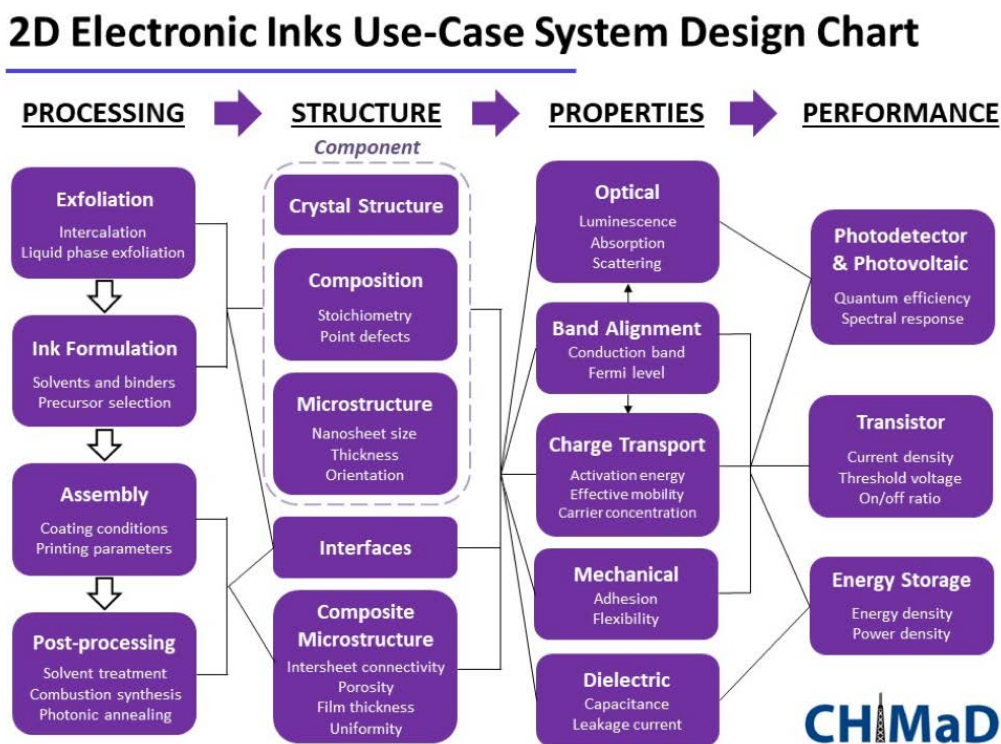


Figure 3.1: The System Design Chart for the 2D Electronic Material Inks Use-Case Group

## 3.2 Research Accomplishments

Over the past year, the 2D Electronic Material Inks Use-Case Group made significant progress towards many of its design goals. Specific accomplishments include:

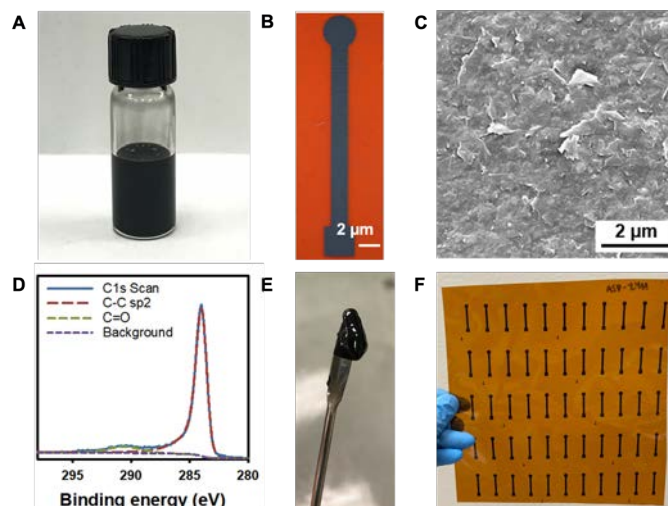


Figure 3.2: Graphene inks and printed devices. (a) Optimized graphene ink for aerosol jet printing. (b) Aerosol-jet-printed graphene dipstick electrodes. (c) SEM of the surface of an AJP graphene film, showing a dense network of percolating nanosheets. (d) XPS of an AJP graphene film showing high  $sp^2$ -carbon content and low carbonyl defects. (e) Optimized graphene ink for screen printing. (f) A sheet of screen-printed graphene dipstick electrodes.

### 3.2.1 Graphene Inks for Printed Electrochemical Biosensors

Previously, the **Hersam** group showed that graphene-ethyl cellulose (GrEC) inks can be aerosol jet printed (AJP) to produce highly conductive films. Building on this finding, GrEC AJP ink formulations were optimized with a solids loading of 10 mg/mL and solvent system of 9:1 ethanol: terpineol (Figure 3.2A). This solvent system inhibits complete evaporation of aerosol droplets during printing and is also shelf stable on the order of months, as confirmed by rheological tests. This ink was used to print graphene dipstick electrodes (Figure 3.2B). Scanning electron microscopy (SEM) confirms the deposition of a dense network of graphene nanosheets with low porosity (Figure 3.2C), and X-ray photoelectron spectroscopy (XPS) reveals a low concentration of graphene defects ( $\bar{0}\%$ ) that are useful for electrode functionalization (Figure 3.2D). These AJP graphene electrodes were used in electrochemical biosensing for COVID-19 diagnostics. These results informed the production of a new graphene screen printing ink with a loading of 140 mg/mL GrEC in terpineol (Figure 3.2E). This formulation was used to screen print graphene dipstick electrodes (Figure 3.2F) with relatively high throughput (i.e., 300 electrodes in 10 min versus 2 devices in 10 min with the aerosol jet printer). The screen-printed electrodes have lower device-to-device variability compared to AJP electrodes and are also being employed for electrochemical biosensing of SARS-CoV-2 coronavirus.

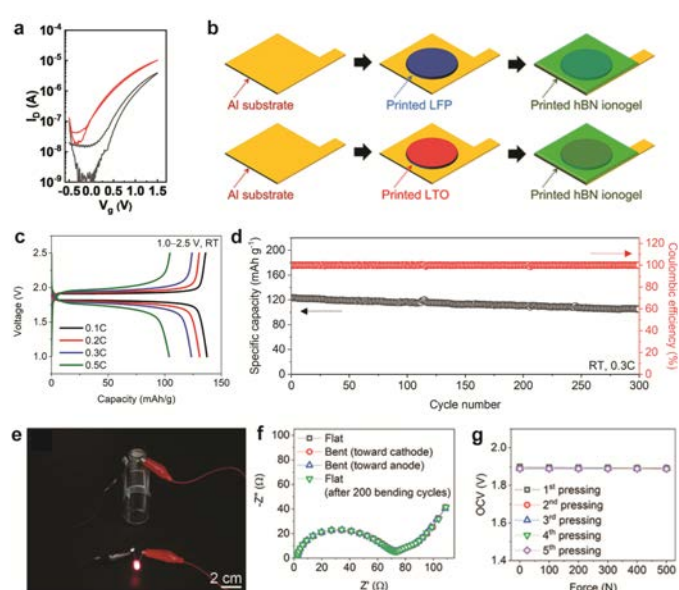


Figure 3.3: (a) Transfer curves of AJP transistors using both the hBN ionogel dielectric (red) and a silica dielectric (black). (b) Schematic depicting the fabrication of fully-screen printed batteries using the hBN ionogel electrolyte. (c) Cycling performance of the printed batteries. (d) Capacity retention and Coulombic efficiency of the printed batteries. (e) Photograph of the flexible battery powering a light-emitting diode. (f) Electrochemical impedance spectroscopy of the printed battery during bending. (g) Open circuit voltage measurements while pressure is applied to the printed batteries.

### 3.2.2 Hexagonal Boron Nitride Ionogel Inks for Printed Sensors, Batteries, and Supercapacitors

Previously, **Hersam** reported the development of hexagonal boron nitride (hBN) ionogel printable inks. By combining the room temperature ionic liquid EMIM-TFSI with exfoliated hBN nanoplatelets, a solid electrolyte gel is formed with high ionic conductivity ( $>1$  mS/cm) and mechanical modulus ( $>1$  MPa). With the addition of ethyl lactate, a non-toxic solvent, the ink rheology can be tuned for various printing methods. During this reporting period, **Hersam** expanded the development of fully printed, hBN ionogel-based transistors, batteries, and supercapacitors.

In collaboration with **Marks**, thin-film transistors were fabricated via aerosol jet printing. The fully printed devices consist of graphene electrodes, an indium gallium zinc oxide (IGZO) semiconductor channel, and an hBN ionogel dielectric. Notably, higher currents were reached using the hBN ionogel dielectric at low operating voltages compared to a traditional SiO<sub>2</sub> dielectric (Figure 3.3A), highlighting the effectiveness of the ionogel for gating.

In another demonstration, hBN ionogel-based thin film batteries were fully screen printed. In this application, a lithium salt is added to the ionogel ink formulation. The battery structure consists of flexible aluminum foil current collectors, an LiFePO<sub>4</sub> cathode, and an LiTi<sub>4</sub>O<sub>12</sub> anode. After the electrodes were printed, the ionogel was printed on each half and then sandwiched to form a full device (Figure 3.3B). The devices were evaluated at multiple scan rates (Figure 3.3C). At 0.3C, the devices have a capacity of 124 mAh/g and a capacity retention of 85% after 300 cycles (Figure 3.3D). Furthermore, the devices are

fully flexible and cycle without disruption while bent. (Figure 3.3E, Figure 3.3F). Finally, the devices maintain a constant open circuit voltage (OCV) even while being compressed with a force of 500 N (Figure 3.3G), demonstrating the high mechanical strength that the ionogel imparts to prevent short circuits.

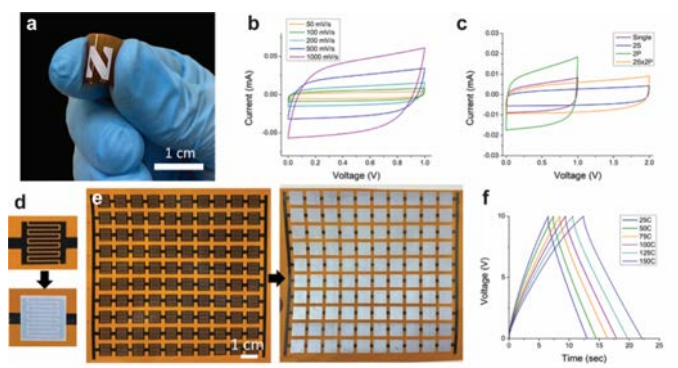


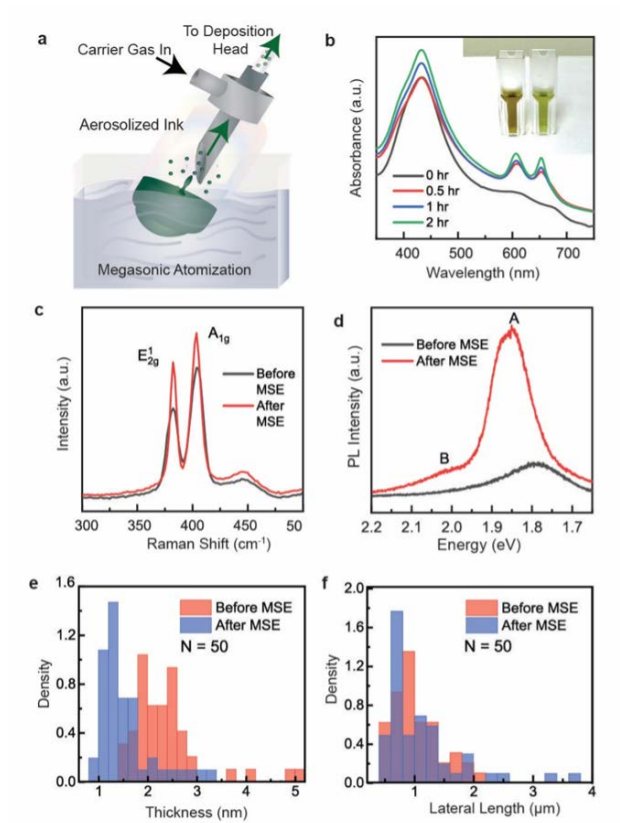
Figure 3.4: (a) Photograph of an hBN ionogel feature printed using an automatic screen printer. (b) Cyclic voltammety curves at various scan rates of printed supercapacitors. (c) Cyclic voltammety curves of printed supercapacitors in various integration configurations: 2S is 2 devices in series, 2P is 2 devices in parallel. (d) Photographs of screen-printed graphene interdigitated electrodes and a supercapacitor device. (e) Photographs of fully printed supercapacitor arrays consisting of 100 total devices. (f) Galvanostatic charge-discharge curves for a supercapacitor array while at elevated temperatures.

In a final demonstration, the large-scale manufacturing capabilities of the hBN ionogel ink were explored via automatic screen printing of supercapacitor devices. By tuning the screen printing parameters, precise hBN ionogel films were achieved (Figure 3.4A). Planar supercapacitor devices were fabricated using screen printed graphene interdigitated electrodes followed by the hBN ionogel electrolyte (Figure 3.4D). The devices achieve an areal capacitance of  $148 \mu\text{F}/\text{cm}^2$  with rectangular cyclic voltammety curves even at high scan rates (Figure 3.4B). The devices maintain their performance when connected in series and parallel configurations using printed graphene interconnects (Figure 3.4C), allowing for increased capacitance and voltage windows. Arrays consisting of 100 devices were fabricated to demonstrate the possibility of large-scale device printing (Figure 3.4E). It is estimated that  $>10^3$  devices/hour can be manufactured using this system. Finally, the arrays can be cycled at elevated temperatures up to  $150^\circ\text{C}$  without degradation and with improved capacitance due to the hBN ionogel elevated ionic conductivity at high temperatures (Figure 3.4F).

### 3.2.3 2D Semiconductor Inks for Printed Photodetectors

Fully printed photodetectors were fabricated using aerosol jet printable (AJP) inks of tetraheptylammonium bromide (THAB)-intercalated  $\text{MoS}_2$  and GrEC inks that were developed by **Hersam**. High-aspect ratio  $\text{MoS}_2$  nanosheets were obtained by THAB intercalation, and the flakes were further thinned by megasonic atomization, which is the process used to create aerosol ink droplets for AJP (Figure 3.5A). Compared to ultrasonication, megasonic atomization operates in a higher frequency regime on the order of MHz, resulting in more controlled cavitation. Optical absorbance and photoluminescence (PL) spectroscopies revealed a blueshift attributable to megasonic exfoliation during AJP, in agreement with  $\text{MoS}_2$  flake thinning (Figure 3.5B, Figure 3.5D). Following AJP, the characteristic Raman

Figure 3.5: (a) Schematic diagram of AJP, depicting aerosolization via megasonic atomization. (b) Optical absorbance spectra after various megasonic atomization times. The inset shows the color comparison of the inks before (left) and after megasonic exfoliation (MSE) (right). (c) Raman spectra before and after MSE. (d) Photoluminescence spectra showing the effects of MSE. (e) Atomic force microscopy flake thickness distribution before and after MSE. (f) Atomic force microscopy flake lateral length distribution before and after MSE.



peaks shift in peak position, suggesting the presence of monolayer and bilayer  $\text{MoS}_2$  (Figure 3.5C). Similarly, atomic force microscopy (AFM) confirms a decrease in average flake thickness from 2.2 nm to 1.3 nm, with lateral sizes of 1 micron before and after megasonic exfoliation (Figure 3.5E, Figure 3.5F).

The  $\text{MoS}_2$  channel was printed on top of graphene electrodes on Kapton substrates (Figure 3.6A). The printed  $\text{MoS}_2$  flakes formed a densely stacked morphology despite their large lateral size due to the addition of 5 vol% of the high boiling point solvent terpineol in the ink formulation, as confirmed by grazing incidence wide-angle X-ray scattering (GIWAXS) from **Richter** (NIST) that revealed a uniaxial texture (Figure 3.6B). AFM showed that without terpineol, the flakes crumple into a ball-like morphology due to uncontrolled evaporation of the carrier solvent (Figure 3.6C, Figure 3.6D). Photocurrent is mainly attributable to the  $\text{MoS}_2$  channel rather than the graphene electrodes, as confirmed by scanning photocurrent microscopy (SPCM) performed by **Lauhon** (Figure 3.7A, Figure 3.7B, Figure 3.7C). Linear current-voltage characteristics between the  $\text{MoS}_2$  and graphene imply nearly Ohmic contacts in these devices (Figure 3.7D).

To remove the stabilizing polymers used in the ink formulation, either thermal annealing at  $280^\circ\text{C}$  or photonic annealing was employed on the printed photodetectors. Overall, the photonic annealed devices performed better than the thermally annealed devices due to increased intermixing between the  $\text{MoS}_2$  and graphene flakes in the contact region. Spectrally resolved photocurrent, obtained by **Lauhon**, further confirmed that the photoresponse arises from interband absorption within the  $\text{MoS}_2$  flakes (Figure 3.8A). Responsivity was optimized as a function of printing passes. The peak in photocurrent occurs at 5 printing passes for photonic annealed films and 15 passes for thermally annealed films, reflecting morphological differences that arise from the two processes

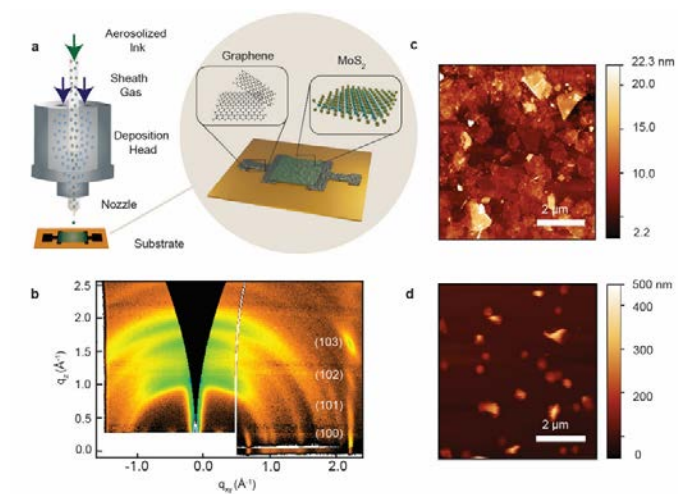


Figure 3.6: (a) Schematic showing AJP deposition and printed photodetector geometry. (b) GIWAXS map of the printed MoS<sub>2</sub> film, showing uniaxial texture along the c-axis that confirms flat, densely stacked flakes. (c) AFM image of MoS<sub>2</sub> deposited by AJP with the addition of the high boiling point solvent terpeneol. (d) AFM image of MoS<sub>2</sub> deposited by AJP without terpeneol, showing crumpling of flakes due to uncontrolled solvent evaporation.

(Figure 3.8B).

The photodetectors exhibited sublinear power dependence (Figure 3.8C). At low intensity ( $7 \times 10^{-5} \text{ W/cm}^2$ ), the highest responsivity for photonicallly annealed devices reached 2730 A/W. The sublinear power dependence suggests the dominance of bimolecular recombination that is expected for direct-bandgap materials, indicative of the high monolayer nanosheet fraction in the megasonically exfoliated MoS<sub>2</sub>. Thus, the exceptionally high photoresponse from our printed MoS<sub>2</sub> photodetectors can be attributed to the atomically thin MSE-derived MoS<sub>2</sub> nanosheets with high aspect ratio. The robustness of the all-printed, flexible photodetectors was verified by stable operation over >1000 bending cycles at a bending radius of 12 mm (Figure 3.8D).

Both types of annealing conditions exhibited relatively fast response times of about 1-2 ms rise time and 5 ms fall time (Figure 3.8E). Significantly, these photodetectors showed 3-4 orders of magnitude higher responsivity than previously reported all-printed photodetectors in the visible light range (Figure 3.8F). Inherent advantages of AJP, such as megasonic exfoliation, high resolution printing, and relaxed constraints on ink formulation, provide a novel additive manufacturing route for harnessing the tunable properties of a diverse range of 2D semiconductors in flexible optoelectronics.

### 3.2.4 Enhancing Semiconducting 2D Ink Performance by Scanning Probe-Informed Modeling

This effort is providing a modeling framework for the concurrent design of MoS<sub>2</sub> nanosheet exfoliation processes and ink formulations by linking component structure and properties to the output characteristics of printed 2D thin-film transistors (TFTs). In the previous reporting period, a gate-dependent resistor network model was solved analytically to predict that higher performance can be achieved by reducing nanosheet thickness to reduce current crowding and interfacial resistance. In particular, surface potential profiles on a model MoS<sub>2</sub>/MoS<sub>2</sub> homojunction consisting of partially overlapped 8 layers were measured to

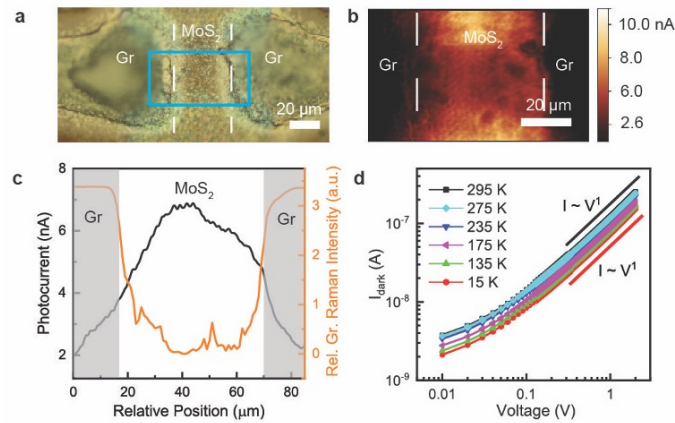


Figure 3.7: (a) Optical microscope image of the graphene-contacted MoS<sub>2</sub> photodetector. The area used for scanning photocurrent microscopy (SPCM) mapping is highlighted with the blue square. (b) The corresponding spatially resolved SPCM map of the scanned area. (c) Averaged horizontal line profile of the photocurrent and relative integrated graphene (Gr) Raman intensity derived from the SPCM image. (d) Current-voltage (I-V) characteristics under dark conditions of the graphene-contacted MoS<sub>2</sub> photodetector, revealing Ohmic behavior for voltages exceeding 0.1 V.

benchmark the model. An abrupt potential drop was observed where the top flake overlaps with the buried edge, suggesting that near-edge resistances limit transport at the junction due to weakly screened trapped charges. In this reporting period, Lauhon evaluated the predictions of the analytical model by imaging MoS<sub>2</sub>/MoS<sub>2</sub> homojunctions with different thicknesses, extracted near-edge resistances by discretizing the resistor network model to capture the measured potential profiles, and completed the physics-based model by including experimentally constrained parameters to simulate the on-state performance of printed 2D TFTs (Figure 3.9A). The edge and interface resistances created distinct tradeoffs when optimizing the microstructure, thus informing ink processing. If transport in the 2D network is limited by the near-edge resistance, the ink formulation must target micron-sized nanosheets to optimize the effective mobility, and the printed film must have a uniform nanosheet density to minimize device-to-device variations, which indicate that the exfoliation, sorting, and printing processes are all critical to TFT performance. If transport is limited by the inter-sheet resistance, then the microstructure generated by the state-of-the-art liquid phase exfoliation and printing is sufficient. Our work suggests that while exfoliation, ink formulation, and assembly processes have been developed to reduce inter-sheet resistance by improving microstructure (i.e., decreasing nanosheet thickness and increasing lateral size and overlap), in-situ and/or post-processing processes that passivate the nanosheet edges should be prioritized next to reduce the near-edge resistance by reducing the density of charged impurities.

By analyzing the potential drops in model transistors, the effective mobility and on-state conductance of partially overlapping nanosheets were found to be limited by the resistance produced by nanosheet edges due to their impact on carrier scattering and depletion. To examine the impact of edge resistance on the optimal microstructure of printed 2D TFTs, the effective mobilities  $\mu_{eff}$  of a device with a 10 μm channel were simulated in relation to the nanosheet thickness, size, and density. A single-sheet mobility of 100



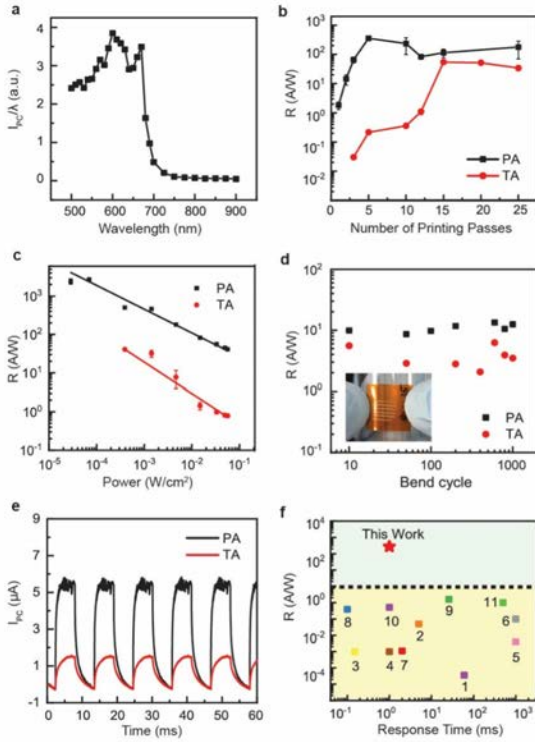
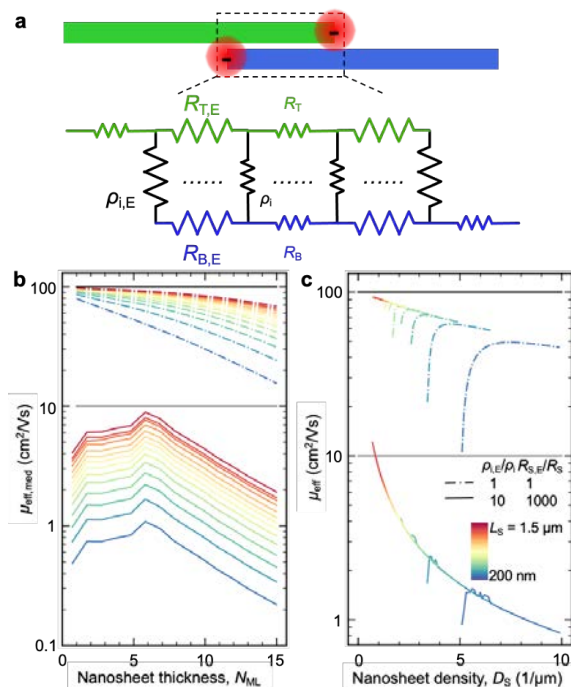


Figure 3.8: (a) Spectral response of the graphene-contacted MoS<sub>2</sub> photodetector. (b) Responsivity as a function of number of printing passes at 40 V using a 515.6 nm laser with an intensity of  $7 \times 10^{-5} W/cm^2$ . All error bars indicate one standard deviation from the mean. (c) Responsivity as a function of power. (d) Bending stability over 1000 bending cycles with a bending radius of 12 mm. (e) Time-dependent photocurrent at 20 V and 515.6 nm illumination. (f) Responsivity and response time comparison to all-printed visible photodetectors previously reported in the literature.

$cm^2V^{-1}s^{-1}$  was used to determine the optimal microstructure for achieving a target  $\mu_{eff}$  of  $10 cm^2V^{-1}s^{-1}$ . The near-edge sheet resistance ratio  $R_{S,E}/R_S = 1000$  and inter-sheet resistivity ratio  $\rho_{i,E}/\rho_i = 10$  were used, based on fitting experimentally measured potential profiles. When transport is limited by the near-edge resistance, an optimal nanosheet thickness is required (Figure 3.9B). Although thinner nanosheets reduce gate screening, the screening of charged impurities is weakened, thus resulting in lower  $\mu_{eff}$ . Moreover,  $\mu_{eff}$  increases monotonically with increasing lateral size due to the proportionally decreasing contribution of the near-edge resistance to the total channel resistance. For a MoS<sub>2</sub> TFT, the optimal nanosheet thickness was found to be 6 layers (4.2 nm), giving an  $\mu_{eff}$  of  $8.9 cm^2V^{-1}s^{-1}$  at the median density for a lateral size of  $1.5 \mu m$ , which is at the high end of liquid phase exfoliation. In contrast, the typical microstructure produced by liquid phase exfoliation has a smaller impact on film performance if transport is limited by the inter-sheet resistance. In this regime (i.e.,  $R_{S,E}/R_S = \rho_{i,E}/\rho_i = 1$ ),  $\mu_{eff}$  increases with decreasing thickness due to reduced gate screening by thinner nanosheets (Figure 3.9B). The effective mobility increases asymptotically with increasing nanosheet size, indicating that thinner nanosheets decrease the device-to-device variation. Given a single-sheet mobility of  $100 cm^2V^{-1}s^{-1}$ , MoS<sub>2</sub> nanosheets with a lateral size of 200 nm and a range of thicknesses from 1 layer to 15 layers are sufficient to achieve a  $\mu_{eff}$  of  $10 cm^2V^{-1}s^{-1}$ .

While the nanosheet thicknesses and sizes can be optimized through improved exfoliation and sorting, it is necessary to control the overlap and density by printing to minimize device-to-device variations. If transport is limited by the near-edge resistance, there is a general trend whereby  $\mu_{eff}$  decreases with increasing sheet density, the slope of which is larger at smaller density, suggesting that while increasing nanosheet size and decreasing density increases  $\mu_{eff}$ , the device-to-device variation becomes larger (Figure 3.9C). In contrast, the variation due to density is reduced in the inter-sheet resistance-limited regime,

Figure 3.9: (a) A resistor network model is used to simulate the on-state device characteristics of a two-nanosheet system containing fixed charge at flake edges.  $R_T$  and  $R_B$  represent the gate-dependent sheet resistances of the top and bottom nanosheets, respectively.  $\rho_i$  represents the specific inter-sheet resistivity. The near-edge resistivities are greater than those in the middle of the junction. (b) Effective mobility  $\mu_{eff,med}$  versus nanosheet thickness  $N_{ML}$  (i.e., number of monolayers per nanosheet) and length  $LS$  at the median density  $DS$  (i.e., number of nanosheets per channel length) for a particular  $LS$ . (c)  $\mu_{eff}$  versus  $DS$  and  $LS$  for devices consisting of 6 layers. The solid lines represent the near-edge resistance-limited regime where the near-edge sheet resistance ratio  $R_{S,E}/R_S = R_{T,E}/R_T = R_{B,E}/R_B = 1000$  and inter-sheet resistivity ratio  $\rho_{i,E}/\rho_i = 10$ , while the dashed lines represent the inter-sheet resistance-limited regime where  $R_{S,E}/R_S = \rho_{i,E}/\rho_i = 1$ . The color scale represents  $LS = 200\text{ nm}-1.5\ \mu\text{m}$ . The channel length is  $10\ \mu\text{m}$ . The single-sheet mobility is  $100\text{ cm}^2\text{V}^{-1}\text{s}^{-1}$ .



which is reflected by the smaller slope in the decrease of  $\mu_{eff}$  with density (Figure 3.9C). At lower density/smaller overlap, the junction resistance is limited by the inter-sheet resistance, resulting in a sharp decrease in  $\mu_{eff}$  with decreasing density, which indicates that film assembly/printing processes must be optimized to ensure sufficient coverage.

### 3.2.5 Designing Edge-Selective Functionalization to Improve Printed 2D Transistor Performance

Informed by the discovery that near-edge resistances limit transport at flake-flake junctions, **Lauhon** initiated an effort to design functionalization schemes for improving 2D ink performance in collaboration with **Marks**. Specifically, the effects of functional groups on the local structure and electronic properties of model  $\text{MoS}_2$  homojunctions with an exposed step edge were considered (Figure 3.10A). Since sulfur vacancies have been observed to dominate the edges of  $\text{MoS}_2$ , initial attempts utilized  $\alpha$ -lipoic acid, which contains a 1,2-dithiolane functional group that was predicted to covalently bind to sulfur vacancies. After 48 hours of functionalization in  $\alpha$ -lipoic acid performed by **Marks**, the molecule was found to functionalize both the basal plane and edges of  $\text{MoS}_2$  (Figure 3.10A, Figure 3.10B). Lauhon then used Kelvin probe force microscopy to measure the change in surface potential after functionalization. Before functionalization, the contact potential differences of 5 layer and 4 layer flakes are equal (Figure 3.10C), suggesting that they both reach the flat-band condition (Figure 3.10E). The surface band bending of few-layer  $\text{MoS}_2$  was modified after functionalization, where the work function of 5 layer flakes became higher than 4 layer flakes by 60 meV (Figure 3.10D). A likely explanation is that the molecules are passivating the sulfur vacancies on the surface of  $\text{MoS}_2$ , lowering the Fermi level and

increasing the work function (Figure 3.10F). As a next step, additional edge-selective functionalization schemes will be explored by strategically designing interactions of the molecule with edge sites and basal planes. For example, molecules with functional groups attached to long, non-polar chains are expected to chemically react with edge sites but only physisorb on the basal plane.

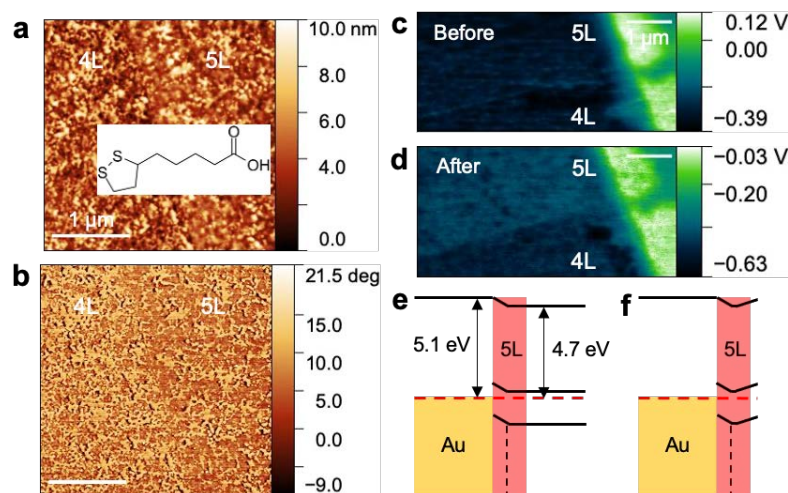


Figure 3.10: (a) AFM topography and (b) phase images of a 5 layer/4 layer junction after 48 hours of functionalization in  $\alpha$ -lipoic acid. The schematic shows the molecular structure of  $\alpha$ -lipoic acid, which contains a 1,2-dithiolane functional group. Kelvin probe force microscopy (KPFM) contact potential maps (c) before and (d) after functionalization, showing that the work function of the 5 layer flake became higher than the 4 layer flake. Schematics of the proposed surface band bending (e) before and (f) after functionalization.

### 3.2.6 Diazonium Functionalization of 2D Indium Monoselenide

In this effort, **Marks** collaborated with the **Hersam** to investigate the covalent functionalization and passivation of InSe flakes with 4-bromobenzene diazonium (Figure 3.11). A range of surface characterization techniques demonstrated that diazonium salts react with InSe, forming a covalently bound organic layer on the semiconductor surface. The structure of this layer can be tuned by varying the reaction conditions and by adding ascorbic acid or other reducing agents, which alter the reactivity of the diazonium salt. The use of a reducing agent (mediated reaction) was found to suppress side reactions that lead to multilayer growth, thus affording a smoother film compared to the non-mediated reaction (Figure 13.11A, Figure 3.11B). This result is the first example of covalent functionalization of InSe using organic reagents. Chemical modification of InSe sheets offers a way to tune their chemical, optical, and electronic properties. Importantly, this approach is also compatible with solution processing of InSe, allowing flakes to be modified in an ink before printing the semiconductor and fabricating devices.

To study the passivation and doping effects of diazonium functionalization, single-flake InSe TFTs were fabricated using a lithography-free shadow mask process (Figure 3.12). Upon functionalization, these n-type transistors retain high mobilities ( $10^2 - 10^3 \text{ cm}^2/\text{Vs}$ ) and on/off ratios ( $> 10^6$ ). A slight drop in performance can be mitigated by limiting the reaction time to achieve a lower level of functionalization. The charge transport data indicate that diazonium chemistry modifies the surface of InSe without negatively affecting

the electronic performance, thus demonstrating that this chemical modification scheme is a promising strategy for passivating InSe in 2D inks.

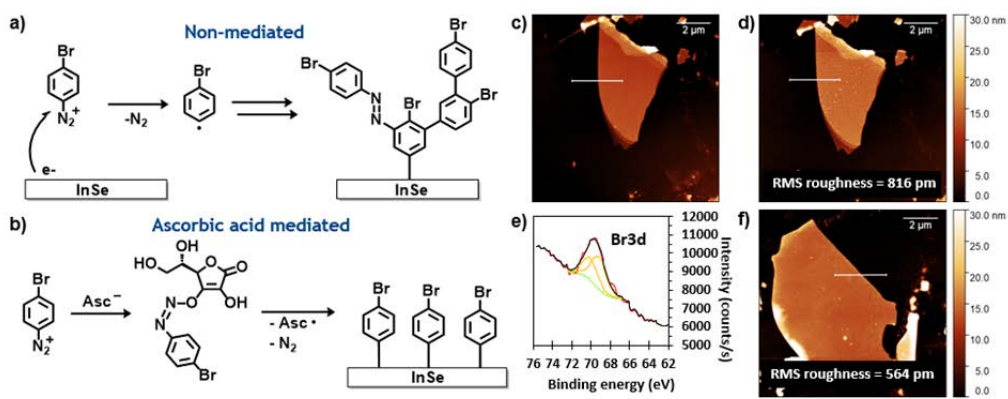


Figure 3.11: Reaction schemes for the non-mediated (a) and ascorbic acid mediated (b) reactions of 4-bromobenzene diazonium with InSe. AFM images of an InSe flake before (c) and after (d) the non-mediated reaction, demonstrating the formation of a 2 nm thick layer on the semiconductor surface. (e) Br 3d X-ray photoelectron spectrum of InSe functionalized by the non-mediated process, indicating the presence of bromophenyl groups in the surface layer. (f) AFM image of an InSe flake after mediated functionalization shows a smoother organic layer compared to (d).

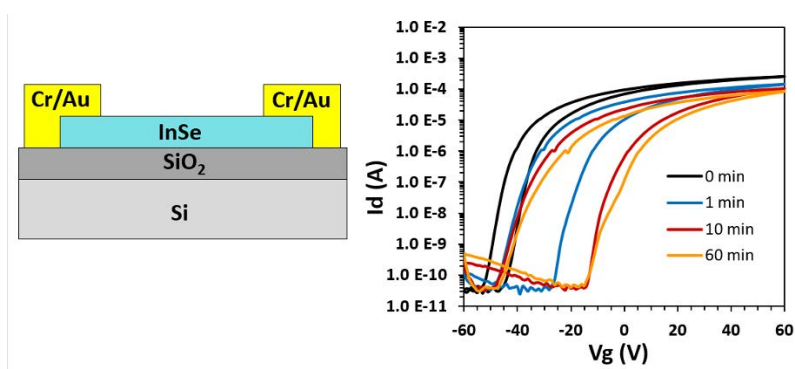


Figure 3.12: (left) Structure of the InSe TFTs used in this study. (right) TFT transfer characteristics for various functionalization reaction times (non-mediated reaction).

### 3.2.7 Trifluoromethylation Based Passivation of 2D Semiconductors

In this project, **Marks** explored trifluoromethylation of 2D materials for the first time. Hydrophobic trifluoromethyl groups are expected to protect the surface of 2D materials from ambient water and oxygen while acting as a p-type surface dopant through a strongly withdrawing inductive effect. In collaboration with **Hersam**, trifluoromethyl thianthrenium triflate (TTT), a versatile new reagent developed for the fluoroalkyl functionalization of organic molecules, was used to functionalize a variety of 2D materials with trifluoromethyl groups. AFM and XPS measurements indicate that TTT deposits trifluoromethyl groups on the surface of 2D chalcogenides, namely  $MoS_2$ ,  $WSe_2$ , and InSe (Figure 3.12). These reactions proceed under mild conditions and afford a dense surface layer of trifluoromethyl groups. Importantly, Raman spectroscopy indicates that this reaction does not affect the crystal structure of the functionalized semiconductor. Optical characterization of the

functionalized semiconductors indicates that trifluoromethylation of the surface modulates the optoelectronic properties of the material. Both  $\text{MoS}_2$  and  $\text{WSe}_2$  exhibit considerable photoluminescence quenching following the reaction, which persists after mild thermal annealing. These results provide further evidence for covalent functionalization of the 2D flakes. Tuning the reaction conditions with TTT may allow for deposition of trifluoromethyl groups on other 2D materials beyond chalcogenides, as well as controlling the structure and density of the surface layer.

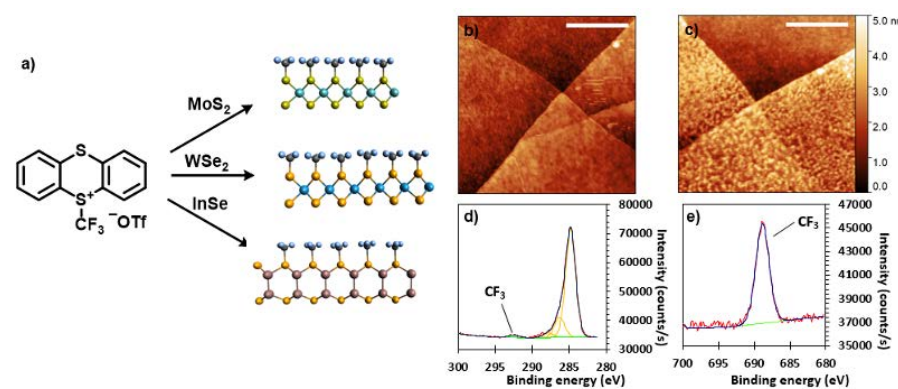


Figure 3.13: (a) Chemical structure of TTT and scheme of the trifluoromethylation reaction resulting in the grafting of  $\text{CF}_3$  groups on  $\text{MoS}_2$ ,  $\text{WSe}_2$ , and  $\text{InSe}$ . AFM of pristine (b) and functionalized  $\text{MoS}_2$  (c), showing the deposition of a dense surface layer. Scale bars = 500nm. (d) C1s and (e) F1s XPS scans showing signature peaks corresponding to  $\text{CF}_3$  on  $\text{MoS}_2$ .

### 3.2.8 Computational Design of Heterostructure Materials for Printed 2D Semiconductor Photodetectors

$\text{MoS}_2$  is a well-known and widely used semiconductor for photodetectors due to its large optical absorption coefficient and efficient carrier generation upon photoexcitation. Recently, multiple heterostructures have been reported in the literature where monolayer  $\text{MoS}_2$  is interfaced with another 2D semiconductor to form heterojunctions that improve photoresponse time and photoresponsivity. In an effort to computationally screen optimal 2D heterojunctions for photodetectors, several of the Ruddlesden-Popper (RP) halide perovskites of the form  $\text{Cs}_2\text{XY}_2\text{Z}_2$  (where X is a transition metal while Y and Z are halogens) were investigated by **Wolverton** group based on their photodetection-related performance when incorporated into heterostructures with monolayer  $\text{MoS}_2$  (Figure 3.14) using density functional theory (DFT). Several properties of the resulting heterostructures were computed including electronic band structure, in-layer carrier transport properties, interfacial charge transport characteristics, and optical absorption coefficients. These properties together provide a reliable estimate of the heterostructure photodetection capabilities. Out of more than 140 RP- $\text{MoS}_2$  lattice stackings, 87 cases were identified to form a heterostructure with a minimal level of lattice strain (<5%).

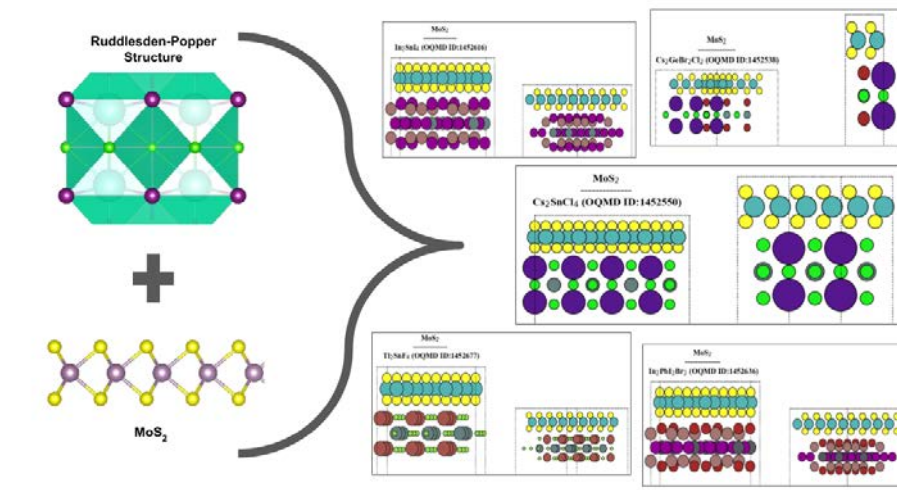


Figure 3.14: (left) Heterostructures are considered computationally from a cleaved Ruddlesden-Popper perovskite structure and monolayer MoS<sub>2</sub>. (rights) A few representative heterostructures that were created using lattice-alignment methods.

## 4. Grain Boundary and Interface Engineering in Thermoelectrics

**Jeffrey Snyder (NU)**, Christopher Wolverton (NU), Changning Niu (QuesTek)

**Martin Green (NIST), Joshua Martin (NIST)**

### 4.1 Design Goals

The Grain Boundary and Interface Engineering in Thermoelectrics Use Case group seeks to apply developments in space-age technology to transform the cooling industry through thermoelectric materials enhancement. We seek to develop high-efficiency thermoelectric materials by improving the thermoelectric figure of merit,  $zT$ , which requires increasing electronic mobility and reducing thermal conductivity.

By applying an integrated computational-experimental approach, the use case group aims to improve the efficiency of thermoelectric materials by improving the figure-of-merit  $zT$ , particularly near room temperature. Optimization of  $zT$  requires increasing charge carrier mobility while reducing the thermal conductivity and is an inherently a multi-scale problem. The atomic structure and composition of the material will determine the electronic structure, and largely defines important intrinsic material properties like Seebeck and conductivity effective mass. The carrier concentration must then be optimized through extrinsic doping. The choice of dopant is determined by its solubility, doping efficiency, and its potential deleterious effects on carrier mobility. Finally, the nano-/microstructure generated by the defect and strain state of a material can determine the speed and lifetime of heat-carrying lattice vibrations. The system design chart below shows the relationship between processing steps and properties in addition to the interrelatedness of thermoelectric properties that leads to a challenging optimization problem. In our use case, the use-case group heavily relies on first-principles theory and analytic physics-based modelling to understand each of the connections shown in the System Design Chart in Figure 4.1.

Another unique attribute of thermoelectric research is the large body of existing literature and high-throughput DFT data available, which has recently become available through open-sourced databases including: (1) *StarryData2*, developed by University of Tokyo and National Institute of Materials Science, Japan (<https://www.starrydata2.org>) and; (2) the *MPContribs Carrier Transport Database* co-developed by **Snyder** (<https://>

contribs.materialsproject.org/projects/carrier\_transport/). The use-case group members heavily rely on this body of data both for new materials discovery and as a test bed for our analytic physics models.

Additionally, the principles developed here both about engineering electrical and thermal transport as well as phase equilibria in multicomponent semiconductors are applicable beyond thermoelectrics. For example, the group's investigations into heat-carrying vibrations are not only useful for decreasing the thermal conductivity in a thermoelectric module, they may also be used to optimize switchable thermal properties in the development of a thermal diode.

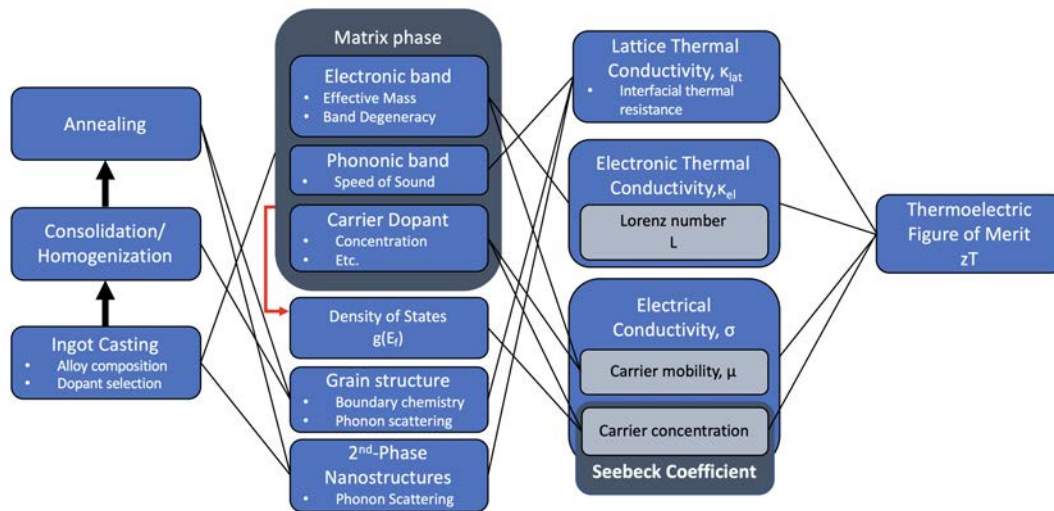


Figure 4.1: The System Design Chart for the Grain Boundary and Interface Engineering in Thermoelectrics use case group

## 4.2 Research Accomplishments

The accomplishments of the Grain Boundary and Interface Engineering in Thermoelectrics use case group in 2021 are as follows:

### 4.2.1 Phase Boundary Mapping

The energetics of defects play a key role in determining the shape of the phase boundaries. Given the dependence of properties such as carrier concentration and Seebeck coefficient on the location of phase diagram in which the compound lines, part of our 2021 research efforts focused on understanding how the energetics of defects shape the phase diagram. We further outlined how slight variations in nominal and actual compositions of experimental compounds may occur due to the chemical conditions present during processing which may lead to marked differences in expected and realized properties of the compounds. Subsequently, we detailed how the choice of chemical conditions can be used to tune defect concentrations and thus the solubilities of dopants to realize the maximum solubility in the system.



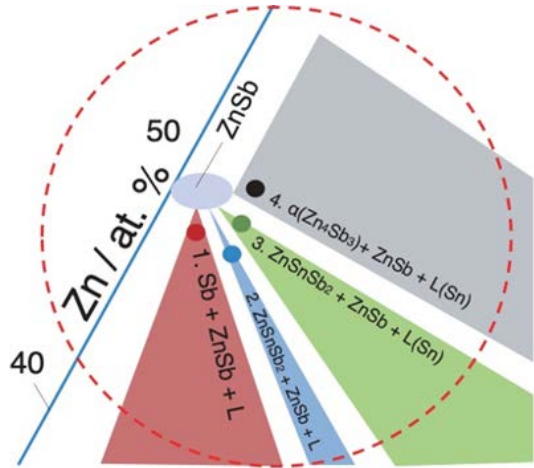


Figure 4.2: The phase diagram zoomed into the ZnSb composition shows four distinct three-phase regions accessible by doping ZnSb with Sn. The defect concentrations, and subsequently the charge carrier concentrations, in ZnSb will be different in each region. The compositions of the four samples presented in this study are indicated by the four points in the phase diagram.

### 4.2.2 Mechanical Properties of Thermoelectric Materials

Dislocations and the residual strain they produce are instrumental for high thermoelectric figure of merit, in lead chalcogenides. However, these materials tend to be brittle, barring them from practical green energy and deep space applications. Nonetheless, the bulk of thermoelectrics research focuses on increasing  $ZT$  without considering mechanical performance. Optimized thermoelectric materials always involve high point defect concentrations for doping and solid-solution alloying. Brittle materials show limited plasticity (dislocation motion), yet clear links between crystallographic defects and embrittlement are hitherto unestablished in PbTe. In recent work, we identified links between dislocation/point-defect interactions and brittleness through Vickers microhardness measurements in single crystal and polycrystalline PbTe samples with varied dopants. Varied routes of point defect-dislocation interaction restrict dislocation motion and drive embrittlement: Dopants with low doping efficiency cause high defect concentrations, interstitial n-type dopants (Ag and Cu) create highly strained obstacles to dislocation motion, and highly mobile dopants can distribute inhomogeneously or segregate to dislocations. These results illustrate the consequences of excessive defect engineering and the necessity to consider both mechanical and thermoelectric performance when researching thermoelectric materials for practical applications.

### 4.2.3 Thermal Transport

Both within-grain and interfacial dislocations play an important role in modulating thermal transport. Dislocations perturb phonon transport both through the bond registry at the dislocation core but also through the long-range strain fields, which induce both anharmonic phonon scattering as well as lattice softening (speed of sound reduction) effects. In 2021, the **Snyder** group assessed the role of dislocations in thermal transport from the standpoint of theory, experiment, and computation. From a theory standpoint, a continuum-level model was developed to predict the interfacial thermal resistance of low-energy interfaces that are composed of dislocation arrays. By accounting for the phonon scattering due to the periodic strain fields produced by these interfacial dislocations, we describe a novel type of phonon scattering at an interface, termed *diffractive scattering*. As shown in Figure 4.4 below, the *diffractive scattering models* sits between two common approximations for phonon scattering at an interface: 1) the *acoustic mismatch model* which assumes specular reflection or transmission and 2) the *diffuse mismatch model* which assumes fully diffuse scattering. Instead, in this work, the dislocation array at the interface acts

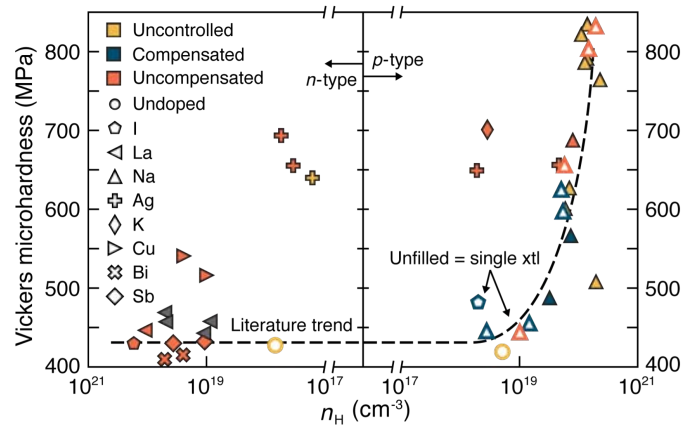


Figure 4.3: Measured Vickers microhardness at different  $n$  and  $p$ -type Hall carrier concentrations ( $n_H$ ) for single crystal ((100) face) and polycrystalline PbTe samples with varied dopants of different ionic sizes. By inspection, crystallinity and ionic size are shown to be insignificant for the defining hardness trend. Samples that were phase boundary mapped to fix intrinsic defect concentrations are colored blue (low intrinsic defects "uncompensated") or orange (high intrinsic defects/"compensated"). Some clear deviations from literature trends are shown, demonstrating where interstitial dopants ( $n$ -type Cu and Ag) and low doping efficiency samples ( $p$ -type samples with K, Ag and I) lead to high hardness.

as a diffraction grating for phonons, leading to certain allowed phonon transitions at the interface. This work reproduces trends observed in experiment and simulation (but not captured in previous analytic theory) between interfacial thermal resistance and grain boundary type and angle.

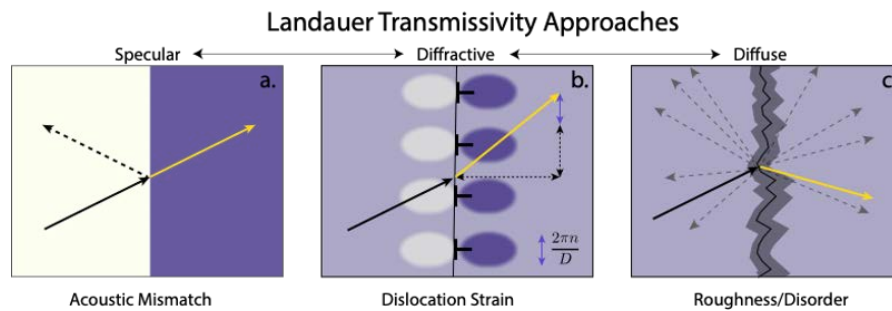


Figure 4.4: Schematic illustrations of phonon-interface scattering models. (a) The acoustic mismatch model across leads to a specular reflection or transmission in analogy to Snell's (b) Our model treats the periodic arrays of dislocations present at many low-energy interfaces. The dislocation array can impart quantized momentum in units of  $2\pi/D$ , where  $D$  is the dislocation spacing. (c) Interfaces serve as a sink for point defects, leading to additional roughness and compositional disorder. In a case of maximal roughness, one can apply the diffuse mismatch model in which the only conserved quantity across the interface is phonon energy.

Molecular dynamics simulations were also used to assess the phonon scattering due to dislocation core and strain effects, separately. With the applied periodic boundary conditions, the dislocations investigated were also arranged in arrays forming low angle grain boundaries. The simulations revealed that dislocation strain is particularly effective in scattering mid-frequency phonons, which constitute a difficult-to-target range of the

phonon spectrum. Other scattering effects such as phonon-phonon interactions and point defect scattering tend to target high-frequency phonons, while simple boundary scattering targets the low-frequency phonon range. Finally, atom probe tomography measurements of dislocations in PbTe (see Figure 4.5) revealed the importance of compositional variation near the dislocation core in phonon scattering. Dopant segregation at the dislocation core led to increased phonon scattering, which was explained as modified lattice anharmonicity in the vicinity of the dislocation.

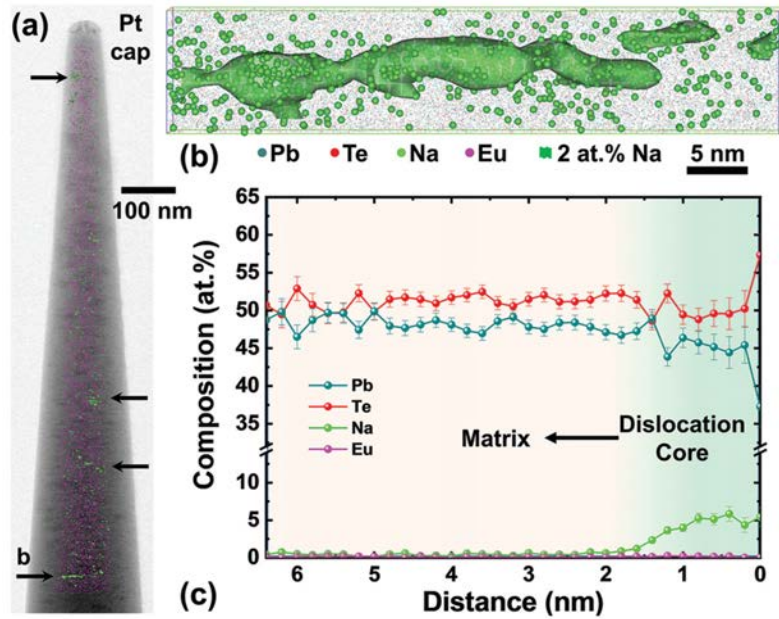


Figure 4.5: Atom probe tomography showing Na dopant segregation to dislocation cores. a) ABF-STEM image of a needle-shaped APT specimen. Iso-composition surfaces of 2 at% Na are highlighted in green, and dislocations are indicated by arrows. b) Magnified image of the bottom of the needle showing the atomic distribution of Na in the vicinity of a dislocation. c) Composition profile near the dislocation core showing the formation of Na-rich atmosphere.

#### 4.2.4 Investigation of Weak-bonding Elements' Influence on Thermoelectric Transport

By screening the Open Quantum Materials Database (OQMD, [www.oqmd.org](http://www.oqmd.org)) with SnS<sub>2</sub>-adjacent phase diagram, **Wolverton** group found two compounds with SnS<sub>2</sub> analogue crystal structure, BaSnS<sub>3</sub> and SrSnS<sub>3</sub>, where Ba and Sr form weak bonding with Sn-S framework. The crystal structure of BaSnS<sub>3</sub> is shown in Figure 4.6. Analyzing the two compounds help us understand the influence of weak-bonding elements in highly symmetric polarized systems resembled SnS<sub>2</sub>. Ba and Sr disturb the bonding between Sn-S, neutralize the polarity of Sn-S ionic covalent bonding, leading to the delocalization of free electrons, and thus the increase of carrier mobility. Structural distortion induced by Ba and Sr also results in differentiation of S, which contributes to the splitting of valence band edge and triggers band convergence. Regarding the heat transport, Ba and Sr soften the lattice and enhance the lattice anharmonicity. More importantly, their weak coherence with Sn-S matrix give rise to local vibration, which induces strong acoustic-optical phonon coupling, significantly increase the phonon scattering rate in the system. In all, our full-scale thermoelectric transport properties calculations based on non-empirical carrier and

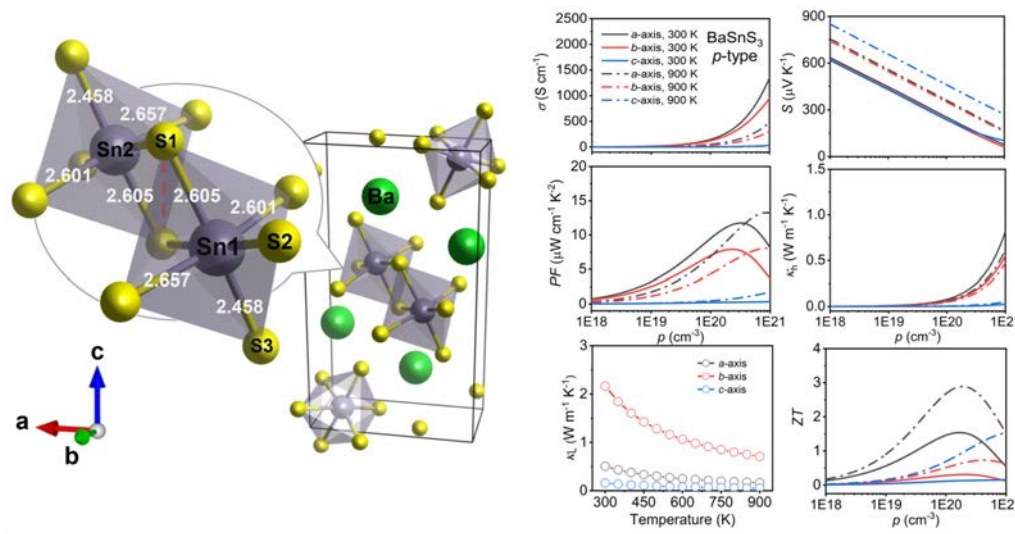


Figure 4.6: Crystal structure of  $\text{BaSnS}_3$ . On the right are full-scale calculated electrical and thermal transport properties of p-type  $\text{BaSnS}_3$  with respect to hole concentration or temperature.

phonon relaxation time reveal the synergic optimization on electrical conductivity, Seebeck coefficient, and lattice thermal conductivity compared to  $\text{SnS}_2$ , which eventually leads to the promising calculated  $ZT \sim 3.0$ .

#### 4.2.5 Rapid Screening of Low Thermal Conductivity Materials using Chemical Bonding Principles

Semiconductors with very low lattice thermal conductivities ( $\kappa_L$ ) are highly desired for applications relevant to thermal energy conversion and management, such as thermoelectrics and thermal barrier coatings. In this project, **Wolverton group** presented effective strategies to induce low lattice thermal conductivity using chemical bonding principles. This strategy is based upon weakening the interatomic interactions and therefore suppressing lattice thermal conductivity in materials. Utilizing the new chemical bond principles, they demonstrated a high-efficiency approach of discovering low  $\kappa_L$  materials by screening the local coordination environments of crystalline compounds. First-principles calculations uncover 30 hitherto unexplored compounds with (ultra)low lattice thermal conductivities from 13 prototype crystal structures (Figure 4.7) contained in the Inorganic Crystal Structure Database. In addition, they also presented an approach of rationally designing high-performance thermoelectrics with the incorporation of cations with stereochemically active lone-pair electrons.

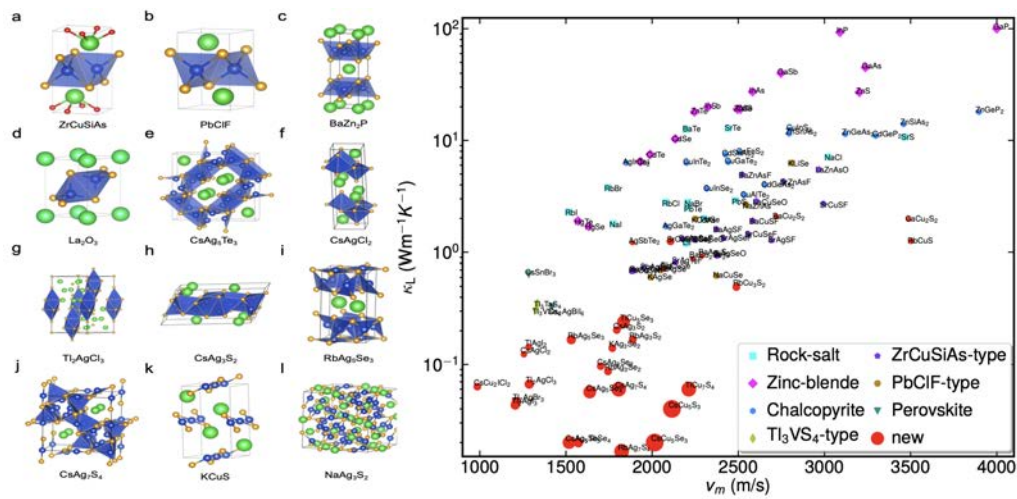


Figure 4.7: Newly discovered prototype structures with low thermal conductivity and lattice thermal conductivities of the compounds as a function of average speed of sound.





## 5. Design of Properties of Polyelectrolyte Complexes

Matthew Tirrell (UC), Juan de Pablo (UC), Monica Olvera de la Cruz (NU), Muzhou Wang (NU), Kenneth Shull (NU)

Vivek Prabhu (NIST), Debra Audus (NIST), Jack Douglas (NIST)

### 5.1 Design Goals

The integrated goals of this Use Case constitute what we call the *8M program: Molecules, Mixtures, Micelles, Materials, Measurement, Moduli, Modelling, Manufacturing*. We use custom-synthesized macromolecules (M1) to study the phase diagrams of complexation in mixtures (M2) of polyelectrolytes and to exploit the micellar (M3) self-assembly possibilities resulting from interaction of charged macromolecules. Self-assembly via complexation is being used to create micelles, encapsulating materials, hydrogels, coatings, and composite materials, all based on charge complexation and ionic interactions as the underlying mechanisms. (M4). Data on phase behavior and micellization routes to new materials are input into searchable databases. Rheological measurement (M5) gives insight into moduli (M6), viscosity, and other viscoelastic properties. Predictive modelling and simulation (M7) of both phase behavior and self-assembly is increasingly advanced. This fundamental work is input into processing and eventually manufacturing, methods (M8) for soft materials based on electrostatic complexation. The ultimate goal is to write down the structure of a set of synthesizable charged macromolecules and, from that structure, be able to know with confidence the properties of the final material, and then, with deeper insight, to do the reverse.

The Use Case is mapping out the phase behavior space of polyelectrolyte complexes and bringing advanced theoretical and computational methods into play to deliver predictive design insight for these materials. The system design chart in Figure 5.1 shows the processing-structure-properties-performance work flow for the Design of Properties of Polyelectrolyte Complexes Use-Case Group.

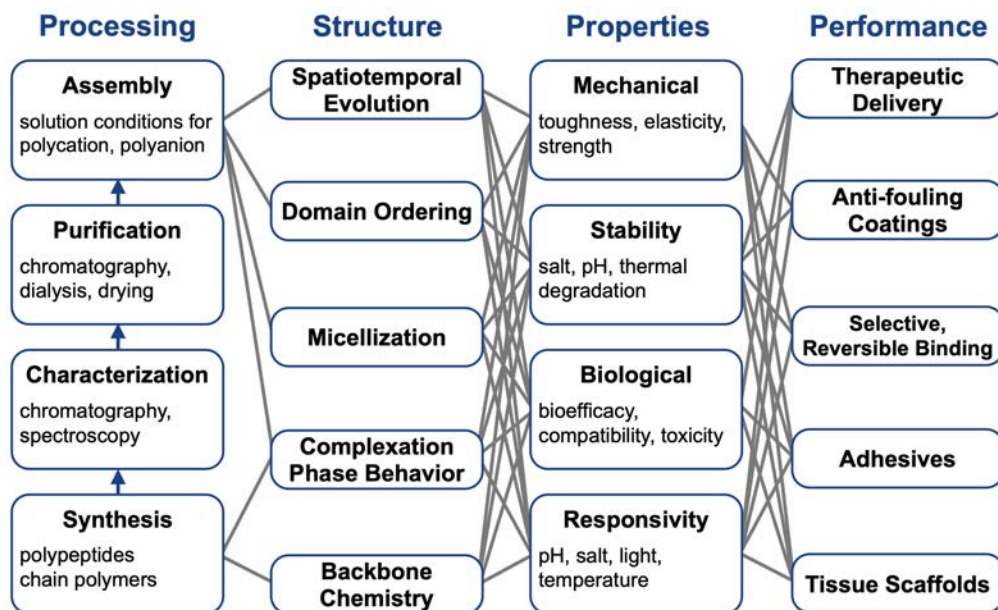


Figure 5.1: Systems design chart for soft matter design based on charged macromolecules

## 5.2 Research Accomplishments

### 5.2.1 Processing polyelectrolyte complexes with deep eutectic solvents

Polyelectrolyte complexes (PECs) formed from mixtures of polycations and polyanions are useful in a variety of applications and can be processed by the addition of salt. Salt mediates the ionic interactions within the polyelectrolyte complexes, with appropriately chosen salts enabling complete dissolution of solid PEC in aqueous media. Substantial complications arise from the crystallization of the salt during subsequent processing steps. **Shull** group has shown that appropriately chosen noncrystallizing deep eutectic solvents can be used to process solid PECs. Mixtures of ethylene glycol and guanidine thiocyanate are used for a particularly effective deep eutectic solvent. The phase behaviors of this deep eutectic system and of its mixtures with a model polyelectrolyte complex were quantified.

### 5.2.2 Diffusion in dense polyelectrolyte systems

Previous and ongoing efforts in this Use Case have mapped the thermodynamics, self-assembly, and interfacial properties in polyelectrolytes. The work in Phase II will now explore dynamic properties, including rheology and diffusion, with the goal of tabulating them into databases to speed materials design for other users. For example, understanding diffusion is important for designing the transport and delivery of drugs and therapeutics.

**Wang** contribution to this effort is through the measurement of polyelectrolyte diffusion in solutions and complexes. We are using advanced optical techniques called single-particle tracking (SPT), where videos of fluorescently-labeled species are acquired on an optical microscope. By analyzing these videos, we can then determine the real-time positions of single polymer chains to tens of nanometer precision and millisecond time scales. Further analysis can determine mean-squared displacements and van Hove distributions to extract diffusion coefficients. Additionally, SPT can examine heterogeneous diffusion, i.e. when some polymer chains are more mobile than others, when single polymers switch between mobile and immobile states, when diffusion is non-Fickian, etc. Such behavior is



potentially possible in polyelectrolyte complexes, as these systems are highly interacting and these associations provide many physical barriers to unrestricted Brownian motion.

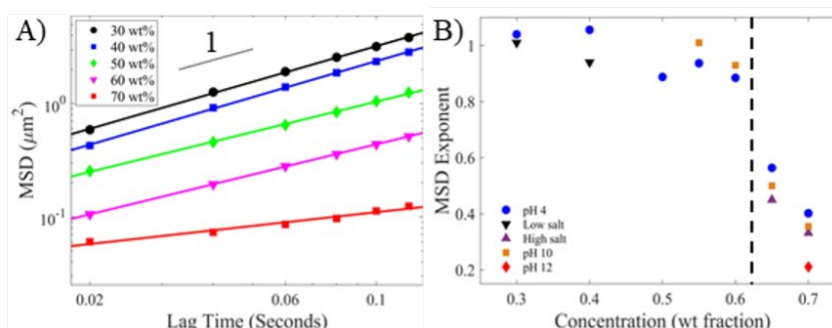


Figure 5.2: A) Mean-squared displacement vs. time of various concentrations of poly(D,L-lysine) hydrobromide in water. B) The exponents of MSD vs.  $t$  at the different concentrations. Data from (A) is labeled as “pH 4,” as this was the native pH when the polymer was dissolved in pure water. “Low salt” was when the HBr was removed by ion exchange chromatography. “High salt” was when 1 M of NaCl was added.

During this reporting period, our group has successfully performed SPT on concentrated polyelectrolyte solutions and shown strong evidence for sub-diffusive non-Fickian diffusion behavior. Using solutions of poly(D,L-lysine) in water, where a small fraction of the polymers were labeled with a Cy3 fluorophore, we found that mean-squared displacement (MSD) vs. time showed power law behaviors that were significantly less than one, at concentrations of 60 wt% and above. We further explored this behavior under various pH and salt concentrations, and it seems to be universal over all conditions. Preliminary experiments on concentrated solutions containing both poly(D,L-lysine) and poly(D,L-glutamic acid) (coacervates) show similar behavior. These results are quite surprising, as sub-diffusive behavior suggests that there are obstacles hindering free motion of the polymers, yet the length scales of this phenomenon seem to extend into 102-103 nm, which is much larger than the size of the polymer chains. It may be related to literature that has suggested long-range correlations and multiple modes of diffusion in polyelectrolyte solutions. We are verifying this phenomenon by collecting even more conditions, and also conducting parallel studies of structural heterogeneity using small-angle neutron scattering (SANS).

An important control experiment for the polyelectrolyte solutions is to also measure neutral polymers. Using aqueous solutions of a custom-synthesized poly(oligoethylene glycol methacrylate) (PEGMA), we have largely not seen the subdiffusive behavior that was present in the polyelectrolyte systems. Instead, our work has shown a bifurcation in the population of MSD vs. time trajectories. This is a strong indication of the coexistence of slow- and fast-diffusing species within our system. The diffusion of both of these species becomes slower with increasing concentration, and obeys the expected scaling relationships. We hypothesize that this two-species effect arises due to hydrophobic clustering of the methyl end groups on the PEG side chains, as seen in prior literature. This was confirmed by SPT experiments in methanol, where the clustering effect is attenuated.

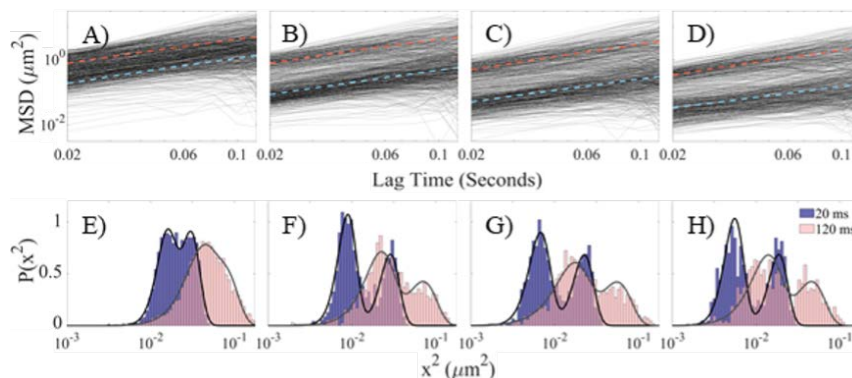


Figure 5.3: MSD vs. time of individual trajectories of PEGMA in water at concentrations of A) 30 wt%, B) 40 wt%, C) 50 wt%, and D) 60 wt%. The red and blue dotted lines are linear fits to populations above and below the bifurcation. E-H) Histograms of the MSD values at 20 and 120 ms are shown at the various concentrations, with a fit of the expected probability distributions for two independently diffusing species.

### 5.2.3 Modeling-based design to engineering protein hydrogels with random copolymers

Inside living organisms, protein enzymes participate in vital processes and perform numerous chemical reactions. In addition, protein enzymes possess a great technological potential. The operation of protein enzymes in technological applications is often required at high temperature, high or low pH, and in organic solvents. In such harsh conditions, however, enzymes undergo denaturation leading to a loss or decline of their activity. Thus, new methods are necessary to preserve the enzymes' functionality outside their native environment. Polymers are promising as supporting materials to immobilize, stabilize, and preserve the enzymatic activity of protein enzymes. In particular, charged polymers offer a simple way to control the direct enzyme-polymer self-assembly using the electrostatic interactions. In addition, ion-containing polymers have important applications in energy storage and conversion, and in water purification and gas separation membranes, to name a few. Using coarse-grained molecular dynamics simulations, the **Olvera de la Cruz** group (ACS Nano 15, 16139-16148 (2021)) performed a modeling-based design to engineering hydrogels formed by the enzymes cytochrome P450 and PETase and the random copolymers of styrene/2-vinylpyridine (2VP)1 (see Figure 5.4a,b). By tuning the copolymer fraction of polar groups and of charged groups via quaternization of 2VP for coassembly with cytochrome P450 and via sulfonation of styrene for coassembly with PETase, we provide quantitative guidelines to select either a protein-polymer hydrogel structure or a single-protein encapsulation. Regardless of the protein surface domains, we find that the presence of polar interactions and hydration effects promote the formation of a more elongated enzyme-polymer complex, suggesting a membrane-like coassembly (see Figure 5.4c). In addition, we observe single-protein encapsulation by decreasing the fraction of polymer polar groups and at charge fractions below 15%. According to our computational analysis, the hydrophobic interactions promote the enzyme-polymer assemblies, which lead the protein nonpolar residues to achieve the maximum coverage and to play the role of the most robust contact points. The mechanisms of coassembly are unveiled in the light of both protein and polymer physical-chemistry, providing bioconjugate phase diagrams for the optimal material design. According to the computational analysis, the hydrophobic interactions promote the enzyme-polymer assemblies, which lead the protein

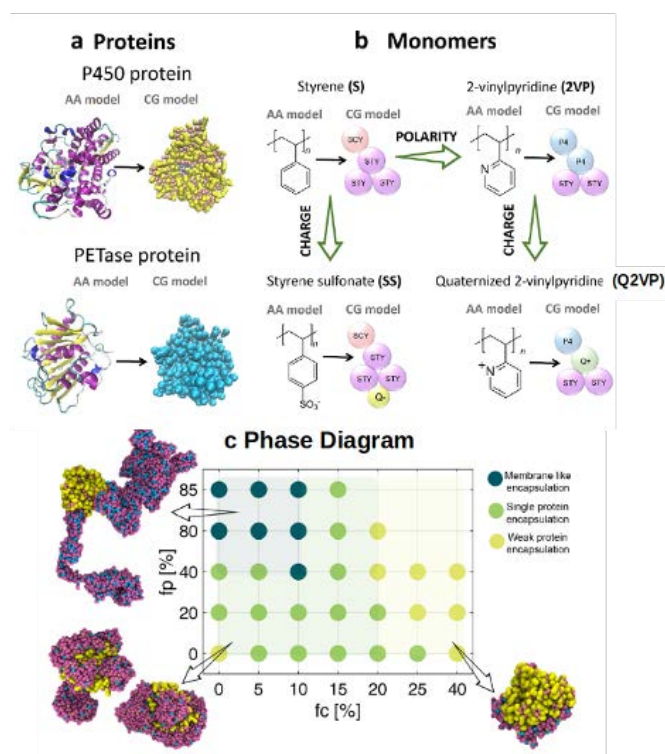


Figure 5.4: Coarse-grained models and simulation setup. (a) Cytochrome P450 and PETase enzymes in both all-atom (AA) and Martini coarse-grained representations. (b) The supporting materials are polymers formed by four monomers (shown in all-atom (AA) and coarse-grained (CG) representations). The negatively charged (-15e) P450 is combined with neutral polar PS-2VP (i) and positively charged (PS-Q2VP (ii) and PS-2VP-Q2VP (iii)) random copolymers. The positively charged (+6e) PETase is coassembled with neutral polar PS-2VP (i), and negatively charged (PSS (ii) and PSS-2VP (ii)) heteropolymers. The  $f_p$  and  $f_c$  fractions are tuned by altering the number of polar ( $N_{\text{polar}}$ ) and charged ( $N_{\text{charged}}$ ) monomers, respectively, over the total number of monomers ( $N_{\text{tot}} = 60$ ) in one single polymer chain. (c) Phase diagram of polymer-P450 enzyme complexes. By tuning the polymer polar ( $f_p$ ) and charged ( $f_c$ ) fractions, we identify three main modes: (i) the membrane-like coassembly displayed with dark green points, (ii) the single-protein encapsulation marked with light green points, and (iii) the weak encapsulation depicted with yellow points.

nonpolar residues to achieve the maximum coverage and to play the role of the most robust contact points. The mechanisms of co-assembly are unveiled in the light of both protein and polymer physical-chemistry, providing bioconjugate phase diagrams for the optimal material design.

#### 5.2.4 Probing the size-dependent polarizability of mesoscopic ionic clusters and their induced-dipole interactions

Ionic clusters composed of oppositely charged mobile species are present in a wide variety of applications including heavy-metal emulsions for recycling and separations, ionomer melts for energy storage, and protein-polymer and protein-colloid nano-assemblies for biocatalysis. Controlling the stability and aggregation of these ionic clusters in solution is of paramount importance in a number of processes and therefore it is necessary to understand their interactions. The polarizability is the ability of the cluster's charges to re-arrange in response to an external electrical field. The cluster's polarizability determines the effective interaction between the clusters. To understand how the interactions between

ionic clusters are affected by their polarization, the **Olvera de la Cruz** group investigated different systems of mesoscopic polarizable electrically neutral clusters using coarse-grained molecular dynamics simulations (J. Chem. Phys. 155, 194901 (2021)). It is found that the polarizability of the ionic clusters decreases as the number of constituent charges increases and/or their Coulombic interaction strength increases for various ion valences, ion densities, and degrees of cluster boundary hardness. Similarly, the polarizability of clusters formed by random ionomers and their counter ions changes with the number of polymer chains.

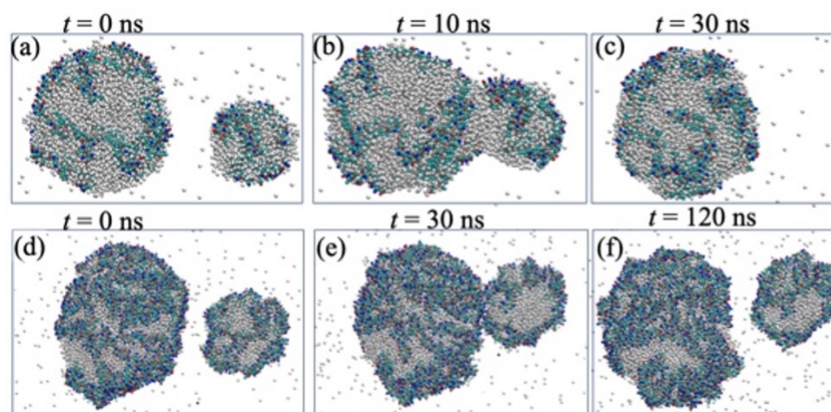


Figure 5.5: Coarse-grained (MARTINI) simulation of two polyelectrolyte clusters in polarizable water. (a-c) Two clusters 1 and 2 containing 48 and 132 charged pairs, respectively, merge into a single droplet after 20 ns. (d-f) Clusters 3 and 4 containing 264 and 1224 charged pairs, respectively, repel each other when they come in contact and remain their entity after more than 120 ns.

Neutral ionic clusters containing a small number of charges are highly polarizable and therefore are attracted towards a larger cluster containing more charges. Figure 5.5 (J. Chem. Phys. 155, 194901 (2021)) contains snapshots from molecular dynamics simulations showing the interaction between two ionic clusters. Figure 5.5a-c, correspond to a simulation of the two clusters that have a small number of charges. At  $t = 0$ , the clusters are separated. During the simulation, the clusters attract to each other and merge to form a single larger cluster. On the contrary, in clusters containing a larger number of charges the induced-dipole interactions decrease substantially leading to repulsive interactions. Figure 5.5d-f, correspond to a simulation of two clusters that have a large number of charges. The clusters may approach due to the forces exerted by the surrounding liquid, however, at short distances they repel due to the dipole-induced interactions. Therefore, it is concluded that the dipole-induced interactions can serve as a counterbalancing force that contributes to the self-limiting aggregation of charge-containing assemblies.

### 5.2.5 A perspective on the design of ion-containing polymers for polymer electrolyte applications

Ion-containing polymers have numerous potential applications as energy storage and conversion devices, water purification membranes, and gas separation membranes, to name a few. Given the low dielectric constant of the media, ions and charges on polymers in a molten state interact strongly producing large effects on chain statistics, thermodynamics, and diffusion properties. In this perspective (J. Phys. Chem. B 125, 3015-3022 (2021)) the **Olvera de la Cruz** group we discuss recent research accomplishments on the effects

of ionic correlation and dielectric heterogeneity on the phase behavior of ion-containing polymers and the progress made in studying ion transport properties in these material systems. Charged block copolymers (BCPs), among all kinds of ion-containing polymers, have a particular advantage owing to their robust mechanical support and ion conducting paths provided by the segregation of the neutral and charged blocks. Coulombic interactions among the charges play a critical role in determining the phase segregation in charged BCPs and the domain size of charge-rich regions (see Figure 5.6, *J. Phys. Chem. B* 125, 3015-3022 (2021)). We show that strongly charged BCPs display ordered phases as a result of electrostatic interactions alone. In addition, bulky charge-containing side groups attached to the charged block lead to the formation of morphologies that provide continuous channels and better dissociation for ion conduction purposes. Finally, a few avenues for designing ion-containing polymers for energy applications are discussed.

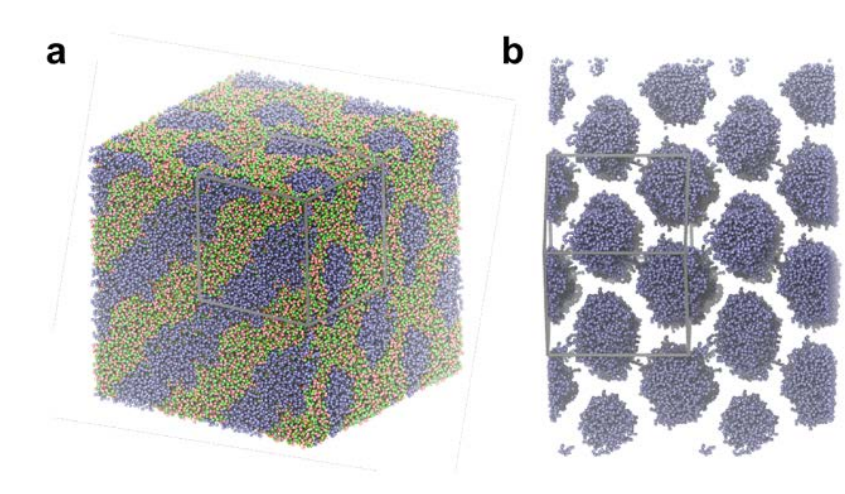


Figure 5.6: Hexagonal cylinder phase formed in charged diblock copolymers represented by pendant model consisting of  $N_A = N_B = 20$  charged and neutral blocks, respectively. The Flory-Huggins parameter is in the range of  $0 < \chi_{AB} < 10.2$  and the electrostatic interaction is given by a Bjerrum length of  $l_B = 10\sigma$ , where  $\sigma$  is the diameter of the polymer beads. The gray box is the actual simulation box, it is replicated twice in all three directions for better display. (a) Hexagonal cylinder phase where pink beads represent backbone monomers in charged block, green beads represent side charge group, yellow beads represent counterions, and blue beads represent monomers in the neutral block. (b) Cylinders consisted of neutral block monomers.

### 5.2.6 Polyelectrolyte complex phase behavior

In the studies of phase behavior, the emphasis this year has been on the role of charge density, specifically, understanding complexation behavior at very low charge density.

**Tirrell** group created a new synthetic system based on random copolymers of PEO and polyallylglycidal ether, Figure 5.7 (left), in which we could functionalize the pendant double bonds with either charge. Figure 5.7 (right), shows the resulting experimental binodal phase diagrams for PECs with charge fraction  $f = 0.30$ – $1.0$  and total CP =  $10$  mg/mL.

As anticipated, the two-phase region shrinks with decreasing charge density. We would like to go to even lower charge density, since that is a region where we could compare with theory, but for polymers of the chain length in the figure above (degree of polymerization

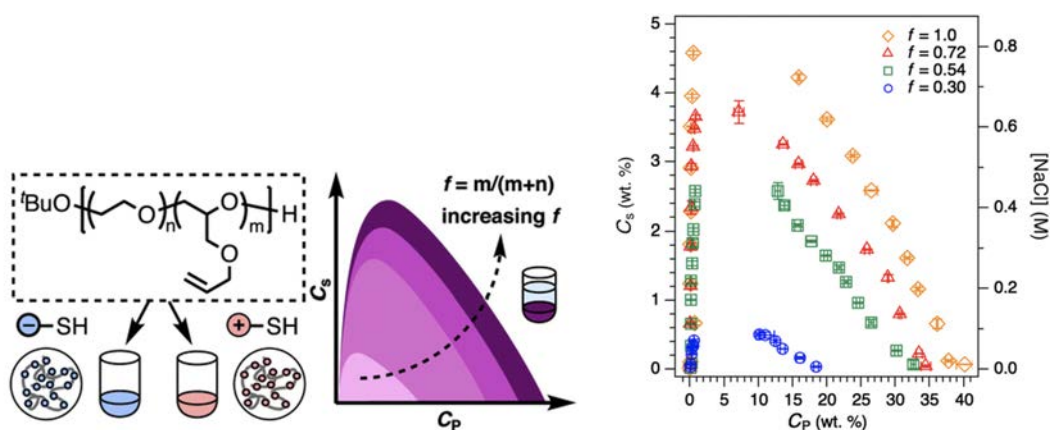


Figure 5.7: (Left) **Tirrell** group created a new synthetic system based on random copolymers of PEO and polyallylglycidal ether, in which they could functionalize the pendant double bonds with either charge. (Right) The resulting experimental binodal phase diagrams for PECs with charge fraction  $f = 0.30$ -1.0 and total  $C_p = 10$  mg/mL.

about 200), no phase separation was observed for  $f < 0.3$ .

### 5.2.7 Polyelectrolyte complex micelle design

In work on PEC micelles, **Tirrell** group has succeeded in determining the scaling laws that allow us to determine in advance and design micelles with specific size characteristics. This is useful information when the micelles are to be used to carry, for example, a therapeutic payload. As Figure 5.8 portrays, **Tirrell** group has used synchrotron x-ray scattering at the APS at Argonne to determine the radius of the electron density rich micellar core and dynamic light scattering in our lab to determine the hydrodynamic radius, which corresponds to the radius from the center to the periphery of the micelle.

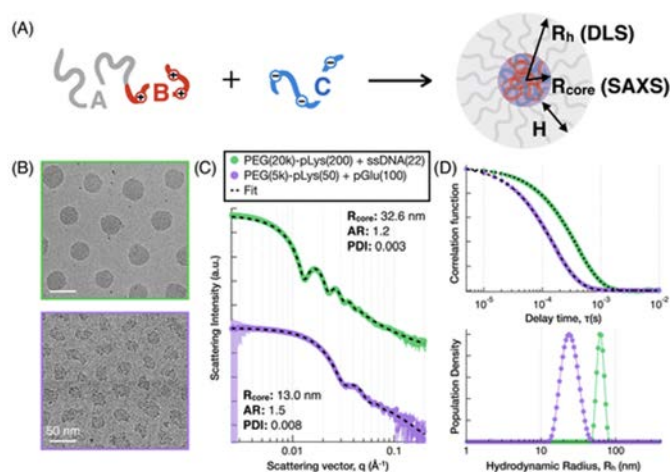


Figure 5.8: Characterization of structure of micelles using X-ray scattering and dynamic light scattering.

The data presented in Figure 5.9 show that the size of the payload-carrying core is fairly insensitive to the sizes of the corona block (A) and of the homopolymer (B) payload but is quite sensitive to the size of the B block in the block copolymer, varying with something

like the 0.75 power. This is new information that can be brought into play in various applications of PEC micelles.

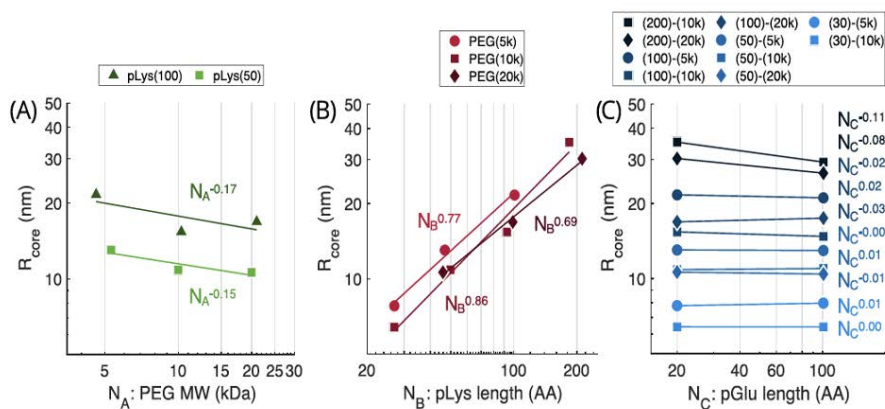


Figure 5.9: Micelles in application: Relations between size of the payload-carrying core ( $R_{core}$ ) to the sizes of the corona block (A) and of the homopolymer (B) payload but is quite sensitive to the size of the B block in the block copolymer.





## 6. Directed Self-Assembly of Soft Matter Systems

Paul Nealey (UC), Juan de Pablo (UC)

Joseph Kline (NIST), Dean Delongchamp (NIST), Debra Audus (NIST), Daniel Sunday (NIST)

### 6.1 Design Goals

This Directed Self-Assembly of Soft Matter Systems use-case group seeks to design block copolymer materials and assembly processes to enable manufacturing via DSA at length scales of 10 nm, scaling to 5 nm, and meet manufacturing constraints with respect to defects ( $0.01/\text{cm}^2$ ), and line edge and width roughness ( $<1$  nm). The structure of the assembled BCP depends on many variables describing material properties (molecular weight, block architecture, interaction parameter ( $\chi$ ) and process parameters (temperature, solvent, assembly time, template chemistry and topography, interfacial energies, and surface energies); our design objectives can only be met by developing and validating predictive multi-scale models. Moreover, the immense parameter space requires evolutionary approaches to simultaneously understand and optimize so many variables, in the context of analysis of experimental data and in the design of new materials and processes.

The system design chart in Figure 6.1 shows the processing-structure-properties-performance work flow for the Directed Self-Assembly of Soft Matter Systems Use-Case Group.

### 6.2 Research Accomplishments

The accomplishments of the DSA use case group in 2021 are as follows:

#### 6.2.1 Resonant Soft X-ray Reflectivity Measurements of A-b-(B-r-C) Copolymers

In collaboration with staff scientists at NIST, the Nealey group studied the self-assembly behavior of the synthesized A-b-(B-r-C) copolymers with resonant soft X-ray reflectivity (RSoXR). By using soft X-rays with energies near the absorption edges of elements present in polymers, such as Carbon and Oxygen, the X-ray contrast between the two polymer blocks can be easily tuned to distinguish the lamellar features in polymer thin films. The

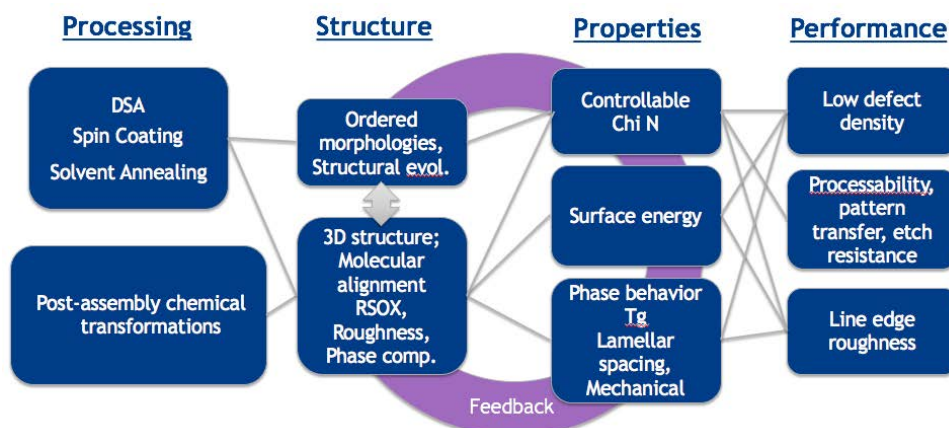


Figure 6.1: Systems design chart for Directed Self-Assembly of Soft Matter Systems

interface width ( $w_M$ ), or degree of mixing between the two polymer blocks, as well as the lamellar spacing ( $L_0$ ) of each polymer blocks in thin films was measured as a function of  $\phi_C$  for copolymer systems synthesized by RAFT and living anionic polymerization. The measured values of  $L_0$  in thin films measured by reflectivity is consistently less than what is measured in the bulk by SAXS. The smaller lamellar dimensions match those measured by scanning electron microscopy in thin film fingerprint samples. These insights into the self-assembly of the block copolymers in thin films are important when designing nanofabrication platforms for high-quality defect-free DSA of the block copolymers. The goal of this project is to connect line edge roughness of aligned block copolymer patterns after DSA to material properties measured by reflectivity in polymer thin films such as interface width in order to enable predictive design of next generation polymers that minimize pattern roughness.

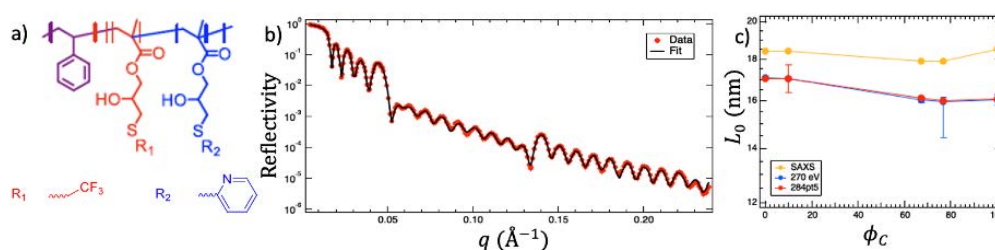


Figure 6.2: (A) Structure of the A-b-(B-r-C) copolymers used in the reflectivity study where  $\phi_C$  refers to the molar composition of the blue component in the random block. (B) Example reflectivity data (red circles) and fit to the real-space model (black line) taken at 270 eV. (C) Lamellar spacing,  $L_0$ , as a function of  $\phi_C$  measured in the bulk from SAXS (yellow) compared to that measured in thin films from reflectivity at 270 eV (blue) and 284.5 eV (red). Error bars represent 95% confidence intervals from the fits to the reflectivity data.

### 6.2.2 Impact of Structural Isomerism On the Self-Assembly of Diblock Copolymers

Structural isomerism, of which the types and numbers of atoms are identical but different in the spatial arrangements, has shown an impact on polymer properties as a collective interaction. A deeper understanding of the structural isomer-property relationship in

polymeric materials is essential and yet understudied subject mainly due to the polydisperse and long-chain nature. In collaboration with scientists at NIST, the **Nealey** group reported a design protocol for high precision structural isomeric block copolymers (SI-BCPs), combining well-defined parent polymer, polystyrene-*block*-poly(glycidyl methacrylate) (S-b-G), synthesis (living anionic polymerization) and post-polymerization modification (thiol-epoxy "click" chemistry) with structural isomer small molecules ( $R_F$ -SH). The resulting S-b-G( $R_F$ ), possessing identical molecular weight and nearly equal dispersity, are ideal for a comprehensive investigation of the sole impact of structural isomerism on the BCP self-assembly. Domain periodicity ( $L_0$ ) and segmental chain length ( $a$ ) are measured using small angle x-ray scattering and multi-angle light scattering techniques. The Flory-Huggins interaction parameter,  $\chi$ , calculated from an equation derived from self-consistent mean field theory, of each SI-BCP shows a significant dependence on the position of fluorine atoms. In collaboration with **de Pablo** group, both simulation and experimental results suggest there is a strong correlation between the orientation of dipole moment and  $\chi$ . This finding from joint collaboration paves a way to a systematic investigation on the structure-property relationship of polymeric materials and further enable a broader scope of new and delicate materials design at the molecular level.

### 6.2.3 Surface energy and density measurements

A-*b*-(B-*r*-C) copolymers are a promising route for designing defect free structures with a specified pitch size because they allow for decoupling surface interactions and chain interactions. **Nealey** group uses PS as A block and different modified-PGMA as B and C blocks. For perpendicular lamellae structures, the surface tension of A should be balanced by the surface tension of B-*r*-C by varying the relative ratio of B to C. One simplified approach for predicting this ratio is to assume that the surface tension of B-*r*-C is a linear function of composition. Using all atom simulations, we determined surface tension of PS and 12 modified-PGMA homopolymers. Then, predicted compositions from homopolymers' surface tensions using a linear approximation for 7 systems that have experimental results available. Out of 7, we find that 5 show a good agreement (Figure 6.2A). We also tested this approximation by simulating a real B-*r*-C system (Figure 6.2B). For this case study, we chose TF and TGM as B and C blocks respectively. Note that TF-TGM has shown a good agreement in Figure 6.2. Also, we find that density of TF-*r*-TGM decreases linearly with the TGM composition. Both surface tension and density are measured at 150°C, the thermal annealing temperature used in the experiment. An understanding of how composition affects surface tension allows for informed design and reduction of the synthetic burden of A-*b*-(B-*r*-C) copolymers.

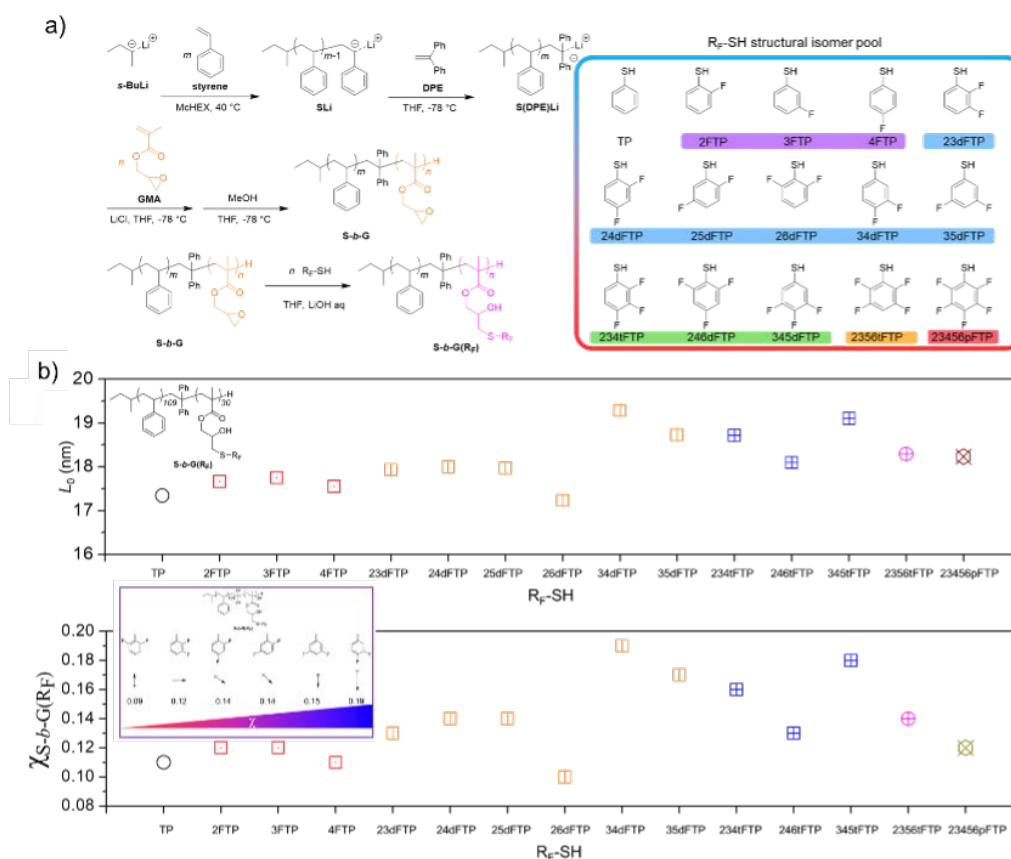


Figure 6.3: (A) Chemistry platform and synthetic scheme of polystyrene-*block*-poly(glycidyl methacrylate) (S-b-G) and fluorinated benzenethiol (R<sub>F</sub>-SH) structural isomers modified polystyrene-*block*-poly(glycidyl methacrylate) (S-b-G(R<sub>F</sub>)). R<sub>F</sub>-SH pool consists of mono-fluorine, di-fluorine, tri-fluorine, tetra-fluorine, and penta-fluorine modified benzenethiols. The abbreviation of each thiol is labelled. (B) The lamellar domain spacing and calculated  $\chi$  values indexed by the R<sub>F</sub>-SH species. The BCPs were annealed at 150 °C for 20 h under vacuum. The inset image shows the correlation between the orientation of dipole vector (pointing towards or away from the backbone) of the fluorinated phenyl ring and the  $\chi$  values of di-fluorinated thiophenol modified SI-BCPs.

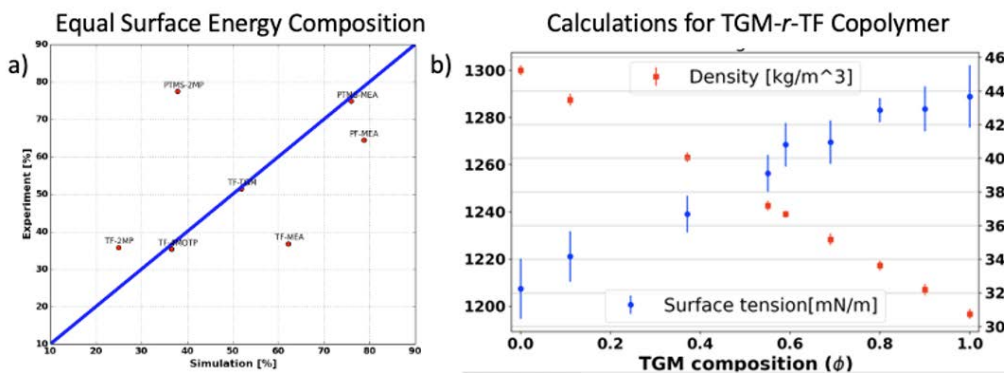


Figure 6.4: (A) Comparison between simulation and experiment for equal surface energy composition for a variety of B-r-C random copolymers. (B) Calculations of density (red) and surface tension (red) as a function of TGM composition for a TGM-*r*-TF random copolymer.



## 7. Materials for High-Performance Impact Mitigation

**Heinrich Jaeger (UC)**, Stuart Rowan (UC), Sidney Nagel (UC), Juan de Pablo (UC)

**Christopher Soles (NIST)**, **Aaron Forster (NIST)**, **Edwin Chan (NIST)**, Marcos Reyes-Martinez (NIST)

### 7.1 Design Goals

Current impact mitigating materials are optimized for compressive loading across a narrow impact frequency range. The Materials for High-Performance Impact Mitigation group aims to develop a new paradigm for meta-material designs for impact protection in sports, industrial and other activities, where relative impact velocities range from 10 m/s to over 100 m/s with impact energies up to 500J or more, all of which could cause severe traumatic brain injury. Specifically, the use case aims to design material systems to attenuate, deflect, and dissipate impact energy over a wider impact frequency range under both linear, shear, and biaxial loading than currently possible.

To achieve this vision for new protective material systems, three integrated thrusts will be pursued:

*(1) Novel Architectures:* Novel non-linear materials and architectures (flexible disordered networks, concentrated particle suspensions, and granular media) that exhibit strain induced state changes to unlock new routes of energy absorption.

*(2) Novel Metrologies:* New dynamic metrologies to measure local stress- and strain-dependent material properties (stiffness, yield or jamming) at (sub-)micrometer to millimeter length scales.

*(3) Novel Models:* New classes of non-linear constitutive models that connect coarse grained and multi-physics finite element simulations to material response physics at the microscale (heat, interface friction, buckling) and centimeter level (adaptive compliance, yield strength, and fracture energy).

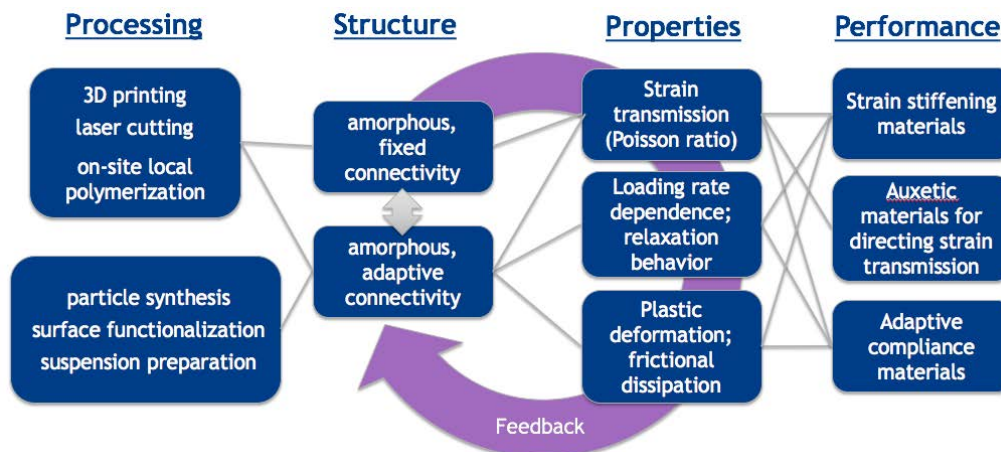


Figure 7.1: Systems design chart for High-Performance Impact Protection

To minimize injury, including mild traumatic brain injury (mTBI), impact protection must reduce linear and rotational accelerations to safe levels. The quantitative design goal of this use case group is to design material systems that stay below 50 g and 3,000 rad/s<sup>2</sup> (a 50% reduction in current recommended levels of 100 g and 6,000 rad/s<sup>2</sup>, respectively) for velocities up to 100m/s and energies up to 500J.

The system design chart in Figure 7.1 shows the processing-structure-properties-performance work flow for the Materials for High-Performance Impact Mitigation use-case group.

## 7.2 Research Accomplishments

### 7.2.1 Harnessing the polymer glass transition for stress-adaptive shear response

Concentrated, or dense, suspensions of small particles in a liquid exhibit striking non-Newtonian behaviors such as shear thickening and shear jamming [1-3]. This shear-induced transformation from an easily flowing state to a state of much enhanced viscosity is fully reversible, and has been leveraged in a range of applications, including flexible stab-proof armor, smart speed bumps, and damping systems for impact mitigation [4,5]. To date, studies have elucidated the structure-property relationship in suspensions of rigid, non-deformable particles, revealing the important roles of inter-particle contact forces. However, an easy yet versatile approach for *in situ* control of suspension rheology is lacking. A collaboration between the **Rowan, de Pablo** and **Jaeger** groups drew inspiration from stimuli-responsive materials to control the shear jamming properties of fluids. This work harnessed the well-known polymer glass transition phenomenon to achieve facile control over the shear thickening/jamming rheology of dense suspensions.

We designed polymer particles with readily accessible glass transition temperatures ( $T_g$ ) so that the mechanical stiffness and inter-particle interactions in a suspension can be tuned *in situ* with temperature. In order to vary  $T_g$ , three types of particles were synthesized, with reaction scheme shown in Figure 7.2a. The storage modulus reduces from  $\sim 1$  GPa to  $\sim 1$  MPa when heated over  $T_g$  (Fig 7.2e). By studying the rheological properties of such thermo-responsive suspension at varying temperatures, we showed for the first time that the shear thickening strength displays strong and non-monotonic temperature dependency (Figure 7.3a), as opposed to conventional suspensions of rigid particles. The shear thickening strength strongly tracks the trend in  $\tan\delta$  (Figure 7.3b), implying the

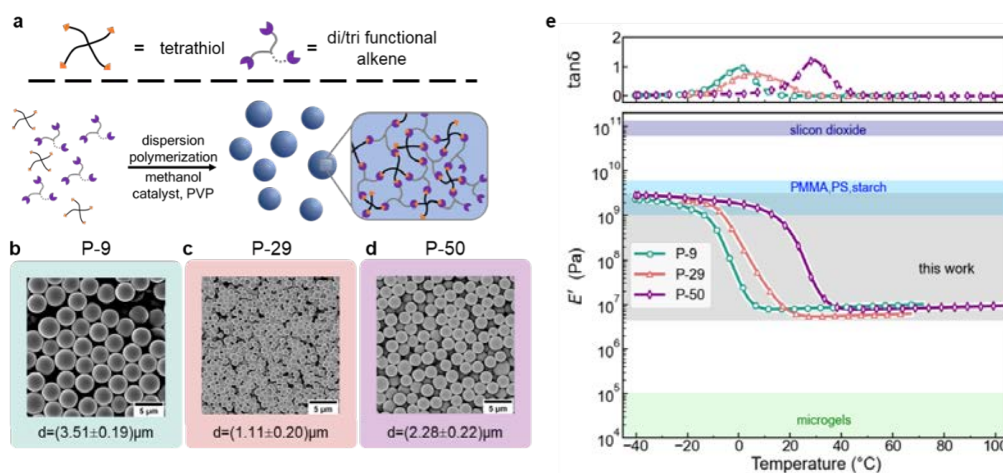


Figure 7.2: a) Schematic diagram of the Thiol-Michael dispersion reaction and the particle network structure. b-d) The scanning electron microscopy images of P-9, P-29 and P-50 particles, respectively. The mean size and the standard deviation are indicated below each image. e) Mechanical stiffness characterization via DMA. The storage modulus ( $E'$ ) and  $\tan \delta = E''/E'$  of the carrier liquid-swollen P-9, P-29 and P-50 polymer films were measured in an immersion setup, using an oscillation frequency  $f=1\text{Hz}$ . The values of  $E'$  for several other particle materials are indicated for comparison. PMMA: Poly (methyl methacrylate) and PS: polystyrene.

general applicability of our approach. Finally, pull test experiments show that our design enables in situ turning on or off of shear jamming simply by varying the temperature relative to  $T_g$ , which lays the groundwork for thermally switchable jamming systems (Figure 7.3c). A paper on this work has been submitted and a preprint is available at [researchsquare.com](https://www.researchsquare.com) [14].

### 7.2.2 Tuning dynamic bond exchange and morphology for impact applications

Benzalcyanoacetate molecules are able to undergo room temperature, catalyst-free dynamic exchange with thiols [6-8]. A key feature of this dynamic bonding motif is the ability to tune the binding constant ( $K_{eq}$ ) by simply varying the electronic moieties on the  $\beta$ -phenyl ring (R groups shown in Figure 7.4a). The widely tunable nature of these dynamic bonding systems is ideal for impact mitigation applications, as the kinetics of exchange may be adjusted to match the timescales of interest during an impact event. Therefore, understanding the impacts of electronic substitution on the dynamic exchange kinetics and stress relaxation properties are essential for future impact mitigation applications.

To measure how the exchange kinetics respond to various electron-donating and -withdrawing groups, the **Rowan** group carried out control studies using in situ NMR spectroscopy on small molecule analogue systems spanning a range of donating and withdrawing groups (-OMe, -Me, -H, -Cl, -CF<sub>3</sub>, NO<sub>2</sub>), see Figure 7.4b. In line with previous results, molecules with stronger electron-withdrawing character were found to have higher overall  $K_{eq}$  values. However, by fitting to a second order forward, first order back dynamic equilibrium model, it was found that the  $K_{eq}$  values were dominated by a reduction in back reaction rate, Figure 7.4c. From a materials standpoint, a slower reaction rate implies a bond with a longer lifetime, which should in turn give rise to longer stress relaxation times.

To assess the effect of the large changes in rate constants for the various Michael acceptors, a suite of dynamic networks were synthesized using a ditopic benzalcyanoacetate

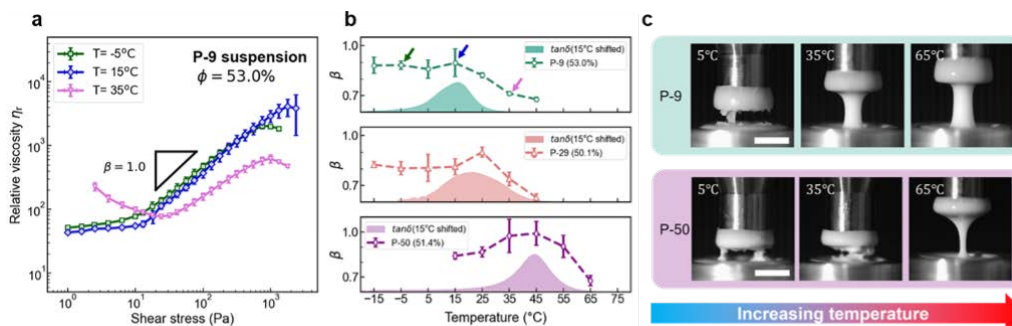


Figure 7.3: a) Stress-controlled steady-state rheometry data for the P-9 suspension with particulate volume fraction  $\phi=53.0$  at  $-5^{\circ}\text{C}$  (green),  $5^{\circ}\text{C}$  (blue) and  $35^{\circ}\text{C}$  (pink), demonstrating that the strength of shear thickening is highly temperature dependent. The black line has a slope of 1 corresponding to DST where the shear rate is constant. b) slope  $\beta$  in the discontinuous shear thickening regime as a function of temperature for a  $\phi=53.0\%$  P-9 suspension, a  $\phi=50.1\%$  P-29 suspension, and a  $\phi=51.4\%$  P-50 suspension. Shaded areas indicate the  $\tan\delta$  results from Figure 7.2, here shifted up by  $15^{\circ}\text{C}$ . Arrows in b indicate  $\beta$  for the conditions measured in panel a. c) Images of the suspensions under extensional deformation taken at  $T=5^{\circ}\text{C}$ ,  $35^{\circ}\text{C}$  and  $65^{\circ}\text{C}$  for P-9 and P-50 suspensions ( $\phi=56.0\%$ ). The pulling rate was 8 mm/s. The scale bar indicates 5 mm.

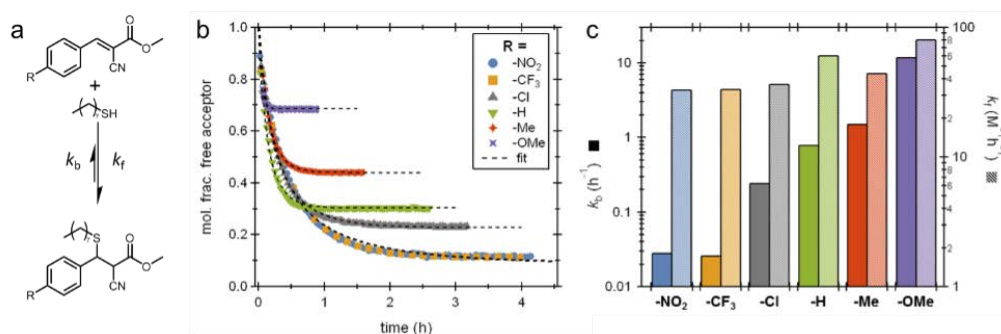


Figure 7.4: a) Reaction scheme of dynamic thia-Michael reactions. b) Kinetic traces from in situ NMR experiments of different Michael acceptors in DMSO- $d_6$ . c) Rate constants extracted from dynamic equilibrium model fits to the kinetic data, showing that the back reaction (solid) is significantly more sensitive to electronics than the forward reaction (hashed).



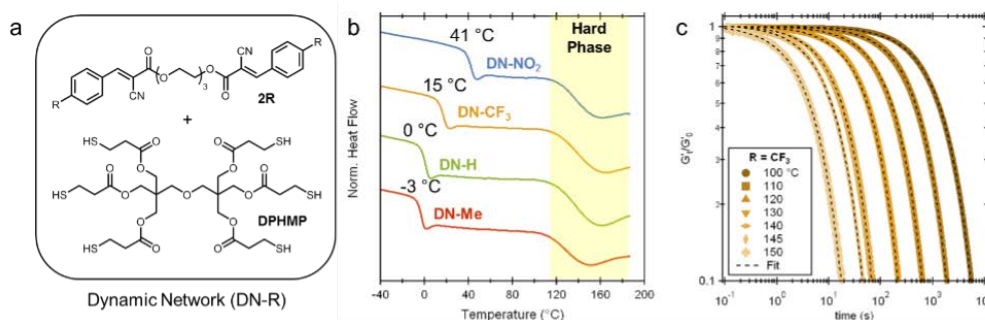


Figure 7.5: a) General composition of dynamic networks studied in this Use Case. b) Differential Scanning Calorimetry thermograms of as-synthesized dynamic networks comprised of crosslinkers bearing different -R groups. As expected, groups with stronger electron withdrawing character have increased  $T_g$  (denoted in black text) and all systems display phase separated morphologies evidenced by an upper transition temperature (highlighted by yellow box). c) Example stress relaxation data suite (collected for DN-CF<sub>3</sub>) showing excellent agreement with the stretched exponential fit (dashed lines).

crosslinker (2R) and a 6-armed thiol species (DPHMP), see Fig 7.5a. Prior to mechanical characterization, differential scanning calorimetry was carried out to determine the glass transition temperature across the range of networks (Fig 7.5b). As expected, higher electron-withdrawing character led to higher  $T_g$  values, however it was also found that all synthesized systems displayed an upper transition temperature related to the development of a phase separated morphology, as previously reported by the group [9,10].

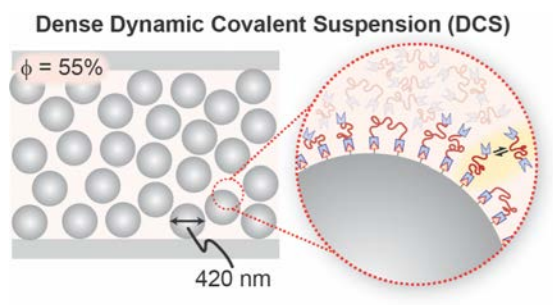
With the thermal properties of these materials analyzed, network samples were sent to our collaborators at NIST (**Forster** and colleagues) for stress relaxation (Figure 7.5c) and rheo-Raman studies. The experimental data collected for each system is well-described by a stretched exponential decay (which assumes a distribution of relaxation modes), giving access to energetic information when analyzed over a range of temperatures. Interestingly, in all samples with sufficiently strong phase separated domains (as measured by rheo-Raman), the stress relaxation behavior was found to be Arrhenius (up to the temperature at which hard phase becomes unstable) and scaled directly with the energetics of the back reaction. This implies the hard phase units act directly to stabilize network crosslinks, giving another handle to tune stress dissipation in dynamic networks.

### 7.2.3 A new class of dynamic covalent suspensions with switchable response

The non-Newtonian behaviors of concentrated, or dense, suspensions arise from a network of particle-particle contacts that smartly and dynamically adapts to imposed shear. Suspensions of this type have wide-spread technological and industrial applications. Over the last few years the Jaeger group developed new approaches, based on chemically functionalizing particle surfaces, that make it possible to design dense suspensions with specific, stress-dependent responses [11,12]. Now a collaboration between the **Jaeger** and **Rowan** groups together with ARL extended these approaches to incorporate, for the first time, dynamic covalent chemistry between particles and a polymeric solvent (Figure 7.6).

Specifically, a room temperature dynamic thia-Michael bond was employed to rationally tune the equilibrium constant ( $K_{eq}$ ) of the polymeric solvent to the particle interface. We demonstrated that low  $K_{eq}$  leads to shear thinning while high  $K_{eq}$  produces antithixotropy, a rare phenomenon where the viscosity increases with shearing time. Based on extensive

Figure 7.6: Illustration depicting a dynamic covalent dense suspension (DCS). These high-particulate-fraction (55% by volume) DCSs contain particles that can form room temperature dynamic covalent bonds with the surrounding fluid polymer matrix, resulting in a bonded polymer graft layer which exchanges dynamically (*inset*).



data from several different chemistries involving dynamic covalent bonds, we propose that an increase in  $K_{eq}$  results in an increase in polymer graft density at the particle surface and that antithixotropy primarily arises from shear induced debonding of the polymeric graft/solvent from particle surface and concomitant formation of shear-induced polymer bridges. Thus, the implementation of dynamic covalent chemistry enables antithixotropy in dense suspensions and provides a new molecular handle with which to tune their macroscopic rheology.

These studies open the door to energy absorbing materials which sense mechanical inputs and adjust their dissipation as a function of time or shear rate, and can switch between these two modalities on demand. A paper on this work has been submitted.

#### 7.2.4 Direct detection of frictional contact network formation in dense piezoelectric suspensions

Control of the frictional contacts between particles in dense suspensions has provided ways to tune the resulting, dynamic response to applied stress. Advances in experimental approaches and simulations have shown that the formation of networks of frictional contacts plays a critical role in the development of a shear thickening regime [1-3]. However, a lack of techniques that allow for the macroscopic observation of frictional networks in optically opaque suspensions makes the direct visualization difficult. A collaboration between the **Jaeger** and **Rowan** groups employed piezoelectric BTO particles to measure the electric charge generated in response to applied shear stress. Simultaneous measurements of conductance and viscosity was shown to provide direct evidence for the formation of frictional networks in the shear thickening regime (Figure 7.7).

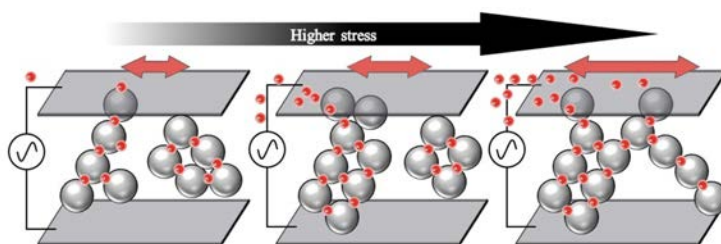


Figure 7.7: Sketch of mechanism for stress-induced piezoelectric conduction mechanism along frictional contact force network in dense suspensions in the shear-thickening regime.

#### 7.2.5 Rigid cluster analysis of dense frictional suspensions

Dense suspensions solidification under stress is a material property ripe for use in impact mitigation technologies. One major obstacle in exploiting this solidification is a lack of a

mesoscopic description of rigidity that would predict when such system begins to transition from fluid to solid. A collaboration between the **de Pablo** and **Jaeger** groups overcame this obstacle by borrowing a rigidity metric from the dry granular community and applying it to simulations of dense suspension flow. This method makes it possible to decompose frictional force networks into mechanically rigid and non-rigid regions. An example of this construction is shown in Figure 7.8. In the left panel the network of frictional particle-particle contacts is shown in red. The right panel shows the subset of the red network that corresponds to rigid clusters. It is clear from this figure that even though the suspension has a fully percolating network of frictional forces (red), this is not enough to produce a system-spanning cluster that is mechanically rigid. Such system-spanning rigid clusters are only found when the particle volume packing exceeds a minimum threshold and the applied shear stress is sufficiently large.

The simulation results provide a fundamental advance in how to understand the evolution of rigidity in dense suspensions as a function of particle packing fraction and applied shear stress. They also give insight into how to engineer the solidification transition in dense suspensions in order to obtain materials with enhanced impact mitigation properties.

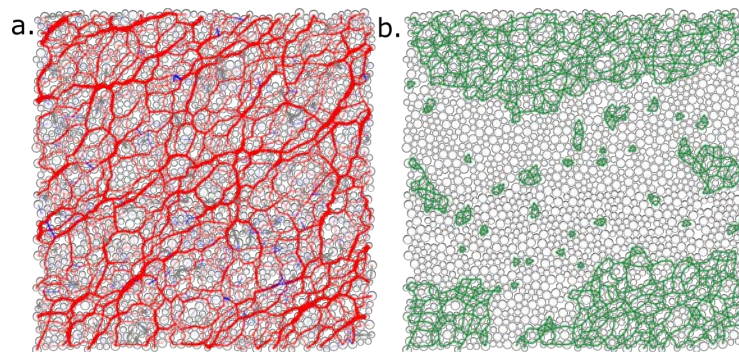


Figure 7.8: Snapshots from simulations of dense suspension. Left panel: Line segments show forces between neighboring particles, with force magnitudes given by the line thickness. Hydrodynamic forces are shown in blue, frictional contact forces in red, and normal contact forces in grey. Right panel: Green line segments show the subset of frictional forces (red in the left panel) that constitute rigid clusters.

### 7.2.6 Stress activated constraints in dense suspensions

A second collaborative project between the **Jaeger** and **de Pablo** groups investigated, via simulations, how the dramatic increase of a suspension's viscosity during shear thickening and shear jamming can be understood within a framework that abstracts details of the forces acting at particle-particle contacts into general stress-activated constraints on relative particle movement. We found that focusing on just two constraints, affecting sliding, and rolling at contact, can reproduce the experimentally observed shear thickening behavior quantitatively, despite widely different particle properties, surface chemistries, and suspending fluids. Within this framework parameters such as coefficients of sliding and rolling friction can each be viewed as proxy for one or more forces of different physical or chemical origin, while the parameter magnitudes indicate the relative importance of the associated constraint. In this way, a new link has been established that connects features observable in macroscale rheological measurements to classes of constraints arising from micro- or nano-scale properties. A paper on this work has been submitted [3].

### 7.2.7 Impact mitigation with network-based meta-materials

In close collaboration with NIST our patented approach for the design of network-based meta-materials for impact absorption was further developed. At NIST this was led by **Soles, Chan** and **Reyes-Martinez**, while the CHiMaD contributions came from the **Nagel, de Pablo** and **Jaeger** groups. Disordered-Network Mechanical Materials (DNMM), comprised of random arrangements of bonds and nodes, have emerged as mechanical metamaterials with the potential for achieving fine control over the elastic properties of open-cell materials. Recent computational studies by the CHiMaD team demonstrated this control whereby an extremely high degree of mechanical tunability can be achieved in disordered networks via a selective bond removal process called pruning. During this reporting period, we experimentally demonstrated how pruning of a disordered network alters its macroscopic dynamic mechanical response and its capacity to mitigate impact. Impact studies with velocities ranging from 0.1 m/s to 1.5 m/s were performed, using a linear actuator and a drop tower at NIST, on 3D printed pruned and unpruned networks comprised of materials spanning a range of stiffness that were 3D printed at UChicago. High-speed videography was used to quantify the changes in Poisson's ratio for each of the network samples. Our results demonstrate that pruning is an efficient way to reduce the transmitted force and impulse from impact in the medium strain rate regime ( $10^1 s^{-1}$  to  $10^2 s^{-1}$ ). This approach provides a useful alternative route for designing materials with tailored impact mitigating properties compared to randomly removing material from open cell foams. A paper on this work was published in *Soft Matter* [13].

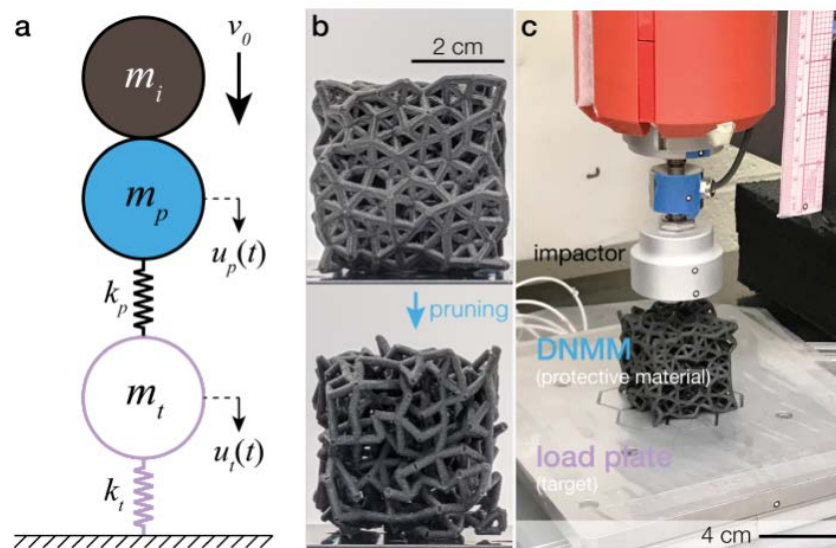


Figure 7.9: Impact behavior of disordered network mechanical metamaterials (DNMM). a) An impact mitigation system represented as a one-dimensional spring-mass system. The schematic shows the time dependent force  $F(t)$ , exerted by the impactor of mass  $m_i$  on the protective material (DNMM) and target with masses  $m_p$  and  $m_t$ , respectively. The masses are coupled by springs representing the stiffnesses  $k_p$  and  $k_t$  of the protective material and target, respectively. b) Images of representative unpruned and pruned 3D-printed DNMM samples. c) The impact experiment is composed of an instrumented impactor, the DNMM sample and an instrumented load plate to measure the transmitted load due to impact.

#### References:

1. Morris, J. F. Shear thickening of concentrated suspensions: recent developments

- and relation to other phenomena. *Annual Review of Fluid Mechanics* 52, 121-144 (2020).
2. Brown, E.; Jaeger, H. M. The role of dilation and confining stresses in shear thickening of dense suspensions. *Journal of Rheology* 56, 875-923 (2012).
  3. Singh, A.; Jackson, G. L.; van der Naald, M.; de Pablo, J. J.; Jaeger, H. M. Stress-activated constraints in dense suspension rheology. Preprint (2021), under review. DOI: arXiv:2108.09860
  4. Cwalina, C. D.; McCutcheon, C. M.; Dombrowski, R. D.; Wagner, N. J. Engineering enhanced cut and puncture resistance into the thermal micrometeoroid garment (TMG) using shear thickening fluid (STF) - Armor<sup>TM</sup> absorber layers. *Composites Science and Technology* 131, 61-66 (2016).
  5. Lee, Y. S., Wetzel, E. D. & Wagner, N. J. The ballistic impact characteristics of Kevlar woven fabrics impregnated with a colloidal shear thickening fluid. *Journal of Materials Science* 38, 2825-2833 (2003).
  6. Serafimova, I. M.; Pufall, M. A.; Krishnan, S.; Duda, K.; Cohen, M. S.; Maglathlin, R. L.; McFarland, J. M.; Miller, R. M.; Frödin, M.; Taunton, J. Reversible Targeting of Noncatalytic Cysteines with Chemically Tuned Electrophiles. *Nat. Chem. Biol.* 8, 471-476 (2012).
  7. Zhong, Y.; Xu, Y.; Anslyn, E. V. Studies of Reversible Conjugate Additions. *European J. Org. Chem.* 2013, 5017-5021 (2013).
  8. Krenske, E. H.; Petter, R. C.; Houk, K. N. Kinetics and Thermodynamics of Reversible Thiol Additions to Mono- and Diactivated Michael Acceptors: Implications for the Design of Drugs That Bind Covalently to Cysteines. *J. Org. Chem.* 81, 11726-11733 (2016).
  9. Herbert, K. M.; Getty, P.; Dolinski, N. D.; Hertzog, J.; de Jong, D.; Lettow, J.; Rowan, S. J. "Reaction-induced phase separation in tunable dynamic covalent networks" *Chemical Science* 11, 5028-5036 (2020).
  10. Herbert, K. M.; Dolinski, N. D.; Boynton, N. R.; Murphy, J. G.; Lindberg, C. A.; Sibener, S. J.; Rowan, S. J. "Controlling the Morphology of Dynamic Thia-Michael Networks to Target Pressure-Sensitive and Hot Melt Adhesives" *ACS Applied Materials & Interfaces* 13, 27471-27480 (2021).
  11. James, N. M., Han, E. D., de la Cruz, R. A. L., Jureller, J. & Jaeger, H. M. "Interparticle hydrogen bonding can elicit shear jamming in dense suspensions" *Nature Materials* 17, 965 (2018).
  12. van der Naald, M., Zhao, L., Jackson, G. L. & Jaeger, H. M. "The role of solvent molecular weight in shear thickening and shear jamming" *Soft Matter* 17, 3144-3152 (2021).
  13. Reyes-Martinez, M. A., Chan, E. P., Soles, C. L., Han, E., Murphy, K. A., Jaeger, H. M., Reid, D. R., de Pablo, J. J., "Tuning the mechanical impedance of disordered networks for impact mitigation," *Soft Matter* (2022), accepted. DOI: 10.1039/D1SM01649K
  14. Chuqiao Chen, Michael van de Naald, Abhinendra Singh, Neil D. Dolinski, Grayson L. Jackson, Heinrich M. Jaeger, Stuart J. Rowan, Juan J. de Pablo, Leveraging the polymer glass transition to access thermally-switchable shear jamming suspensions. Preprint, under review (2022). DOI: 10.21203/rs.3.rs-1193286/v1





## 8. Alloy Design for Additive Manufacturing

**Greg Olson (NU), Jian Cao (NU), Wing Kam-Liu (NU), Peter Voorhees (NU)**

**Dana Frankel (QuesTek), Jason Sebastian (QuesTek), Jiadong Gong (QuesTek), Zaynab Mahbooba (QuesTek), Maytham Alzayer (QuesTek)**

**Mark Stoudt (NIST), Lyle Levine (NIST), Carelyn Campbell (NIST), Ursula Kattner (NIST), Zhi Liang (NIST), Fan Zhang (NIST), Maureen Williams (NIST), Kil-won Moon (NIST), Brandon Lane (NIST), David Deisenroth (NIST), Paul Witherell (NIST), Yan Lu (NIST), Ho Yeung (NIST), Tesfaye Moges (NIST), Zho Yang (NIST), Orion Kafka (NIST), Thien Pang (NIST)**

### 8.1 Design Goals

Building on CHiMaD Phase I research by CHiMaD Precipitation-strengthened Alloys use-case group and Additive Manufacturing Seed Group, the CHiMaD's Alloy Design for Additive Manufacturing use case group is focused on materials design to enable the new technology of additive manufacturing (AM). Based on feasibility assessments previously conducted under CHiMaD-sponsored and lead projects in Northwestern and MIT's Materials Design classes, the scope of our design applications includes steels, Co superalloys and Ti-based alloys, the latter including transformation-toughened alloys as well as precipitation-strengthened shape memory alloys.

Studies, in collaboration with NIST, center on on current Ni superalloys and stainless steels such as 17-4PH which are notoriously incompatible with additive manufacturing as revealed in ongoing studies at both NIST and QuesTek. New steel designs address strength levels of 1.2GPa YS and greater, with special attention to processability constraints to avoid hot tearing during deposition. Composition design for control of oxide distributions is also important due to the elevated oxygen levels inherent in powder processing.

Building on our developing design tools and databases for precipitation hardened alloys, the printable Co alloy design seeks to exploit slow precipitation kinetics to allow quench suppressible precipitation hardening during deposition while achieving final properties,

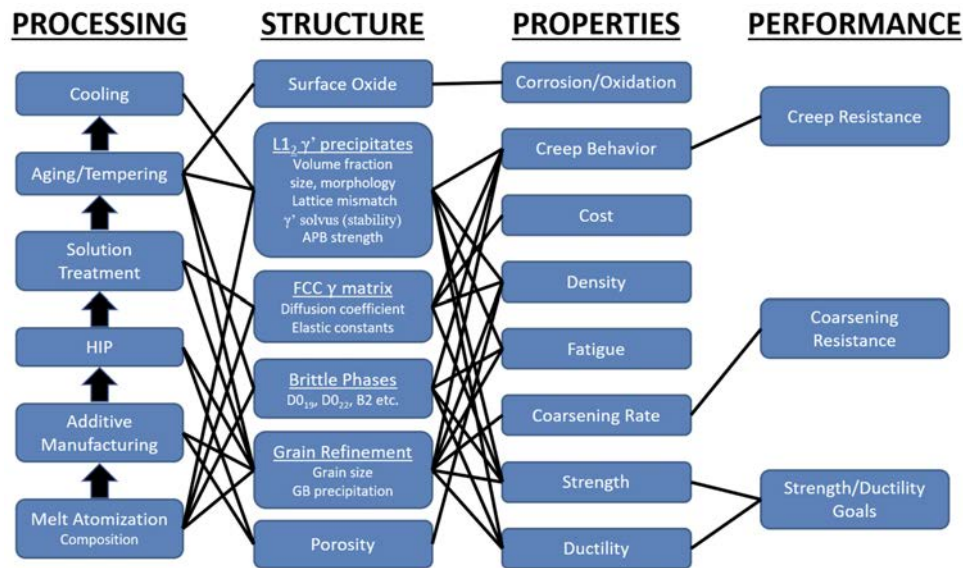


Figure 8.1: Printable Co Superalloy System Chart.

strength level of 1GPa YS@ 800C, exceeding those of Ni718, the best performing printable Ni-based superalloy. The system design chart showing the PSPP relations for a printable Co superalloy is shown in Figure 8.1.

Continuing research at QuesTek on enhancement of the AIM Accelerated Qualification method is now focused on the certification of additively manufactured components, with emphasis on UQ of probabilistic property forecasts in collaboration with the UQPET tool group.

In support of achieving these alloy design goals, the CHiMaD Alloy Design for Additive Manufacturing use case group is also focusing on: (1) developing data-driven property predictions for additively manufactured alloys; (2) establishing data-driven models in multi-scale manufacturing simulation schemes, in collaboration with *CHiMaD Artificial Intelligence and High-Performance Data Mining* tool group; and (3) fundamental studies to further our currently lacking understanding of dendritic solidification during the additive manufacturing processes.



## 8.2 Research Accomplishments

### 8.2.1 Printable Cobalt Superalloy, Olson Group

It was previously determined that Re has the lowest diffusivity in Co, so design work this year at MIT has explored small additions of Ru to minimize the  $\gamma'/\gamma$  partition coefficient for improved high temperature creep resistance. QuesTek defined additional design requirements for the printable Co-superalloy which include achieving a solvus temperature greater than 900°C, gamma prime content greater than 40%, lattice misfit of -0.1%, a microstructure free of undesirable competing phases, and cracking susceptibility / hot cracking susceptibility within a printable range.

Defending his Northwestern doctoral thesis on printable SMA design in November 2020, Chuan Liu in 2021 took the position of CHiMaD NIST Fellow previously held by Dr. Peisheng Wang. He was based at MIT in 2021 working with Prof Olson, collaborating with Ursula Kattner and Carrie Campbell on thermodynamic and mobility database development, in support of the Co databases. He assisted Olson in supervision of new MIT doctoral student Krista Biggs focused on printable Co superalloy design. In collaboration with the UQPET tool group the design projects explored methodologies of Design with Uncertainty integrating quantified model accuracy.

#### Computational Design of Co-based Superalloys

(at%)	Co	Ni	Al	Ti	W	Cr	Ta	Re
$\gamma$	67.0	7.9	4.4	2.4	2.5	15.3	0.24	0.34
$\gamma'$	63.4	11.2	5.7	7.3	5.1	6.1	1.06	0.28
A (65% $\gamma'$ )	64.6	10.0	5.2	5.6	4.2	9.3	0.8	0.3

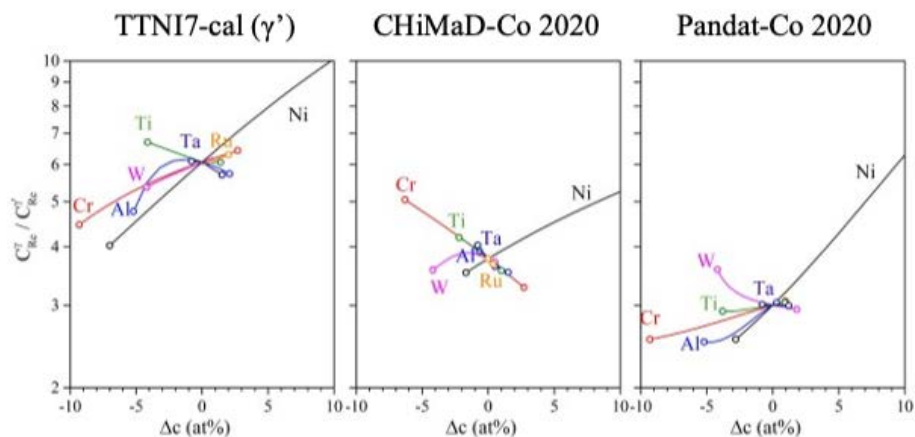


Figure 8.2: Comparative database predictions for alloying effects on Re partitioning in reference 2-phase alloy composition established by evaluation of 1st-iteration design prototype.

Dr. Liu used the results of the measurement of the 4-phase equilibrium found by the Co Use Case group in the prototype alloy of the preliminary design conducted in the 2019 Materials Design class to define a 2-phase composition as a reference composition for exploring alloying effects on Re partitioning as summarized in Figure 8.2, where the strongest effect identified is increasing Ni content. Building on this assessment, he coached a team in the 2021 Computational Materials Design class at MIT designing an alloy intended as a benchmark for design specifically for 3D printing. Figure 8.3 shows good agreement

between databases for the suitability of the composition as a solution-treatable 2-phase alloy to be experimentally validated in 2022.

### 2021 CMD Design - Prototype

Co-36Ni-12.8Al-4Cr-3.3Ta-2.2W-1Re-1Ru (CHiMaD-Co) (at%)								
T = 900 °C	Co	Ni	Al	Cr	Ta	W	Re	Ru
$\gamma$ (33.5%)	50.78	28.16	7.34	6.05	2.95	0.86	2.68	1.17
$\gamma'$ (66.5%)	34.07	40.00	15.57	2.97	3.48	2.88	0.12	0.91
$K^{\gamma/\gamma'}$	0.67	1.42	2.12	0.49	1.18	3.33	0.04	0.78

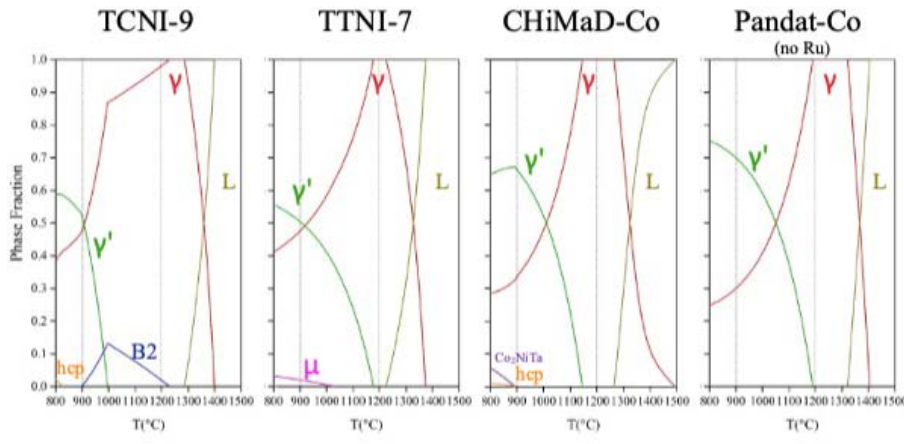


Figure 8.3: Equilibrium phase fraction step diagrams comparing database predictions for 2021 design prototype alloy.

### 8.2.2 Design of Printable TRIP Steel, Olson Group

A design class project at MIT in 2020 built on previous ONR sponsored work on transformation toughening mechanisms to design a printable precipitation-strengthened transformation-toughened austenitic TRIP steel. The concept explored by the all-undergraduate team was to apply transformation toughening to tolerate residual porosity from additive deposition, to eliminate the need for HIP consolidation. The contour plots of Figure 8.4 summarize the final optimization of Cr and Ni content in the alloy, balancing yield strength in MPa (red), an "HCS" hot cracking susceptibility parameter (black), and as-deposited delta ferrite fraction (blue), while meeting a required "ASP" austenite stability parameter (yellow) for optimal transformation toughening. Under CHiMaD support, MIT doctoral student Brandon Snow has assessed the team's calculations in preparation for experimental validation of the design in 2022.

### 8.2.3 Optimization of Printable 17-4PH Stainless Steel, Olson Group & QuesTek

In continued coordination with [Stoudt](#) (NIST) on optimization of current alloys, QuesTek has developed alternative compositions for the 17-4PH martensitic stainless steel to facilitate complete martensitic transformation while enhancing corrosion resistance. Designs have demonstrated alloys usable with print-and-age treatment, as well as an alloy achieving good properties in the as-built condition exploiting carbide autotempering during deposition. Further development and qualification of these steels is being conducted under Navy support. Also in coordination with efforts at [NIST](#), QuesTek is exploring under NASA

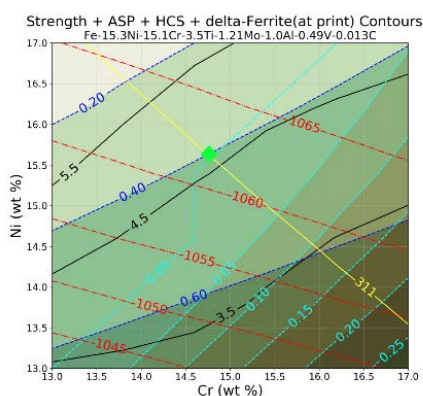


Figure 8.4: Cross-plot for optimization of Cr and Ni levels in printable transformation-toughened austenitic steel.

support the predictive process optimization of printed Ni superalloys including 718 and 625, with the ultimate goal of design of new printable Ni alloys with higher performance.

#### 8.2.4 Printable Titanium Alloys, Olson Group

After completing his ONR-supported doctoral research at Northwestern on design of transformation-toughened Titanium-based alloys, Dr. Fan Meng joined QuesTek and initiated work on design of Ti alloys specifically for additive manufacturing. Research was coordinated with the Ti alloy design activities at NIST by Dr. Liang, who had attended Olson's design class at NU as a Visiting Scientist under CHiMaD auspices. In 2021 Dr. Liang joined QuesTek and continued the work started by Dr. Meng, focusing on achieving an equiaxed deposition grain structure in wire-based printing.

#### 8.2.5 SRG Design Consortium Projects and Design Class Interactions, Olson Group

CHiMaD/SRG Design Consortium projects are the primary source of student projects in Olson's Materials Design class with supported researchers serving as coaches to the team projects. The revised class in Computational Materials Design at MIT, conducted in 2021 in virtual mode, continued to draw from CHiMaD research for these team projects. In addition to the Printable Co Superalloy project coached by Dr. Liu, further application of the ONR-supported transformation toughening research addressed martensitic naval hull steels toughened by dispersed austenite. Building on our strong relation with Apple as enhanced by Dr. Jim Yurko joining the CHiMaD TAB, Apple served as client to a project on controlled-melting-point lead-free solder alloys. A project on printable steels in collaboration with Universitat Paderborn in Germany addressed high-strength tool steels. A project on high-strength aluminum alloys drew on the new DSO-Singapore program. Staffing of the coaching and team participation was enhanced by virtual Visiting Scholars from Germany, Greece, and Singapore.

#### 8.2.6 X-ray Diffraction Analysis of QuesTek Co Alloy Prototypes, QuesTek

Microscopy results, shown in Figure 8.6 (left), of an etched prototype #1 aged at 900°C for 24 hours revealed a significantly larger fraction of the gamma prime phase than the 40 mole% predicted to be present at equilibrium. To obtain a quantitative measure for comparison to the predictions, x-ray diffraction was performed on the heat-treated button material.

Due to the large grain structure of the arc-melted and heat-treated button, the material needed to be mechanically milled to remove the interference of orientation-based diffrac-

## 3.041/3.321 Computational Materials Design

Spring 2021  
Design Projects

- |   |  |
|---|--|
| <p><b>I. Printable Co Superalloy</b><br/>Client: NIST-CHiMaD<br/>Advisor: Dr. Chuan Liu<br/>Team: Yannick Naunheim, Noriaki Arai*</p>                                     | <p><b>III. Lead -Free Solder</b><br/>Client: Apple (Dr. Zack Feinberg)<br/>Advisor: Edward Pang<br/>Team: Spencer Hu, Nutth Tuchinda</p>                     |
| <p><b>II. HSLA150: Transformation - Toughened Naval Hull Steel</b><br/>Client: NIST-CHiMaD, ONR, SPI<br/>Advisor: Clay Houser<br/>Team: Julian Rackwitz, Brandon Snow</p> | <p><b>IV. Printable Tool Steel</b><br/>Client: NIST-CHiMaD, U Paderborn<br/>Advisor: Florian Hengsbach<br/>Team: Krista Biggs, Gary Whelan*</p>              |
|   | <p><b>V. UHS Al Plate Alloy</b><br/>Client: DSO-Singapore<br/>Advisor: Dr. Margianna Tzini<br/>Team: Alvin Tan, Jonathan Lim, Huan-Chin Koh, Wei-Lin Tan</p> |

Figure 8.5: Design class projects conducted at MIT.

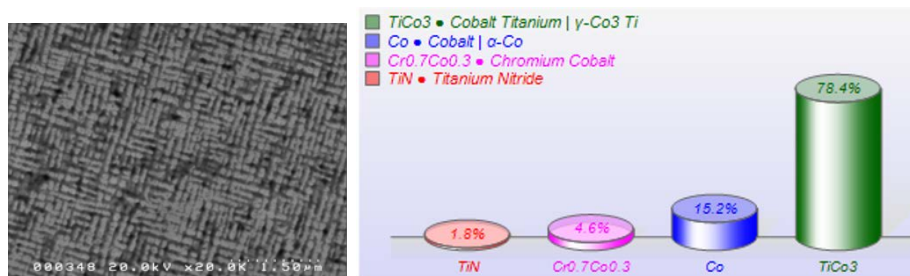


Figure 8.6: (left) Scanning electron microscope image of prototype #1 cobalt alloy. Etched using waterless Kalling's reagent; (right) Quantification of XRD spectra intensity ratios and identified crystal structures into volume fractions of phases.

tion. The risk of strain-induced transformation in the alloy was concluded to be low enough risk that it would not affect the measurement of the  $\gamma$  and  $\gamma'$  phase fractions.

After an 18hr scan was completed, the detected peak intensities were quantified and separated into bins based on their identified crystal structure, as presented in Figure 8.6 (right). The TiCo<sub>3</sub>  $\gamma'$  phase was measured to be 78.4% volume fraction of the milled material, agreeing well with the microscopy results observed within the etched microstructure. Titanium nitride particles were characterized in the as-cast microstructure and persisted throughout heat treatment. These were concluded to be introduced by the minor impurity of the raw materials. The chromium-cobalt compound was not anticipated and will be considered in further characterization efforts.

### 8.2.7 Printable Cobalt Alloy Thermodynamic Database Development, QuesTek

Based on the latest XRD analysis results, the QuesTek Co thermodynamic database was preliminarily updated to address the discrepancies in  $\gamma'$  volume fraction at 900°C. Multiple binary L1<sub>2</sub> ( $\gamma'$  phase definition in the database) end members were updated to have consistent enthalpies of formation with DFT calculation as well as ternary interaction parameters. The most significant contribution came from the Co<sub>3</sub>Cr end member, which is more stable compared with its pre-calibration value according to DFT enthalpy of formation, and its entropy contribution is calibrated according to Co-Cr binary phase

diagram to ensure it remains correctly unstable in the binary system. The updated database provides better consistency with XRD characterization as shown by the comparison in Figure 8.7. Further calibration of the database based on composition characterization will further enhance the accuracy of the database, especially critical in predicting  $\gamma/\gamma'$  segregation and misfit.

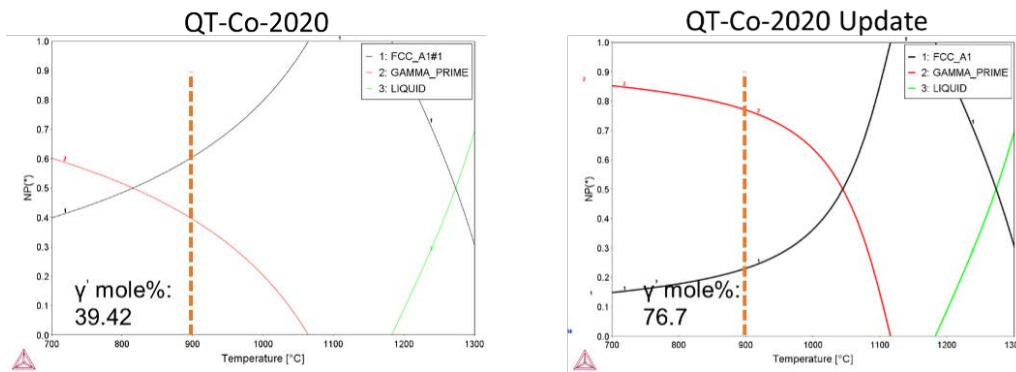


Figure 8.7: Comparison of calculation results for prototype #1 between (left) previous database and (right) latest calibrated database.

### 8.2.8 Latest Printable Cobalt Alloy Design Cross-plots with Updated Thermodynamic Database, QuesTek

With the updated database, QuesTek calculated the cross plots for the initial designs, prototypes #1 and #2, illustrating the effect of Cr and W variations on  $\mu$  phase appearance, misfit and coarsening rate at 900°C as shown in Figure 8.8. Indicated by the colored arrows, the calculated properties of prototype compositions meet the pre-set requirements. Upon further calibration of the database, this design activity will be conducted again.

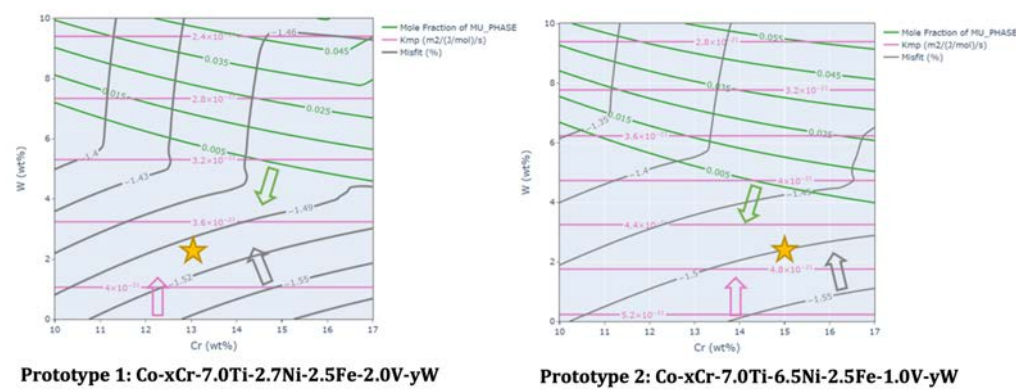


Figure 8.8: Cross plots for the initial designs, (left) prototype #1 and (right) prototype #2, with varying Cr and W contents, showing  $\mu$  phase fraction, misfit and coarsening rate at 900°C. The starred compositions are the prototype compositions, and the colored arrowing locations are the desired contour thresholds.

### 8.2.9 Solidification During Additive Manufacturing, Voorhees Group

In metal additive manufacturing (AM), the solidification microstructures that form during processing dictate the *printability* of the material and the final properties of the component.

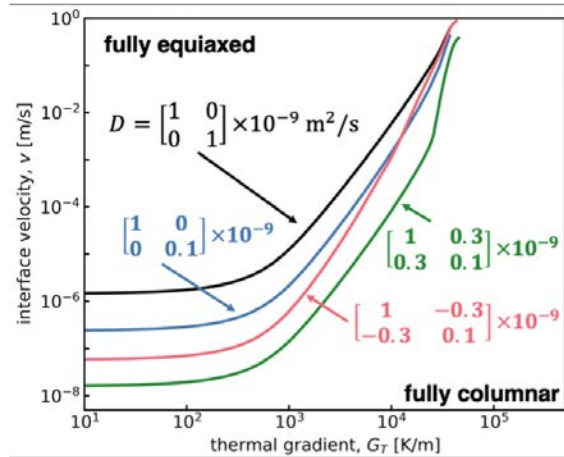


Figure 8.9: a morphology selection map for a model ternary system, showing the effects of various diffusion matrices on the location of the CET.

For example, the columnar-to-equiaxed transition (CET) describes the shift from elongated columnar grains that grow in the direction of the melt pool to equiaxed grains. The former is highly vulnerable to hot-cracking and results in anisotropic properties, while the latter is much more resistant to solidification strains and imparts isotropic properties. A model of the CET allows for the construction of morphology selection maps that link the expected microstructure to solidification conditions and processing parameters, which can be used to develop processing strategies that create the desired microstructure.

We have combined existing models for the CET and multicomponent dendrite growth to calculate morphology selection maps for the concentrated, multicomponent alloys relevant to modern metallurgy and additive manufacturing. Figure 8.9 shows such a processing map for a model ternary system for various diffusion matrices. It is clear that both adding slow-diffusing species and accounting for diffusional interactions can significantly shift the location of the CET; thus, diffusional interactions should not be ignored when modeling concentrated alloys. Additionally, working with researchers at Mines ParisTech, we have coupled the multicomponent dendrite growth model with ThermoCalc, which allows for the treatment of non-linear phase diagrams, improving the accuracy of these calculations for concentrated alloys.

Additionally, the solidification conditions present in additive manufacturing cause the interface to depart from local equilibrium, which introduces kinetic undercooling effects. While the previous analysis does not incorporate the effects of kinetic undercooling, we used a dissipation relation to derive the two *interfacial response functions* (IRFs) describing non-equilibrium phase transformations in concentrated multicomponent alloys. The first response function describes the velocity of the interface, and the second describes the concentrations in each phase at the interface. Additionally, we have used the dissipation relation to self-consistently incorporate an effect known as *partial solute drag* in both IRFs to provide a more physical model of the interfacial behavior. Taken together, the IRFs completely describe the kinetic effects during rapid solidification, which will improve the accuracy of these processing maps under the solidification conditions present in AM.

### 8.2.10 AM-CFD development for porosity prediction, Liu Group

A finite volume method (FVM) based Navier-Stokes solver is developed to solve an additive manufacturing (AM) process that considers moving heat source. The solver framework considers multiple physical phenomena of AM process at the part, melt pool

and microstructure scales to link process parameters to material structure and properties. The code base also considers statistical variability in the process to account for changes in melt pool width and depth in the AM process. The stochasticity of the process is possible to calibrate with limited available experimental data and then extend the analysis for part scale AM simulation. The Liu group's developed award winning FVM based C++ code has the capability to predict the lack-of-fusion porosity considering a multi-track multi-layer AM process. Combined with the stochastic process, the code has the capability to predict with higher accuracy the surface roughness and porosity in an AM manufactured part with higher accuracy which is a key requirement to study the fatigue life of an AM processed part. In addition to lack-of-fusion porosity, AM processing leaves porosities arising from vapor depression that is recognized as keyhole porosity. The keyhole formation is a highly transient phenomenon, and the morphology of the keyhole varies significantly to affect the material distribution as the AM process advances. The overview of the capabilities and research focus on AM-CFD is shown in Figure 8.10.

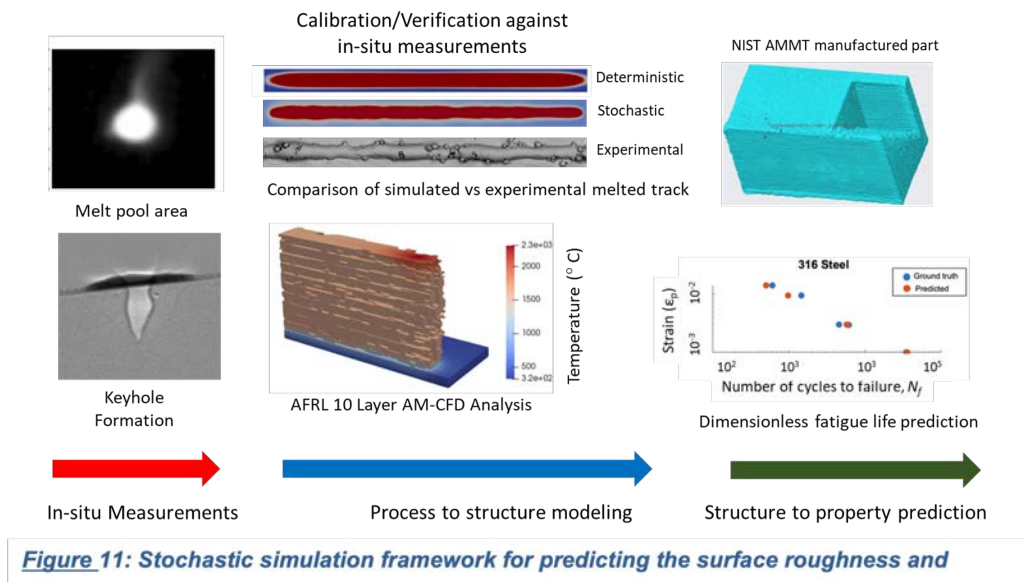


Figure 8.10: Stochastic simulation framework for predicting the surface roughness and porosity.

### 8.2.11 Dimensionless Learning, Liu Group

It is challenging to identify the explicit causal relationship between various parameters in a complex system. These highly correlated parameters lead to the complexity of experimental design and process control. Dimensionless numbers and scaling laws provide a simple but powerful way to analyze the causal relationships among parameters, but classical dimensional analysis cannot give unique dimensionless numbers and highly relies on researchers' personal experience.

To this end, we proposed a data-driven dimensional analysis, dimensionless learning, to automatically identify the dominant dimensionless numbers and the best scaling laws from experimental data. By incorporating physical knowledge about physical dimensions into machine learning algorithms, we successfully reduce the parameters into a few dimensionless numbers, which reduces the notorious overfitting problem given a small amount of data. The identified dimensionless numbers not only have a good physical

explainability but can be used to discover scaling laws that give fundamental insights into complex systems. The proposed framework is validated in three complex engineering problems: turbulent Rayleigh-Benard convection, keyhole dynamics in laser melting of metals, and porosity formation in 3D printing.

### Dimensionless learning applied to surface-roughness-fatigue life estimation

One major challenge in estimating the fatigue life of additively manufactured alloys with microstructure-based models is that those models cannot directly incorporate the effect of the surface roughness. The microstructure-based models are representative volume element-based which only considers one material point at part scale and expands it to a representative microstructure. However, surface roughness only exists at the surface and does not directly affect the material points at the center of the coupon in terms of fatigue. To alleviate this inconvenience, we proposed a dimensionless learning paradigm for fatigue life estimation from surface roughness and material parameters as a function of micromechanical quantities such as micro-stress or plastic strain. The idea here is to come up with the micromechanical quantity (such as plastic strain or microstress) from detailed simulation and use the dimensionless number-driven model as a surrogate to compute the fatigue life (similar to the concept of fatigue-indicating parameter). The initial study to discover a material independent model considered surface energy, shear modulus, Poisson's ratio, surface roughness, plastic strain, and cycles to failure as parameters. The analysis came up with three non-dimensional numbers with data from literature and a prediction was made for 316 Stainless Steel. The result is shown in the Figure 8.11. The model can give satisfactory results to match with the experimental result.

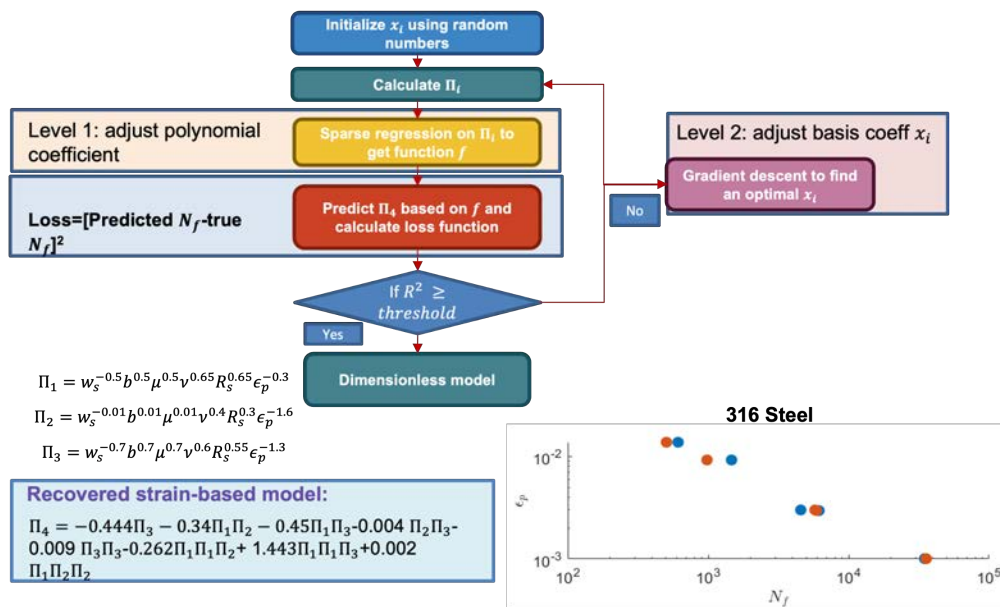


Figure 8.11: The dimensionless parameters discovery from data. A test example for 316 stainless steel.

### 8.2.12 Simulation-guided Process Design, Cao Group

Melt pool control is essential in metal additive manufacturing processes since the melt pool geometry directly affects geometric accuracy and material properties of the fabricated part. In this work we developed a general framework for a simulation-guided process



design method to control the melt pool depth with focus on the directed energy deposition (DED) process. The developed method enables the possibility of finding a laser power profile that achieves a desired melt pool depth using just one simulation. Figure 8.12 illustrates the basic idea of the simulation-guided process design framework. The idea of simulation-guided process design is to implement a controller in the thermal FEM simulation to control the melt pool depth and to use the calculated variable laser power profile from the simulation to command the laser in the DED process. Since no iterative simulations and experiments are required, the developed framework can achieve the laser power profile design to control the melt pool depth in just one simulation, enabling a fast process design for DED. The approach is also applicable in other laser AM processes, e.g., powder bed fusion (PBF).

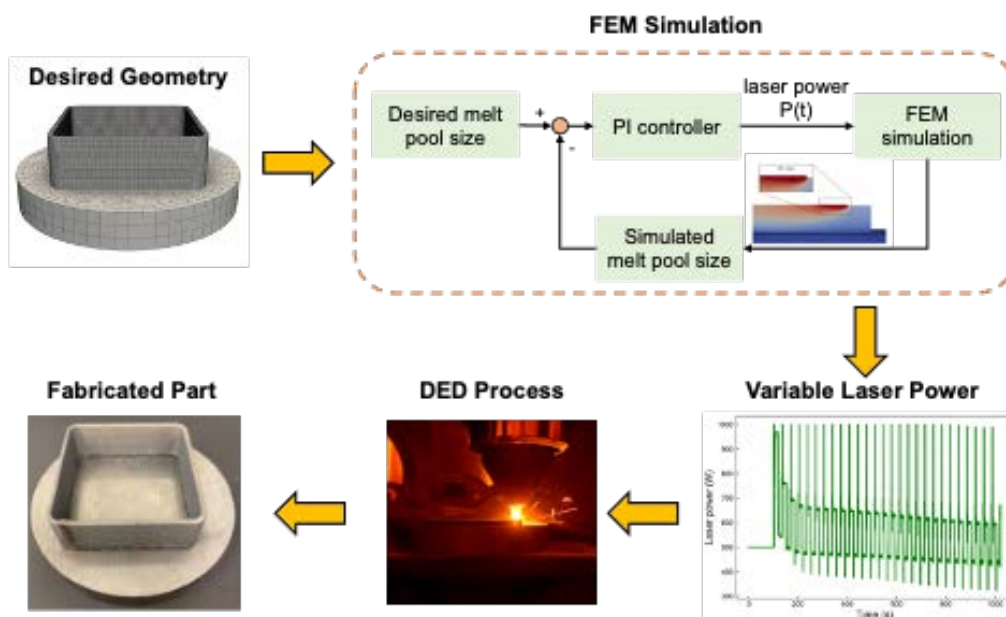


Figure 8.12: Schematic of the simulation-guided variable laser power design method.

In the current work, the developed simulation-guided process design framework is applied to two example cases using as-deposited 718 Ni. The first case is a bidirectional-scanned thin wall with uniform melt pool control, of which the simulation results are shown in Figure 8.13. Figures 8.13A and B are the comparisons of the melt pool depth vs. time with and without control in the simulation. From the results one can see that when using a constant laser power without control, the melt pool depth continuously increases as more and more layers are deposited. Additionally, there is a sharp peak at the start of each layer because of the heat accumulation when the laser turns around. Figure 8.13C is the comparison of the probability densities of the melt pool depth with and without control. 88.2% of the measured melt pool depth are in the range of  $1.4 \text{ mm} \pm 0.1 \text{ mm}$ , which indicates that the melt pool depth is controlled to be mostly uniform at 1.4 mm with the tuned PI controller. The simulation took 64 mins running on a Nvidia RTX 8000 GPU. In the next step, the laser power profile is filtered with a moving average filter to guarantee the smooth change of the laser power, as shown in Figure 8.13D. and then implemented in the DED experiment by modifying the machine code. The temperature fields in the experiment captured by an IR camera with a constant laser power and the designed laser power are shown in Figure 8.14. The experimental results clearly show that using the

resulting laser power profile from the simulation leads to a much uniform melt pool depth during the process.

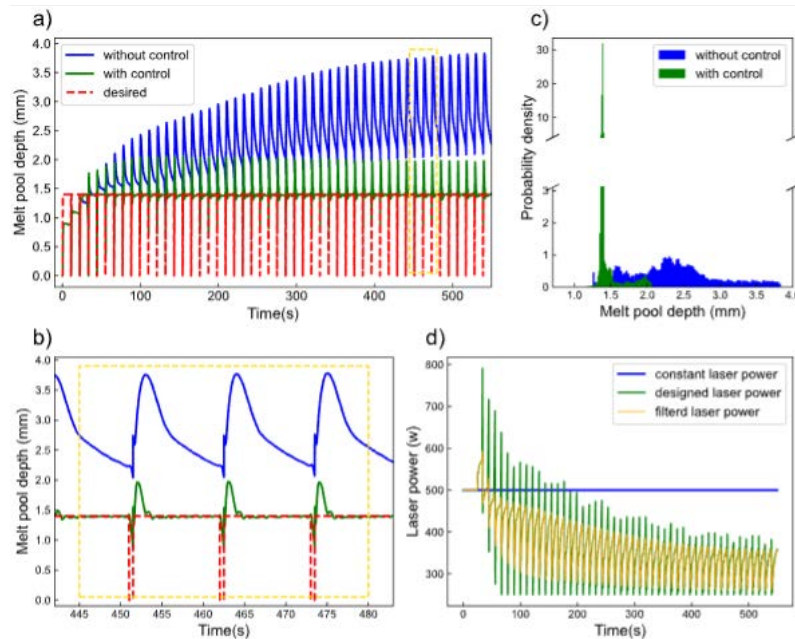


Figure 8.13: Simulation results of the bidirectional-scanned thin wall.

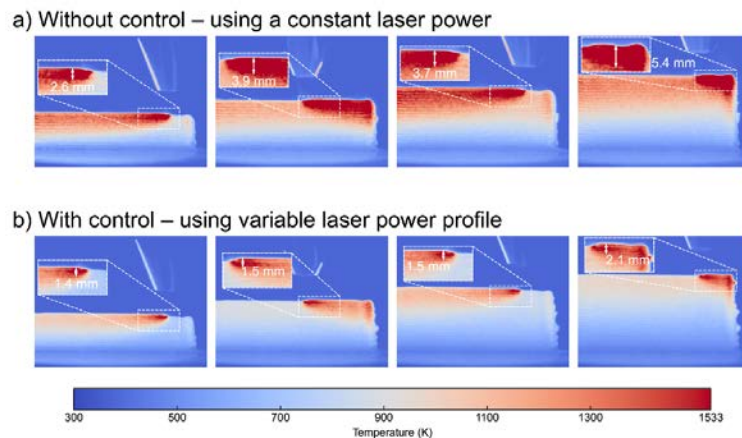


Figure 8.14: Visualization of the temperature field in the experiment (a) using a constant laser power (b) using the resulting laser power profile simulation.

In the second case, site-specific control is implemented for a rounded-square geometry in which one half of the part is controlled with a melt pool depth of 1.4 mm and the other half is controlled with a melt pool depth of 2.0 mm. The intention of this case is to make the two halves of the part undergo different thermal histories and, therefore, lead to different mechanical properties. The simulation took 103 mins running on a Nvidia RTX 8000 GPU. The final built rounded-square part using the designed laser power profile is shown in Figure 8.15A. To compare the mechanical properties of the material built with different melt pool depths, tensile tests were performed on specimen cut from each half of the part.

The size of the tensile specimen is given in 8.15B. Both sides of each of the walls were faced using wire electrical discharge machining (EDM), and then the tensile specimens are cut vertically from the walls also using wire EDM. Three tensile tests for each group of the part were performed on a Psylotech tensile testing platform, where results are shown in Figure 8.15 (right). The results show that with the same melt pool depth, each group of the tensile specimens has very similar tensile properties, while the tensile properties between the two groups vary significantly. The material built with a melt pool depth of 2.0 mm has an average 0.2% offset yield stress (YS) of 416.5 MPa and an average ultimate tensile strength (UTS) of 728.2 MPa, while the material built with a melt pool depth of 1.4 mm has an average YS of 384.0 MPa and an average UTS of 708.2 MPa. It is shown in our previous work on 718 Ni that the UTS and YS increase with a decrease in solidification time because of the larger and farther spaced Laves phase dendrites, and an increase in cooling time (927K-1,130K) due to more  $\delta$ -phases breaking up the Laves phase dendrites. In this case, when the melt pool depth is larger, both the solidification time and the cooling time increase and the effect of the cooling time dominates, which leads to a larger UTS and YS.

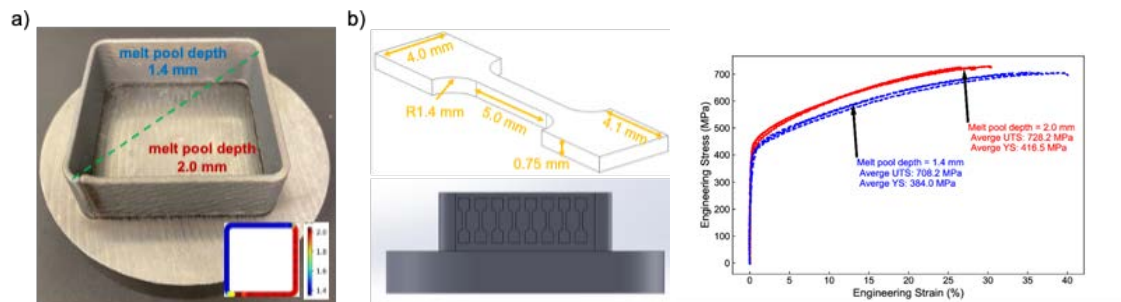


Figure 8.15: (left) (a) The built rounded-square part, (b) Size of the tensile specimen, (right) Results of the tensile test: strain-stress curve, average UTS and YS.

Despite recent advancements in data-driven modeling of AM processes, the generalizability of such models across a wide range of geometries has remained a challenge. Here, we propose a graph-based representation using neural networks to capture spatiotemporal dependencies of thermal responses in AM processes. Two neural network architectures for spatiotemporal prediction of AM thermal responses are developed in the current work, as shown in Figure 8.16. The GNN architecture predicts the single-time step update in each training instance given the node and element features at the time-step and the RGNN architecture predicts and trains multi-time step interactions where at each time step the network receives a temporal nodal-based encoded representation, a non-temporal element-based representation, and the hidden state of the previous stacked GRU cell and outputs the thermal distribution over the geometry. Both architectures can be recursively evaluated to produce thermal outputs of arbitrary length.

A database is developed based on high-fidelity finite element simulations, which has allowed us to have access to the thermal histories of all geometric points. Heat conduction, convection, radiation, and external heat flux as the result of the laser beam, are modeled in our simulations, where stainless steel 316L is used as the material. To ensure that we train and test the proposed models on diverse geometries, we selected 55 different industrial-grade geometries from the ABC database, where 45 of them are used for training and 10 geometries are randomly separated for testing.

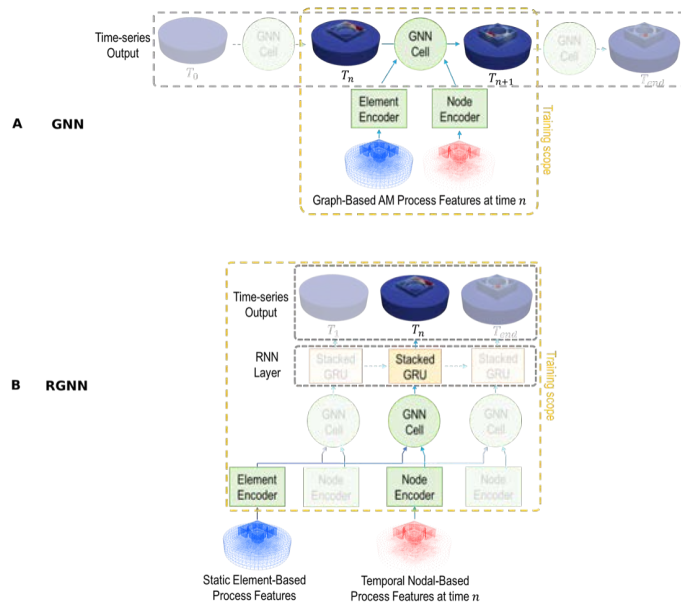


Figure 8.16: Schematics of the two architectures for spatiotemporal prediction of AM thermal responses: (A) The GNN architecture (B) The RGNN architecture.

Figure 8.17 depicts the training and testing results of the two proposed models. A baseline solution, which is the same as the developed GNN architecture, only without the previous temperature as the input is added for comparison. The output of the developed data-driven models for a sample case in the test set is shown in Figure 8.17B. The baseline results in a  $4.49e^{-4}$  MSE, the GNN model in  $3.57e^{-5}$  MSE, and the RGNN model in  $5.32e^{-5}$  MSE averaged over all nodes of the simulation. Qualitatively, the results show a good agreement between both GNN and RGNN models and the ground truth.

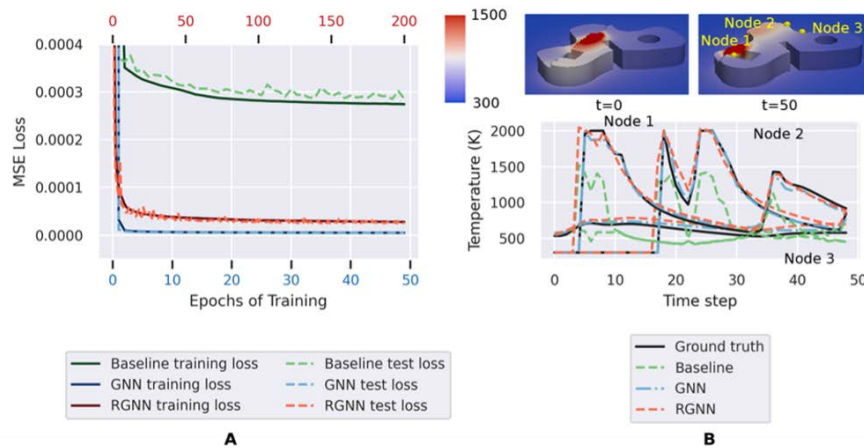


Figure 8.17: Training and evaluation results for the baseline, GNN and RGNN formulations: (A) The evolution of the train and test losses; (B) An example simulation and the predicted thermal history at three points with the location of points depicted on the top right and the comparison of histories between baseline, GNN, RGNN and the ground truth on the lower right.

To further investigate the stability and capability of the model for long simulations, we evaluated the models on 55 samples (45 for training and 10 for test sets) over 1,000 time steps, which is 1,000X and 20X the training span of the GNN and RGNN models, respectively. A similar conclusion can be drawn by observing the RMSE evolution over all training and test samples as shown in Figure 8.18 where the GNN model results in a

RMSE of  $1.5e^{-2}$  for the training set and  $1.44e^{-4}$  for the test set, while the RGNN model shows a small error propagation with a RMSE of  $9.58e^{-3}$  on the training set and  $9.32e^{-3}$  on the test set.

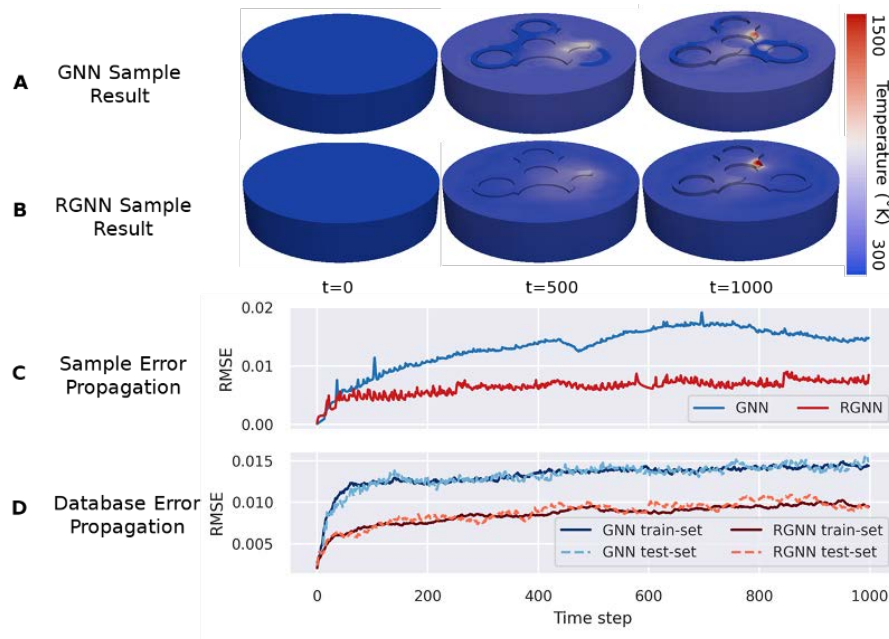


Figure 8.18: : Evaluation of the trained models' capability to produce long-term simulations. The evolution of the thermal field on a sample simulation is depicted for the GNN and RGNN models (A and B). The error propagation of the sample simulation and all database simulations for both models are shown (C and D).





## 9. Cobalt-based Superalloys for High-Temperature Use

**Peter Voorhees (NU), David Dunand (NU),** David Seidman (NU), Jiadong Gong (QuesTek), Olle Heinonen (ANL), Chris Wolverton (NU)

**Carelyn Campbell (NIST), Ursula Kattner (NIST), Kil-Won Moon (NIST), Zhi Liang (NIST), Maureen Williams (NIST), Andrew Reid (NIST)**

### 9.1 Design Goals

The design goal is a high-volume fraction  $\gamma$ - $\gamma'$  Co alloy that can be printed using additive manufacturing approaches and will yield improved microstructural stability at higher temperature along with an improved creep and oxidation resistance and printability compared to IN718.

To achieve this goal, it is necessary to avoid cracking upon processing. Thus, we are focusing on an alloy that has a small freezing range ( $< 100$  degrees), and are exploring the use of grain refiners to yield an equiaxed structure and reduce the number of high angle grain boundaries. To allow for precipitation of  $\gamma'$  from a single-phase alloy, the temperature difference between the  $\gamma'$  solidus and solvus should be 40C. For the creep and tensile strengths as volume fraction of  $\gamma'$  should be in the range of 50-70%. To maximize the creep resistance, the coarsening resistance should be increased and the misfit between  $\gamma$  and  $\gamma'$  should be small. The formation of deleterious TCP phases should also be avoided. To strengthen the grain boundaries B and C additions are being considered. Oxidation resistance is achieved through the addition of Cr. An additional goal is a density less than  $8.74 \text{ g/cm}^3$ .

The system design chart in Figure 9.1 shows the processing-structure-properties-performance links considered by the Cobalt-based Superalloys for High-Temperature Use.

### 9.2 Research accomplishments

#### 9.2.1 Co Database Development

The development of CALPHAD-based databases with thermodynamic, diffusion mobility and molar volume descriptions to support the design of the new Co superalloys continues

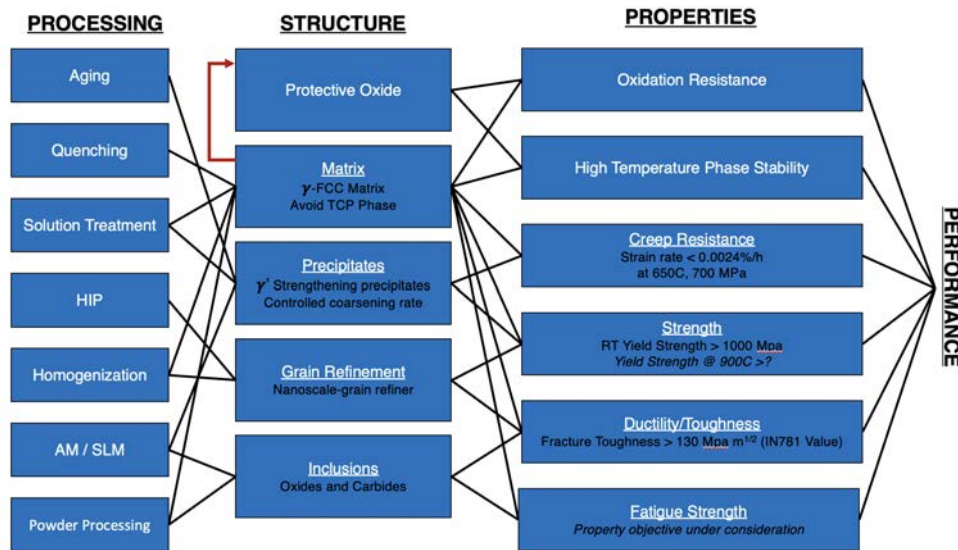


Figure 9.1: Systems design chart for additive manufactured high-strength Co-based  $\gamma - \gamma'$  superalloys

at NIST under the guidance of **Campbell** and **Kattner**. When comparing the current CHiMaD Co-based thermodynamic database predictions with the observed microstructures for the CHiMaD 2019 design prototype it became apparent that additional work was needed to improve the descriptions of the TCP phases. Thus the current work has focused on how to systematically improve the descriptions for the most relevant TCP phases in the database. To improve the modeling of the TCP phases, Griesemer (**Wolverton** Group) and **Wolverton** performed density functional theory (DFT) calculations for the binary endmember compounds of the TCP phases ( $\mu, \sigma, \chi$  Laves (C14, C15, C36)) for 10 elements. Test calculations by Liu for the ternary Co-Cr-Ta system showed that the addition of energy values for the binary endmembers was insufficient to realistically predict the ternary homogeneity ranges of the TCP phases. This appears to be a typical behavior of the compound energy formalism (CEF) when only binary endmembers are considered. The effective bond energy formalism (EBEF) holds great promise to overcome this problem. For this formalism the formation energies from the DFT calculations need to be translated into effective pair bond energies using either an optimization or a matrix inversion approach. These two approaches are currently being evaluated together with the evaluation of whether the simplifications used within the CEF are also feasible for the EBEF. Figure 9.2 shows the value in the EBEF approach in the prediction of the  $\sigma$  in the Ni-Mo-Re system.

To further improve the current diffusion mobility descriptions for the Co-Al-W-Ni-Cr-Ta-Ti-Re system in the FCC phase, new diffusion multiple stacks were designed, and all the individual end-member components have been produced. The focus of the new diffusion multiple stacks is to improve the mobility descriptions for the Co-based Ti and Re systems. Each new diffusion multiple has 16 interfaces and schematic of the diffusion stacks is shown in Figure 9.3. All the individual end-member components are single-phase FCC compositions at the annealing temperatures of interest (1000°C and 1200°C).

## 9.2.2 Computationally Designed Alloys

After the experimental assessment of the first iteration design alloy (MSE390 alloy) and updates to the thermodynamic databases, a new high-temperature, creep-resistant, and



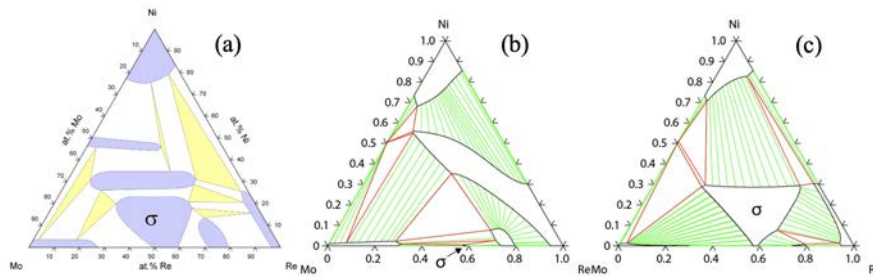


Figure 9.2: Homogeneity range of the  $\sigma$  phase in Mo-Ni-Re. (a) Experimental observation of phase equilibria at 1425 K compared to the calculated homogeneity range at 1500 K using the DFT data for the binary endmembers with the CEF (b) and EBEF (c), respectively. The homogeneity range of the sigma phase in CEF prediction (b) is unrealistically small. The EBEF prediction (c) is much closer to the experimental observations.

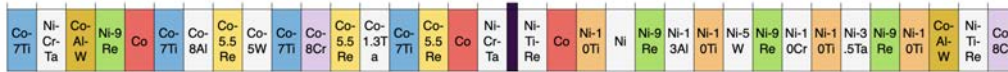


Figure 9.3: Schematic of FCC diffusion multiple stacks that are in the process of being assembled and will be annealed at 1000°C for 500 h and at 1200°C for 100 h. The ternary composition include are Ni-0.10Cr-0.04Ta mole fraction and Ni-0.035Ti-0.035Re mole fraction.

printable Co-based superalloy composition (labelled as 1Re1Ru in Table 9.4) is optimized using thermodynamic modelling and databases. To examine the effects of the slow diffusers (Re and Ru), two additional alloy compositions are also assessed (labelled as Base and 1Re in Table 9.4).

All alloys are cast by arc-melting and homogenized at 1250°C for 20 h. The samples are aged at two different temperatures (1000°C and 1100°C) and at three different times (48 h, 192 h, and 1000 h). Figure 9.4a demonstrates that the three alloys exhibit a pure  $\gamma$ (f.c.c.)/ $\gamma'$ ( $L_{12}$ -structure) two-phase microstructure, after aging at 1000°C for 1000 h. The composition and partitioning behavior are examined employing atom-probe tomography (APT) for long-time aged samples at 1000°C in Figure 9.5. Figure 9.4b demonstrates that Re strongly partitions towards the  $\gamma$ (f.c.c.)-phase, and W partitions less towards the  $\gamma'$ ( $L_{12}$ -structure)-phase with the addition of 1 at. % Re.

Samples that are aged at 1100°C include a Ta-rich precipitate-phase in addition to the  $\gamma$ (f.c.c.)/ $\gamma'$ ( $L_{12}$ ) two-phase microstructure, Figure 9.6. The Ta-rich precipitate-phase is distributed homogeneously, to first order, in the grain interiors and at the grain boundaries. Further analyses will be performed to determine its exact composition and crystallographic structure of this precipitate phase, employing APT, TEM and high-resolution TEM.

Using TC-Python, the mobility descriptions of Co-Re in the current CHiMaD mobility

Alloy (at.%)	Co	Ni	Al	Cr	Ta	W	Re	Ru
Base	41.7	36	12.8	4	3.3	2.2	0	0
1Re	40.7	36	12.8	4	3.3	2.2	1	0
1Re1Ru	39.7	36	12.8	4	3.3	2.2	1	1

Table 9.1: Nominal compositions of Base, 1Re, and 1Re1Ru alloy

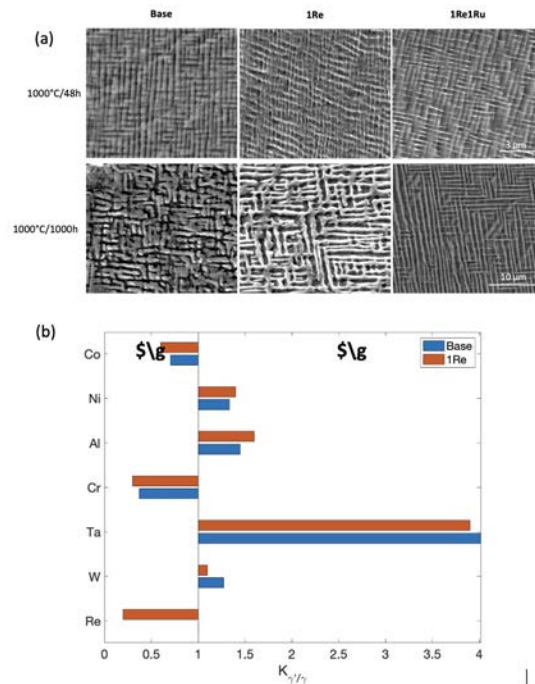


Figure 9.4: (a) Characteristic microstructures of the three alloys aged at 1000°C for 48h and 1000 h. (b) Partitioning coefficients of each element in the base and 1Re alloys aged at 1000°C for 1000 h.

Alloy (at.%)	Co	Ni	Al	Cr	V	Ti	Nb	Ta	B	$\gamma'$ Areal Fraction (%)
10Ni-4Cr	Bal.	10	5	4	3	2	1.5	1.5	0.08	$32 \pm 4$
20Ni-4Cr	Bal.	20	5	4	3	2	1.5	1.5	0.08	$37 \pm 3$
30Ni-4Cr	Bal.	30	5	4	3	2	1.5	1.5	0.08	$49 \pm 6$
10Ni-8Cr	Bal.	10	5	8	3	2	1.5	1.5	0.08	$44 \pm 8$
20Ni-8Cr	Bal.	20	5	8	3	2	1.5	1.5	0.08	$45 \pm 5$
30Ni-8Cr	Bal.	30	5	8	3	2	1.5	1.5	0.08	$45 \pm 2$

Table 9.2: NiCr-series alloy nominal compositions (at.%)

database, developed by **Campbell** at NIST, is optimized based on experimental diffusion profiles and interdiffusivity values. The mobility parameters are optimized by minimization of the error between all experimental and predicted values.

### 9.2.3 W-Free Cobalt-based Superalloys

In an effort to decrease the density of Co-alloys, six new W-free Co-based superalloys were studied, given by the compositions listed in Table 9.2, where for the first time, the three Ta, Nb and V refractory metals are present simultaneously (at a combined level of 6 at.%), in the absence of W and Mo. These low-density alloys expand on previously developed 2018-19 CHiMaD alloys, which had two refractory elements (either Ta+V or Nb+V), and investigates additions of Ni and Cr. All six alloys display  $\gamma + \gamma'$  microstructures, with no other precipitates, after 1000 hours of aging at 850°C. The alloys contain Ni (to stabilize the microstructure and reduce alloy cost); Cr (to decrease lattice parameter misfit and improve oxidation and corrosion resistance); Al, V, Ti, Nb, and Ta (as  $\gamma'$ -formers); and B (for grain boundary strengthening). Based on these experimental findings, V is being added to thermodynamic databases developed by **Kattner** and **Campbell** at NIST. Predictions based on these databases will form the basis of new alloys to be studied experimentally.

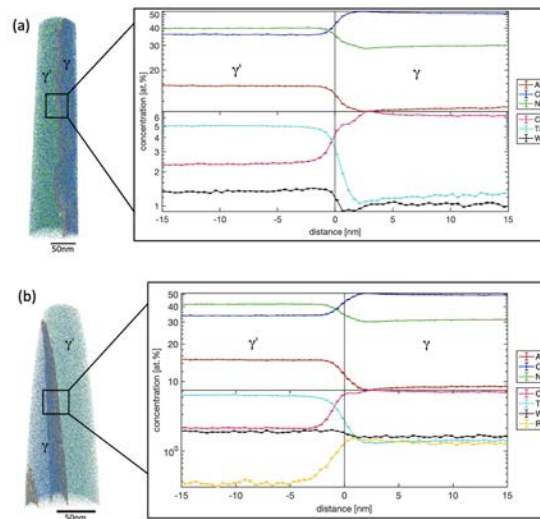


Figure 9.5: (a) 3D reconstruction of an APT tip from the Base alloy aged at 1000°C for 1000 h with the proxigram across the  $\gamma$ (f.c.c.)/ $\gamma'$ (L<sub>12</sub>-structure) interface. The isoconcentration surface is at Co = 42.5%. (b) 3D reconstruction of an APT nanotip from the 1Re alloy aged at 1000°C for 1000 h with the proximity histogram across the  $\gamma$ (f.c.c.)/ $\gamma'$ (L<sub>12</sub>-structure) interface. The isoconcentration surface is at Co = 41%.

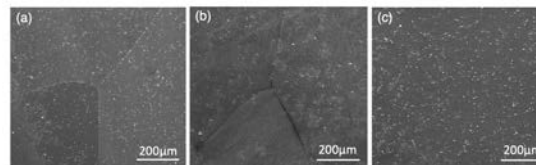


Figure 9.6: Low magnification SEM images of: (a) Base alloy; (b) 1Re alloy; and (c) 1Re1Ru alloy aged at 1100°C for 48 h. The Ta-rich precipitate-phase appears as small white precipitates in the three alloys.

Figure 9.6: Low magnification SEM images of: (a) Base alloy; (b) 1Re alloy; and (c) 1Re1Ru alloy aged at 1100°C for 48 h. The Ta-rich precipitate-phase appears as small white precipitates in the three alloys.

Alloys were produced by arc-melting and homogenizing for 48 h at 1200°C. After ensuring that the homogenized sample is single-phase, samples were aged at 850°C to 1000 h. Figure 9.7a shows SEM micrographs of each alloy after the final aging time. In the 4-Cr series, increasing the Ni concentration results in higher fractions of the  $\gamma'$ -phase. The 8-Cr series maintains a near-constant  $\gamma'$ -area-fraction, independent of the concentration of Ni.

Lattice misfit was measured with a combination of synchrotron x-ray diffraction on aged samples, and lab XRD on recrystallized and aged samples, as shown in Figure 9.7b. Lattice misfits are between 0.6 and 1%, nearly independent of Cr and Ni content.

Isothermal creep tests were performed on specimens aged one week at 850 °C, as shown in Figure 9.7c. All alloys exhibit power-law creep behavior at 850°C, with a stress exponent of 10-12. The addition of Ni slightly improves creep resistance for all alloys. Increasing Cr results in slightly improved creep resistance for alloys with 20 and 30% Ni, but worse creep performance for alloys with 10% Ni.

Solvus, solidus, and liquidus transformation temperatures were measured with DSC, as shown in Figure 9.8a. Solvus temperatures increase by 15-20°C per 10 at.% Ni addition,

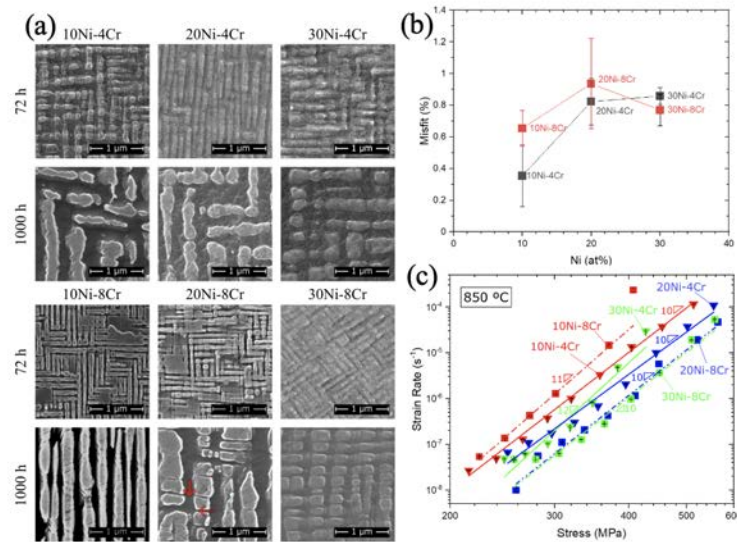


Figure 9.7: (a) Characteristic microstructures of each alloy after aging for 72 and 1000 h at 850 °C. (b) Lattice misfit for each alloy at room temperature plotted as a function of composition. (c) Plot of strain rate vs. compressive stress at 850°C for each alloy.

and 15-20°C as Cr doubles from 4 to 8 at.%, so that 30Ni-8Cr has the highest value: 1031°C. There is no clear trend for solidus and liquidus temperatures, but each alloy is within ~15 °C of the others. Oxidation resistance was measured in a TGA at 850 °C for 20 h in laboratory air, as shown in Figure 9.8b which plots normalized mass gain as a function of time.

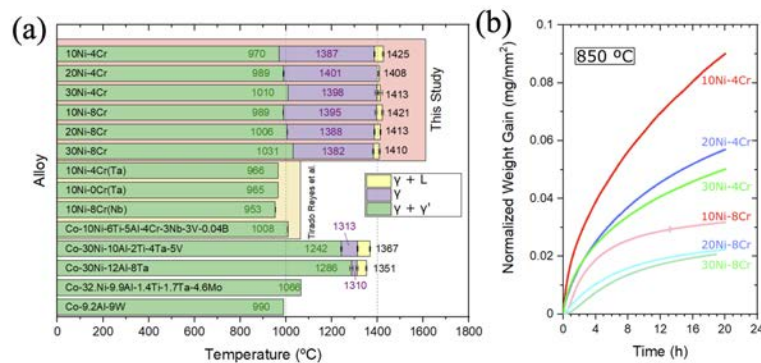


Figure 9.8: (a) Characteristic microstructures of each alloy after aging for 72 and 1000 h at 850 °C. (b) Lattice misfit for each alloy at room temperature plotted as a function of composition. (c) Plot of strain rate vs. compressive stress at 850°C for each alloy.

Based on a preliminary result which showed that substituting 10 at% Fe for Ni in the 30Ni-4Cr/8Cr alloys maintained a stable  $\gamma/\gamma'$  microstructure, six additional alloys were created with increasing substitutions of Fe for Ni, for the same two levels of 4 and 8% Cr, as shown in Table 9.3. All six alloys displayed a  $\gamma/\gamma'$  microstructure after aging 1000 h at 850°C, although high-Fe and -Cr alloys also formed TCPs at higher aging time, as shown in Figure 9.9.

Isothermal creep tests were performed on specimens aged (168 h (1 week) at 850 °C, as

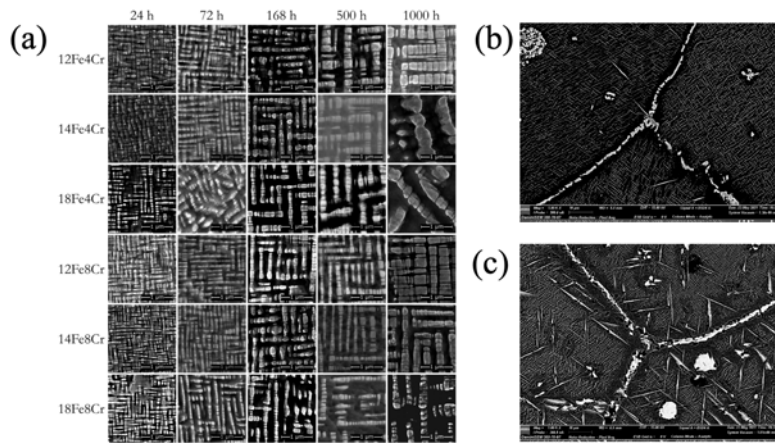


Figure 9.9: (a) Secondary SEM images of  $\gamma + \gamma'$  region in all alloys at all aging conditions. (b) Low-mag SEM image which shows TCPs in 18Fe-4Cr and (c) 18Fe8Cr after aging 1000h at 850°C.

Alloy (at.%)	Co	Ni	Fe	Al	Cr	V	Ti	Nb	Ta	B
12Fe-4Cr	Bal.	18	12	5	4	3	2	1.5	1.5	0.08
14Fe-4Cr	Bal.	16	14	5	4	3	2	1.5	1.5	0.08
18Fe-4Cr	Bal.	12	18	5	4	3	2	1.5	1.5	0.08
12Fe-8Cr	Bal.	18	12	5	8	3	2	1.5	1.5	0.08
14Fe-8Cr	Bal.	16	14	5	8	3	2	1.5	1.5	0.08
18Fe-8Cr	Bal.	12	18	5	8	3	2	1.5	1.5	0.08

Table 9.3: NiCr-series alloy nominal compositions (at.%)

shown in Figure 9.10a. Fe additions show a clear reduction in creep resistance. In 12Fe and 14Fe, Cr addition increases creep resistance, but Cr reduces creep resistance in 18Fe, likely due to accelerated formation of TCPs.

Solvus, solidus, and liquidus temperatures were measured with DSC, as shown in Figure 9.10b. Increasing Fe from 0Fe-30Ni to 12Fe-18Ni increases solvus by  $>150^\circ\text{C}$ , and reduced solidus and liquidus values by  $\sim 50\text{-}100^\circ\text{C}$ . Fe additions continue to monotonically increase solvus even up to 18Fe. The addition of 4 at.% Cr also slightly increases solvus by  $5\text{-}10^\circ\text{C}$ . Solidus and liquidus values decreased by  $\sim 5^\circ\text{C}$  with the addition of 4 at.% Cr, but were not affected by Fe in the range of 12-18 at.%.

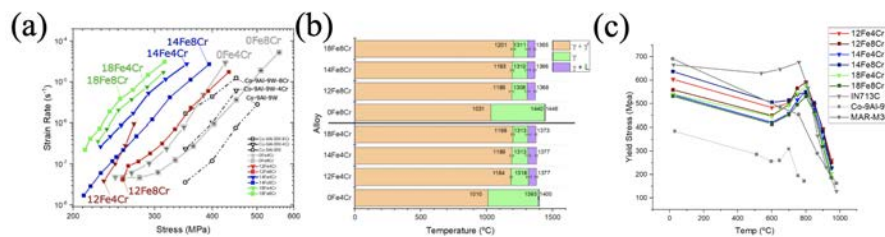


Figure 9.10: a) Plot of strain rate vs. compressive stress at 850°C for each alloy. (b) DSC results showing solvus, solidus, and liquidus temperatures for each alloy. (c) Compressive yield strength vs. test temperature for each alloy.

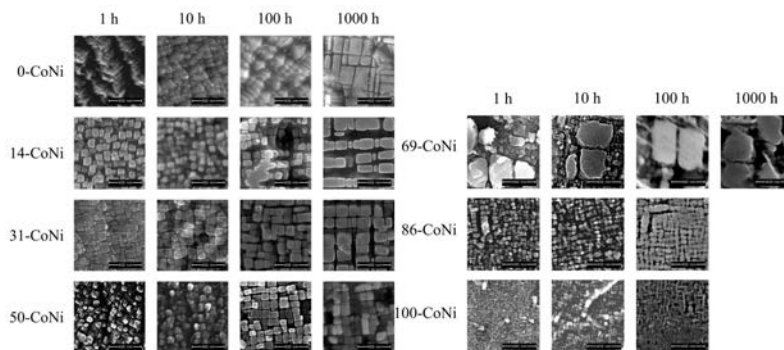
Alloy (at.%)	Co/(Co+Ni) fraction	Co	Ni	Ta	Al
CoNi 0	0	0	87.5	0	12.5
CoNi 14	14	12.5	75.0	1.8	10.7
CoNi 31	32	27.5	60.0	3.9	8.6
CoNi 50	50	43.5	44.0	6.2	6.3
CoNi 69	69	60.0	27.5	8.6	3.9
CoNi 86	86	75.0	12.5	10.7	1.8
CoNi 100	100	87.5	0	12.5	0

Table 9.4: CoAlNiTa quaternary series nominal compositions (at.%)

Yield strength as a function of temperature was measured with a compression tester, as shown in Figure 9.10c. Fe additions result in a weakening effect, but all six alloys show strong anomalous yield strength with a peak around 800°C.

Seven quaternary alloys along the tie line between Ni-12.5Al and Co-12.5Ta, created prior to 2021 at University of Cambridge by collaborators Prof. Stone and Prof. Jones, were studied to establish whether a continuous  $\gamma + \gamma'$  region exists, as shown in Table 9.4.

Microstructure for each alloy is shown in Figure 9.11, aged up to 1000 h at 750°C. Alloys from 0CoNi to 69CoNi exhibit a two-phase  $\gamma + \gamma'$  structure, but 86CoNi and 100CoNi show a  $\gamma + \lambda 3$  microstructure after homogenization. Upon aging at 750°C, the  $\gamma$  matrix forms  $\gamma'$  precipitates. At longer aging times, the cubic-shaped  $\gamma'$  phase forms discontinuous precipitates with a lamellar shape.

Figure 9.11: Secondary SEM images for  $\gamma + \gamma'$  region in each alloy at each aging temperature

Solvus, solidus, and liquidus values were measured with DSC, as shown in Figure 6a and show monotonic decrease in solidus and liquidus with increasing Co.

Lattice parameters for  $\gamma$  and  $\gamma'$  phases, which had been measured via neutron diffraction, were fit with GSAS-II, to calculate lattice misfit and interfacial stress. Both lattice parameters increased with increasing Co, but the  $\gamma'$  parameter increased more than the  $\gamma$  parameter, so that lattice misfit also increased with increasing Co. Interfacial stress also increased with increasing Co, with the exception of 50CoNi, which has lower interfacial stress than its neighbors.

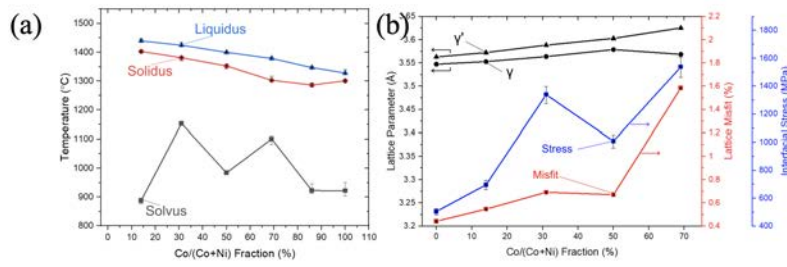


Figure 9.12: (a) DSC results for selected alloy. (b) Lattice parameters, lattice misfit, interfacial stress for selected alloys.

### 9.2.4 Machine learning model for creep life

Additionally, an archival literature summary of mechanical properties in Co-based superalloys was created in 2020-21, which collected data concerning transformation temperatures, lattice parameter misfit, microhardness, yield strength, and creep results from over 750 Co-based superalloys. These data, as well as CALPHAD predictions from NIST, are being used to power a machine-learning model with the goal of predicting creep life of Co-based superalloys for a given element composition, in collaboration with Dr. **Campbell** (NIST) and Jesse Ji (NIST SURF student). The machine-learning model currently takes inputs of composition with Magpie chemical descriptors (developed by **Wolverton** group) and  $\gamma/\gamma'$  composition and volume fraction according to CALPHAD predictions, to correlate with literature values of creep life calculated as time to 1% strain based on steady-state strain rate at a particular stress and temperature. The algorithm randomly assigns 90% of the datapoints as “training” data to build a model, then uses the remaining 10% “test” data, which the model did not see, to evaluate its accuracy. The results of the model’s prediction for this test data, compared to the true measured value of the test data, is shown in Figure 9.13.

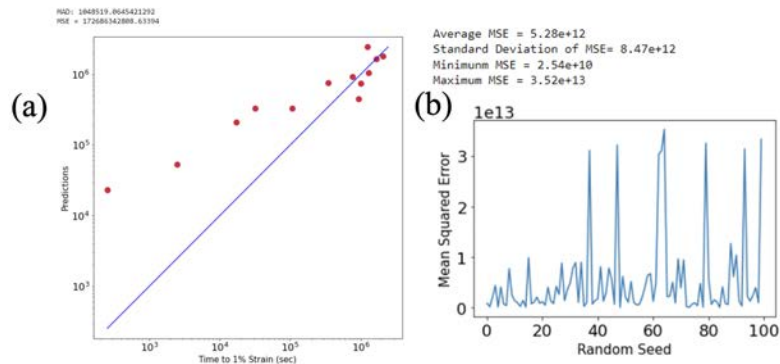


Figure 9.13: (a) Plot of “test data” for creep time to 1% strain (measured values) vs. machine-learning predicted values. Points which fall exactly on the blue  $y=x$  line are values which the algorithm has perfectly predicted. (b) Error between predicted values and true values, for 100 random splits of test data versus training data.

In another study in collaboration with Kookmin U., the design goal is to create a microlattice-architecture Co-based superalloy (Co-Ni-Al-W) by using a combination of extrusion-based 3D printing and pack cementation. To prevent Al depletion occurring during the creep test in air (Figure 9.13a) that was an issue in the previous study as well as to improve the creep performance, additional Al deposit was applied on an already homogenized Co-Ni-W-Al

microlattice, followed by aging the sample. As shown in Figure 9.14b, the additional Al deposit after homogenization achieved an Al-rich layer with a mean thickness of up to  $\sim 30\mu\text{m}$  which can act as an Al-reservoir for  $\text{Al}_2\text{O}_3$  formation, while protecting the  $\gamma/\gamma'$  microstructure from oxidation.

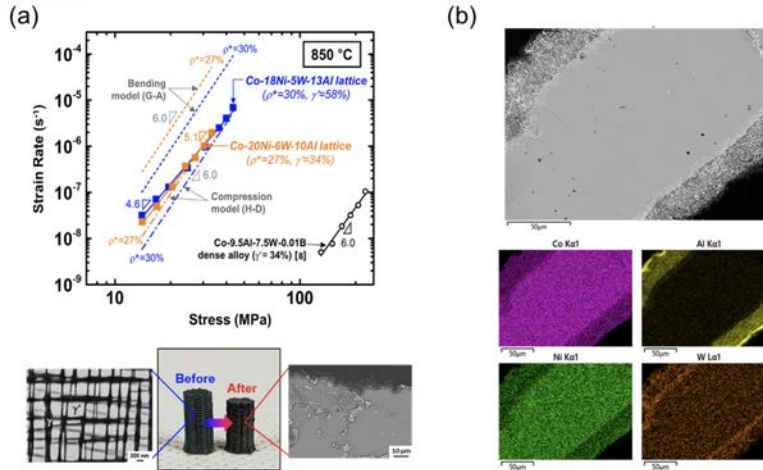


Figure 9.14: (a) Double logarithmic plots of secondary creep strain rate versus applied compressive stress for Co-20Ni-6W-10Al and Co-18Ni-5W-13Al microlattices aged at 900 °C for 65 h and compression tested at 850°C. (b) SEM and EDS mapping images showing the Al-rich top-layer on cross-sections of struts of homogenized Co-20Ni-7W-9Al microlattices aluminized at 1000°C.

In a new 2021 industrial collaboration, the role of grain-boundary precipitates on the creep property of a novel, commercial Co-Ni based superalloy are studied via compressive creep tests on two different initial microstructures. Dominant species of grain boundary precipitates were controlled by changing aging condition as shown in Figure 9.15a and 9.15b. The intragranular Vickers microhardness indicated that the amount and the size of intragranular  $\gamma'$  particles in both microstructures are almost identical. Compressive creep tests at 800°/ 409 MPa indicated that the difference of grain-boundary-precipitation species have a large influence on the creep properties, as shown in Figure 9.15.

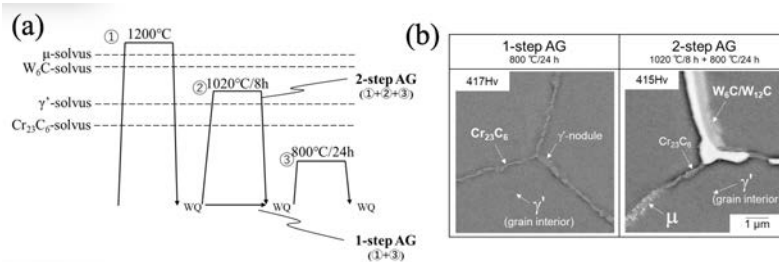


Figure 9.15: (a) Schematic illustration of the heat treatment condition for the alloy studied. (b) Backscattered electron images of the microstructures after 1-step-aging and 2-step aging conditions.

In a new project, Co-20Ni-11Al-8W (at.%) alloys, based on a composition provided by NIST, were fabricated using blends of elemental powders via selective laser melting under different laser input energy density. Relative density of printed alloys increases with increasing laser energy density, as shown in Figure 9.16. Two samples per each energy density were printed, whose relative density are marked as blue and red dots, respectively. Microstructure of printed alloys were investigated. Nearly homogenized  $\gamma$  microstructure



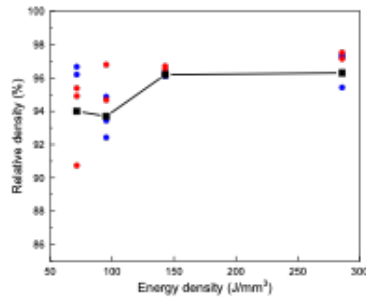


Figure 9.16: Relative density of printed Co-20Ni-11Al-8W (at.%) alloys as a function of laser energy density.

was observed with occasional partially-melted W powders. Work is ongoing to homogenize the alloys to achieve full  $\gamma + \gamma'$  microstructure, and to measure mechanical properties

### 9.2.5 Predicting Phase Stability Using Machine Learning

For materials design, it is important to know the phase stability of the material to determine its properties. For material systems that are less explored, it is time-consuming and costly to generate sufficient experimental data to optimize the composition. Density functional theory (DFT) calculations provide high fidelity data, but it is computationally expensive to compute a wide range of complex compounds at elevated temperatures. Our goal is to develop a surrogate model that can efficiently predict the phase stability of multi-component material systems at finite temperature. Currently, we have fitted a preliminary Latent Variable Gaussian Process (LVGP) model, which predicts formation energies per atom with input data concerning composition, crystal system, and number of atoms. The benefit of using the LVGP model allows for the categorical values (e.g., crystal structures) to be mapped to a quantitative latent space, which can be analyzed for physical insights. The training and testing datasets are collected from Materials Project and Open Quantum Materials Database (OQMD). Six elements of interest are identified (Al, Co, Ni, W, Pb, Te) and the dataset consist of pure elements, binary and ternary compounds of these elements. Figure 5 demonstrates how the test dataset performs with the current LVGP model. The relative root-mean-square error (RRMSE) ranges from 0.49-0.67, which will be further improved on.

### 9.2.6 Machine learning in phase-field sensitivity analysis

For more accurate Co-based superalloy designs, a better understanding of how different parameters influence the  $\gamma'$  precipitate morphology is needed. A phase-field sensitivity analysis is conducted on a ternary Co-Al-W alloy system with a focus on four parameters: initial concentration ( $c_0$ ), double well barrier potential ( $\omega$ ), gradient energy density coefficient ( $\kappa$ ), and lattice parameter misfit strain ( $\epsilon_{misfit}$ ). A Gaussian Process Regression (GPR) model is used to fit an initial set of samples, which is then coupled with a Bayesian Optimization (BO) process to suggest additional samples in an efficient manner. This provides a more data-driven approach for sensitivity analysis and creates a flexible surrogate model compared to standard bi-linear fit. The BO approach is also a more efficient way to update the GPR model iteratively. Figure 9.17 displays the final version of the GPR surrogate models of the precipitate's radius and morphology. From the surface plots, we observe that  $c_0$  and  $\omega$  have the greatest influence on the precipitate radius and morphology, respectively. The precipitate radius description is precise, and thus can be fitted with a low noise tolerance. Alternatively, the precipitate morphology description has some variability

due to irregular  $\gamma'(L1_2)$ -precipitates simulated. Therefore, the precipitate morphology model needs a higher noise tolerance to avoid overfitting.

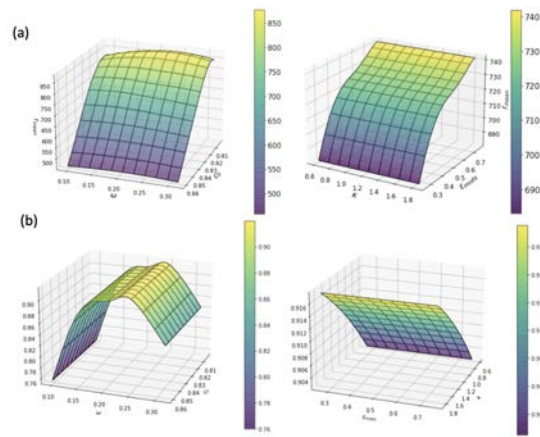


Figure 9.17: Gaussian Process Regression (GPR) model of a precipitate: (a) radius and (b) morphology in terms of (left) initial concentration and double well barrier potential, and (right) gradient energy density coefficient and lattice parameter misfit strain

### 9.2.7 Phase Field Modeling of Co-based superalloys

We completed phase field modeling of morphology evolution of three-dimensional Co-based superalloy precipitates. Particular foci of the work were (i) using experimental or first-principle data for bulk chemical free energy, element mobility and interfacial energy, and (ii) investigate the sensitivity of precipitate size and shape to input parameters within reasonable and physical ranges. We constructed a latin hypercube (see Figure 9.18 top) over the following parameters space: initial Co-concentration  $c_0$ , double-well potential barrier  $\omega$  used for the phase field  $\eta$ , gradient energy coefficient  $\kappa$ , and misfit strain  $\epsilon_{misfit}$ . The parameters  $\eta$  and  $\kappa$  are directly related to the interfacial free energy and the interface thickness. The phase field mobility,  $L$ , was kept in a range where the morphology evolution is diffusion-limited; this covers a large range of  $L$  within which the results are insensitive to  $L$ . Therefore,  $L$  could be excluded from the sensitivity analysis.

Figures 9.18 middle and bottom, show different precipitate morphologies varying the gradient energy coefficient  $\kappa$  and the misfit strain  $\epsilon_{misfit}$ , respectively. Increasing  $\kappa$  increases the interfacial energy, which tends to drive the precipitate to a more spherical shape. In contrast, increasing  $\epsilon_{misfit}$  increases the elastic energy cost of the precipitate and also drives it to a more cuboidal shape; if  $\epsilon_{misfit}$  becomes too large, the energy cost of forming an equilibrium precipitate is prohibitive, and the precipitate dissolves.

We constructed a response surface by fitting normalized output parameters for precipitate shape and size to bilinear functions of the (normalized) input parameters. Figure 3 depicts a graphical summary of the sensitivity analysis. This figure shows that the main drivers for precipitate size are initial Co-concentration, and its product with barrier height  $\omega$  and misfit strain  $\epsilon_{misfit}$ . This dependence on initial concentration just expresses the fact that the bulk chemical free energy is a main driver for the size of the precipitate. The drivers for precipitate shape are more complicated. Main drivers here are barrier height  $\omega$ , to a lesser extent misfit strain  $\epsilon_{misfit}$ , and then various crossproducts of  $\omega$  and  $\kappa$  with other parameters. This expresses that the shape is largely driven by a competition between elastic energy (primarily represented by the misfit strain) and the interfacial energy ( $\omega$  and  $\kappa$ ):

Sample No.	$c_0$	$\omega$ (aJ nm <sup>-3</sup> )	$\kappa$ (aJ nm <sup>-1</sup> )	$\epsilon_{misfit}$ (%)	$R_0$ (nm)	$L$ (nm <sup>3</sup> s <sup>-1</sup> aJ <sup>-1</sup> )
0	0.830	0.173	1.000	0.500	75.00	100.0
1	0.849	0.128	1.366	0.545	95.93	55.37
2	0.803	0.161	1.180	0.324	25.38	87.21
3	0.834	0.297	0.699	0.852	184.6	119.0
4	0.843	0.191	0.762	0.265	53.12	184.4
5	0.860	0.314	0.607	0.990	120.0	66.92
6	0.841	0.209	1.007	0.757	175.6	76.32
7	0.823	0.111	0.535	0.424	67.22	60.26
8	0.817	0.141	1.834	0.474	77.51	114.0
9	0.829	0.096	1.592	0.373	45.22	155.4
10	0.808	0.251	0.995	0.595	34.66	150.0

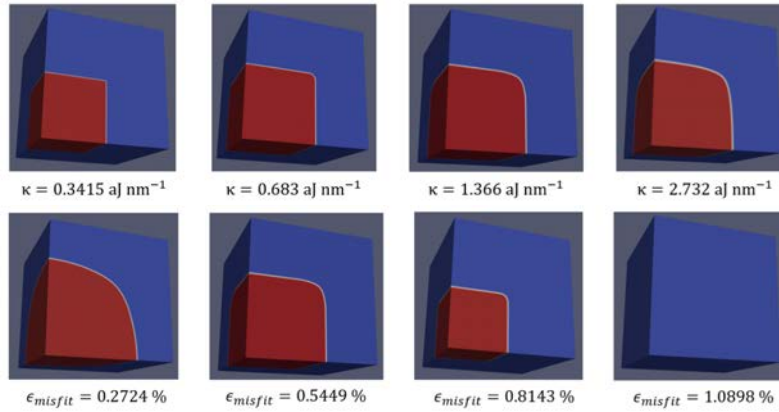


Figure 9.18: (top) Parameters for the latin hypercube. (middle) Equilibrium precipitate (in red) for different gradient energy coefficient  $\kappa$ . The other parameters are those of Sample 1 in Table at top. (bottom) Equilibrium precipitate for different misfit strain  $\epsilon_{misfit}$  the other parameters are those of Sample 1 in Table at top.

increasing the misfit strain drives the shape more cuboidal, while increasing the interfacial energy (which is proportional to  $\kappa\sqrt{w}$ ) tends to drive the precipitate shape more spherical. A manuscript is under review with Acta Materialia.

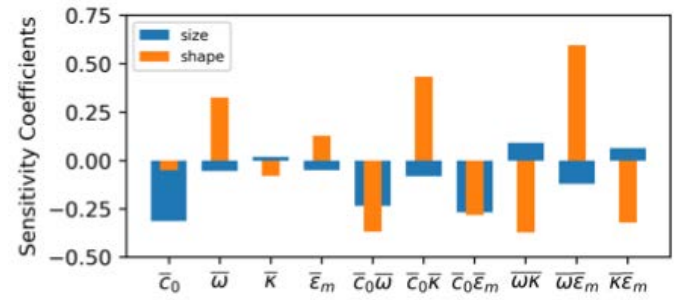


Figure 9.19: . Sensitivity coefficients for precipitate size and shape. Negative values means that increasing the parameter or parameter product decreases the precipitate size or makes the shape less cuboidal.

After completing the work on the sensitivity analysis of a single precipitate, we turned our focus on the evolution of multiple precipitates and their responses to applied stresses. Roughly speaking, a small misfit strain tends to make particles coalesce and yields a relatively weak response to applied uniaxial compressive or tensile stress. In contrast, a larger misfit strain yields larger response to applied uniaxial stresses, and whether or not the precipitates coalesce depends on the stress (compressive or tensile). Compressive

stress flattens the precipitates and makes them coalesce more easily, while tensile stress elongates them (along the stress) and tends to prevent them from coalescing. We are finishing analysis of the result and are preparing a manuscript for submission.

Inspired by the initial sensitivity analysis of the single-precipitate shape and size, we started a project using AI-inspired tools to more systematically improve the sensitivity analysis. We used Optimized Experimental Design (OEM), a version of active learning methods that is particularly suited for constructing surrogate models when the available data set is small and the acquisition of new data points is expensive. OEM is iterative: based on a surrogate model constructed from  $N$  data points, the OEM can give good guidance for where in parameter space one should acquire data point  $N+1$ . In our case, we constructed surrogate models using Gaussian Process Regression, which includes a flexible set of basis functions, and also produces an uncertainty metric. We used the Expected Improvement approach for acquisition, which basically seeks to minimize the uncertainty in the surrogate model. Using an initial set of data points from the earlier sensitivity analysis, we expanded the data set using OEM. The surrogate model for the response function is markedly different in some respects from the earlier bilinear fit. We are currently finishing analyzing the results, and we are preparing a manuscript.



## 10. High-Performance Composite Design for Extreme Environments

**Kenneth Shull** (NU), Sinan Keten (NU), Ange-Therese Akono (NU)

**Christopher Soles** (NIST), Stephan Stranick (NIST), Jack Douglas (NIST), Frederick Phelan (NIST), Jan Obrzut (NIST), Jeremiah Woodcock (NIST), Gale Holmes (NIST), Edwin Chan (NIST), Lilian Johnson (NIST), Ketan Khare (NIST), Ami Ahure Powell (NIST)

### 10.1 Design Goals

The goal of the CHiMaD High-Performance Composite Design for Extreme Environments use case group is to develop and utilize a materials design strategy for fiber reinforced polymer matrix composites used in extreme environments, including ultra-low temperatures or very high strain rates. Of particular interest is cryogenic storage applications where mechanical toughness and stiffness must be maintained at temperatures from -200 °C to 200 °C. A secondary goal involves design for composites exposed to aqueous or humid environments for long periods of time. A generalized design chart for high-performance composite design with potential applications in cryogenic liquid storage, infrastructure and protection applications is shown in Figure 10.1.

Specific design goals of the use case group towards cryogenic liquid storage include the following: (1) A matrix resin with a fracture toughness,  $K_{IC}$ ,  $> 1.5 \text{ MPa}\cdot\text{m}^{1/2}$  throughout the temperature range of -100 °C to 200 °C; (2) Development of model sizings for carbon fibers that can be deposited from aqueous suspension, but which adsorb less than 20 wt% water at a relative humidity of 75%; (3) Composite systems for which the maximum interfacial shear stress remains less than 50 MPa during temperature cycling between -200 °C and 200 °C.

The CHiMaD High-Performance Composite Design for Extreme Environments use case group is also interested in quantifying the equilibrium content of cryogenic liquids adsorbed within the material and within model fiber treatments based on cellulose nanocrystals.

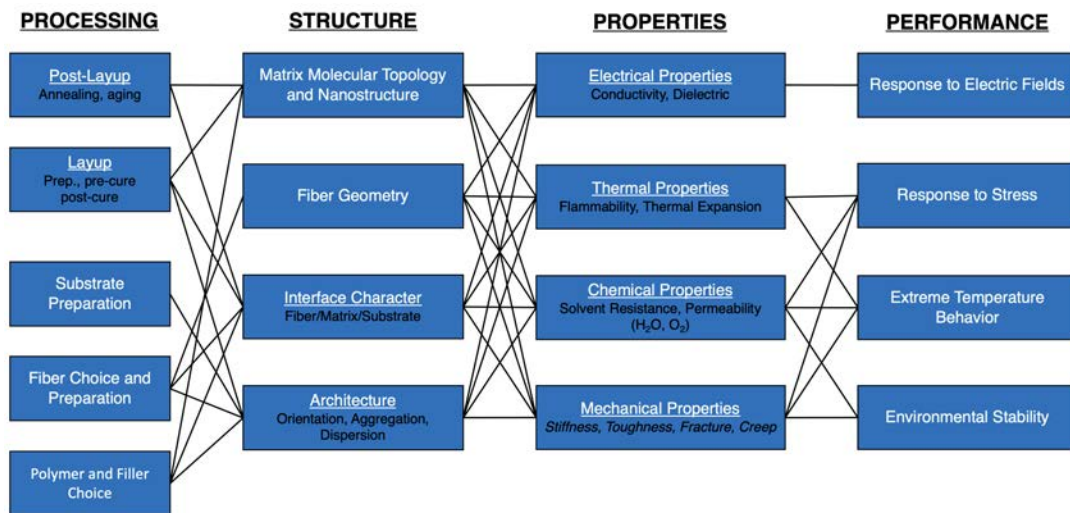


Figure 10.1: Systems design chart for high-performance composite design for extreme environments

## 10.2 Research Accomplishments

### 10.2.1 Modeling the Single Fiber Fragmentation Test

The single fiber fragmentation test is the among the most powerful methods for characterizing the interfacial strength of the fiber/matrix interface in fiber reinforced polymer matrix composites. As shown in Figure 10.2a, the experiment involves applying a tensile force to a polymer sample in which a single fiber is embedded. Recent advances at NIST (**Holmes** and **Powell**) have led to the development of an automated experimental protocol that is able to generate much more data from a single experiment, including the full history of the time and location at which different breaks appear. **Akono** and **Shull** are working with the NIST team to develop nonlinear viscoelastic models needed both to extract the true interfacial stress during complex loading conditions, including those that accompany extreme excursions in the temperature. An example model fit to a load data obtained from a single fiber fragmentation test is shown in Figure 10.2b.

### 10.2.2 Glassy Polymer Dynamics in the Megahertz Frequency Regime

Small molecule plasticizers are often used to modify the local-scale dynamics of glassy polymers, which in turn affects the glass transition behavior, fracture toughness and other properties that are relevant to polymer matrices used in composite systems. These dynamics are commonly assessed by dielectric measurements, which requires that a coupling between mechanical and dielectric properties exist in the material, and that the material not be electrically conducting. The NIST group (**Douglas, Obrzut, Soles**) has been very involved in this previous work. **Shull** has collaborated with NIST colleagues to obtain quantitative information in the high frequency regime with quartz crystal resonators. This technique measures the material response directly at a fixed angular frequency of  $\approx 10^8 \text{ s}^{-1}$ , and was used to probe the temperature-dependent dynamics of polycarbonate blended with dioctyl terephthalate (DOTP) (Figure 10.3a). The thin film geometry used in these experiments enables a range of DOTP concentrations to be investigated in a single experiment, by progressively driving off the small molecule during successive temperature ramps (Figure 1b). The modulus (Figure 10.3c) and phase angle (Figure 10.3d) data for the PC/DOTP systems show the following trends with increasing DOTP weight fraction, as indicated by

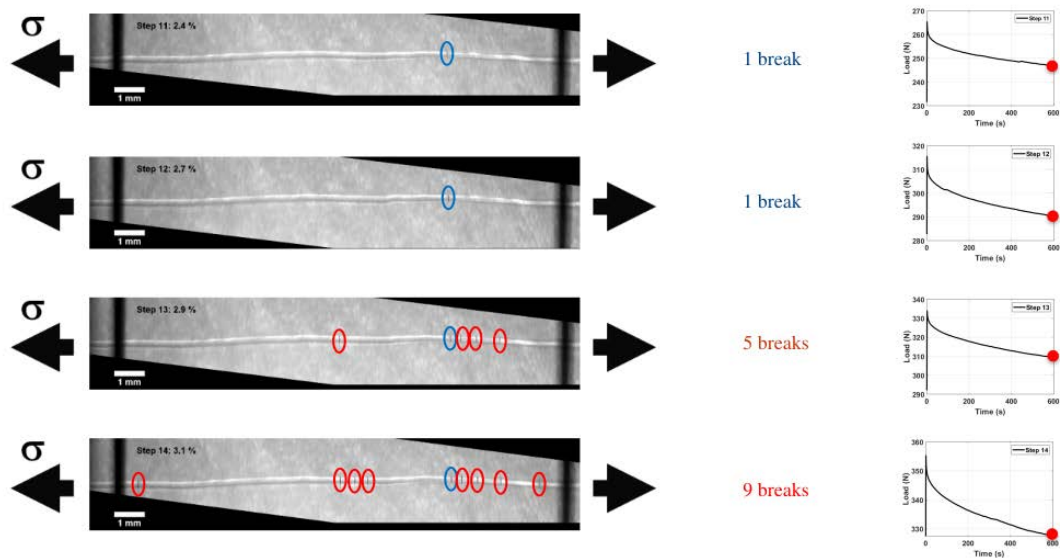


Figure 10.2: a) Single fiber fragmentation test showing a sequence of images at increasing applied step strains; b) Experimental and modeled values of the stress during the application of a series of step strains.

the arrows in Figure 10.3:

1. DOTP increases the modulus of PC in the glassy regime, an 'antiplasticization' effect that has been previously observed in polycarbonate.
2. DOTP decreases the glass transition, seen as an increase in the phase angle at higher temperatures.
3. DOTP decreases the magnitude of the sub- $T_g$  relaxation at 50 °C, resulting in decrease in the peak in the phase angle centered at this temperature.

Because the technique employed here measures the mechanical response directly, it can be used to study electrically conducting materials, including those with common conductive nanofillers like carbon black. Also, the technique measures properties at a time scale of tens of nanoseconds, which is accessible by some of the simulation techniques being developed within the use case and described in more detail below.

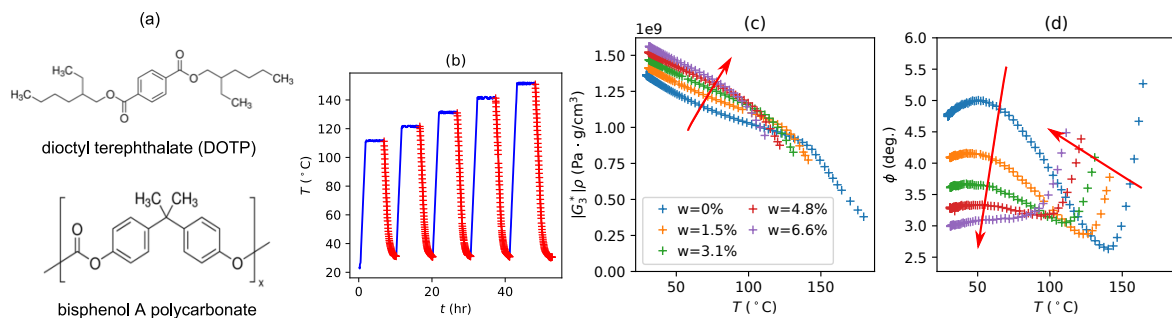


Figure 10.3: Temperature-dependent rheological data obtained for polycarbonate/dioctyl terephthalate films (structures in part a) with the quartz crystal microbalance: b) temperature ramps used to generate temperature-dependent data for a range of DOTP concentrations; c) temperature dependence of the modulus-density product at a frequency of 15 MHz; d) temperature dependence of the viscoelastic phase angle at 15 MHz.

### 10.2.3 Development of Coarse-graining Methodologies for Computational Investigations of Polymer Deformation

Creating coarse-grained models greatly reduces computational expense, but at the cost of the work required to parameterize these models. This is known to be a lengthy and intensive process that can take months of labor for even relatively simple systems. This limits the complexity of the materials that can be coarse-grained. Machine-learning techniques, including Gaussian process surrogate models, were implemented by **Keten** to parameterize nonbonded interactions for coarse-grained epoxy resins (see Figure 10.4).

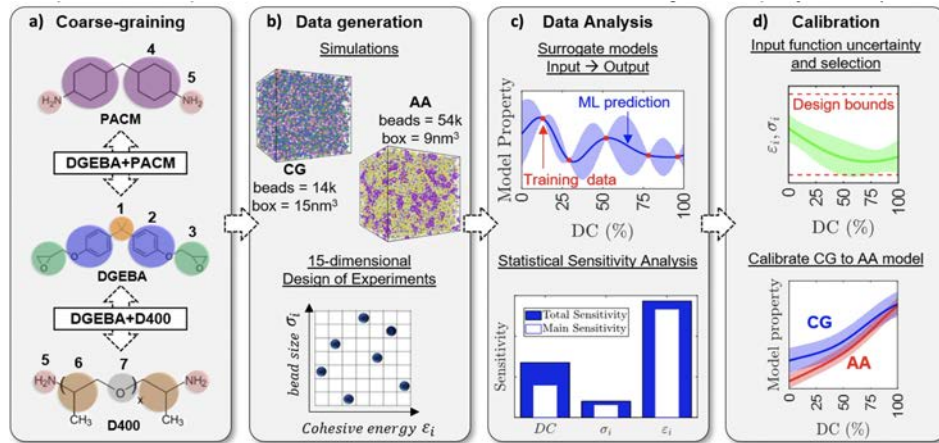


Figure 10.4: Overview of the application of machine learning techniques to parameterization and calibration of non-bonded interactions for coarse-grained cross-linked epoxy resin systems.

These methods reduce the effort required for a complex parameterization such as coarse-grained cross-linked epoxy resin models, and also increase the accuracy of the models and material behavior predictions. As a result, the feasible region of coarse-grained molecular dynamics simulations is expanded, enabling exploration of even more material designs.

### 10.2.4 Effective potential for polymer-grafted nanoparticles

Polymer-grafted nanoparticles are a developing material class that show great promise for creation of tailored materials. **Keten** has explored the effects of variations in the length and density of polymer chains grafted onto a representative nanoparticle surface, using chemistry-specific parameterization to propose a means of coarse-graining models of entire polymer-grafted nanoparticles (PGNs) for use in molecular dynamics simulations. Tensile and compressive simulations were performed, and the potential of mean force (PMF) was used to characterize the response, as this reflects the interaction energies among the polymer chains (see Figure 10.5). The application of coarse-graining procedures to polymer-grafted nanoparticles is anticipated to reduce computational time required to

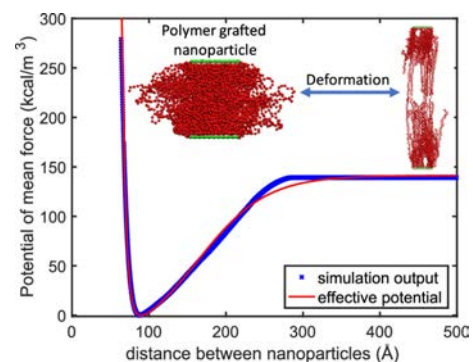


Figure 10.5: Representative potential of mean force between two contacting polymer-grafted nanoparticle surfaces.



simulate these systems by 6-7 orders of magnitude.

### 10.2.5 Data Centric Materials Design via Mixed-Variable Bayesian Optimization

**Chen** has developed a data-centric mixed-variable Bayesian Optimization framework for design of complex material systems with both qualitative and quantitative variables. This has been further extended as a data centric design framework to concurrently identify optimal composition and microstructure in design of polymer nanocomposites. Polymer nanocomposites have the potential to be widely used across multiple industries. Tailoring nanocomposites to meet application specific requirements remains a challenging task, owing to the vast, mixed-variable design space that includes composition (i.e. choice of polymer, nanoparticle, and surface modification) and microstructures (i.e. dispersion and geometric arrangement of particles) of the nanocomposite material. Modeling properties of interphase, the region surrounding a nanoparticle, introduces additional complexity to the design process and requires computationally expensive simulations. As a result, previous attempts at designing polymer nanocomposites have focused on finding the optimal microstructure for only a fixed combination of constituents. With our approach, optimal composition and microstructure can be identified concurrently. Our proposed framework (Figure 10.6) integrates experimental data with state-of-the-art techniques in interphase modeling, microstructure characterization & reconstructions and machine learning. Our proposed Latent Variable Gaussian Processes (LVGPs) quantifies the lack-of-data uncertainty over the mixed-variable design space that consists of qualitative and quantitative material design variables. The design of electrically insulating nanocomposites is cast as a multicriteria optimization problem with the goal of maximizing dielectric breakdown strength while minimizing dielectric permittivity and dielectric loss. Within tens of simulations, our method identifies a diverse set of designs on the Pareto frontier indicating the tradeoff between dielectric properties. These findings project data centric design, effectively integrating experimental data with simulations for Bayesian Optimization, as an effective approach for design of engineered material systems.

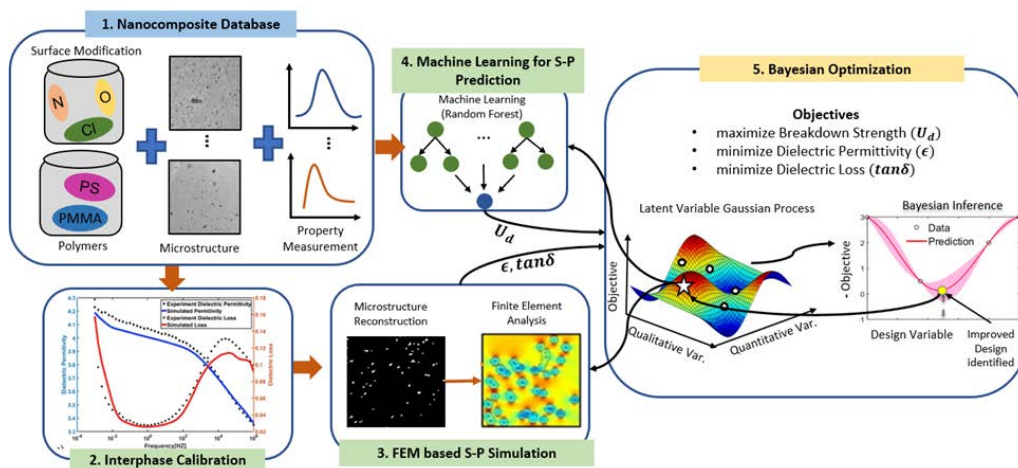
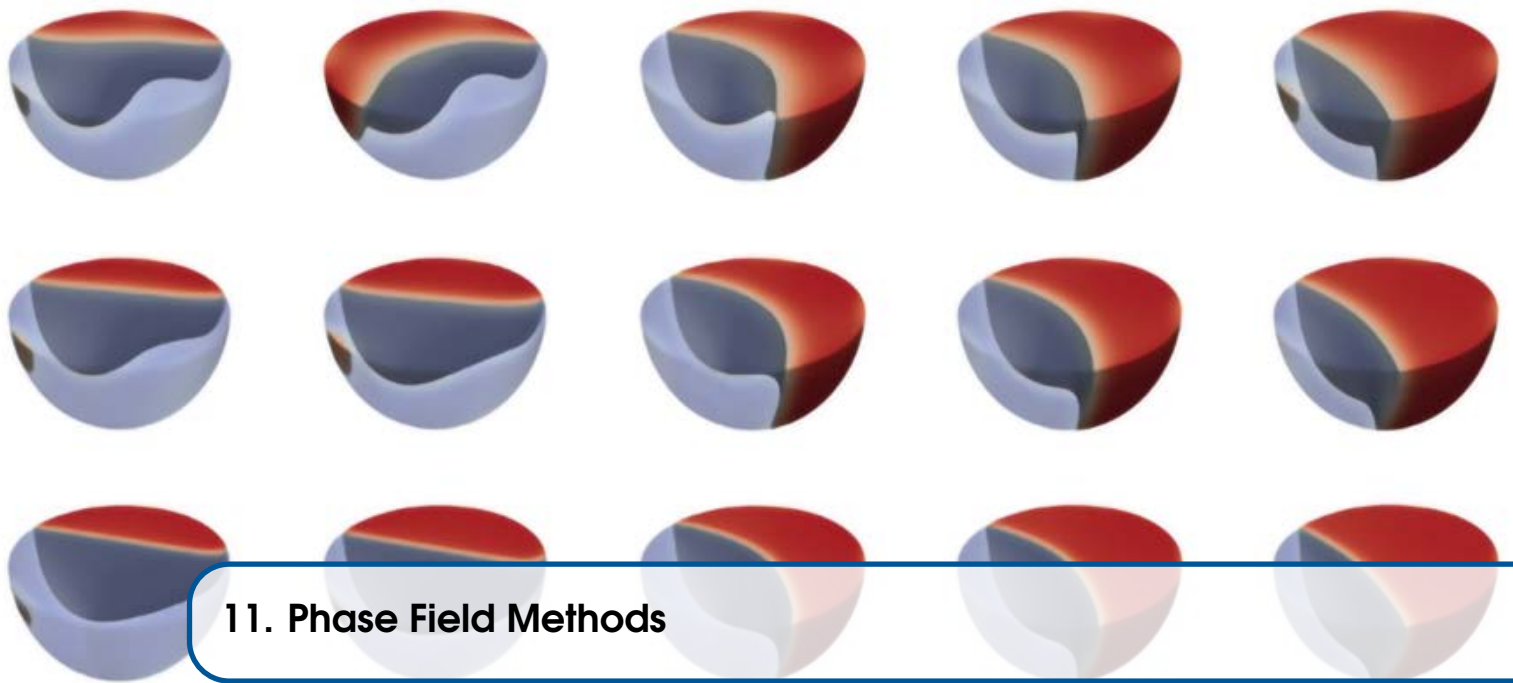


Figure 10.6: Data centric design framework for polymer nanocomposites.





## 11. Phase Field Methods

**Olle Heinonen** (ANL), Peter Voorhees (NU)

**James Warren** (NIST), **Jonathan Guyer** (NIST), Daniel Wheeler (NIST), Trevor Keller (NIST)

### 11.1 Design Goals

The goal of this tool group is broadly to develop *quantitatively predictive* phase field models and efficient algorithms, and to apply them to a range of materials problems, such as grain growth, solidification, and coarsening. One particular goal is to develop benchmark problems for phase field modeling that can be used by developers to benchmark accuracy of codes, and as pedagogical tools for researchers who are entering the field.

### 11.2 Research Accomplishments

#### 11.2.1 Benchmark Problems

We finished work on the nucleation benchmark problems. A manuscript was submitted to *Comp. Mat. Sci.* and was accepted and published ("Phase field benchmark problems for nucleation", W. Wu, D. Montiel, J.E. **Guyer**, P.W. **Voorhees**, J.A. **Warren**, D. **Wheeler**, L. Granasy, T. Pusztai, and O.G. **Heinonen**, *Comp. Mat. Sci.* 193, 110371 (2021)).

Based on discussions in the Phase Field Workshops, we started work on a benchmark problem that focuses on the effects of anisotropic surface energy. The idea is to use a Cahn-Hilliard framework with a free energy that is expanded in higher-order derivatives in the conserved order parameter. By restricting the derivatives to a specific symmetry (eg tetragonal in three dimensions, or rectangular in two dimensions), the effect is a surface energy that is anisotropic with the designated symmetry. The advantage of this approach in contrast with approaches that use spherical harmonics in the gradient director is that the resulting system avoids potentially unphysical effects. The disadvantage is that higher-order derivatives necessarily make numerical implementations a bit more complicated. This is especially the case for finite-element weak formulations, where the higher-order derivatives make significant contributions to residuals and Jacobians, and higher-order shape functions have to be used. However, modern code frameworks for

finite-element methods typically include high-order shape functions, and this formulation of the benchmark problem using higher-order derivatives is pedagogically and technically a good way to approach the use of higher-order shape functions.

## 11.2.2 Phase Field modeling of Additive Manufacturing

The velocities of interfaces during additive manufacturing are in the regime where the interfaces are likely not in local equilibrium. Thus, **Voorhees** group has developed a computationally efficient phase field model that allows the degree of interfacial nonequilibrium, specifically solute trapping and interfacial temperature, to be controlled. The finite solid-liquid interface width in phase-field models leads to non-equilibrium effects, including solute trapping. Prior phase field modeling has shown that this extra degree of freedom, when compared to sharp-interface models, results in solute trapping that is well captured when realistic values are employed. Increasing the interface width, which is desirable for computational reasons, leads to artificially enhanced trapping thus making it difficult to model departure from equilibrium quantitatively. In the present work, we develop a phase-field model in which non-equilibrium effects such as solute trapping, drag and interface kinetics can be introduced in a controlled manner. Performing an asymptotic analysis of the model, an analytical expression for the diffusion potential jump is derived which allows tuning of the model parameters from experiments, atomistic simulation, or sharp interface theories to obtain *correct* trapping while using significantly larger interface widths. Tuning the kinetic coefficient, in turn, controls the energy dissipated in solute drag. The model is applied to Si-9 at% As and Ni-5 at% Cu systems and the numerical performance of the model is highlighted through convergence of partition coefficient and interface temperature for different interface widths. A comparison with the other phase-field models suggests that interface width of about two to seven times larger than current best-in-class models can be employed depending upon the material system at hand leading to a speed-up by a factor of  $W^{d+2}$ , where  $W$  and  $d$  denotes the interface width and dimensions, respectively. Therefore, increasing the interface width by a factor of two speeds up the computation time by a factor of 16 in two dimensions and 32 in three dimensions. This implies a tremendous gain in computation time when the model is applied to simulate microstructures in two and three dimensions.

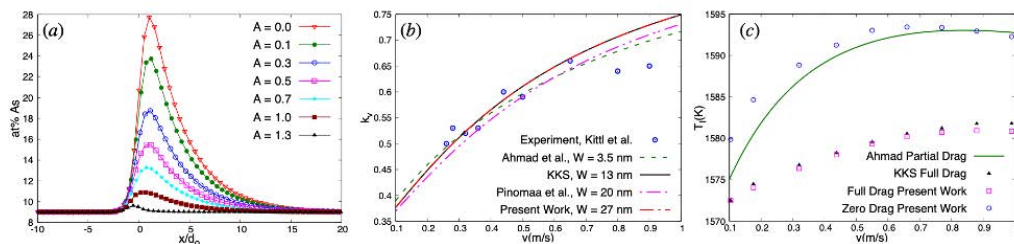


Figure 11.1: (a) The solute segregation profiles as a function of solute trapping parameter  $A$  for the Si-9 at% As system. (b) Comparison of the partition coefficient ( $k_v$ ) with velocity ( $v$ ) and the permissible interface width ( $W$ ) obtained from the present work and previously developed phase-field models of Ahmad et al. (Phys. Rev. E, 58, 3436, 1998), Kim-Kim-Suzuki (Phys. Rev. E, 60, 7186, 1999), Pinomaa and Provatas (Acta Mater., 168, 167, 2019) and experiment of Kittl et al. (Acta Mater., 48, 4797, 2000). (c) Comparison of the interface temperature. The present model allows us to tune the amount of energy dissipated in terms of solute drag.

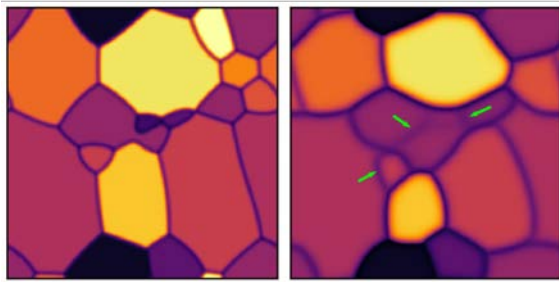


Figure 11.2: (left) An isotropic multi-order-parameter simulation of grain growth, showing all trijunctions having nearly-120 angles. (right) Simulation from the same initial condition, but using our orientation-field model with misorientation-dependent boundary energy and mobility, and inclination-dependent energy with cubic symmetry. The green arrows mark low angle grain boundaries which are lower in energy and therefore have a pronounced impact on the resulting morphology and trijunction angles.

### 11.2.3 Orientation-field model for grain growth

Recent advances in experimental measurements of grain growth highlight the need to account for crystallographic and topological dependence of grain boundary properties when modeling grain coarsening. The grain boundary energy and mobility can both depend on the five crystallographic degrees of freedom; this dependence must be included in phase field models of grain growth. **Voorhees** group has developed an orientation-field model for grain growth that allows for dependence of boundary properties on crystallography. The model uses a single-well potential to avoid the liquid phase, removing wetting effects. We demonstrated that this model reproduces analytical triple junction dihedral angles, has no anomalous trijunction drag, and reproduces Wulff shapes for the case of grain boundary energy anisotropy with cubic symmetry. We demonstrate a pronounced effect on grain boundary evolution when including misorientation dependence of the grain boundary energy, particularly when many low-angle grain boundaries are involved (Figure 11.2).

This model shows promise for use in large scale simulations of grain coarsening in a wide range of systems. Because the grain orientation is tracked by a single orientation field variable, the computational burden is lessened compared to multi-order-parameter models, particularly when simulating many grain orientations. In addition, the model has flexibility for tuning the dependence of the grain boundary energy and mobility with addition of extra parameters, allowing for its use in high-throughput characterization of grain boundary properties by comparison to time-resolved x-ray tomography experiments.

### 11.2.4 PFHub Website

PFHub is a community effort spearheaded by the Center for Hierarchical Materials Design at Northwestern University and the National Institute of Standards and Technology in support of phase-field code development. The current PFHub deployment focuses on improving cross-collaboration between phase-field code developers and practitioners by providing a standardized set of benchmark problems and a workflow for uploading and comparing benchmark results from different phase-field codes.

PFHub relies heavily on GitHub infrastructure as well as various third party apps to support its web deployment and upload workflow. PFHub is transitioning away from a Javascript / app based stack to a GitHub Actions / Python based stack. This will reduce the maintenance overhead associated with supporting the PFHub effort and allow broader engagement. Figure 3 shows a schematic of the current PFHub framework and upload workflow.

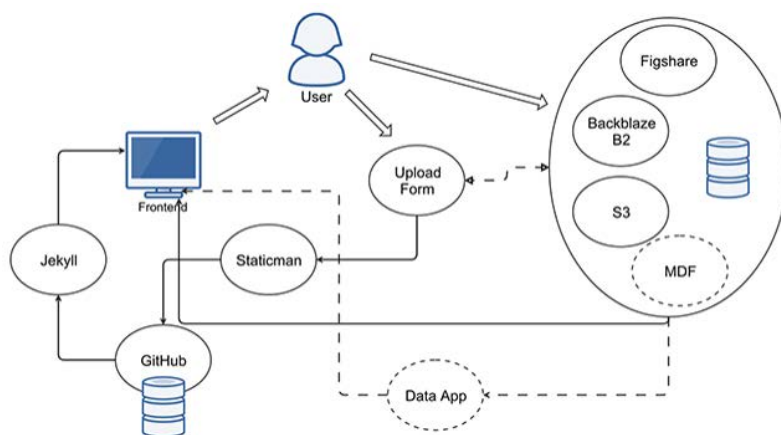


Figure 11.3: Schematic overview of the PFHub framework for building scientific research portals, simply.

Recent activity has focused on the transition to a more systematic workflow relying on a set of tools that are commonly used in research software. In particular, the infrastructure is being ported to a combination of GitHub Actions, Jupyter Notebooks, Pandas and Plotly. These tools are all widely used across the research software development community and, thus, exploring PFHub data will be more accessible to a wider audience.

The following bullets highlight progress towards the PFHub transition as described in the previous paragraph:

- Implementation of a Python module that facilitates aggregation of data using Pandas and subsequent plotting with Plotly.
- Transition the nucleation benchmark aggregation page from using the JavaScript Plotly library to the Python Plotly library from within a Jupyter Notebook. As this process is now complete, subsequent transitions from JavaScript to Plotly will be straightforward.
- Implement a Cachix service to store the packages and dependencies used by PFHub. This allows for fast deployment on all continuous integration systems.
- New uploads from two new phase field codes, [Symphas] and [MEUMAPPS]. The code developers cited PFHub in their initial publications about the codes. The developers described PFHub as providing considerable assistance in verifying and validating their codes.
- Moved the data processing app used by PFHub to Heroku from Google App Engine. This facilitated the use of memcache to cache the frontend views of the data making loading data much faster. However, this change will be redundant once the transition from JavaScript to Python is complete.

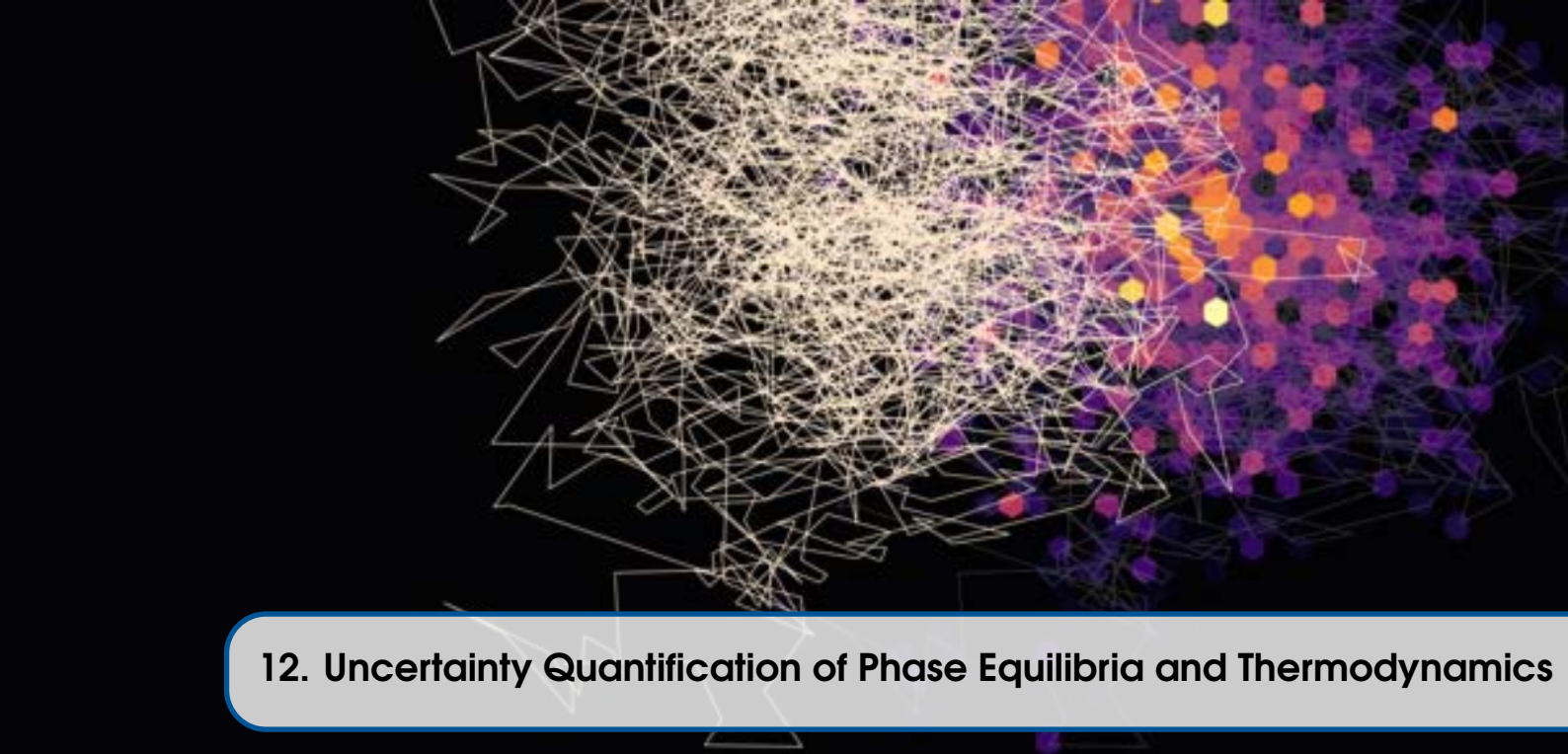
### 11.2.5 CHiMaD Phase Field Workshop Series

We held two workshops, PF XI and PF XII in April/May of 2021 and Nov. 2-4, 2021. Because of COVID restrictions, the workshops were both virtual. Both these workshops were very well attended with between 50 and 70 participants in each session. PF XI focused mainly engaging the broader community and highlighting phase field work on the forefront with two invited presentations per day spread over four days plus a virtual poster session highlighting work by graduate students and postdocs. The speakers were

literally from around the world (Germany, Finland, India, Canada) and for the first time we also had a speaker from a commercial software developer/vendor, COMSOL. PF XII was focused on action-items that emerged during discussions in PF XI, in particular benchmark problems (new problems, cleaning up older problems on PFHub) and PF Best Practices. The workshop also featured a session with brief presentations by postdocs and students. The discussions were lively and engaging with very concrete outcomes and actions.







## 12. Uncertainty Quantification of Phase Equilibria and Thermodynamics

Noah Paulson (ANL), Peter Voorhees (NU), Changning Niu (QT)

Ursula Kattner (NIST), Francesca Tavazza (NIST), Carelyn Campbell (NIST), Kevin Brady (NIST), Benjamin Long (NIST), Hariharan Iyer (NIST)

### 12.1 Design Goals

The design goal of the Uncertainty Quantification of Phase Equilibria and Thermodynamics (UQPET) tool group is to develop at least one publicly available software able to quantify uncertainty and evaluate quality of thermodynamic models (with a focus on phase equilibrium diagrams). To achieve the goal, the main objectives are:

- Target minimum 3 applications that include unary and binary systems with impact on CHiMaD use groups, the materials science community and industry. Extend to 1 ternary system pending upon availability of effort and computational resources.
- Build a community of at least 20 uncertainty quantifiable software users, with a focus on the UQPET software. The tool group has already developed close collaborations regarding uncertainty quantification (UQ) adoption with NIST, QuesTek and commercial CALPHAD companies such as ThermoCalc and CompuTherm.
- Coordinate data analysis and curation with material databases and data analysis tools at NIST and CHiMaD (MDF).
- Enhance awareness regarding the UQ capabilities available from UQPET and the positive impact on material design via at least 2 UQPET workshops.

Figure 12.1 shows the core methodology used by the UQPET tool group to evaluate uncertainty.

### 12.2 Research Accomplishments

#### 12.2.1 Bayesian automated weighting of simulated and experimental data

In 2021, we continued the development of methods for estimating uncertainty in simulated sources (density functional theory and molecular dynamics) of data for CALPHAD thermodynamic modeling and appropriately weighting them alongside experimental measurements. This was realized in a journal article published in *Materialia* (graphical abstract

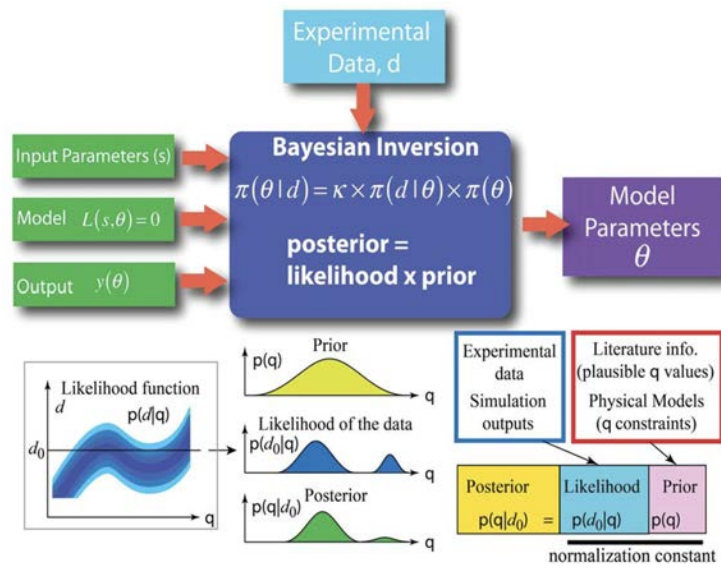


Figure 12.1: Core methodology used to quantify uncertainty of data and material models.

shown in Figure 12.2 using aluminum as a case study. Aluminum is an important element for several multi-component alloys and was hence chosen as a case study. The end product of the work was a thermodynamic model for aluminum with quantified uncertainty derived for the solid phase (0 K to 933.5 K) as well as the liquid phase (933.5 K to 1600 K) and an illustration of how a Bayesian approach can be used to select and appropriately weight data from both experimental and simulated sources. Regarding the data sources in aluminum, past assessments have shown that experimental data for the liquid phase of aluminum is more uncertain than that of the solid phase because of measurement difficulties at high temperature. Furthermore, datasets had been excluded in past assessments because of high deviations between datasets (more than 5%). Hence, simulated data was considered as a source to supplement the existing experimental datasets. MD derived enthalpy data for the liquid was included in addition to DFT computed heat capacity data and MD derived enthalpy data for the solid. Furthermore, this was the first study known to the research team to include uncertainties on simulated data sourced from DFT and MD, alongside all experimental datasets and their uncertainties, towards inferring a thermodynamic model with uncertainty quantification from the aggregated dataset of DFT+MD+experiments. Notably, experimental datasets were not excluded because they strongly deviated from the other datasets. Instead, all were included with their estimated uncertainty and the final weights were determined as part of the Bayesian inference (Bayesian automated weighting approach of Paulson et al.) To supplement the experimental data sets, candidate lists of simulated data sources were compiled. Among the candidate simulated data sources, data set selection was performed on the MD enthalpy datasets for the liquid phase because of deviations in melting point prediction between experiment and simulated data. This presented the challenge of selecting the MD enthalpy dataset most compatible with the experimental datasets, towards building an aggregated model inferred from both experiments and simulation. This MD enthalpy dataset selection was done in the following manner: for the liquid phase, candidate model forms of constant heat capacity and linear heat capacity were compared using Bayesian model selection, i.e, the marginal likelihood ratio (Bayes factor) was used to determine which model form was most supported by the data. The Bayesian model selection was first performed considering the experimental datasets alone

and the conclusion was that the constant heat capacity was most supported by the experimental datasets. A similar Bayesian model selection was then performed, considering one MD enthalpy dataset at a time. In only one case (using the MD enthalpy dataset MIS1999), the constant heat capacity model was most supported, and hence, MIS1999 was selected for developing the aggregated model with experimental datasets. Bayesian model selection through the marginal likelihood ratio (Bayes factor) was used to assess the model form most supported by a dataset. Finally, this study compared thermodynamic models built from the different selections of data-source-groups (only experiments, only simulations, and an aggregation of both) and showed the impact of neglecting one type of data-source. We found that the aggregated model agreed best with all the available data and was within 3 J/mol.K of commercially used thermodynamic models such as the SGTE and HSC Chemistry.

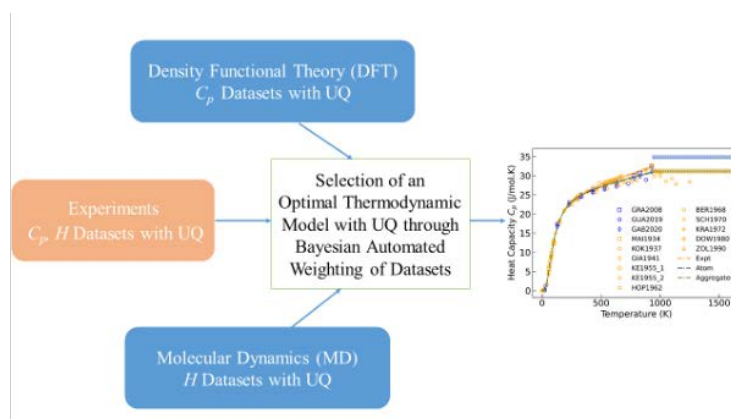


Figure 12.2: Graphical abstract showing sources of data and the final model: aggregated (green), experiments alone (orange), and simulation alone (blue).

This work involved the generation and collection of simulated thermodynamic data for aluminum. The datasets can be found on github at [https://github.com/npaulson/UnaryBayes/blob/master/data\\_process/aluminum\\_DFT\\_MD\\_Experiments\\_Supplement.xlsx](https://github.com/npaulson/UnaryBayes/blob/master/data_process/aluminum_DFT_MD_Experiments_Supplement.xlsx) in addition to experimental data collected for aluminum in past publications. The excel spreadsheet provides both the datasets with their estimated uncertainties and the rescaled uncertainties obtained as part of the Bayesian automated weighting. Further, the spreadsheet is also available on the MDF at <https://doi.org/10.18126/to2p-1mot>. The paper also describes the uncertainty estimation approaches used for the DFT and MD datasets. For both DFT and MD, only epistemic uncertainties were estimated. For DFT, these epistemic uncertainties were estimated from the choice of exchange-correlation functional and DFT input parameters. For each MD dataset, the epistemic uncertainty was estimated using the method of block-averaging. Notably, these were uncertainty estimation approaches and the goal of this work was not to find the most accurate uncertainties or compare approaches to estimation. Rather, the goal of the work was to generate simulated datasets, estimate their uncertainties from known sources, then infer a model with Bayesian automated weighting, and finally observe the rescaled uncertainty in the context of all the other datasets included in the inference. **This provides powerful insight into how simulated data sources with their estimated uncertainties can be included alongside other experimental data sources and their uncertainties towards inferring an aggregated model with quantified uncertainty for any property that has a candidate list of model forms.** With regards to the candidate model forms for heat capacity and enthalpy:

for the solid phase, segmented regression with the Debye or Einstein for low-temperature effects were compared, while for the liquid phase, a constant heat capacity was compared with a liquid heat capacity model.

With regards to sources of simulated data, heat capacity data from density functional theory calculations and enthalpy data from molecular dynamics simulations were considered. Heat capacity data with uncertainty was estimated for three different DFT approaches (shown in Figure 12.3a,b), with the Bayesian Error Estimation Functional (BEEF) notably having the highest uncertainty estimates among the three. In blue, is heat capacity data calculated in this work and with uncertainty estimated using the difference between two exchange correlation functionals known to overestimate and underestimate the lattice parameters of aluminum. The question of selecting a compatible molecular dynamics source dataset was addressed in the paper by first creating a candidate list of MD interatomic potentials from the many available AI-based interatomic potentials on the NIST interatomic potential repository. This candidate list was generated by choosing interatomic potentials whose literature reported melting points were within 150 K of the experimental melting point of aluminum (933.5 K). Figure 12.3c) shows the enthalpy data as a function of temperature for these candidate interatomic potentials, with the legend indicating their respective melting points. The candidate list was diverse in that it included interatomic potentials developed for Al and its binary alloys using the embedded atom method (EAM) and machine learning potentials (MLP). Bayesian model selection through the marginal likelihood ratio (Bayes factor) was used to find the model most strongly supported by the data. When considering experimental data alone, we found that the constant heat capacity model was the most supported. Out of this candidate list of enthalpy data, we found that the enthalpy data generated by the interatomic potential according to Mishin (EAM  $T_m = 1043$  K), strongly supported the constant heat capacity model over the linear heat capacity model. This shows that using the predicted melting point is not a sufficient guide to dataset selection. Bayesian model selection resulted in a stronger ground for selection and avoided biasing the results based on possible limitations in the physics of a particular simulated source of data. We note that in this approach to

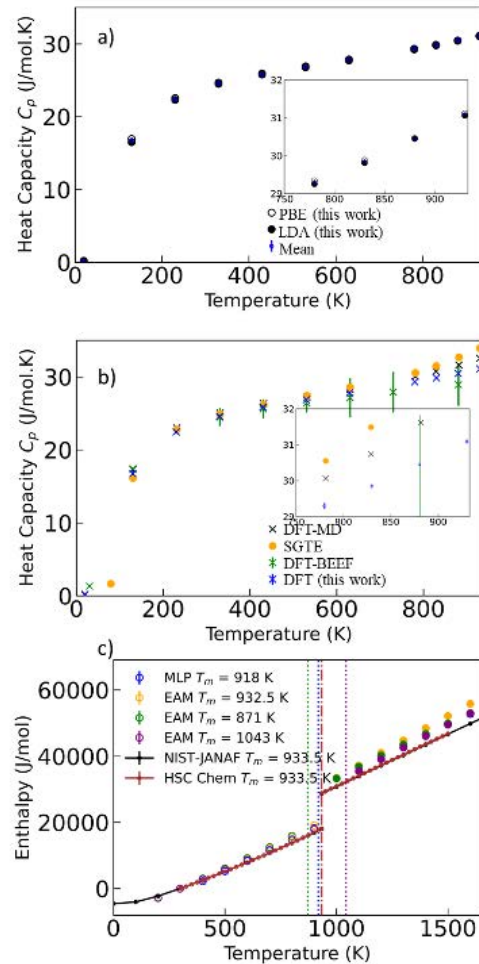


Figure 12.3: Simulated data sources and their estimated uncertainty (a) DFT heat capacity data generated in this work (b) compared with DFT in literature and SGTE, and (c) MD enthalpy data generated in this work.

selecting an MD enthalpy dataset, using the Bayesian model selection, we assumed that the model best supported by experiments (in this case, constant heat capacity) could be considered as closest to the ground truth. We note that the choice to trust the experiments more than simulation was justified for the particular case of aluminum. Compared to other metals, there is lesser uncertainty in experimental measurements of the melting point as well as the enthalpy of liquid aluminum.

Finally, this work presented the rescaled uncertainties of each dataset and compared how each experimental data and simulated data source fared against each other, in the different contexts of experiments alone, simulations alone, and the aggregated model. We note that the rescaled uncertainty did not differ by more than 1 J/mol.K between each of those data selection scenarios in the case of both experimental and simulated heat capacity data, while the rescaled uncertainty differed by 2000 J/mol for the MD generated enthalpy. Of the simulated data sources, the Bayesian error estimation functional from DFT (shown as GUA2019 in the Figure 12.4a had the least rescaling out of all of the methods (DFT and MD). The MD enthalpy dataset (MIS1999) was rescaled the most in the liquid phase in the aggregated model.

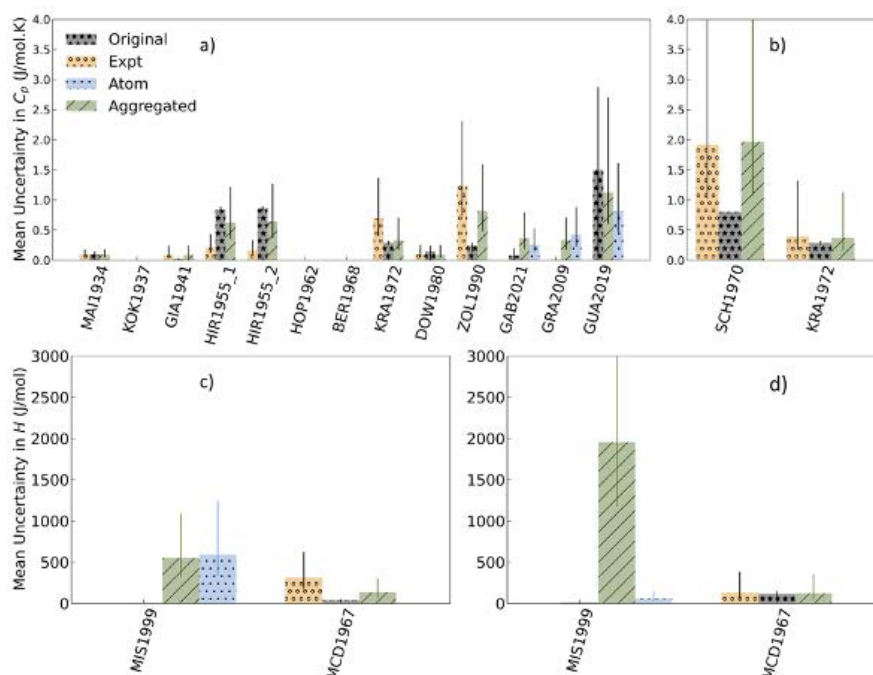


Figure 12.4: Mean uncertainty in heat capacity for (a) solid and (b) liquid datasets, and mean uncertainty in enthalpy for (c) solid and (d) liquid phases.

### 12.2.2 Propagation of uncertainty from unary to binary phase diagram

A method to propagate uncertainty from a unary posterior onto a binary phase diagram was developed and a manuscript is in preparation in the context of the binary Cu-Mg system. The interest in the propagation of uncertainty arose from the community workshop report compiled at the start of 2021. Some preliminary results, which were presented at the CHiMaD Annual Meeting 2021 are shown below. As shown in Figure 12.5, propagation means sampling the posterior distributions of each unary parameter and propagating it during the inference of the binary phase diagram. Prior to the propagation, both the

## Chapter 12. Uncertainty Quantification of Phase Equilibria and Thermodynamics

thermodynamic model for the unary and the binary are inferred independently of each other. The starting point for the propagation is the binary phase diagram without any unary propagation. As shown in Figure 12.6, to visualize the effects of the propagation, we plot the phase fractions of the phases. We then evaluate differences of the phase fractions between  $N$  iterations of the unary propagation and the initial phase diagram with no unary propagation. The phase fraction is itself a distribution and is characterized by a mean and 95% Bayesian credible interval (CI). They indicate that there is an increase in uncertainty in the overall phase diagram when uncertainty in the unary thermodynamic functions is propagated.

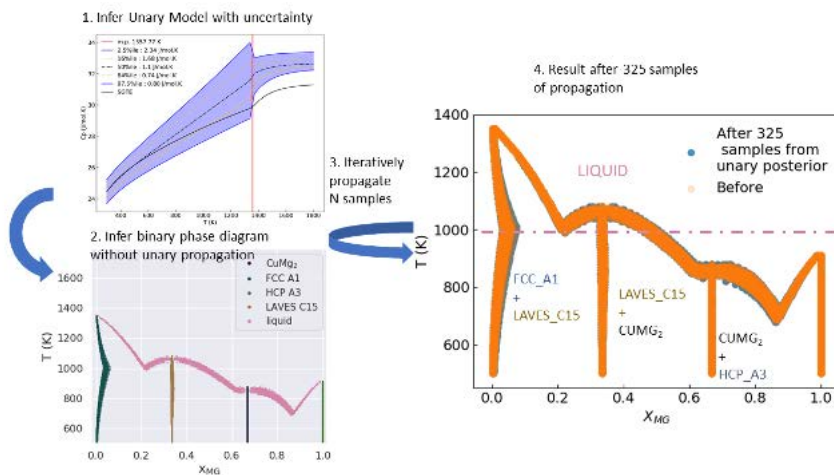


Figure 12.5: Uncertainty Propagation Workflow: First, 1. unary model (eg: Cu) and 2. binary phase diagram posterior distributions are inferred independent of each other, followed by 3. iteratively sampling and propagating  $N$  samples from the unary posterior resulting in a superimposed phase diagram (4) where uncertainty in the phase boundaries increases with 325 samples of unary posterior (blue) over the phase diagram without unary propagation (orange).

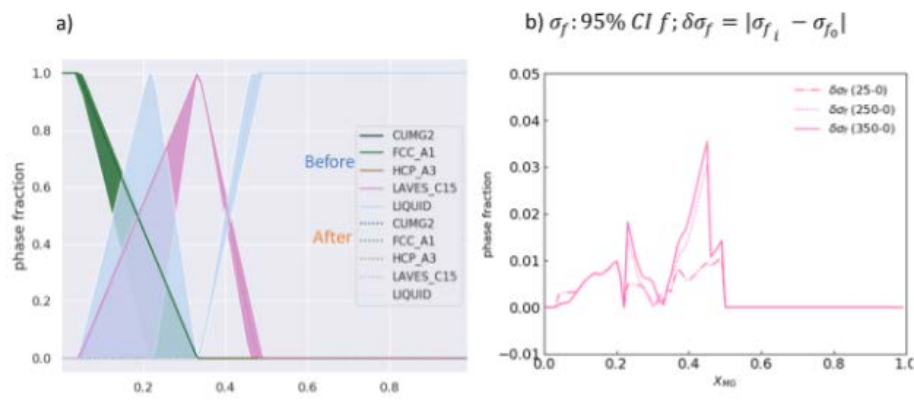


Figure 12.6: Visualizing impact of unary uncertainty propagation through the a) phase fraction of each phase at 1000 K and b) difference in the 95% CI of the phase fraction of the liquid phase at  $T=1000$  K at different iterations of the propagation.

### 12.2.3 Community workshop report on uncertainty quantification for thermodynamic properties

Following up on the successful international and all-virtual CHiMaD UQPET workshop in 2020, we put together a workshop report compiling the thoughts and insights of academic researchers in national laboratories and universities as well as engineers and leaders of commercial thermodynamic software companies and materials design companies. The report examined the meaning of uncertainty quantification in the context of thermodynamic property models and presented the existing open-source UQPET python package and its commercial counterparts. The importance of uncertainty quantification in materials design decision making was also highlighted. Gaps and opportunities were identified in i) uncertainty propagation from thermodynamic models of the elements to multi-component material systems, ii) thermodynamics of thermoelectrics, iii) challenges with experimental measurements of thermodynamic and kinetic information for alloy design, and iv) advances in Bayesian approaches to uncertainty quantification. The report was internally reviewed and released at Argonne and NIST and is available at CHiMaD. It presents a continued community effort and roadmap for implementing uncertainty quantification techniques for materials design from the view of thermodynamic property modeling.

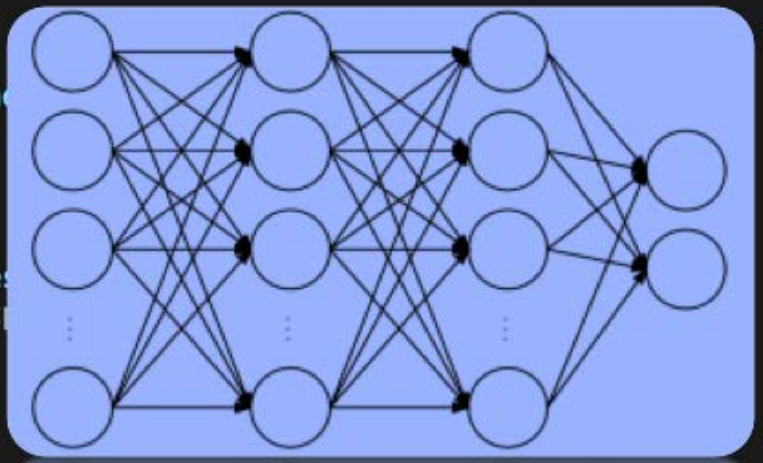




```

layer_type = layer_specs['layer_type']
activation_fn = ReLU
dropOut = 0.8
assert layer_type in ['conv2d', 'fully_conn
# Neural network training algorithm
if layer_type == 'max_pool2d':
    strides = layer_specs['strides']
elif layer_type == 'fully_connected':
    num_output_nodes = layer_specs['num_node
    output_shape = [self.BATCH_SIZE, num_out
elif layer_type == 'conv2d':
    padding = layer_specs['padding']
    filter_size = layer_specs['filter_size']
for i in range(nodes_for_layer):
    for l_num in next_layers:
        self.model_node_layers_assign[temp_node_rank].append((l_num, [start, end]))
net = slim.layers_conv2d(net, num_filters, filter_size,
    stride, padding, activation_fn, weights_initializer,
    weights_regularizer)
net = activation_fn(net)
return net

```



## 13. Artificial Intelligence and High-Performance Data Mining

Alok Choudhary (NU), Ankit Agrawal (NU), Wei Chen (NU), Abhinav Saboo (QuesTek)

Christopher Wolverton (NU), Ian Foster (UC), Jian Cao (NU), Greg Olson (NU)

Brian DeCost (NIST), Francesca Tavazza (NIST), Andrew Reid (NIST), Gilad Kusne (NIST), Jason Hattrick-Simpers (NIST), Kamal Choudhary (NIST)

### 13.1 Design Goals

The CHiMaD Artificial Intelligence and High-Performance Data Mining tool group aims to accelerate materials property prediction, discovery, and design by: (1) Developing data-driven analytics for materials science to enable automatic, fast, and accurate extraction of PSPP (processing-structure-property-performance) relationships; (2) Actively bringing deep learning advances in materials science; (3) Design and developing software deploying materials informatics for the community to use and build upon.

### 13.2 Research Accomplishments

#### 13.2.1 Cross-property Deep Transfer Learning Framework for Enhanced Predictive Analytics on Small Materials Data

Although the size and availability of materials datasets is increasing, the field of materials science is still in the small data regime for the most part. This small data problem is especially prevalent for experimental materials data, which is often significantly more expensive and time-consuming than simulations. Thus, building accurate predictive models for small experimental datasets is a major and common challenge in materials science. Transfer learning is usually used in such cases, but a key limitation of existing transfer learning models is the need for the availability of a large source dataset of the same property as the target property, which is not an issue for some properties like formation energy, but there are numerous other materials properties such as exfoliation energy, for which large source datasets are not readily available to directly perform transfer learning. In order to address this limitation, **Agrawal** and **Choudhary**, in collaboration with **Choudhary**, **Tavazza**, and **Campbell**, have developed a cross-property transfer learning framework,

wherein the source and target properties are allowed to be different. In addition to the fine-tuning method usually used for transfer learning, feature extraction-based transfer learning was also explored, which uses the source model to extract features or semantic vectors on the target dataset, which could then be used as alternate representations of the materials in the target dataset to build any machine learning or deep learning model on top of it. The cross-property transfer learning models were evaluated on 39 different target properties and were found to be more accurate than scratch models in 38/39 cases when both type of models used only raw elemental fractions as input. In a more stringent test for cross-property transfer learning models, only the scratch models were allowed to use more informative physical attributes as input, and the cross-property transfer learning models still performed better than scratch models in 27/39 cases, underscoring the wide applicability and usefulness of the framework to tackle the small data challenge in materials science (Figure 13.1). This work was recently published in *Nature Communications*.

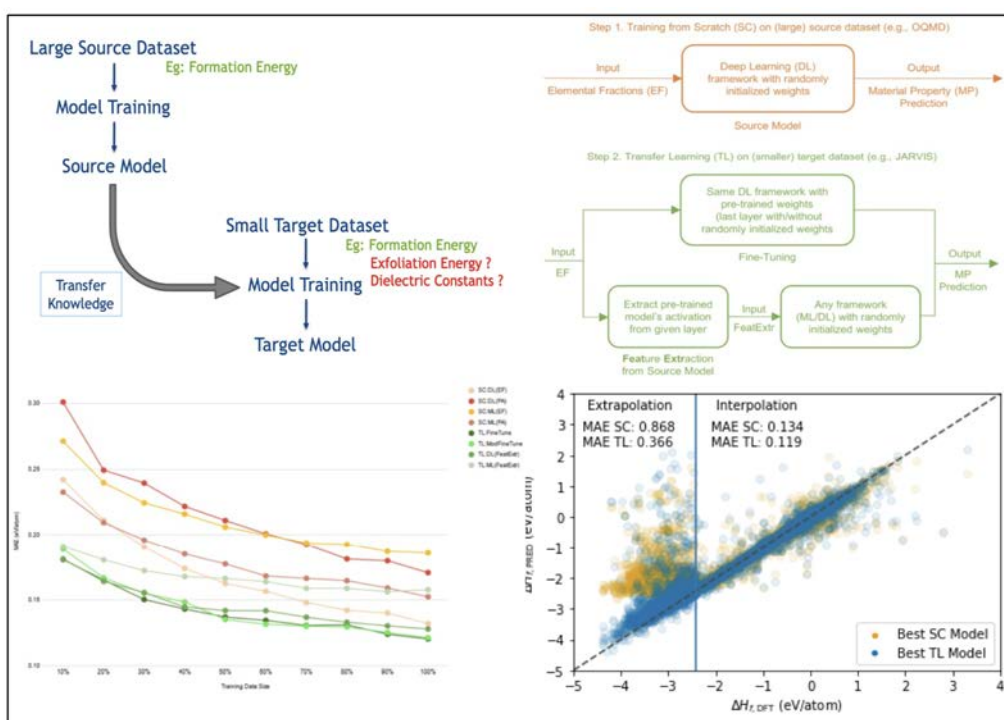


Figure 13.1: The top-left subfigure illustrates the concept of cross-property deep transfer learning, and the top-right subfigure shows the two steps of transfer learning, along with the two ways of transferring knowledge from source model to the target model. The bottom-left subfigure shows that transfer learning models are significantly more accurate than the models trained from scratch even for very small training data sizes, and the bottom-right subfigure shows the extrapolative power of transfer learning models.

### 13.2.2 Enabling Deeper Learning on Big Data for Materials Informatics Applications

Although materials datasets are typically not as big as in some other fields, they can still contain hundreds of thousands of samples at present, especially simulation-based datasets, and are regularly increasing in size. Given the demonstrated potential and advantages of deep learning and the increasing availability of big materials datasets, it is attractive

to build deeper neural networks in a bid to boost model performance, but it usually leads to performance degradation due to the vanishing gradient problem. **Agrawal** and **Choudhary**, in collaboration with **Wolverton** and **Foster**, have developed a general deep learning framework based on Individual Residual learning (*IRNet*) composed of very deep neural networks that can work with any vector-based materials representation as input to build accurate property prediction models, and demonstrated how to enable deeper learning for cases where big materials data is available. *IRNet* models were recently tested on a variety of materials datasets based on density functional theory (DFT) simulations, such as OQMD, AFLOW, Materials Project, and JARVIS, as well as experimental datasets, with sizes ranging from a few thousand to a few hundred thousand. The models were found to not only successfully alleviate the vanishing gradient problem and enable deeper learning, but also build significantly (up to 47%) better predictive models for a variety of materials properties as compared to as compared to plain deep neural networks and traditional ML techniques for a given input materials representation in the presence of big data (Figure 13.2). This work was recently published in *Scientific Reports*.

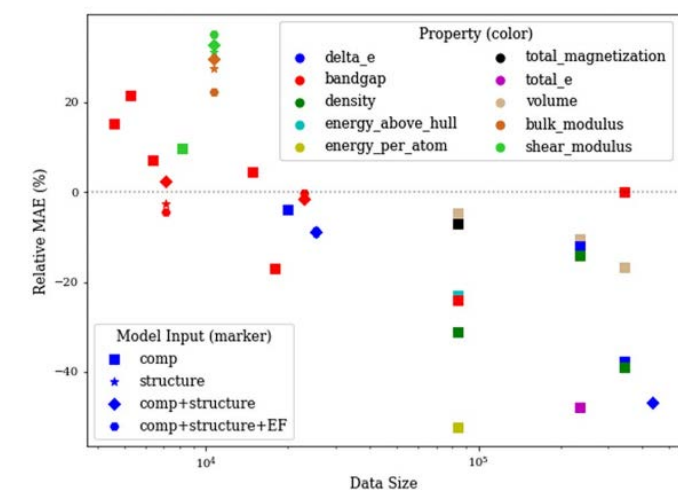


Figure 13.2: Error performance of IRNet models on multiple datasets of different properties, sizes, and input representations. The x-axis shows the dataset size on a log scale, and y-axis shows the percentage change in MAE of IRNet w.r.t. the best traditional ML model (calculated as  $(MAE_{IRNet}/MAE_{BestML} - 1) \times 100\%$ ). IRNet models consistently outperform traditional machine learning models for bigger datasets by enabling deeper learning.

### 13.2.3 Data Centric Materials Design via Mixed-Variable Bayesian Optimization

Polymer nanocomposites have the potential to be widely used across multiple industries. Tailoring nanocomposites to meet application specific requirements remains a challenging task, owing to the vast, mixed-variable design space that includes composition (i.e., choice of polymer, nanoparticle, and surface modification) and microstructures (i.e., dispersion and geometric arrangement of particles) of the nanocomposite material. Modeling properties of interphase, the region surrounding a nanoparticle, introduces additional complexity to the design process and requires computationally expensive simulations. As a result, previous attempts at designing polymer nanocomposites have focused on finding the optimal microstructure for only a fixed combination of constituents. **Chen** has developed a data-centric mixed-variable Bayesian Optimization framework for design of complex

material systems with both qualitative and quantitative variables. This has been further extended as a data centric design framework to concurrently identify optimal composition and microstructure in design of polymer nanocomposites. With this approach, optimal composition and microstructure can be identified concurrently. The developed framework integrates experimental data with state-of-the-art techniques in interphase modeling, microstructure characterization & reconstructions and machine learning. Latent Variable Gaussian Processes (LVGPs) quantifies the lack-of-data uncertainty over the mixed-variable design space that consists of qualitative and quantitative material design variables. The design of electrically insulating nanocomposites is cast as a multicriteria optimization problem with the goal of maximizing dielectric breakdown strength while minimizing dielectric permittivity and dielectric loss. Within tens of simulations, our method identifies a diverse set of designs on the Pareto frontier indicating the tradeoff between dielectric properties. These findings project data centric design, effectively integrating experimental data with simulations for Bayesian Optimization, as an effective approach for design of engineered material systems (Figure 13.3). This work has recently been accepted in *Engineering*.

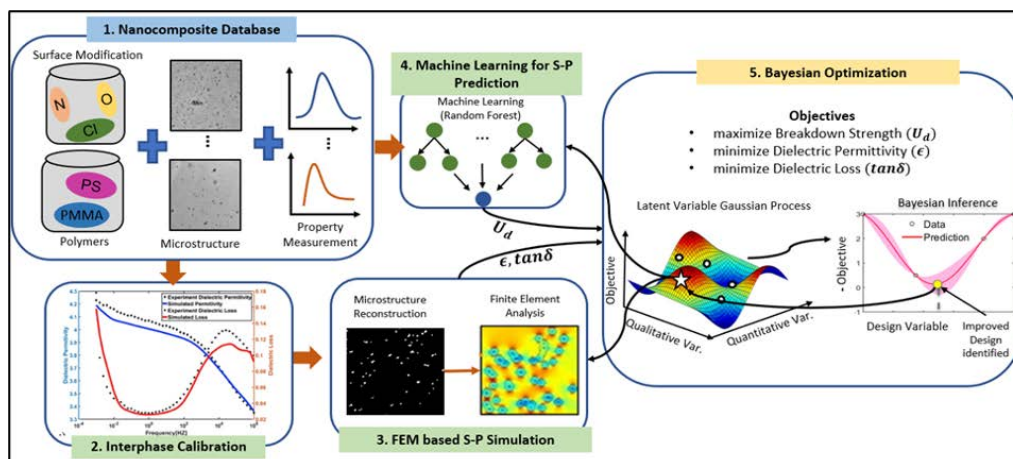


Figure 13.3: Data centric design framework for polymer nanocomposites.

### 13.2.4 Data-Driven and Topological Design of Structural Materials for Fracture Resistance

Material macroscopic properties rely heavily on its meso/microscopic structural architectures. Data science provides novel and diverse opportunities for the design of structural metamaterials attaining exceptional mechanical properties. **Chen** has demonstrated that porous structures composed of brittle constitutive materials can be strong and tough through topological optimization and data-driven techniques. It was shown that brittle fracture properties can be tailored through the linear control of the homogenized stress and non-periodic microstructures from a multiscale perspective. Huge size effects of the data-driven multiscale structures indicate great designability of mechanical fracture resistance across different scales. These tough advanced structural metamaterials pave the way to multiscale components with exceptional mechanical fracture properties (Figure 13.4). This work was recently published in *Extreme Mechanics Letters*.

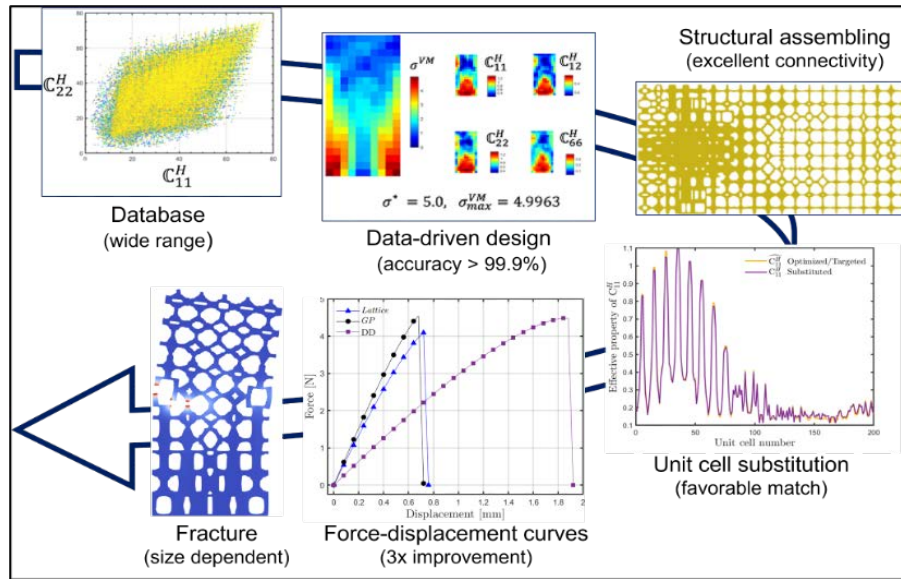


Figure 13.4: Data-driven topological design of structural materials for fracture resistance.

### 13.2.5 Steel Fatigue Data Mining for Design of Improved Steels

Research work at QuesTek on data mining led by **Saboo** has been focused on generating human-interpretable machine learning models for properties of a material. Such interpretable models are useful in the process of design of materials using a systems-based design approach. By being human-interpretable, the inner workings of models can be interpreted and provide a certain degree of explainability to material designers. This will provide higher confidence in the predictions and enable recognition of any model limitations. QuesTek has utilized the rotary bending fatigue strength data on 342 steels (with varying composition and processing) published by NIMS, Japan. Using prior material science knowledge, the raw composition and processing data is featurized into quantities representing microstructural and properties that are known to be affecting the fatigue phenomenon in steels. These quantities include retained austenite content, austenite stability parameter, hardness and defect (inclusion) distribution. The machine learning technique used to generate human-interpretable models was symbolic regression using genetic programming. Python package `gplearn` was used to perform the model fitting. The goal of symbolic regression is to find a relationship between stability of austenite phase (defined as energy per unit mole) and fatigue strength, as it has been shown that steel with optimum stability of austenite can help in improving the strain hardening behavior and toughness which translates to increased resistance to fatigue crack initiation and propagation. Hence, the experimental data can help elucidate the effect of austenite stability on fatigue while accounting the effect of other factors, such as hardness, defects. Figure 13.5 shows the symbolic regression results.

### 13.2.6 Enhancing Phase Mapping for High-throughput X-ray Diffraction Experiments using Fuzzy Clustering

X-ray diffraction (XRD) is a widely used experimental technique in materials science to understand the composition-structure-property relationships of materials for designing and discovering new materials. A key aspect of XRD analysis is that the composition-phase diagram is composed of not only pure phases but also their mixed phases. Hard

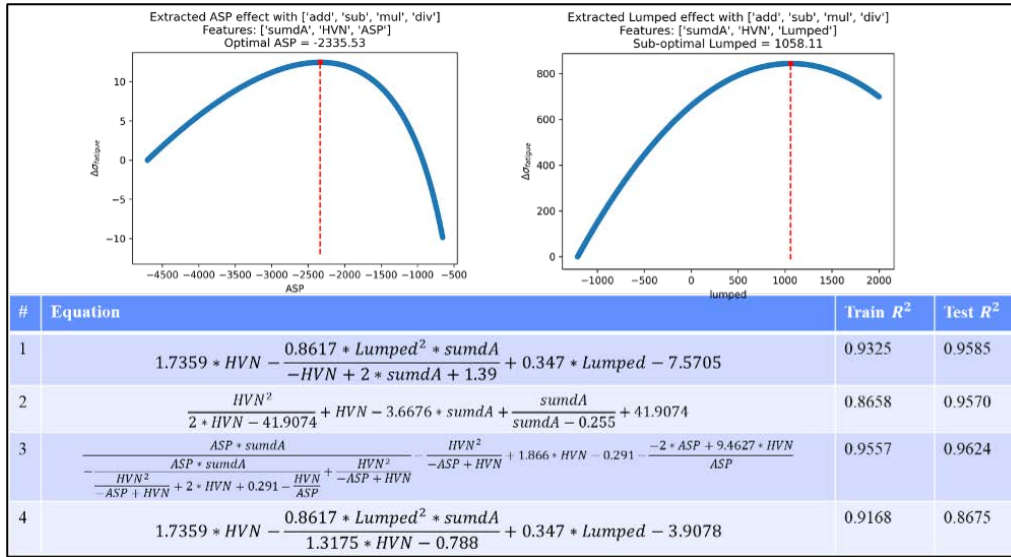


Figure 13.5: Results from symbolic regression using genetic programming with plots of effect of ASP on fatigue strength.

clustering approach treats the mixed phases as separate independent clusters from their constituent pure phases, hence, resulting in incorrect phase diagrams which complicate the next steps. **Agrawal** and **Choudhary**, in collaboration with Mike Bedzyk (NU) and Chung (NU) have developed a novel clustering approach of XRD patterns by leveraging a fuzzy clustering technique that can significantly enhance the potential phase mapping and reduce the manual efforts involved in XRD analysis. The proposed approach first generates an initial composition-phase diagram and initial pure phase representations by applying the fuzzy c-means clustering algorithm, followed by hierarchical clustering to accomplish effortless manual merging of similar initial pure phases to generate the final composition-phase diagram. The proposed method is evaluated on the XRD samples from two high-throughput composition-spread experiments of Co-Ni-Ta and Co-Ti-Ta ternary alloy systems. The results demonstrate significant improvement compared to hard clustering and significantly reduce manual efforts. Verified by the domain scientists on the team, the results achieved good agreement with the manually computed ground-truth phase diagrams for the two ternary alloy systems. This work was accepted and presented at *ICPRAM 2021*.

### 13.2.7 Data-Driven Multi-Scale Modeling and Optimization for Elastic Properties of Cubic Microstructures

In the structure-property optimization design problem, the objective is to obtain microstructures that leads to a desired optimal property in an accurate, fast and complete fashion. The microstructure can be represented by a set of statistical descriptors, such as the orientation distribution function (ODF). Properties like the stiffness constant  $C_{11}$ , Young's modulus  $E_{11}$ , can be theoretically computed as functions of ODF in the homogenization step, which is the forward problem. However, the inverse problem of microstructure optimization is much harder. Existing gradient-based optimization methods can find one optimum single-crystal solution but usually fail to discover multiple polycrystalline solutions, which is important for inverse problems. **Agrawal** and **Choudhary**, in collaboration with **Choudhary**, **Tavazza**, and Pinar Acar (Virginia Tech), have developed a machine learning based

optimization method that reduces the dimensions of the ODF space to perform more guided search. The application of the method on data for Al, Ni, and Si from the JARVIS-DFT database revealed that it can discover multiple polycrystalline solutions while maintaining (near-)optimality. Polycrystalline designs are advantageous over single crystals in terms of better manufacturability. This work was recently accepted in *Integrating Materials and Manufacturing Innovation (IMMI)*.

### 13.2.8 Semi-Parametric Functional Calibration and Uncertainty Quantification

While most calibration methods focus on inferring a set of unknown but assumed to be constant model parameters, many engineering problems have model parameters that are functionally related to the model variables. Being able to formulate a low-dimensional approximation of the calibration functions affords the ability to use low-fidelity models to reliably explore physical phenomena at length and time scales unattainable with their high-fidelity simulations/experiments. **Chen** has developed a semi-parametric uncertainty quantification-based decision support framework that enables modelers to select and calibrate an appropriate class of calibration functions. The purpose of this approach is to identify an appropriate balance between model complexity and calibration accuracy. The framework starts with a candidate set of high-dimensional calibration functions for which we quantified the first two statistical moments through an approximate Bayesian computational sampling scheme. Subsequently, through this analysis a modeler can select and calibrate a more appropriate and low-dimensional class of calibration functions. The strength of this framework is that it provides a structured approach to synthesize domain knowledge from physical experiments, simulation models, and expert insight.

### 13.2.9 Improving Scalability of Parallel CNN Training by Adaptively Adjusting Parameter Update Frequency

Training deep learning networks is very computationally expensive, which is typically done using some variant of stochastic gradient descent (SGD). It is thus highly desirable to parallelize and accelerate SGD, for which the most common strategy is synchronous SGD with data parallelism, but it suffers from expensive inter-process communications of averaging gradients among all workers. The iterative parameter updates of SGD cause frequent communications and it becomes the performance bottleneck. Liao, **Choudhary** and **Agrawal** have developed a lazy parameter update algorithm that adaptively adjusts the parameter update frequency to address the expensive communication cost issue. The developed algorithm accumulates the gradients if the difference of the accumulated gradients and the latest gradients is sufficiently small. The less frequent parameter updates reduce the per-iteration communication cost while maintaining the model accuracy. Results demonstrate that the lazy update method remarkably improves the scalability while maintaining the model accuracy. For ResNet50 training on ImageNet, the developed algorithm achieves a significantly higher speedup (739.6 on 2048 Cori KNL nodes) as compared to the vanilla synchronous SGD (276.6) with negligible (<0.2%) loss in accuracy. This work was recently published in *Journal of Parallel and Distributed Computing*.







## 14. Materials Data Facility

**Ian Foster (UC), Benjamin Blaiszik (UC)**

Marcus Schwarting (ANL), Jonathon Gaff (UC), Hong Zhi (UC), Tyler Skluzacek (UC)

**James Warren (NIST), Debra Audus (NIST), Chandler Becker (NIST), Daniel Wheeler (NIST), Trevor Keller (NIST)**

### 14.1 Design Goals

The high level goals of the Materials Data Facility are to make it more simple for users to publish, discover, and use materials data in their research. MDF consists of four modular services that together help to meet these goals: MDF Publish, MDF Discover, MDF Connect, and XTract. MDF Publish provides the capabilities of a decentralized dataset repository, allowing datasets to be published by a user to any Globus endpoint, identified with a permanent identifier, and screened through curation workflows. MDF Discover provides a scalable, flexible, access-controlled, cloud-hosted, materials-specific search index, coupled with software tools to simplify user searches. XTract is a new service that allows for scalable, distributed, domain-specific metadata extraction from a set of input files. MDF Connect is the central element that connects MDF Publish, Discover, XTract, and also external services (Figure 14.1), enabling programmatic access (e.g. via Python or REST API) or form-driven access to the MDF services.

### 14.2 Research Accomplishments

In order to meet the challenges of the 21st Century, we need to discover new materials to speed electrification and revolutionize transportation, identify new medical therapeutics to halt acute and chronic disease processes, discover new reaction pathways for green chemistry, and tackle complex problems across scientific domains. New scientific and technological discoveries will drive economic growth and help provide economies of abundance while simultaneously caring for and protecting the environment. With the co-emergence of new AI methods, advances in high performance computing, software, and infrastructure platforms, and advanced robotics, materials science research will undergo a

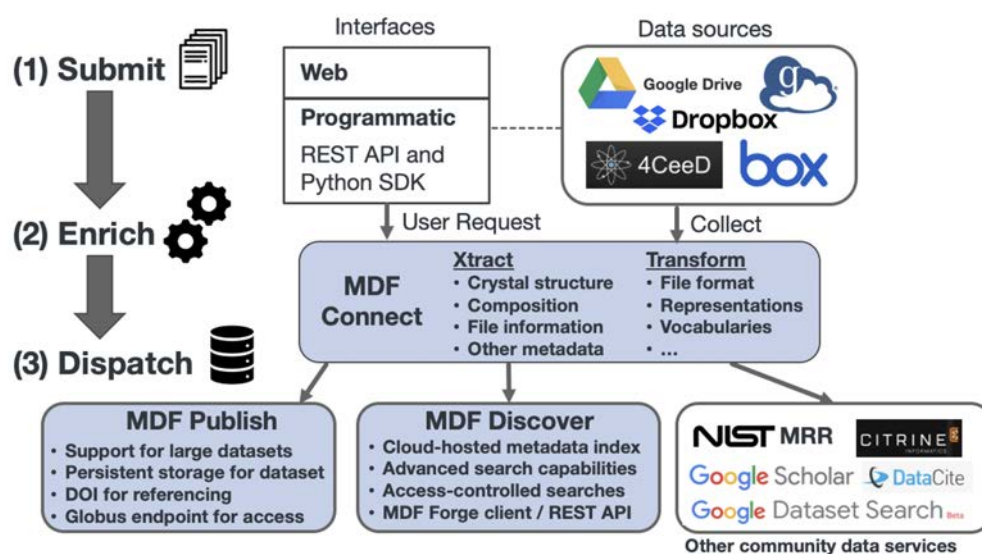


Figure 14.1: Overview of the Materials Data Facility. A user submits data from any of the data sources shown through a web form or via Python script (using the MDF Connect client). The data are collected by MDF Connect, enriched through extraction of materials-specific information, and transformed into shapes compatible with various services via the XTract service. The original data or extracted metadata are then dispatched, as appropriate, to MDF services and other community services.

transformation in the next decade as a vastly more productive research enterprise built on these new capabilities realizes the key goals of the Materials Genome Initiative. Linking these capabilities into a national materials design and innovation fabric requires, not least, advanced data infrastructure. The high-level goals of the Materials Data Facility Use Case are to perform foundational research and create services to 1) simplify materials data publication, discovery and usage; 2) automate metadata extraction for materials science and other domains; and 3) apply advanced deep learning techniques to extract structured information from unstructured scientific literature documents. We next discuss our efforts towards each goal.

### 14.2.1 Data Publication and Discovery

The Materials Data Facility (MDF) provides data services and interfaces for data publication, integration, and discovery, promoting simplified access, reuse, and synthesis. MDF supports self-service publication and persistent identification of datasets on distributed storage with heterogeneous data formats and sizes; automated extraction of descriptive metadata from structured formats and natural language text, and unified programmatic discovery and access to dataset contents both within MDF and from other repositories and services. As MDF data volumes increase, we seek to provide researchers unprecedented machine learning (ML) opportunities. MDF will also serve as an integration hub for CHiMaD/NIST, MGI projects, and broader materials community efforts.

MDF has published and collected >70 TB of data comprising 603 datasets representing datasets from 998 unique authors (Figure 14.2). Over the past 6 months, users have moved a total of 12 TB of data and

Datasets	Data Volume	Published Researchers
603	>70 TB	998

Figure 14.2: Select MDF data publication metrics

621,392 files. MDF provides the community with a unique capability to publish large datasets, e.g., we have published datasets as large as 7.1 TB (Figure 14.3) and datasets with millions of files. These datasets are traditionally too large for publication services and would otherwise be inaccessible to the community. Further, we provide additional value by indexing the contents of the datasets at an individual file level. With MDF, each dataset and the accompanying contents are searchable, made available on high performance storage for easy access, and preserved for future use. Further, their contents have been indexed with MDF materials-aware data extractors (see section 14.2.2) to make the dataset contents searchable at the file level.

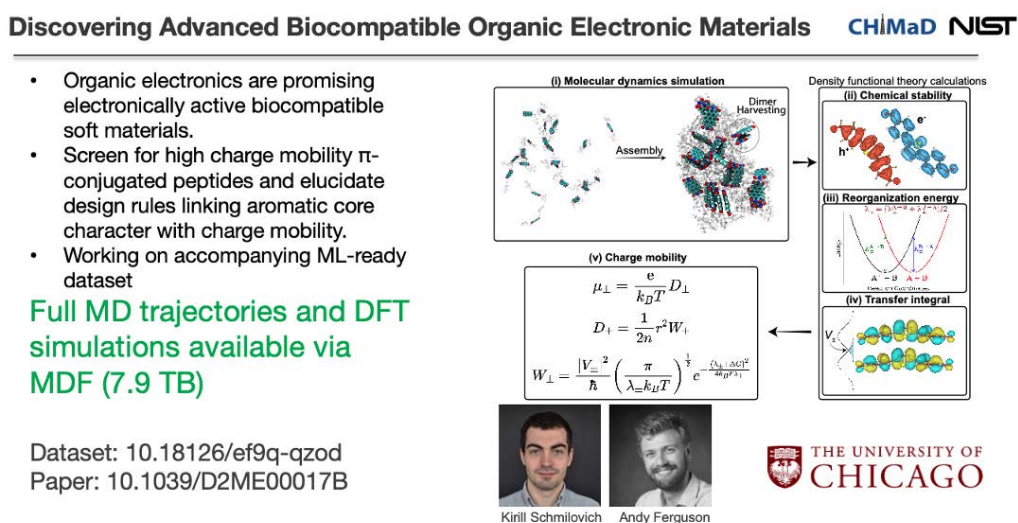


Figure 14.3: Dataset screening high charge mobility  $\pi$ -conjugated peptides to establish design rules for organic electronic materials. This dataset showcases the MDF capability to publish exceptionally large datasets; in this case 7.9 TB.

### Simple Data Access Interfaces

It is critical that published data be made available to the community in ways that make them easy to understand, synthesize with other datasets, explore, and use in modeling efforts. MDF serves as the back end and data repository to support a dramatically simplified way to access high quality machine learning (ML)-ready datasets<sup>1</sup>. Figure 14.4 shows a CHiMaD dataset of molecular solvation energies accessed using Foundry and MDF. To load a dataset, a researcher simply provides the dataset DOI, and calls the load method (Figure 14.4a). The load method fetches important metadata about the dataset including the ML task, the number of entries, dataset splits (e.g. training, test, validation), and keys split by inputs and targets (Figure 14.4b). With this information, we are able to construct automated data loaders that allow users with just two more lines of code to cache data locally using Globus or HTTPS and manipulate them in e.g., a Jupyter notebook (Figure 14.4c). With this approach, access to materials data that may have previously taken months, now takes only a few minutes.

<sup>1</sup>This work highlights a new collaboration between the MDF team and the University of Wisconsin (external NSF funding)

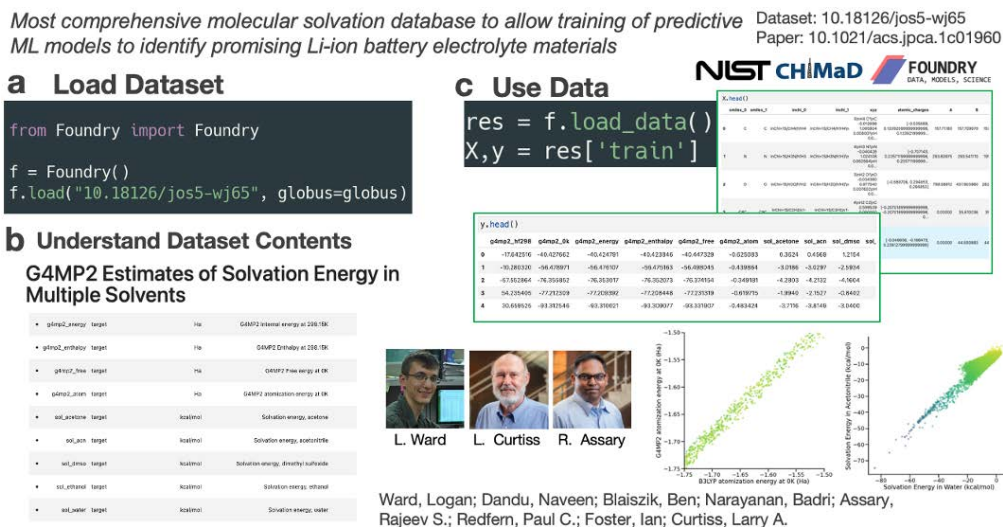


Figure 14.4: Compiled dataset of molecular solvation and formation energies to enable discovery of new Li-ion battery electrolytes. The data are made trivially accessible to researchers who can fetch the results of >600,000 calculations with several lines of code.

### ML-Ready Dataset Availability and Impact

The MDF team has published ML-ready datasets for applications including from Zeolite synthesis (via MIT), computing molecular solvation energy in various solvents (shown in Figure 14.4 - via UChicago/Argonne/CHiMaD), automating labeling of dendrite from tomographic data (via Northwestern/CHiMaD), an atom position benchmark (via UW-Madison and Oak Ridge National Lab), and predicting material band gaps (combining data from Materials Project, OQMD, experimental literature, and National Renewable Energy Laboratory). We are working with NIST researchers to collect and publish data from JARVIS ([Choudhary](#)) and impact mitigation use-case group ([Forster](#)) in these ML-ready formats. Further, these new interfaces are proving helpful to educational pursuits, as they have been included in classes taught at Northwestern and UChicago, and U. Utah and are planned to be included in further classes at UW-Madison and U. Toronto in 2022. These materials have also been made available on NanoHub for public access.

### 14.2.2 Automating Materials-Aware Metadata Extraction

Science data repositories can be valuable troves of research artifacts, but the volume and variety of data create significant challenges in creating searchable indexes over these data. Metadata extraction systems can automatically mine rich, searchable metadata from these collections, but no current system is tuned for the scale, decentralization, and heterogeneity of these data. As part of this project we have constructed a domain-independent extraction system called Xtract that is capable of extracting metadata from these collections. In the following I discuss recent efforts to intelligently apply metadata extractors to files, construct schedules based on predicted metadata quality, and study whether the metadata outputs enhance repository navigability and overall research value for real science users. File type identification (FTI) is a field concerned with mapping files to one or more file types. In the context of metadata extraction, one can leverage FTI methods to predict the extractors that will yield metadata from a file. The leading tool used by Apache Tika to map extractors to files, libmagic, as we show in Figure 14.5, is unable to correctly identify many types of files in the Carbon Dioxide Information Analysis Center (CDIAC), primarily

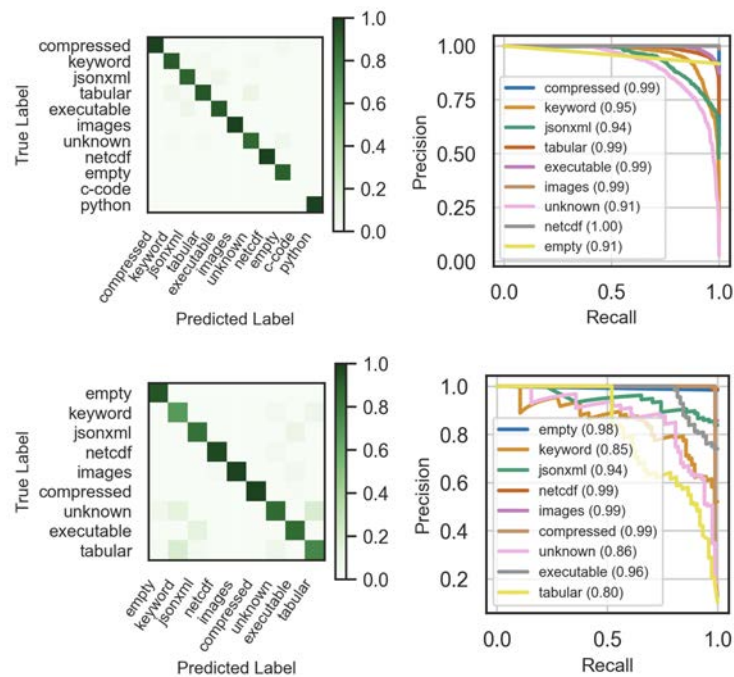


Figure 14.5: Imbalanced (top) and balanced (bottom) confusion matrices and PR curves for random forests model trained on first 512 bytes of each file.

due to the files not adhering to mimeType or schema convention. To this end, we explored various multi-output models, and found that a random forests model trained on the first 512 bytes of a file sufficiently identified over 89% of files, as shown in Figure 14.6. We successfully predict the types of 35% more files than libmagic.

We created an automatic metadata quality analysis tool to schedule metadata extractors for a full-repository metadata extraction job. The scheduler takes as input the FTI probability vector and metadata sizes to determine a priority-order for all possible extractor-to-file invocations. Specifically, the goal is to frontload extractions

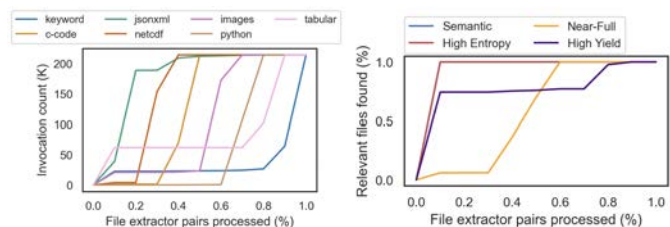


Figure 14.6: Extractors executed over time (left) and cumulative quality files encountered over time.

that produce value in a given context; for instance, one might want rich, semantic metadata when data are to be explored in a search index, or one might want complete numeric metadata when automatically tuning scientific instruments. We illustrate in Figure 5 that a scheduler that maximizes metadata yield per second effectively pushes the extraction from rich, semantic files to the start of the queue. We have packaged these metadata quality metrics into a public Python package.

To explore the value of metadata on research tasks, we conducted an IRB-approved (University of Chicago) user study in which users navigated metadata to solve research scenarios. We recruited six users of large national lab science repositories, and engaged them in two parts: (1) an informational interview in which we learned about the current metadata

needs of their science repository as well as potential libraries for conducting new metadata extractors, and (2) a series of interactive exercises where users navigated an interface for their repository’s automatically extracted metadata. We showed in both spectroscopy and battery modeling groups that, regardless of the search interface, users correctly completed 28% more simulated research tasks, and performed these tasks significantly faster (>10X, on average) than via their best alternative approaches. Importantly, we find that 100% of participants claim that the automatically extracted metadata are not only helpful, but more helpful than their existing approaches in navigating their science data. The survey responses to these exercises are shown in Figure 14.7. We also used this opportunity to collect qualitative feedback about Xtract’s metadata.

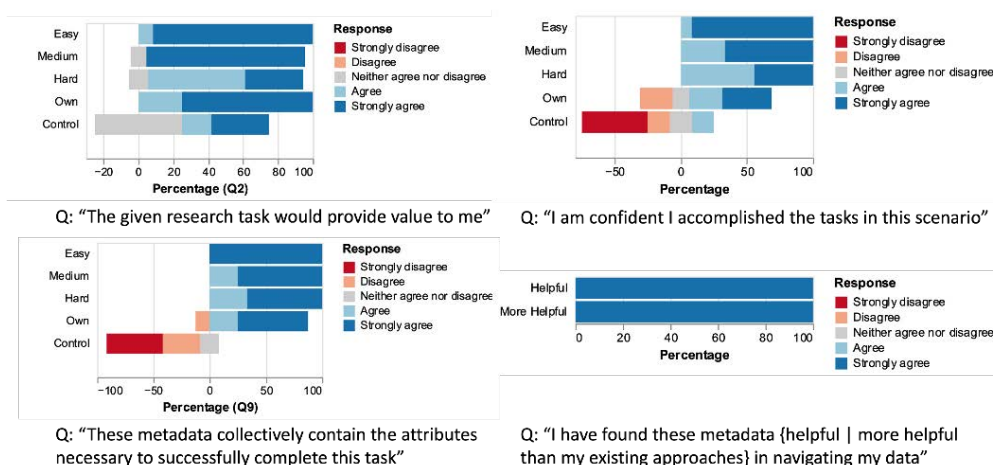


Figure 14.7: Xtract metadata user study survey results at multiple levels of question difficulty.

In summary, we have continued to iterate on Xtract - a metadata extraction system for science. We developed a scheduling module to intelligently apply extractors to files, constructed a quality toolkit to automatically analyze the quality of metadata outputs, and have observed users’ collective ability to leverage these metadata to navigate their repositories.

### 14.2.3 Natural Language Processing

Data is taking the center stage in materials engineering, yet vast amounts of data remain and continue to be buried in written papers, inaccessible to humans and machines. In recent years, significant progress has been made by the computer science community on techniques for automated information extraction from free text. Yet, transformative application of these techniques to scientific literature remains elusive. After a comprehensive review of the technical and logistical challenges of applying state-of-the-art NLP techniques to materials literature[1], we have concluded that transformer-based language models are best-suited for information extraction in materials science literature. Unlike traditional task-specific nlp models, transformer-based models can be pretrained unsupervised on a large corpus, thus greatly reducing the need for labeled data.

A number of transformer-based language models have been developed for various scientific domains, such as biology (BioBERT[2], PubMedBERT[3]) and Computer Science (SciBERT[4]). However, their applications for information extraction in materials science remain limited. We propose adapting these state-of-the-art language models by training

	<b>ScholarBERT</b>	<b>ScholarBERT-XL</b>
Hidden Layers	24	36
Attention Heads	16	20
Dropout	0.1	0.1
Activation Function	GeLU	GeLU
Layer Normalization	1e-05	1e-05
Hidden Dimension	1024	1280
Intermediate Dimension	4096	5120

Table 14.1: Model parameters of two sizes of ScholarBERT.

<b>Model</b>	<b>Parameters</b>	<b>Pre-training Corpus</b>	
		<b>Datasets</b>	<b>Tokens</b>
BERT-Large	340M	15M Wikipedia pages and novel books	3.3B
SciBERT	110M	1.14M CS and Bio papers from Semantic Scholar	3.1B
BioBERT	110M	PubMed abstracts, plus BERT corpus	7.8B
PubMedBERT	110M	PubMed abstracts and PubMedCentral full texts	16.8B
MatSciBERT	110M	150K MatSci papers from Elsevier Science Direct	285M
ScholarBERT	340M	67M English-language research articles	221B
ScholarBERT-XL	770M	67M English-language research articles	221B

Table 14.2: Comparison of model size and pre-training corpus of scientific language models.

them on a massive corpus consisting of exclusively scientific literature. To this end, we present ScholarBERT and ScholarBERT-XL, two language models that have been shown to outperform the current state-of-the-art systems in named entity recognition tasks. Table 14.2.3 listed the hyperparameters of ScholarBERT. Table 14.2.3 compares the size and the pre-training corpus of six transformer-based language models.

Typically, language models follow a pre-train then fine-tune paradigm, where pre-training consists of training a model from scratch using a large unlabelled corpus and fine-tuning tweaks the resulting model’s weights to optimize the downstream task performance on a domain specific task. There have been efforts towards building language models for science, but most of them focus on the biomedical sciences. More recently, we have seen some work that aims at pretraining language models for the materials science domain, such as MatSciBERT.

We use the Solid State Dataset [5] consisting of 800 hand-labeled materials science abstracts to evaluate the performance of our models on downstream named entity recognition tasks. The abstracts contain at least one inorganic material and a synthesis or characterization method for inorganic materials. These abstracts are labeled on an entity-level into seven different entity types including inorganic materials (MAT), symmetry/phase labels (SPL), sample descriptors (DSC), material properties (PRO), material applications (APL), synthesis methods (SMT), and characterization methods (CMT). We compare the results of our fine-tuned models to existing models in the literature including MatSciBERT and SciBERT. Both SciBERT and MatSciBERT have 110M parameters and are trained on specific domains. On the other hand, ScholarBERT and ScholarBERT-XL have 340M and 770M parameters respectively and are trained on a diverse scientific corpus.

Understanding scientific concepts and their associated domains is crucial to identify relevant texts in a noisy corpus, which most other models simply assume is done in a separate preprocessing step by a different model or classifier. Figure 14.9 shows the results of projecting word vectors of entities in material science (red) and another discipline (blue, e.g., chemistry) onto the discipline difference word vector (e.g., *chemistry - material science*). The word vectors are extracted from ScholarBERT and five other transformer-based scientific language models. Figure 14.9 shows that ScholarBERT is able to correctly associate entities with their domains and cleanly separate entities from different domains, while the other models cannot.

In summary, we have developed ScholarBERT, the largest scientific language model to the best of our knowledge. Due to its vast training corpus and large number of hidden parameters, it is able to outperform the other scientific language models on recognizing and classifying materials science entities. Further analysis of its hidden representations of the entities revealed its superior ability to differentiate scientific concepts.

#### References:

1. Hong, Zhi, Logan Ward, Kyle Chard, Ben Blaiszik, and Ian Foster. "Challenges and Advances in Information Extraction from Scientific Literature: a Review." *JOM* 73, no. 11 (2021): 3383-3400.
2. Lee, Jinhyuk, Wonjin Yoon, Sungdong Kim, Donghyeon Kim, Sunkyu Kim, Chan Ho So, and Jaewoo Kang. "BioBERT: a pre-trained biomedical language representation model for biomedical text mining." *Bioinformatics* 36, no. 4 (2020): 1234-1240.
3. Gu, Yu, Robert Tinn, Hao Cheng, Michael Lucas, Naoto Usuyama, Xiaodong Liu, Tristan Naumann, Jianfeng Gao, and Hoifung Poon. "Domain-specific language model pretraining for biomedical natural language processing." *ACM Transactions on Computing for Healthcare (HEALTH)* 3, no. 1 (2021): 1-23.
4. Beltagy, Iz, Kyle Lo, and Arman Cohan. "SciBERT: A pretrained language model for scientific text." *arXiv preprint arXiv:1903.10676* (2019).
5. L. Weston, V. Tshitoyan, J. Dagdelen, O. Kononova, A. Trewartha, K. A. Persson, G. Ceder, and A. Jain. "Named Entity Recognition and Normalization Applied to LargeScale Information Extraction from the Materials Science Literature" *Journal of Chemical Information and Modeling* 2019 59 (9), 3692-3702.

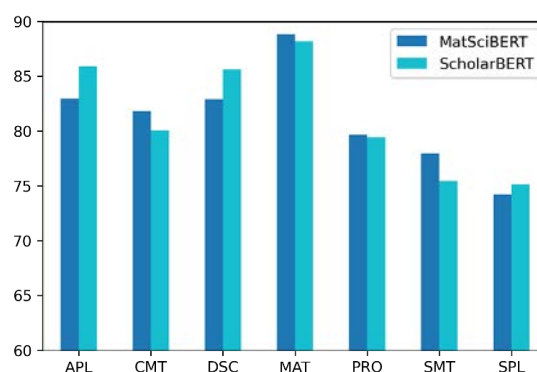


Figure 14.8: F1 scores of ScholarBERT and MatSciBERT on the Solid State Dataset. ScholarBERT has an advantage in recognizing material applications, sample descriptors, and symmetry/phase labels. Overall it achieved an F1 score of 83.3%, while MatSciBERT got 82.9%



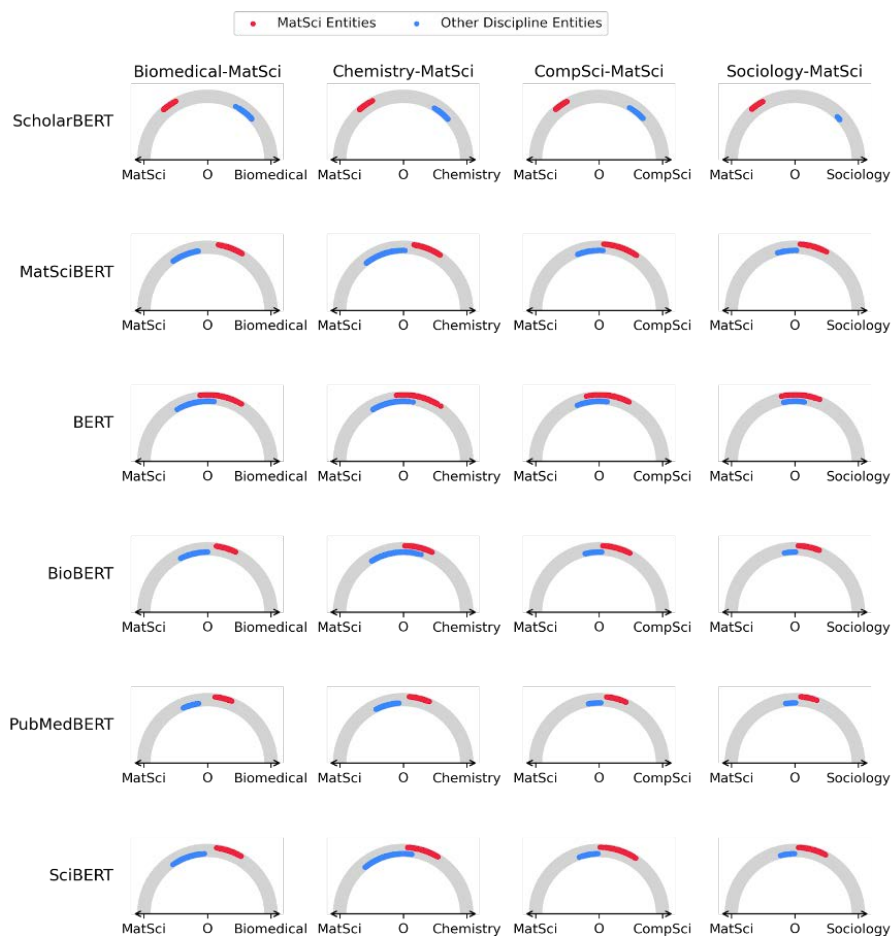


Figure 14.9: Visualization of projection of *materials science* vs *other* entities. Materials Science (MatSci) entities (blue) are expected to be in the negative (left) after projection, and entities in the other domain (red) are expected to be in the positive after projection (right). Of all the language models tested, only the vectors extracted from ScholarBERT performed as expected, demonstrating its superior encoding of entities.

### 14.3 Community Support and Other Collaborations

#### Phase Field Hub (PFHub) - MDF Integration

*Daniel Wheeler* (NIST), *Trevor Keller* (NIST), *Olle Heinonen* (CHiMaD, Argonne) *Ben Galewsky* (UIUC), *Jonathon Gaff* (CHiMaD, UC), *Ian Foster* (CHiMaD, UC/Argonne), *Ben Blaiszik* (CHiMaD, UC/Argonne)

The MDF team is working with the PFHub team at NIST to leverage MDF capabilities to enable simplified benchmark challenge submission, long-term storage of results on high performance storage, and association of DOIs with each submission to enable citation. A prototype has been developed to index prior submissions from PFHub.

#### Polymer Property Database (PPPDB)

*Debbie Audus* (NIST), *Roselyne Tchoua* (CHiMaD, UC), *Zhi Hong* (CHiMaD, UC), *Ian Foster* (CHiMaD, UC/Argonne), *Ben Blaiszik* (CHiMaD, UC/Argonne)

The MDF team has worked with NIST to generate PPPDB. In 2022, we will integrate the PPPDB back end with MDF to simplify data access and enable deposit from users outside the direct PPPDB team.

### AI Driven Automated Laboratories

*Ben **Blaiszik** (CHiMaD, UC/Argonne), Ian **Foster** (CHiMaD, UC/Argonne), Logan Ward (CHiMaD, Argonne), Marcus Schwarting (CHiMaD, Argonne), Juan **de Pablo** (CHiMaD, UC/Argonne), Heinrich **Jaeger** (CHiMaD, UC)*

MDF has been working to explore concepts in laboratory automation to understand the data infrastructure necessary to support wider and more rapid adoption of AI-driven automated laboratories and to deploy a prototype of such an automated experimental system coupled with machine learning and data infrastructure components towards problems in polymer science. This work led to a newly funded DOE project with the PIs listed above. In 2022, we connect these efforts to those at NIST (e.g., Brian **DeCost**) to exchange information on laboratory automation capabilities.

### 3M - CHiMaD Collaboration

*Christina Thomas (3M), Marcus Schwarting (CHiMaD, Argonne), Ben **Blaiszik** (CHiMaD, UC/Argonne), Logan Ward (CHiMaD, UC/Argonne), Ian **Foster** (CHiMaD, UC/Argonne), Juan **de Pablo** (CHiMaD, UC/Argonne), Matthew **Tirrell** (CHiMaD, UC/Argonne)*

The MDF team, along with others at Chicago have worked to engage industrial contacts at 3M on problems of polymer discovery and process optimization. MDF team has visited 3M, and 3M representatives have visited Chicago. MDF is in discussion with 3M to leverage MDF capabilities and to support data sharing and publication for data generated via their academic collaborators.

### Joint Center for Energy Storage Research (JCESR) - MDF

*Logan Ward (CHiMaD, Argonne), Larry Curtiss (Argonne), Badri Narayanan (University of Louisville), Rajeev Assary (Argonne), Ben **Blaiszik** (CHiMaD, UC/Argonne), Ian **Foster** (CHiMaD, UC/Argonne)*

The MDF team has worked with JCESR for several years to enable data publication from select projects, and to build predictive machine learning models on the available datasets. For example, we published the largest database of G4MP2 accuracy molecular calculations and molecular solvation energies. Based on this work, a newly funded project was initiated, leading to the hiring of Logan Ward (CHiMaD postdoc) as a full Argonne scientist.

### Development of a Foam Property Database

*Aaron **Forster** (NIST), Ben **Blaiszik** (CHiMaD, UC/Argonne), Ian **Foster** (CHiMaD, UC/Argonne)*


Leverage MDF data infrastructure to create a public community resource of experimental foam properties for applications in impact mitigation.

**Development of Shared Metadata Extractors**

*Josh **Taillon** (NIST), Ben **Blaiszik** (CHiMaD, UC/Argonne), Ian **Foster** (CHiMaD, UC/Argonne)*

We are working together to develop joint materials-specific metadata extraction capabilities for use in NIST LIMS systems. This work will leverage prior MDF work in the MaterialsIO software package.





## 15. CHiMaD Outreach: Training and Professional Development

**Begum Gulsoy (NU), Laura Bartolo (NU)**, Greg Olson (NU), Peter Voorhees (NU), Juan de Pablo (UC), Paul Nealey (UC), Olle Heinonen (ANL), Marius Stan (ANL), Noah Paulson (ANL), Ian Foster (UC), Ben Blaiszik (UC), Carrie Wilson (ASM), Aziz Asphahani (QT), Jason Sebastian (QT)

James Warren (NIST), Carelyn Campbell (NIST), Chandler Becker (NIST), Debra Audus (NIST), Zachary Trautt (NIST), Jon Guyer (NIST), Daniel Wheeler (NIST)

### 15.1 Goals

CHiMaD has designed an extensive program with outreach and training to high school students, K-12 STEM educators, undergraduate students, graduate students, postdoctoral researchers, researchers and industry and government professionals. **Gulsoy** oversees the entire outreach program and **Bartolo** leads the data-specific outreach efforts. However, wide breadth of CHiMaD outreach is possible through the participation of many other CHiMaD and NIST PIs, postdocs and students as well as other collaborators - lead organizers for events are indicated in more detail with each event and initiative listed below.

The restrictions due to the COVID-19 pandemic has certainly disrupted CHiMaD outreach events but also brought forth new opportunities to convene the community and increase the impact of CHiMaD's activities. The next section describes what CHiMaD team was able to accomplish and develop in 2021 under its Outreach program.

### 15.2 Accomplishments: Outreach and Training

#### 15.2.1 CHiMaD Materials Design Training

*Begum Gulsoy (NU), Clay Houser (NU), Jonathan Emery (NU), Aaron Geller (NU), Greg Olson (NU)*

Designing novel materials of specific properties for a particular application requires simultaneously utilizing physical theory, advanced computational methods and models, materials properties databases and complex calculations. This approach stands in contrast

to the traditional trial-and-error method of materials discovery. CHiMaD focuses this approach on the creation of novel hierarchical materials which exploit distinct structural details at various scales, from the atomic on up, to obtain enhanced properties. The center's research focuses on both organic and inorganic advanced materials in fields as diverse as self-assembled biomaterials, smart materials for self-assembled circuit designs, advanced ceramics and metal alloys.

The CHiMaD Materials Design Training aims to introduce and further the attendees' knowledge of the Materials by Design philosophy and related practical design concepts. The CHiMaD design training is commonly held in two parts: (1) a core training session to *introduce* the participants to the concept and workings of materials design; and (2) a specialized small-group session to guide participants as the participants apply what they have learned to materials systems of their own choice using the technical knowledge represented in the small group. During the latter, small, diverse groups with varying types of expertise are lead through discussions on building System Design Charts. This exercise allows for the organization and visualization of the processing-structure-property-performance links of a material system while identifying unique design goals and strategies while identifying unique design goals and strategies. The hands-on approach allows to showcase the strength of accommodating different types and even levels of expertise for design.

CHiMaD design team lead training sessions for CHiMaD researchers and worked on further developing the training tools for industry use during the year. In 2021, a virtual CHiMaD Materials Design Training was held for CHiMaD researchers, mainly focusing on Design of Polyelectrolyte Complexes and Directed Self Assembly of Soft Materials use-case groups, on November 1, 2021 with the lead of **Gulsoy**, Jonathan Emery (NU) and Clay Houser (NU). This followed the training organized in 2020 focusing on 2D Electronic Materials Inks, Thermoelectric Design and Composite Design use-cases for content development. The latest training also served as a test-bed for the newly developed CHiMaD System Design Toolbox, generating first-time user-feedback towards further development.

Since 2018, CHiMaD has been customizing its CHiMaD Materials Design Training for professionals with the aim to introduce and integrate the materials design methodology into the materials development cycle.

A major effect of the ongoing pandemic in 2020 was the move to fully virtual events. A positive development from the year has been the opportunity to rethink what it means to run a hands-on session in a fully virtual format without losing the engagement or interest of participants due to the medium. The CHiMaD Materials Design training historically prides itself on providing an engaging discussion on materials systems of interest to clients with active participation of small groups of researchers. In-person this may mean researchers discussing around a table, or over a white board, physically moving post-its around together to build a system chart. While Power Point presentations had been incorporated into earlier trainings, this approach was dropped due to being disengaging.

In 2021, CHiMaD design team their invested time and efforts in further developing web-based tools which can be used to engage individuals in the training while crowd-sourcing technical knowledge to determine the discrepancies in the understanding and definition of the materials systems being discussed. The idea behind the expansion is to be able to take this tool from being CHiMaD-training specific to a community-tool which can be utilized



Figure 15.1: Homepage for The CHiMaD System Design Toolbox

by people all levels of knowledge in different ways and settings, be it in a classroom or industry training. To do this, **Gulsoy**, Jonathan Emery (NU), and Clay Houser (NU) have partnered with Aaron Geller, a Research Assistant Professor at Northwestern's Center for Interdisciplinary Exploration and Research in Astrophysics (CIERA), who specializes in visualizations. Together, in 2020, the design team had built the first-version of several web-based tools: (1) A method to self-categorize a "training" materials summary; (2) A tool to identify the links of the system design chart of the "training" materials system; (3) A method to simultaneously visualize the crowd-sourced answers and compare them. These tools were unveiled in industry and internal trainings in 2020. Using participant feedback and lessons learned during the training, the team further developed these tools in 2021 and migrated them to Northwestern's servers for better security and maintenance. They have expanded the tools capabilities to three modules:

- **Collaboration Module: Think and Train Together**

This module is intended to be a training or discussion tool for groups where the group would discuss a Materials Summary paragraph, picking either from a CHiMaD developed one or uploading their own. The tools allows for polling the trainees on their categorization of pre-determined key words, leading discussions on the outcomes of the training polls, converting the keywords and the results of the training into a visual System Design Chart and finally polling the trainees again on what are the appropriate links between different boxes of the system design chart.

- **Individual Module: Think and Train Together**

This module is intended for one person, or a small group, to create a system design chart on their own. It provides greater flexibility than the collaboration module.

- **Customization Module**

This module provides a lot of flexibility in further formatting the system design chart produced. Users are able to add/delete boxes and the text in them, change the direction of processing arrows, and add bullet points to name a few. It also allows users to export in three different formats (.svg, .png, .ppt) depending on the intended use.

The CHiMaD System Design Toolbox, shown in Figure 15.1, can be accessed at <http://>

chima-d-trainings.rcs.northwestern.edu. Documentation such as "Getting Started" has been added to the toolbox website, and further user-guidance documentation is being produced. The new version of the toolbox is currently under pilot testing at NU's Materials Design (MSE 390) course lead by **Shull**. A manuscript is also in preparation.

### 15.2.2 CHiMaD Focus Workshop Uncertainty Quantification of Phase Equilibria and Thermodynamics

Noah **Paulson** (ANL), Carelyn **Campbell** (NIST), Begum **Gulsoy** (NU)

The CHiMaD Uncertainty Quantification of Phase Equilibria and Thermodynamics (UQPET) Focus Workshop, was held virtually on October 27 & 29, 2021. In recent years, uncertainty quantification techniques have gained special attention in thermodynamics and phase equilibria. This increase in interest in uncertainty quantification has been mirrored in many scientific and engineering disciplines. This second workshop in the series, explored the impact of uncertainty quantification in atomistics, thermodynamic phase diagrams, experiments and computations, artificial intelligence, and design strategy. Identifying links between these disparate areas, has potential to transform materials and process design. The workshop will be conducted virtually over two days, with research talks, an industry panel, and open discussions.

The 48 workshop participants achieved this goal through a mix of presentations and panel discussions held over two days. Presentations included:

- The Value of Label Uncertainty in Training Data  
Maxwell Hutchinson (Citrine Informatics)
- The Role of Optimization in Uncertainty Quantification: Instrument Artifacts and Physical Principles  
Paul Patrone (NIST)
- Bayesian Hierarchical Random Effects Framework for UQ Applied to CALPHAD Databases  
Steve Niezgodra (The Ohio State University)
- Virtual oxides as a test bed for DFT methods and codes  
Stefaan Cottenier (Ghent University)
- Uncertainty in Multiscale Materials Modeling and Design  
David McDowell (Georgia Institute of Technology)
- Industry Panel  
David Furrer (Pratt & Whitney), Changing Niu (QuesTek), Edward Glaessgen (NASA Langley), Louis Hector (General Motors R&D)

### 15.2.3 CHiMaD Focus Workshop CHiMaD Phase Field Methods Workshop Series

Olle **Heinonen** (ANL), Peter **Voorhees** (NU), James **Warren** (NIST), Jonathan **Guyer** (NIST), Daniel **Wheeler** (NIST), Trevor **Keller** (NIST), Begum **Gulsoy** (NU)

The goal of the CHiMaD Phase Field Methods Workshop series is to develop benchmark problems for the global phase field community and to engage this elite team of invited Phase Field experts and framework developers for in providing input during this development.



In response to the ongoing pandemic, the CHiMaD Phase Field Methods Workshop was converted to a virtual format in 2020 and remained in this format during 2021. The 11th CHiMaD Phase Field Methods Workshop in the series took place as two-hour long sessions on April 26-27 and May 3-4, 2021. The workshop had the most international attendance and presentations to date as well as the first industry presentation. The 87 registrants held in-depth discussions spearheaded by 7 invited presentations:

- *Britta Nestler, Karlsruhe Institute of Technology (Germany)*  
Multi-Phase Solidification
- *Mike Tonks, University of Florida*  
Concurrently Modeling Multiple Length Scales by Coupling the Phase-Field Method to Spatially-resolved Cluster Dynamics
- *Abhik Choudhury, Indian Institute of Science - Bangalore (India)*  
Influence of Solid-Solid Anisotropy and Solute Diffusivity Contrast on Three-phase Growth Patterns in Ternary Eutectics
- *Nick Provatas, McGill University (Canada)*  
Modeling Rapid Solidification Kinetics Quantitatively Using Phase-Field Models
- *Ivan Yashchuk, Aalto University (Finland)*  
Experiences of Using Firedrake/FEniCS for Development of Phase-Field Solvers
- *Alex Guo, COMSOL (Industry Presentation)*  
Phase Field Modeling with COMSOL Multiphysics
- *Steve DeWitt, Oak Ridge National Laboratory*  
Preparing for Exascale Phase-Field Modeling: Phase-Field Code Development in ExaAM

The 11th workshop also included the first virtual poster presentation by students and postdocs with a Poster Session organized over Gather.Town with the participation of 4 posters, Figure 15.2.

The 12th CHiMaD Phase Field Methods Workshop was originally planned as an in-person meeting however was ultimately converted to a virtual meeting due to the continuing pandemic. The 12th workshop took place virtually on November 2-4, 2021, in a similar format to the in-person meetings but with longer breaks to avoid zoom-fatigue. The 73 registrants held in-depth discussions spearheaded by 4 invited presentations:

- *Olle Heinonen (ANL) & Daniel Wheeler (NIST)*  
Current Benchmark Problems, Traffic to PFHub
- *Michael Tonks (University of Florida)*  
Phase Field Best Practices, presentation and discussion
- *Fadi Abdeljawad (Clemson University)*  
Grain Boundary Segregation and Microstructural Evolution
- *Ellad Tadmor (University of Minnesota)*  
Atomistically-Informed Multiscale Modeling

There was also a session dedicated to short presentations from students and postdocs, with the aim to highlight their work and contributions to the field, as well as enable any workforce transfer. The Phase Field tool group has had a high-success rate of retaining students and postdocs in the field and in the CHiMaD Phase Field community. Many former postdocs continue to be part of the workshop series as professionals. The short presentations were as follows:

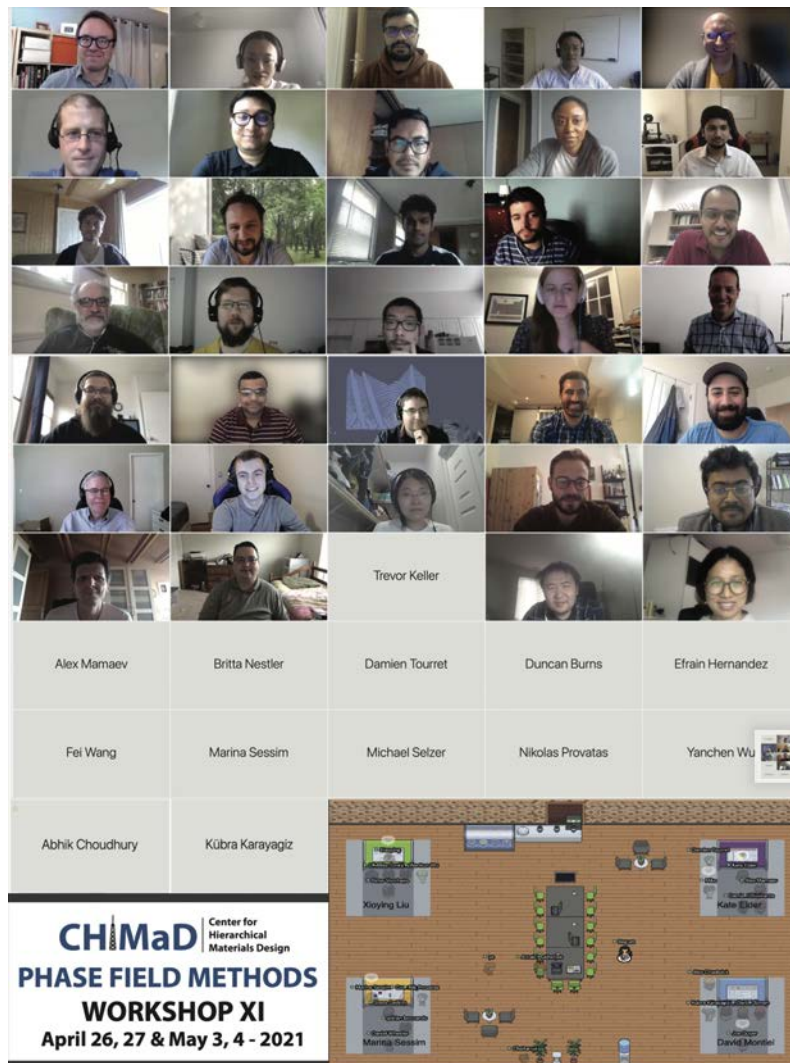


Figure 15.2: 11th CHiMaD Phase Field Workshop, organized in Spring of 2021.

- Jin Zhang (Northwestern) - Phase Field Modeling of Li Dendrite
- William Beck Andrews (U of Freiburg) - Crack Paths in Elastically Heterogeneous Materials via Phase Field Fracture
- Dharma Raj Basula (U of Connecticut) - Modeling Thermoelectric Phenomena In Simple and Complex Material with FEM
- Adrian Boccardo (NUI Galway) - Resolution of Phase-Field Models By Means of FFT and GPU
- Whitney Tso (Northwestern U) - Machine Learning Aided Exploration Of Phase-field Sensitivity Analysis
- Jose Mancias (Texas A&M) - A Julia GPU Parallelized Implementation of the Nucleation Benchmark

Further details are presented in CHiMaD Phase Field Methods tool group section of this report, on Chapter 11.

### 15.2.4 CHiMaD Professional Development Workshops

*Begum Gulsoy (NU)*

A new addition to the CHiMaD outreach programs is the Professional Development Workshops aimed at building soft-skills of postdoctoral and early-career researchers. This series was kicked off in Fall 2021 with a workshop by Kellogg School of Management Professor, Loran Nordgren on *personal branding and overcoming resistance for new ideas*. Prof. Nordgren presented on his research, summarized in his latest book **The Human Element**; all registered attendees also received a copy this book in preparation for the workshop.

In the follow-up survey, feedback was also collected on what other topics are of interest to the attendees. Some areas identified were (1) Strategies for effective speaking or writing, (2) Data presentation and powerpoint construction.

*October 26, 2021 (Registered: 43, Attendees: 15)*

#### **Leadership Presence: Building your personal brand**

Loran Nordgren (Kellogg School of Management, Northwestern)

**Abstract** People begin to form impressions of your character from the moment you meet. In fact, within milliseconds of a first encounter, people have already formed snap judgments about whether you are leadership material. This session examines how these largely unconscious judgments are made. We then use these insights to define and craft your leadership brand.

**Bio** Loran Nordgren is a scientist, lecturer, and consultant on the topics of leadership, influence and behavior change. Loran's research examines how the unconscious mind guides our thoughts and actions. He uses theory-driven insights to create interventions and policy recommendations that improve decision-making and well-being. His research has been published in leading journals such as *Science* and is regularly discussed in prominent forums such as the *Harvard Business Review*. In recognition of his work, Professor Nordgren has received the Theoretical Innovation Award in experimental psychology. A former Fulbright Scholar, Professor Nordgren has received numerous teaching awards for excellence in the classroom including Kellogg's Management and Organization's Teacher of the Year. He is one of Poets & Quants' 40 under 40 business school professors. He is the author of the recent bestselling book **The Human Element** (<https://www.humanelementbook.com>).

### 15.2.5 SRG Annual Meeting

*Greg Olson (NU), Begum Gulsoy (NU)*

The 37th SRG Annual Meeting was first postponed then virtually held (via Webex) on October 5, 2021 with 108 registered attendees. This year's meeting was meant to be held conjunction with the CHiMaD Annual Meeting, however the CHiMaD Annual Meeting was postponed to January 2022 and the SRG meeting was ultimately moved to a virtual format. The meeting agenda was again modified to be a single-day event, with a reduced number of 11 presentations. The presentations were as follows:

- QuesTek IDE - C. Niu (QT)
- Fracture Simulation - M. Parks (MIT)

- The Grain Boundary Genome - C. Schuh (MIT)
- The Liquid Genome - A. Allanore (MIT)
- LEAP Microanalysis - D. Seidman (NU)
- High Throughput Design - W. Xiong (University of Pittsburgh)
- Naval Martensitic Steels - C. Houser (NU/MIT)
- Printable Tool Steels - F. Hengsbach (Paderborn University, Germany)
- Cobalt Superalloys - C. Liu (NU)
- ULTIMATE - D. Frankel (QT)
- QuesTek Japan - J. Sebastian (QT)
- QuesTek Digital - J. Gong (QT)

### 15.2.6 CHiMaD Annual Meeting

*Peter Voorhees (NU), Juan de Pablo (UC), Greg Olson (NU), Begum Gulsoy (NU)*

The 2021 CHiMaD Annual Meeting, originally scheduled to take place in October (in-person) was postponed to January 2022 with the aim to keep it in-person however ultimately it was held virtually as a two-day event on 24-25 January 2022 with the registration and participation of 250+ attendees.

### 15.2.7 Materials Genome Toolkit Program

*Greg Olson (NU), Paul Mason (ThermoCalc), Begum Gulsoy (NU), Carrie Wilson (ASM), Jeane Deathrage (ASM)*

The ongoing program addresses several CHiMaD objectives by helping the next generation of scientists and engineers become proficient with materials-by-design tools and techniques and by contributing to efforts that are advancing the collective knowledge on material systems and methodologies. This program was established in 2015 and, to date, 24 U.S. universities were awarded the Materials Genome Toolkit. The following university was the recipients of the 2021 Materials Genome Toolkit Award:

- **University of Alabama, Tuscaloosa**  
Department of Mechanical Engineering *PI: Kasra Momeni*

*Materials Genome Toolkit Renewal Program* To ensure and motivate the continued implementation of MGI tools in U.S. undergraduate engineering curricula, a license *renewal* program was created in 2018 in partnership with ThermoCalc and the ASM Materials Education Foundation. Each license is provided at a highly discounted rate through the long-standing educational partnership with ThermoCalc. In 2021, the Foundation, lead by **Wilson**, worked with three universities to renew their licenses (for the first time) for 3-years at 50% cost to the universities; and worked with another three universities (for the second time) for 3-years at 50% cost to the universities. The program leverages CHiMaD funds by matching them to the university funds.

### 15.2.8 Undergraduate Education in Materials Design

*Greg Olson (MIT), Kenneth Shull (NU)*

The undergraduate-level Materials Design courses at NU, lead by **Shull**, and at MIT, lead by **Olson** aim to build teams of students focusing on real materials design problems, lead by graduate students and/or postdoctoral researchers. With the move of **Olson** to MIT, the materials design core class at NU is lead by **Shull** focusing mostly on non-hard materials.

Due to the ongoing pandemic, the classes were once again offered virtually in 2021. The projects in both classes remain CHiMaD-partnered or CHiMaD-inspired.

CHiMaD/SRG projects are the primary source of student projects in Olson's Materials Design class with supported researchers serving as coaches to the team projects. The revised class in Computational Materials Design at MIT, conducted in 2021 in virtual mode, continued to draw from CHiMaD research for these team projects. In addition to the Printable Co Superalloy project coached by Dr. Liu, further application of the ONR-supported transformation toughening research addressed martensitic naval hull steels toughened by dispersed austenite. Building on our strong relation with Apple as enhanced by Dr Jim Yurko joining the CHiMaD TAB, Apple served as client to a project on controlled-melting-point lead-free solders alloys. A project on printable steels in collaboration with U Paderborn in Germany addressed high-strength tool steels. A project on high-strength aluminum alloys drew on the new DSO-Singapore program. Staffing of the coaching and team participation was enhanced by virtual Visiting Scholars from Germany, Greece, and Singapore. Figure 15.3 shows the projects completed in the **Olson's** design course at MIT.

### 3.041/3.321 Computational Materials Design

Spring 2021  
Design Projects

- |   |  |
|---|--|
| <p><b>I. Printable Co Superalloy</b><br/>Client: NIST-CHiMaD<br/>Advisor: Dr. Chuan Liu<br/>Team: Yannick Naunheim, Noriaki Arai*</p>                                     | <p><b>III. Lead -Free Solder</b><br/>Client: Apple (Dr. Zack Feinberg)<br/>Advisor: Edward Pang<br/>Team: Spencer Hu, Nutth Tuchinda</p>                     |
| <p><b>II. HSLA150: Transformation - Toughened Naval Hull Steel</b><br/>Client: NIST-CHiMaD, ONR, SPI<br/>Advisor: Clay Houser<br/>Team: Julian Rackwitz, Brandon Snow</p> | <p><b>IV. Printable Tool Steel</b><br/>Client: NIST-CHiMaD, U Paderborn<br/>Advisor: Florian Hengsbach<br/>Team: Krista Biggs, Gary Whelan*</p>              |
|   | <p><b>V. UHS Al Plate Alloy</b><br/>Client: DSO-Singapore<br/>Advisor: Dr. Margianna Tzini<br/>Team: Alvin Tan, Jonathan Lim, Huan-Chin Koh, Wei-Lin Tan</p> |

Figure 15.3: Design class projects conducted at MIT.

### **University of Chicago Collegiate Scholars Program Summer School Molecular Engineering Course**

*Juan de Pablo (UC), Paul Nealey (UC), Xiaoying Liu (UC), Begum Gulsoy (NU)*

In continued successful partnership with the University of Chicago Collegiate Scholars Program that aims to prepare Chicago Public Schools students in grades 10-12 for admission and success at colleges and universities, CHiMaD PIs lead the Program's Molecular Engineering course offered during the summer quarter. The 6-week engineering course is designed to illustrate the concepts and principles of polymeric, composite, and nanoscale materials and demonstrate the relationship between molecular structures and material properties in the context of real-world applications, with an emphasis on materials design. Students learn the fundamentals of materials science and molecular engineering, including material types and properties, design of materials and experiments, and material characterization and analysis, through lectures, hands-on experience, reading assignments, and technical communication practice. Techniques for measuring material properties and

monitoring experimental processes are integrated throughout the course by use of a variety of laboratory instruments and tools. The students have shown great interest and enthusiasm in participating in the lab experiments and discussions. They have learned the key elements of a comprehensive material design process and important material systems, including polymers, composite materials, nanomaterials and semiconductors, in a stimulating and constructive environment.

In 2021, the summer session was held virtually and the course content was modified to accommodate the change. Multiple modules were taught by **Nealey, de Pablo**, Xiaoying Liu (UC) and **Gulsoy**. The 6-week *Engineering Core Course* took place between July 2020, as two 1.5-hour sessions each week. The module presented by **Gulsoy** focused on getting high-school students to think about materials they already interact with in their lives as well as why and where materials design comes into play. A common example used to explain the concept was use of materials in bicycles. Further, drawing inspiration from the system design chart of ice-cream, **Gulsoy** lead the students in pound cake-design.

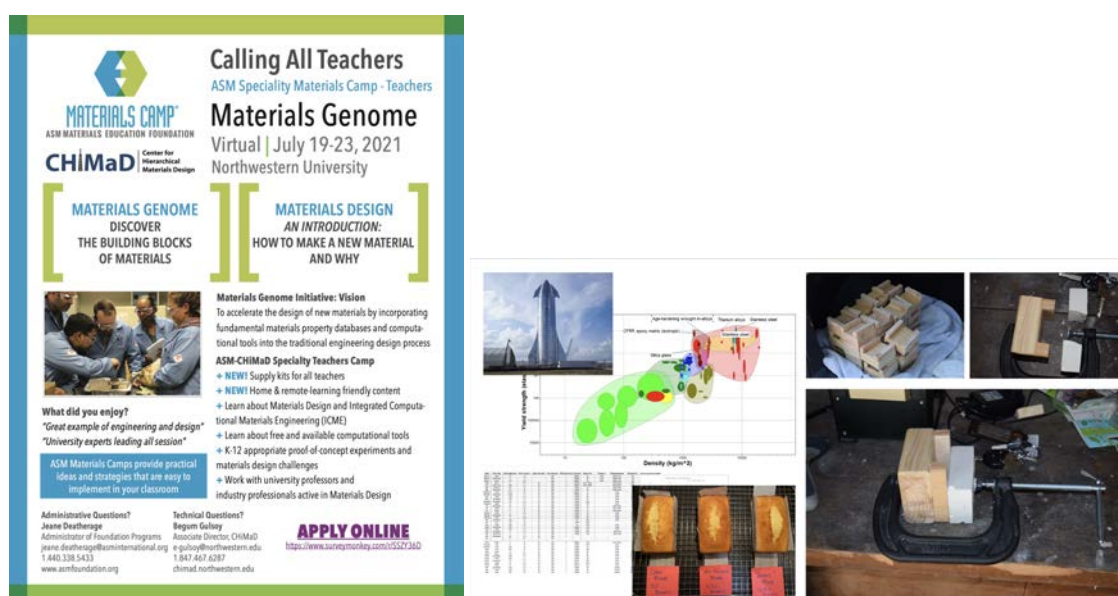


Figure 15.4: (Left) Flyer for the virtual 2021CHiMaD-ASM Materials Genome Camp for K-12 STEM Educators. (Right) Photos representative of Materials Selection, Cake Design and Composite Design Modules.

### 15.2.9 CHiMaD-ASM Materials Genome Camp for K-12 STEM Educators

*Begum Gulsoy (NU), Jonathan Emery (NU), Clay Houser (NU), Manuel Esparragoza (QT/ASM Chicago Chapter), Jacqueline Hardin (QT/ASM Chicago Chapter), Greg Olson (NU), Aziz Asphahani (QT), Carrie Wilson (ASM), Jeane Deatherage (ASM)*

To achieve a higher-impact outreach to high school students as well as underrepresented minorities, CHiMaD has partnered with ASM Materials Education Foundation in 2017 to host the annual CHiMaD-ASM Materials Genome Camp for K-12 STEM Educators, which runs under the umbrella of ASM's Teacher Camps. The camp also provides further workforce education, with undergraduates from the Materials Design course at Northwestern acting as teaching assistants for the duration for the camp.

The summer 2021 Camp was developed as a fully-virtual camp. Towards this, not only the content was modified to be home and remote friendly, but also a supply kit was introduced to the camp and sent to the teacher's preferred addresses. The camp flyer and photos from the content taught are shown in Figure 15.4. Three main modules taught during the 2021camp include:

1. **Materials Selection**, drawing inspiration from industry use-cases such as SpaceX's Star ship as well as familiar objects such as musical instruments.
2. **Cake Design**, following in the spirit of the most popular system design chart, ice-cream, a new module was developed to not only explain system design charts but also introduce concepts of materials data, databases, and data management. Teachers not only got to do the experiments but were able to contribute measurements from their cakes to a class-wide database, which was then used for design discussions. Moreover, the module was supported by a guest presentation by Manuel Esparragoza (QT) on Critical Materials. This concept was strengthened by an analogy to designing gluten-free cakes.
3. **Composite Design**, this is an already-established and popular module, which was modified to be home-friendly/safe. This year, to demonstrate computational materials design, Finite Element Analysis using COMSOL was introduced the design process.

The 2021 Camp concluded with a poster session, where 12 teachers presented posters on class modules that can be inserted into their classrooms using ideas from the camp. Given the range of topics taught and the resources available, this was decided to be the most realistic outcome of the Camp in being able to translate content into real classrooms across U.S. To encourage the actual implementation of the ideas on the teachers' posters, CHiMaD partnered with ASM Chicago Chapter for poster awards. This partnership was spearheaded by Manuel Esperragoza (QT, ASM Chicago Chapter Treasurer) and Jacqueline Hardin (QT, ASM Chicago Chapter Educational Outreach Chair). With a \$10,000 support from the ASM Chicago Chapter, each presenting teacher won \$200 towards the implementation of their ideas. In addition, four grand prizes of \$800 (or a 3D printer) were awarded to posters which best implemented Materials Design into their proposed modules. As a result, CHiMaD and ASM were able to create an impact for 1000+ students across the country, Figure 15.5

CHiMaD - ASM Materials Genome Camp 2021 Posters				
Color indicates answer: majority of my students are low-income or URM				
Color indicates answer: some of my students are low-income or URM				
Color indicates answer: very few of my students are low-income or URM				
Poster #	Name	Affiliation	Title	#Students
1	Pete Carpico	Louisville City (Ohio) School District	Engaging Science Club Members with Material Design	125
2	Jan Cook	Choate Rosemary Hall	Design a Better Superball	30
3	Leonard Friedhof	Aquin Js Sr High School, Freeport, IL	Cast Molding Design	45
4	Patricia Liedes	Powell County High School, Deer Lodge, Montan	Little Green Cookies Challenge	110
5	Maynard Morin	Hingham Public Schools, Hingham, MA	Keep Water Calm	
6	Sara Chen and Eleonor Nulud	Anne Arundel County Public Schools	Sustainable Living Classrooms	140
7	Ania Ossowska	Edmonton School District	Mathematical Expression: Finite Element Analysis	240
8	Rachelle Rasco	Carroll County High School	Designing the Best Chocolate Chip Cookie	120
9	Tiska Rodgers	Hayti High School	Materials Science - Why Do I Need to Learn This?	125
10	Ada Zareba	Webb School of Knoxville, Knoxville, TN	Concrete Barge Design	
11	Katie Spendlow	St. Vrain Valley School District	Concrete Design System Charts	80
12	Priscilla Lumbreras	Granbury High School, Granbury, TX		150

Figure 15.5: List of posters presented and name of presenters.

One example of the CHiMaD composites module in a real classroom is shown in Figure 15.7. Rachelle Rasco of Carroll County High School in Hinsville, VA, whose students are majorly low-income or URM, integrated the CHiMaD composites module to her 2021 class. In another example, Sara Chen and Eleonor Nulud of Anne Arundel Country Public School in Edgewater, MD were able to build concepts sustainability and materials life

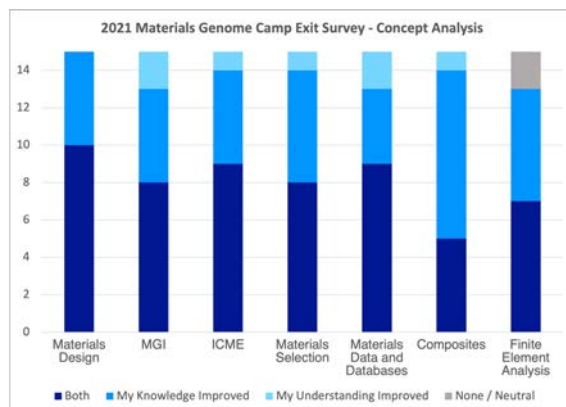


Figure 15.6: Following feedback survey showed a satisfactory outcome of improving the teachers' knowledge and understanding of materials design concepts.

cycles into their sustainable classroom project and competition. **Gulsoy** and Jonathan Emery (NU) were invited to their class presentations as judges.



Figure 15.7: (Left) Students from Carroll County High School working on designing and strengthening their concrete blocks. (Right) Students drop-testing the composite blocks.

### 15.3 Accomplishments: Data Outreach

In 2021 CHiMaD was invited to participate in numerous data meetings led by NSF and RDA. It also led the organization of the Materials Research Data Alliance (MaRDA) 2021 Annual Meeting. In Fall 2021 CHiMaD began joint work based on NIST's open-source automated workflow of experimental data capture and storage, Nexus/LIMS. The joint work involves NIST, CHiMaD, NUANCE, Euclid Labs (Bolinbrook, IL) and NU ORIT and is currently active. CHiMaD data efforts were largely divided into two main areas: 1) Events to which CHiMaD was invited to participate and 2) Events that CHiMaD led: CHiMaD/NIST Office of Data Informatics Monthly Seminar Series.

#### 15.3.1 Data-focused Events to which CHiMaD was invited to participate

- *January 13-15, 2021* [Invited attendance]  
NITRD: Big Data Interagency Working Group Workshop



- *February 21-23, 2021* [CHiMaD Lead Organizer]  
MaRDA 2021 Annual Meeting
- *April 20-22, 2021* [RDA attendee]  
P18 Annual Meeting & Co-Organizer, Mat'ls Data Apr 21, 2021
- *June 28, 2021* [Invited Advisory Board Member]  
OpenKIM NSF Review
- *August 2021 - present*;  
Began monthly meetings on automated workflow for experimental data capture & storage:  
Participants: NIST, NUANCE, Euclid Labs (Bolinbrook, IL) & ORIT
- *September 2021*; [Invited to be Advisory Board Member]  
Materials Open Research, Francis & Taylor

### 15.3.2 CHiMaD/NIST Office of Data Informatics Monthly Seminar Series

In Fall 2021 CHiMaD and NIST Office of Data Informatics sponsored a monthly seminar series which has continued into 2022. Organized by Laura **Bartolo** (CHiMaD) and Chandler **Becker** (NIST), the intent of the seminars was to raise the visibility of database efforts within CHiMaD and NIST and to highlight their efforts to integrate FAIR Data Principles into their databases as encouraged by federal funding agencies. CHiMaD PIs, Postdoctoral researchers, graduate students, industrial partners and NIST collaborators were invited. Seminar surveys indicated that in general more than half the registrants were not familiar with the databases before the presentations and more than 80% were interested in data management best practices. Listed below by date are the 2021 seminar titles, presenters and brief abstracts.

*October 12, 2021* (Attendees: 50)

#### **Implementation of FAIR Data Principles in the OQMD**

Abhijith Gopakumar, (Wolverton Research Group, CHiMaD/Northwestern University)

The Open Quantum Materials Database (OQMD) is an open source database containing computationally generated thermodynamic, structural, and electronic structure data of more than 800,000 materials. This talk will describe the recent implementations of FAIR data principles in OQMD, including the support for OPTIMADE RESTful API data transfer, persistent identifiers for materials via Handles, and the availability of structured data for web search engines to better index the material data.

*November 9, 2021* (Attendees: 50)

#### **The NIST-JARVIS Infrastructure for Materials Design**

Kamal Choudhary; Francesca **Tavazza** (NIST)

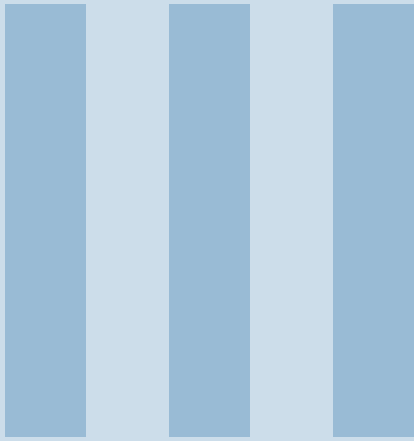
The Joint Automated Repository for Various Integrated Simulations (JARVIS) is an integrated infrastructure to accelerate materials discovery and design using density functional theory (DFT), classical force-fields (FF), and machine learning (ML) techniques. This talk will cover recent updates from the JARVIS platform such as: 1) Atomistic Line Graph Neural Network (ALIGNN) models for solids and molecules, 2) AtomVision models for 2D STM/STEM images, 3) QCMat for quantum computation algorithms for solids, 4) OPTIMADE for data-sharing and 5) UQ ML for uncertainty quantifications.

*December 14, 2021* (Attendees: 60)

**A FAIR Approach towards Fully Realizing the Impact of AI and Machine Learning Materials Science**

Ben **Blaiszik** (University of Chicago)

This talk presents latest results and shows demonstrations of developments from two key projects, 1) The NIST-CHiMaD supported Materials Data Facility (MDF) highlighting advanced publication, discovery, and automation software and services; and 2) Foundry, Python software built on the Materials Data Facility to collect, describe, and serve ML-ready materials science and chemistry datasets, and link these with predictive models.



# Products





## 16. Products

### 16.1 Publications

CHiMaD principle investigators and researchers have presented their CHiMaD-funded work in 103 peer-reviewed journal publications, advanced access articles, proceedings as well as arXiv pre-print articles in 2021. Among these, 12 publications are co-authored by NIST and CHiMaD. In this list we also report 10 which have been published in 2021 as advanced access. In the list below, CHiMaD Principle Investigators are bolded in black, and NIST Investigators are bolded in blue.

1. Marras, AE; Ting, JM; Stevens, KC; **Tirrell**, MV (2021) *Advances in the Structural Design of Polyelectrolyte Complex Micelles* JOURNAL OF PHYSICAL CHEMISTRY B, Vol 125, Is 26, pp.7076-7089, DOI: <https://doi.org/10.1021/acs.jpccb.1c01258>
2. Nguyen, TD; Jimenez-Angeles, F; **de la Cruz**, MO (2021) *Probing the size-dependent polarizability of mesoscopic ionic clusters and their induced-dipole interactions* JOURNAL OF CHEMICAL PHYSICS, Vol 155, Is 19, Ar 194901, DOI: <https://doi.org/10.1063/5.0064267>
3. Peng, J; Grayson, M; **Snyder**, GJ (2021) *Matter of Opinion What makes a material bendable? A thickness-dependent metric for bendability, malleability, ductility* MATTER, Vol 4, Is 9, pp.2694-2696, DOI: <https://doi.org/10.1016/j.matt.2021.07.015>
4. Cox, ME; Schwalbach, EJ; **Blaiszik**, B; Groeber, MA (2021) *AFRL Additive Manufacturing Modeling Challenge Series: Overview* INTEGRATING MATERIALS AND MANUFACTURING INNOVATION, Vol 10, Is 2, pp.125-128, DOI: <https://doi.org/10.1007/s40192-021-00215-6>
5. Anand, S; Male, JP; **Wolverton**, C; **Snyder**, GJ (2021) *Visualizing defect energetics* MATERIALS HORIZONS, Vol 8, Is 7, pp.1966-1975, DOI: <https://doi.org/10.1039/d1mh00397f>
6. Jha, D; Gupta, V; Ward, L; Yang, ZJ; **Wolverton**, C; **Foster**, I; Liao, WK; **Choudhary**, A; **Agrawal**, A (2021) *Enabling deeper learning on big data for materials informatics applications* SCIENTIFIC REPORTS, Vol 11, Is 1, Ar 4244, DOI: <https://doi.org/10.1038/s41598-021-83193-1>

7. Li, L; Rumyantsev, AM; Srivastava, S; Meng, SQ; **de Pablo**, JJ; Tirrell, MV (2021) *Effect of Solvent Quality on the Phase Behavior of Polyelectrolyte Complexes* MACROMOLECULES, Vol 54, Is 1, pp.105-114, DOI: <https://doi.org/10.1021/acs.macromol.0c01000>
8. Gupta, V; **Choudhary**, K; **Tavazza**, F; **Campbell**, C; Liao, WK; **Choudhary**, A; **Agrawal**, A (2021) *Cross-property deep transfer learning framework for enhanced predictive analytics on small materials data* NATURE COMMUNICATIONS, Vol 12, Is 1, Ar 6595, DOI: <https://doi.org/10.1038/s41467-021-26921-5>
9. Ma, BR; **de la Cruz**, MO (2021) *A Perspective on the Design of Ion-Containing Polymers for Polymer Electrolyte Applications* JOURNAL OF PHYSICAL CHEMISTRY B, Vol 125, Is 12, pp.3015-3022, DOI: <https://doi.org/10.1021/acs.jpcc.0c08707>
10. Jha, D; Narayanachari, KVLV; Zhang, RF; Keane, DT; Liao, WK; **Choudhary**, A; Chung, YW; Bedzyk, MJ; **Agrawal**, A (2021) *Enhancing Phase Mapping for High-throughput X-ray Diffraction Experiments using Fuzzy Clustering* PROCEEDINGS OF THE 10TH INTERNATIONAL CONFERENCE ON PATTERN RECOGNITION APPLICATIONS AND METHODS (ICPRAM), pp.507-514, DOI: <https://doi.org/10.5220/0010229905070514>
11. Huang, W; Chen, JH; Wang, G; Yao, Y; Zhuang, XM; Pankow, RM; Cheng, YH; **Marks**, TJ; Facchetti, A (2021) *Dielectric materials for electrolyte gated transistor applications* JOURNAL OF MATERIALS CHEMISTRY C, Vol 9, Is 30, pp.9348-9376, DOI: <https://doi.org/10.1039/d1tc02271g>
12. van Beek, A; Ghumman, UF; Munshi, J; Tao, SY; Chien, TY; Balasubramanian, G; Plumlee, M; Apley, D; **Chen**, W (2021) *Scalable Adaptive Batch Sampling in Simulation-Based Design With Heteroscedastic Noise* JOURNAL OF MECHANICAL DESIGN, Vol 143, Is 3, Ar 31709, DOI: <https://doi.org/10.1115/1.4049134>
13. Li, JJ; Rincon-Delgado, PA; Suh, HS; Mannaert, G; **Nealey**, PF (2021) *Understanding Kinetics of Defect Annihilation in Chemoepitaxy-Directed Self-Assembly* ACS APPLIED MATERIALS & INTERFACES, Vol 13, Is 21, pp.25357-25364, DOI: <https://doi.org/10.1021/acsami.1c03830>
14. Abdellaoui, L; Chen, ZW; Yu, Y; Luo, T; Hanus, R; Schwarz, T; Villoro, RB; Cojocar-Miredin, O; **Snyder**, GJ; Raabe, D; Pei, YZ; Scheu, C; Zhang, SY (2021) *Parallel Dislocation Networks and Cottrell Atmospheres Reduce Thermal Conductivity of PbTe Thermoelectrics* ADVANCED FUNCTIONAL MATERIALS, Vol 31, Is 20, Ar 2101214, DOI: <https://doi.org/10.1002/adfm.202101214>
15. Saha, S; **Kafka**, OL; Lu, Y; Yu, C; **Liu**, WK (2021) *Microscale Structure to Property Prediction for Additively Manufactured IN625 through Advanced Material Model Parameter Identification* INTEGRATING MATERIALS AND MANUFACTURING INNOVATION, Vol 10, Is 2, pp.142-156, DOI: <https://doi.org/10.1007/s40192-021-00208-5>
16. Adekoya, AH; Zhang, YH; Peters, M; Male, J; Chart, Y; Dong, J; Franks, R; Furlong, A; Guo, BH; Agne, MT; **Olson**, G; **Snyder**, GJ (2021) *Iterative design of a high zT thermoelectric material* APPLIED PHYSICS LETTERS, Vol 119, Is 20, Ar 202101, DOI: <https://doi.org/10.1063/5.0069327>
17. Chen, YL; **Shull**, KR (2021) *Processing Polyelectrolyte Complexes with Deep Eutectic Solvents* ACS MACRO LETTERS, Vol 10, Is 10, pp.1243-1247, DOI: <https://doi.org/10.1021/acsmacrolett.1c00494>

18. Duong, TC; **Paulson**, NH; **Stan**, M; Chaudhuri, S (2021) *An efficient approximation of the supercell approach to the calculation of the full phonon spectrum* CALPHAD-COMPUTER COUPLING OF PHASE DIAGRAMS AND THERMOCHEMISTRY, Vol 72, Is ,Ar 102215, DOI: <https://doi.org/10.1016/j.calphad.2020.102215>
19. Gabriel, JJ; **Paulson**, NH; Duong, TC; **Becker**, CA; **Tavazza**, F; **Kattner**, UR; **Stan**, M (2021) *Bayesian automated weighting of aggregated DFT, MD, and experimental data for candidate thermodynamic models of aluminum with uncertainty quantification* MATERIALIA, Vol 20, Ar 101216, DOI: <https://doi.org/10.1016/j.mtla.2021.101216>
20. Huang, TY; Gao, JY; Sun, QP; Zeng, D; Su, XM; Liu, WK; **Chen**, W (2021) *Stochastic nonlinear analysis of unidirectional fiber composites using image-based microstructural uncertainty quantification* COMPOSITE STRUCTURES, Vol 260, Ar 113470, DOI: <https://doi.org/10.1016/j.compstruct.2020.113470>
21. Saha, S; **Kafka**, OL; Lu, Y; Yu, C; **Liu**, WK (2021) *Macroscale Property Prediction for Additively Manufactured IN625 from Microstructure Through Advanced Homogenization* INTEGRATING MATERIALS AND MANUFACTURING INNOVATION, Vol 10, Is 3, pp.360-372, DOI: <https://doi.org/10.1007/s40192-021-00221-8>
22. Marras, AE; Campagna, TR; Vieregge, JR; **Tirrell**, MV (2021) *Physical Property Scaling Relationships for Polyelectrolyte Complex Micelles* MACROMOLECULES, Vol 54, Is 13, pp.6585-6594, DOI: <https://doi.org/10.1021/acs.macromol.1c00743>
23. Na, B; Zhou, BC; **Wolverton**, C; Kim, K (2021) *First-principles Calculations of Bulk and Interfacial Thermodynamic Properties of the T-1 phase in Al-Cu-Li alloys* SCRIPTA MATERIALIA, Vol 202, Ar 114009, DOI: <https://doi.org/10.1016/j.scriptamat.2021.114009>
24. Gurunathan, R; Hanus, R; Graham, S; Garg, A; **Snyder**, GJ (2021) *Thermal resistance at a twist boundary and a semicoherent heterointerface* PHYSICAL REVIEW B, Vol 103, Is 14 ,Ar 144302, DOI: <https://doi.org/10.1103/PhysRevB.103.144302>
25. Bennett, JL; Liao, HG; Buergel, T; Hyatt, G; Ehmann, K; **Cao**, J (2021) *Towards bi-metallic injection molds by directed energy deposition* MANUFACTURING LETTERS, Vol 27, pp.78-81, DOI: <https://doi.org/10.1016/j.mfglet.2021.01.001>
26. Yeom, J; Stan, T; Hong, S; **Voorhees**, PW (2021) *Segmentation of experimental datasets via convolutional neural networks trained on phase field simulations* ACTA MATERIALIA, Vol 214, Is ,Ar 116990, DOI: <https://doi.org/10.1016/j.actamat.2021.116990>
27. Roth, LK; Han, ED; **Jaeger**, HM (2021) *Intrusion into Granular Media Beyond the Quasistatic Regime* PHYSICAL REVIEW LETTERS, Vol 126, Is 21 ,Ar 218001, DOI: <https://doi.org/10.1103/PhysRevLett.126.218001>
28. Bambach, M; Sizova, I; Szyndler, J; Bennett, J; Hyatt, G; **Cao**, J; Papke, T; Merklein, M (2021) *On the hot deformation behavior of Ti-6Al-4V made by additive manufacturing* JOURNAL OF MATERIALS PROCESSING TECHNOLOGY, Vol 288, Is ,Ar 116840, DOI: <https://doi.org/10.1016/j.jmatprotec.2020.116840>
29. Yu, C; **Kafka**, OL; **Liu**, WK (2021) *Multiresolution clustering analysis for efficient modeling of hierarchical material systems* COMPUTATIONAL MECHANICS, Vol 67, Is 5, pp.1293-1306, DOI: <https://doi.org/10.1007/s00466-021-01982-x>

30. Sun, YD; Zhou, YG; Gurunathan, R; Zhang, JY; Hu, M; Liu, W; Xu, B; **Snyder, GJ** (2021) *Phonon scattering in the complex strain field of a dislocation in PbTe* JOURNAL OF MATERIALS CHEMISTRY C, Vol 9, Is 27, pp.8506-+, DOI: <https://doi.org/10.1039/d1tc00902h>
31. Hong, Z; Ward, L; Chard, K; **Blaiszik, B; Foster, I** (2021) *Challenges and Advances in Information Extraction from Scientific Literature: a Review* JOM, Vol 73, Is 11, pp.3383-3400, DOI: <https://doi.org/10.1007/s11837-021-04902-9>
32. Hong, Z; Pauloski, JG; Ward, L; Chard, K; **Blaiszik, B; Foster, I** (2021) *Models and Processes to Extract Drug-like Molecules From Natural Language Text* FRONTIERS IN MOLECULAR BIOSCIENCES, Vol 8, Is ,Ar 636077, DOI: <https://doi.org/10.3389/fmolb.2021.636077>
33. Cardellini, A; Jimenez-Angeles, F; Asinari, P; **de la Cruz, MO** (2021) *A Modeling-Based Design to Engineering Protein Hydrogels with Random Copolymers* ACS NANO, Vol 15, Is 10, pp.16139-16148, DOI: <https://doi.org/10.1021/acsnano.1c04955>
34. **Kafka, OL**; Jones, KK; Yu, C; Cheng, PK; **Liu, WK** (2021) *Image-based multiscale modeling with spatially varying microstructures from experiments: Demonstration with additively manufactured metal in fatigue and fracture* JOURNAL OF THE MECHANICS AND PHYSICS OF SOLIDS, Vol 150, Ar 104350, DOI: <https://doi.org/10.1016/j.jmps.2021.104350>
35. Gan, ZT; Jones, KK; Lu, Y; **Liu, WK** (2021) *Benchmark Study of Melted Track Geometries in Laser Powder Bed Fusion of Inconel 625* INTEGRATING MATERIALS AND MANUFACTURING INNOVATION, Vol 10, Is 2, pp.177-195, DOI: <https://doi.org/10.1007/s40192-021-00209-4>
36. Giuntoli, A; Hansoge, NK; van Beek, A; Meng, ZX; **Chen, W; Ketten, S** (2021) *Systematic coarse-graining of epoxy resins with machine learning-informed energy renormalization* NPJ COMPUTATIONAL MATERIALS, Vol 7, Is 1, Ar 168, DOI: <https://doi.org/10.1038/s41524-021-00634-1>
37. Roth, LK (2021) *ConStant speed penetration into granular materials: drag forces from the quasistatic to inertial regime* GRANULAR MATTER, Vol 23, Is 3, Ar 54, DOI: <https://doi.org/10.1007/s10035-021-01106-5>
38. Imasato, K; Anand, S; Gurunathan, R; **Snyder, GJ** (2021) *The effect of Mg<sub>3</sub>As<sub>2</sub> alloying on the thermoelectric properties of n-type Mg-3(Sb, Bi)(<sub>2</sub>)* DALTON TRANSACTIONS, Vol 50, Is 27, pp.9376-9382, DOI: <https://doi.org/10.1039/d1dt01600h>
39. Eaton, MD; Brinson, LC; **Shull, KR** (2021) *Temperature dependent fracture behavior in model epoxy networks with nanoscale heterogeneity* POLYMER, Vol 221, Is ,Ar 123560, DOI: <https://doi.org/10.1016/j.polymer.2021.123560>
40. Hansoge, NK; Gupta, A; White, H; Giuntoli, A; **Ketten, S** (2021) *Universal Relation for Effective Interaction between Polymer-Grafted Nanoparticles* MACROMOLECULES, Vol 54, Is 7, pp.3052-3064, DOI: <https://doi.org/10.1021/acs.macromol.0c02600>
41. Arai, N; **Stan, T**; Macfarland, S; **Voorhees, PW**; Muyanjan, NS; Shahani, AJ; Faber, KT (2021) *Coarsening of dendrites in solution-based freeze-cast ceramic systems* ACTA MATERIALIA, Vol 215, Is ,Ar 117039, DOI: <https://doi.org/10.1016/j.actamat.2021.117039>
42. Park, H; Choe, H; **Dunand, DC** (2021) *Microstructure and compressive properties of 3D-extrusion-printed, aluminized cobalt-based superalloy microlattices* MATE-



- RIALS SCIENCE AND ENGINEERING A-STRUCTURAL MATERIALS PROPERTIES MICROSTRUCTURE AND PROCESSING, Vol 815, Ar 141262, DOI: <https://doi.org/10.1016/j.msea.2021.141262>
43. Park, CW; Kornbluth, M; Vandermause, J; **Wolverton**, C; Kozinsky, B; Mailoa, JP (2021) *Accurate and scalable graph neural network force field and molecular dynamics with direct force architecture* NPJ COMPUTATIONAL MATERIALS, Vol 7, Is 1 ,Ar 73, DOI: <https://doi.org/10.1038/s41524-021-00543-3>
  44. Eaton, MD; Domene-Lopez, D; Wang, QF; Montalban, MG; Martin-Gullon, I; **Shull**, KR (2021) *Exploring the effect of humidity on thermoplastic starch films using the quartz crystal microbalance* CARBOHYDRATE POLYMERS, Vol 261, Ar 117727, DOI: <https://doi.org/10.1016/j.carbpol.2021.117727>
  45. Neitzel, AE; de Hoe, GX; **Tirrell**, MV (2021) *Expanding the structural diversity of polyelectrolyte complexes and polyzwitterions* CURRENT OPINION IN SOLID STATE & MATERIALS SCIENCE, Vol 25, Is 2 ,Ar 100897, DOI: <https://doi.org/10.1016/j.cossms.2020.100897>
  46. Ozen, M; Yahyaoglu, M; Candolfi, C; Veremchuk, I; Kaiser, F; Burkhardt, U; **Snyder**, GJ; Grin, Y; Aydemir, U (2021) *Enhanced thermoelectric performance in  $Mg_{3+x}Sb_{1.5}Bi_{0.49}Te_{0.01}$  via engineering microstructure through melt-centrifugation* JOURNAL OF MATERIALS CHEMISTRY A, Vol 9, Is 3, pp.1733-1742, DOI: <https://doi.org/10.1039/d0ta09993g>
  47. Hanus, R; Gurunathan, R; Lindsay, L; Agne, MT; Shi, JJ; Graham, S; **Snyder**, GJ (2021) *Thermal transport in defective and disordered materials* APPLIED PHYSICS REVIEWS, Vol 8, Is 3 ,Ar 31311, DOI: <https://doi.org/10.1063/5.0055593>
  48. Sun, YD; Zhou, YG; Hu, M; **Snyder**, GJ; Xu, B; Liu, W (2021) *Probing the phonon mean free paths in dislocation core by molecular dynamics simulation* JOURNAL OF APPLIED PHYSICS, Vol 129, Is 5, Ar 55103, DOI: <https://doi.org/10.1063/5.0038265>
  49. Male, JP; Hanus, R; **Snyder**, GJ; Hermann, RP (2021) *Thermal Evolution of Internal Strain in Doped PbTe* CHEMISTRY OF MATERIALS, Vol 33, Is 12, pp.4765-4772, DOI: <https://doi.org/10.1021/acs.chemmater.1c01335>
  50. Ting, JM (2021) *Safety Moments in Chemical Safety Education* JOURNAL OF CHEMICAL EDUCATION, Vol 98, Is 1, pp.9-14, DOI: <https://doi.org/10.1021/acs.jchemed.0c00220>
  51. Hanus, R; George, J; Wood, M; Bonkowski, A; Cheng, YQ; Abernathy, DL; Manley, ME; Hautier, G; **Snyder**, GJ; Hermann, RE (2021) *Uncovering design principles for amorphous-like heat conduction using two-channel lattice dynamics* MATERIALS TODAY PHYSICS, Vol 18, Ar 100344, DOI: <https://doi.org/10.1016/j.mtphys.2021.100344>
  52. Hanus, R; Rangnekar, SV; Mollah, S; Hussain, K; Hines, N; Heller, E; **Hersam**, MC; Khan, A; Graham, S (2021) *Thermoreflectance Imaging of (Ultra)wide Band-Gap Devices with MoS<sub>2</sub> Enhancement Coatings* ACS APPLIED MATERIALS & INTERFACES, Vol 13, Is 35, pp.42195-42204, DOI: <https://doi.org/10.1021/acsami.1c11528>
  53. Griesemer, SD; Ward, L; **Wolverton**, C (2021) *High-throughput crystal structure solution using prototypes* PHYSICAL REVIEW MATERIALS, Vol 5, Is 10, Ar 105003, DOI: <https://doi.org/10.1103/PhysRevMaterials.5.105003>
  54. Herbert, KM; Dolinski, ND; Boynton, NR; Murphy, JG; Lindberg, CA; **Sibener**, SJ; **Rowan**, SJ (2021) *Controlling the Morphology of Dynamic Thia-Michael Networks*

- to Target Pressure-Sensitive and Hot Melt Adhesives* ACS APPLIED MATERIALS & INTERFACES, Vol 13, Is 23, pp.27471-27480, DOI: <https://doi.org/10.1021/acsami.1c05813>
55. Gan, ZT; **Kafka**, OL; Parab, N; Zhao, C; Fang, LC; **Heinonen**, O; Sun, T; **Liu**, WK (2021) *Universal scaling laws of keyhole stability and porosity in 3D printing of metals* NATURE COMMUNICATIONS, Vol 12, Is 1, Ar 2379, DOI: <https://doi.org/10.1038/s41467-021-22704-0>
  56. Tirado, FLR; **Dunand**, DC (2021) *Increasing gamma ' volume fraction in Co-Nb-V- and Co-Ta-V-based superalloys* JOURNAL OF MATERIALS RESEARCH AND TECHNOLOGY-JMR&T, Vol 11, pp.2305-2313, DOI: <https://doi.org/10.1016/j.jmrt.2021.02.028>
  57. Pal, K; Xia, Y; **Wolverton**, C (2021) *Microscopic mechanism of unusual lattice thermal transport in TlInTe2* NPJ COMPUTATIONAL MATERIALS, Vol 7, Is 1 ,Ar 5, DOI: <https://doi.org/10.1038/s41524-020-00474-5>
  58. Orenstein, R; Male, JP; Toriyama, M; Anand, S; **Snyder**, GJ (2021) *Using phase boundary mapping to resolve discrepancies in the Mg2Si-Mg2Sn miscibility gap* JOURNAL OF MATERIALS CHEMISTRY A, Vol 9, Is 11, pp.7208-7215, DOI: <https://doi.org/10.1039/d1ta00115a>
  59. Lindenmeyer, A; Webster, S; Zaeh, MF; Ehmann, KF; **Cao**, J (2021) *Template-bayesian approach for the evaluation of melt pool shape and dimension of a DED-process from in-situ X-ray images* CIRP ANNALS-MANUFACTURING TECHNOLOGY, Vol 70, Is 1, pp.183-186, DOI: <https://doi.org/10.1016/j.cirp.2021.03.011>
  60. Wood, M; Toriyama, MY; Dugar, S; Male, J; Anand, S; Stevanovic, V; **Snyder**, GJ (2021) *Phase Boundary Mapping of Tin-Doped ZnSb Reveals Thermodynamic Route to High Thermoelectric Efficiency* ADVANCED ENERGY MATERIALS, Vol 11, Is 20 ,Ar 2100181, DOI: <https://doi.org/10.1002/aenm.202100181>
  61. Schneider, L; **de Pablo**, JJ (2021) *Combining Particle-Based Simulations and Machine Learning to UnderStand Defect Kinetics in Thin Films of Symmetric Diblock Copolymers* MACROMOLECULES, Vol 54, Is 21, pp.10074-10085, DOI: <https://doi.org/10.1021/acs.macromol.1c01583>
  62. Luo, T; Kuo, JJ; Griffith, KJ; Imasato, K; Cojocar-Miredin, O; Wuttig, M; Gault, B; Yu, Y; **Snyder**, GJ (2021) *Nb-Mediated Grain Growth and Grain-Boundary Engineering in Mg3Sb2-Based Thermoelectric Materials* ADVANCED FUNCTIONAL MATERIALS, Vol 31, Is 28, Ar 2100258, DOI: <https://doi.org/10.1002/adfm.202100258>
  63. Horwath, JP; **Voorhees**, PW; Stach, EA (2021) *Quantifying Competitive Degradation Processes in Supported Nanocatalyst Systems* NANO LETTERS, Vol 21, Is 12, pp.5324-5329, DOI: <https://doi.org/10.1021/acs.nanolett.1c01516>
  64. Marciel, AB; Srivastava, S; Ting, JM; **Tirrell**, MV (2021) *SAXS methods for investigating macromolecular and self-assembled polyelectrolyte complexes* LIQUID-LIQUID PHASE COEXISTENCE AND MEMBRANELESS ORGANELLES, Vol 646, pp.223-259, DOI: <https://doi.org/10.1016/bs.mie.2020.09.013>
  65. Slade, TJ; Anand, S; Wood, M; Male, JP; Imasato, K; Cheikh, D; Al Malki, MM; Agne, MT; Griffith, KJ; Bux, SK; **Wolverton**, C; Kanatzidis, MG; **Snyder**, GJ (2021) *Charge-carrier-mediated lattice softening contributes to high zT in thermoelectric semiconductors* JOULE, Vol 5, Is 5, pp.1168-1182, DOI: <https://doi.org/10.1016/j.joule.2021.03.009>

66. Pal, K; Xia, Y; Shen, JH; He, JG; Luo, YB; Kanatzidis, MG; **Wolverton, C** (2021) *Accelerated discovery of a large family of quaternary chalcogenides with very low lattice thermal conductivity* NPJ COMPUTATIONAL MATERIALS, Vol 7, Is 1, Ar 82, DOI: <https://doi.org/10.1038/s41524-021-00549-x>
67. Neitzel, AE; Fang, YN; Yu, BY; Romyantsev, AM; **de Pablo, JJ**; **Tirrell, MV** (2021) *Polyelectrolyte Complex Coacervation across a Broad Range of Charge Densities* MACROMOLECULES, Vol 54, Is 14, pp.6878-6890, DOI: <https://doi.org/10.1021/acs.macromol.1c00703>
68. Wang, G; Zhuang, XM; Huang, W; Yu, JS; Zhang, HW; Facchetti, A; **Marks, TJ** (2021) *New Opportunities for High-Performance Source-Gated Transistors Using Unconventional Materials* ADVANCED SCIENCE, Vol 8, Is 20, Ar 2101473, DOI: <https://doi.org/10.1002/advs.202101473>
69. Eckstein, BJ; Melkonyan, FS; Wang, G; Wang, BH; Manley, EF; Fabiano, S; Harbuzaru, A; Ortiz, RP; Chen, LX; Facchetti, A; **Marks, TJ** (2021) *Processable High Electron Mobility pi-Copolymers via Mesoscale Backbone Conformational Ordering* ADVANCED FUNCTIONAL MATERIALS, Vol 31, Is 15, Ar 2009359, DOI: <https://doi.org/10.1002/adfm.202009359>
70. Al-Bahrani, R; Jha, D; Kang, Q; Lee, S; Yang, ZJ; Liao, WK; **Agrawal, A**; Choudhary, A (2021) *SIGRNN: Synthetic Minority InStances Generation in Imbalanced Datasets using a Recurrent Neural Network* PROCEEDINGS OF THE 10TH INTERNATIONAL CONFERENCE ON PATTERN RECOGNITION APPLICATIONS AND METHODS (ICPRAM), pp.349-356, DOI: <https://doi.org/10.5220/0010348103490356>
71. Wu, W; Montiel, D; **Guyer, JE**; **Voorhees, PW**; **Warren, JA**; **Wheeler, D**; Granasy, L; Pusztai, T; **Heinonen, OG** (2021) *Phase field benchmark problems for nucleation* COMPUTATIONAL MATERIALS SCIENCE, Vol 193, Is ,Ar 110371, DOI: <https://doi.org/10.1016/j.commatsci.2021.110371>
72. Romyantsev, AM; Jackson, NE; **de Pablo, JJ** (2021) *Polyelectrolyte Complex Coacervates: Recent Developments and New Frontiers* ANNUAL REVIEW OF CONDENSED MATTER PHYSICS, VOL 12, 2021, Vol 12, pp.155-176, DOI: <https://doi.org/10.1146/annurev-conmatphys-042020-113457>
73. Yu, BY; Romyantsev, AM; Jackson, NE; Liang, HY; Ting, JM; Meng, SQ; **Tirrell, MV**; **de Pablo, JJ** (2021) *Complex coacervation of statistical polyelectrolytes: role of monomer sequences and formation of inhomogeneous coacervates* MOLECULAR SYSTEMS DESIGN & ENGINEERING, Vol 6, Is 10, pp.790-804, DOI: <https://doi.org/10.1039/d1me00076d>
74. Umantsev, AR (2021) *Bifurcation theory of plasticity, damage and failure* MATERIALS TODAY COMMUNICATIONS, Vol 26, Is ,Ar 102121, DOI: <https://doi.org/10.1016/j.mtcomm.2021.102121>
75. Glerum, J; Bennett, J; Ehmann, K; **Cao, J** (2021) *Mechanical properties of hybrid additively manufactured Inconel 718 parts created via thermal control after secondary treatment processes* JOURNAL OF MATERIALS PROCESSING TECHNOLOGY, Vol 291, Is ,Ar 117047, DOI: <https://doi.org/10.1016/j.jmatprotec.2021.117047>
76. **Sunday, DF**; Thelen, JL; Zhou, C; Ren, JX; **Nealey, PF**; **Kline, RJ** (2021) *Buried Structure in Block Copolymer Films Revealed by Soft X-ray Reflectivity* ACS NANO, Vol 15, Is 6, pp.9577-9587, DOI: <https://doi.org/10.1021/acsnano.0c09907>

77. Andersen, CW; Armiento, R; Blokhin, E; Conduit, GJ; Dwaraknath, S; Evans, ML; Fekete, A; Gopakumar, A; Grazulis, S; Merkys, A; Mohamed, F; Oses, C; Pizzi, G; Rignanese, GM; Scheidgen, M; Talirz, L; Toher, C; Winston, D; Aversa, R; Choudhary, K; Colinet, P; Curtarolo, S; Di Stefano, D; Draxl, C; Er, S; Esters, M; Fornari, M; Giantomassi, M; Govoni, M; Hautier, G; Hegde, V; Horton, MK; Huck, P; Huhs, G; Hummelshoj, J; Kariryaa, A; Kozinsky, B; Kumbhar, S; Liu, MH; Marzari, N; Morris, AJ; Mostofi, AA; Persson, KA; Petretto, G; Purcell, T; Ricci, F; Rose, F; Scheffler, M; Speckhard, D; Uhrin, M; Vaitkus, A; Villars, P; Waroquiers, D; **Wolverton**, C; Wu, MC; Yang, XY (2021) *OPTIMADE, an API for exchanging materials data* SCIENTIFIC DATA, Vol 8, Is 1 ,Ar 217, DOI: <https://doi.org/10.1038/s41597-021-00974-z>
78. Wang, BH; Huang, W; Lee, S; Huang, LZ; Wang, Z; Chen, Y; Chen, ZH; Feng, LW; Wang, G; Yokota, T; Someya, T; **Marks**, TJ; Facchetti, A (2021) *Foundry-compatible high-resolution patterning of vertically phase-separated semiconducting films for ultraflexible organic electronics* NATURE COMMUNICATIONS, Vol 12, Is 1 ,Ar 4937, DOI: <https://doi.org/10.1038/s41467-021-25059-8>
79. Ward, L; Dandu, N; **Blaiszik**, B; Narayanan, B; Assary, RS; Redfern, PC; **Foster**, I; Curtiss, LA (2021) *Graph-Based Approaches for Predicting Solvation Energy in Multiple Solvents: Open Datasets and Machine Learning Models* JOURNAL OF PHYSICAL CHEMISTRY A, Vol 125, Is 27, pp.5990-5998, DOI: <https://doi.org/10.1021/acs.jpca.1c01960>
80. Webster, S; Lin, H; Carter, FM; Ehmman, K; **Cao**, J (2021) *Physical mechanisms in hybrid additive manufacturing: A process design framework* JOURNAL OF MATERIALS PROCESSING TECHNOLOGY, Vol 291, Is ,Ar 117048, DOI: <https://doi.org/10.1016/j.jmatprotec.2021.117048>
81. Agne, MT; Lange, FRL; Male, JP; Siegert, KS; Volker, H; Poltorak, C; Poitz, A; Siegrist, T; Maier, S; **Snyder**, GJ; Wuttig, M (2021) *Disorder-induced Anderson-like localization for bidimensional thermoelectrics optimization* MATTER, Vol 4, Is 9, pp.2970+, DOI: <https://doi.org/10.1016/j.matt.2021.07.017>
82. Li, GP; Zhang, XH; Jones, LO; Alzola, JM; Mukherjee, S; Feng, LW; Zhu, WG; Stern, CL; Huang, W; Yu, JS; Sangwan, VK; **DeLongchamp**, DM; Kohlstedt, KL; Wasielewski, MR; **Hersam**, MC; Schatz, GC; Facchetti, A; **Marks**, TJ (2021) *Systematic Merging of Nonfullerene Acceptor pi-Extension and Tetrafluorination Strategies Affords Polymer Solar Cells with >16% Efficiency* JOURNAL OF THE AMERICAN CHEMICAL SOCIETY, Vol 143, Is 16, pp.6123-6139, DOI: <https://doi.org/10.1021/jacs.1c00211>
83. M. D. Garrison, S. G. Wallace, L. C. Baldwin, Z. Guo, L. Kuo, J. E. Estevez, A. L. Briseno, M. C. **Hersam**, and A. J. Baca (2021) *Accelerated decomposition kinetics of ammonium perchlorate via conformal graphene coating* CHEMISTRY OF MATERIALS, Vol 33, Is 24, pp.9608-9617, DOI: <https://doi.org/10.1021/acs.chemmater.1c03100>
84. V. K. Sangwan, J. Kang, D. Lam, J. T. Gish, S. A. Wells, J. Luxa, J. P. Male, G. J. **Snyder**, Z. Sofer, and M. C. **Hersam** (2021) *Intrinsic carrier multiplication in layered Bi<sub>2</sub>O<sub>2</sub>Se avalanche photodiodes with gain bandwidth product exceeding 1 GHz* NANO RESEARCH, Vol 14, pp.1961-1966, DOI: <https://doi.org/10.1007/s12274-020-3059-3>
85. Mozaffar M., Liao S., Lin H., Ehmman K., **Cao** J. (2021) *Geometry-agnostic data-driven thermal modeling of additive manufacturing processes using graph neural*

- networks* ADDITIVE MANUFACTURING, Vol 48, PART B, Ar 102449, DOI: <https://doi.org/10.1016/j.addma.2021.102449>.
86. Yang Z. et al. (2021) Heterogeneous Feature Fusion Based Machine Learning on Shallow-Wide and Heterogeneous-Sparse Industrial Datasets. In: Del Bimbo A. et al. (eds) Pattern Recognition. ICPR International Workshops and Challenges. ICPR 2021. Lecture Notes in Computer Science, vol 12664. Springer, Cham. DOI: [https://doi.org/10.1007/978-3-030-68799-1\\_41](https://doi.org/10.1007/978-3-030-68799-1_41)
87. Ward, L., Babinec, S., Dufek, E.J., Howey, D.A., Viswanathan, V., Aykol, M., David A.C., Beck et al. (2021) *Principles of the Battery Data Genome* arXiv Preprint, DOI: <https://doi.org/10.2109.07278>
88. A. R. Naik, Y. Zhou, A. A. Dey, D. L. Gonzalez Arellano, U. Okoroanyanwu, E. B. Secor, M. C. **Hersam**, J. Morse, J. P. Rothstein, K. R. Carter, and J. J. Watkins (2022) *Printed microfluidic sweat sensing platform for cortisol and glucose detection* LAB ON A CHIP, Vol 22, Is 156, DOI: <https://doi.org/10.1039/D1LC00633A>
89. He, J., Xia, Y., Lin, W., Pal, K., Zhu, Y., Kanatzidis, M. G., and **Wolverton**, C. (2022) *Accelerated Discovery and Design of Ultralow Lattice Thermal Conductivity Materials Using Chemical Bonding Principles* ADVANCED FUNCTIONAL MATERIALS, Vol 34, Is 2, pp.1289-1301, DOI: <https://doi.org/10.1002/adfm.202108532>
90. Mozaffar, M., Liao, S.H., Xie, X.Y., Saha, S., Park, C., **Cao**, J. **Liu**, W.K. and Gan, Z. (2022) *Mechanistic Artificial Intelligence (Mechanistic-AI) for Modeling, Design, and Control of Advanced Manufacturing Processes: Current State and Perspectives* J. MATERIALS PROCESSING TECHNOLOGY DOI: <https://doi.org/10.1016/j.jmatprotec.2021.117485>
91. **Chen**, W., Iyer, A., and Bostanabad, R. (2022) *Data-Centric Design of Microstructural Materials Systems* ENGINEERING IN PRESS., DOI: <https://doi.org/10.1016/j.eng.2021.05.022>
92. Da, D., Chan Y.C., Wang, L, and **Chen**, W. (2022) *Data-driven and topological design of structural metamaterials for fracture resistance* EXTREME MECHANICS LETTERS, Vol 50, Ar 101528, DOI: <https://doi.org/10.1016/j.eml.2021.101528>
93. Lee, S., Kang, Q., Al-Bahrani, R., **Agrawal**, A., **Choudhary**, A., and Liao, W., (2022) *Improving scalability of parallel CNN training by adaptively adjusting parameter update frequency* Journal of Parallel and Distributed Computing, Vol 159, pp.10-23, DOI: <https://doi.org/10.1016/j.jpdc.2021.09.005>
94. Reyes-Martinez, M.A., **Chan**, E.P., **Soles**, C.L. , Han, E. , Murphy, K. A., **Jaeger**, H.M., Reid, D.R., and **de Pablo** J. J. (2022) *Tuning the mechanical impedance of disordered networks for impact mitigation* SOFT MATTER, Vol 10 DOI: <https://doi.org/10.1039/d1sm01649k>
95. Clyde, A., Galanie, S., Kneller, D.W., Ma, H., Babuji, Y., **Blaiszik**, B., Brace A. et al. (2022) *High-Throughput Virtual Screening and Validation of a SARS-CoV-2 Main Protease Noncovalent Inhibitor*. Journal of chemical information and modeling, Vol 62, Is 1, pp.116-128, DOI: <https://doi.org/10.1021/acs.jcim.1c00851>
96. Zeng, MX; Zavanelli, D; Chen, JH; Saeidi-Javash, M; Du, YP; LeBlanc, S; **Snyder**, GJ; Zhang, YL (2022) *Printing thermoelectric inks toward next-generation energy and thermal devices* CHEMICAL SOCIETY REVIEWS, Vol 51, pp.485-512, DOI: <https://doi.org/10.1039/d1cs00490e>
97. Murphy, JG; Raybin, JG; **Sibener**, SJ (2021) *Correlating polymer structure, dynamics, and function with atomic force microscopy* JOURNAL OF POLYMER

- SCIENCE, DOI: <https://doi.org/10.1002/pol.20210321>
98. Moore, DC; Jawaid, A; Busch, R; Brothers, M; Miesle, P; Miesle, A; Rao, R; Lee, J; Beagle, LK; Motala, M; Wallace, SG; Downing, JR; Roy, A; Muratore, C; **Hersam**, MC; Vaia, R; Kim, S; Glavin, NR (2022) *Ultrasensitive Molecular Sensors Based on Real-Time Impedance Spectroscopy in Solution-Processed 2D Materials* ADVANCED FUNCTIONAL MATERIALS, Vol 32, Is 12, Ar 2106830, DOI: <https://doi.org/10.1002/adfm.202106830>
  99. Sangwan, VK; Rangnekar, SV; Kang, J; Shen, JN; Lee, HS; Lam, D; Shen, JH; Liu, XL; de Moraes, ACM; Kuo, LD; Gu, J; Wang, HH; **Hersam**, MC (2021) *Visualizing Thermally Activated Memristive Switching in Percolating Networks of Solution-Processed 2D Semiconductors* ADVANCED FUNCTIONAL MATERIALS, Vol 31, Is 52, Ar 2107385, DOI: <https://doi.org/10.1002/adfm.202107385>
  100. Male, JP; Abdellaoui, L; Yu, Y; Zhang, SY; Pieczulewski, N; Cojocar-Miredin, O; Scheu, C; **Snyder**, GJ (2021) *Dislocations Stabilized by Point Defects Increase Brittleness in PbTe* ADVANCED FUNCTIONAL MATERIALS, Vol 31, Is 52, Ar 2108006, DOI: <https://doi.org/10.1002/adfm.202108006>
  101. Zhang, XH; Li, GP; Mukherjee, S; Huang, W; Zheng, D; Feng, LW; Chen, Y; Wu, JL; Sangwan, VK; **Hersam**, MC; **DeLongchamp**, DM; Yu, JS; Facchetti, A; **Marks**, TJ (2021) *Systematically Controlling Acceptor Fluorination Optimizes Hierarchical Morphology, Vertical Phase Separation, and Efficiency in Non-Fullerene Organic Solar Cells* ADVANCED ENERGY MATERIALS, Vol 12, Is 1, Ar 2102172, DOI: <https://doi.org/10.1002/aenm.202102172>
  102. Li, X-G., **Blaiszik**, B., Schwarting, M.E., Jacobs, R., Scourtas, A., Schmidt, K. J., Voyles, P.M., and Morgan, D. (2021) *Graph network based deep learning of bandgaps*, JOURNAL OF CHEMICAL PHYSICS, Vol. 155, no. 15: 154702., DOI: <https://doi.org/10.1063/5.0066009>
  103. Wei, J., **Blaiszik**, B., Morgan, D., and, Voyles P. (2021), *Benchmark tests of atom-locating CNN models with a consistent dataset*, MICROSCOPY AND MICRO-ANALYSIS, Vol. 27, No. S1, pp.2518-2520, DOI: <https://doi.org/10.1017/S1431927621008989>

## 16.2 Presentations

CHiMaD principle investigators and researchers have presented their CHiMaD-funded work in 126 presentations in 2021. In addition, some groups, such as Phase Field Methods, UQPET, have organized CHiMaD focus workshops in their areas; detailed information on these events can be found under the Outreach chapter.

1. Zhehao Zhu, Joon-Seok Kim, Michael Moody, and Lincoln J. **Lauhon**, Towards the rational design of printed 2D materials, 63rd EMC Meeting, June 2021, Virtual Oral Presentation
2. G. B. **Olson**, “Genomic Materials Design: From CALPHAD to Flight,” MRSEC Colloquium, UC-Irvine, 2/12/21 (virtual)
3. G. B. **Olson**, “Computational Materials Design: Affordable Change,” Alternative Materials Workshop, Boston University, 2/17/21 (virtual)
4. G. B. **Olson**, “Genomic Computational Design: Materials for Sustainability,” TMS Annual Meeting, 3/15/21 (virtual)
5. G. B. **Olson**, “Genomic Materials Design: From CALPHAD Data to Flight,” Hume-Rothery Symposium, TMS Annual Meeting, 3/15/21 (virtual)

6. G. B. **Olson**, “Concurrent Design of a Multimaterial Niobium Alloy System for Next-generation Turbine Applications,” ARPA-E ULTIMATE Program Kickoff, 3/19/21 (virtual)
7. G. B. **Olson**, “Genomic Materials Design: From CALPHAD to Flight,” U. Pittsburgh, 3-22-21 (virtual)
8. G. B. **Olson**, “HSLA150 Design,” DoD Steel Performance Initiative Meeting, 3/31/21 (virtual)
9. G. B. **Olson**, “HSLA150 Design,” Navy FCS Seminar, Naval Surface Warfare Center Carderock Division, 4/8/21 (virtual)
10. G. B. **Olson**, “Genomic Materials Design: From CALPHAD to Flight,” MIT DMSE 3.020 Thermodynamics class Guest lecture, 4/28/21(virtual)
11. G. B. **Olson**, “Biological Martensitic Transformations,” MIT DMSE Faculty Lunch Talk, 5-14-21 (virtual)
12. G. B. **Olson**, “Genomic Materials Design: CALculated PHase Dynamics,” CALPHAD’21, 6/17/21 (virtual)
13. G. B. **Olson**, “Genomic Materials Design: Present & Future,” ASM Materials Genome Teachers Camp, 7/23/21 (virtual)
14. G. B. **Olson**, “Materials Genome Advances,” Materials Genome Engineering Center Advisory Meeting, USTB Beijing 9/23/21 (virtual)
15. G. B. **Olson**, “Materials Design Overview,” SRG Design Consortium Annual Meeting, 10/5/21 (virtual)
16. G. B. **Olson**, “Designing Materials Design,” Sir H.K.D.H. Bhadeshia Retirement Symposium, U. Cambridge, 11/11/21 (virtual)
17. G. B. **Olson**, “State of the Genome,” NSF DMREF Review Panel, 11/17/21 (virtual)
18. Saha, S., Gan, Z., Xie, X., **Liu**, W. K., Exploring Machine Learning Techniques to Obtain Salient Relationship between Thermal History and Mechanical Properties of Additively Manufactured IN718, 14th WCCM and Ecomas Congress, Paris, France, 11-15 January, 2021.
19. Saha, S., Lu, Y., **Liu**, W. K., Advanced Identification of Material Law for Micro- and Macro-deformation of Additively Manufactured Alloys, USNCCM16, Chicago, IL, USA, 25-29 July, 2021.
20. Saha, S., Gan, Z., Xie, X., **Liu**, W. K., Mechanistic Wavelet-based Deep Learning (MWDL) for Virtual Experimentation and Classification, MMLDT-CSET, San Diego, CA, USA, 26-29 Sep, 2021
21. Xie, X., Gan, Z., Saha, S., **Liu**, W. K., Mechanistic digital twin of metal additive manufacturing, MMLDT-CSET, San Diego, CA, USA, 26-29 Sep, 2021.
22. Xie, X., Gan, Z., **Liu**, W. K., DimensionNet: A Deep Learning Network for Discovering Dimensionless Numbers, USNCCM16, Chicago, IL, USA, 25-29 July, 2021.
23. Lu, Y., Jones, K., Gan, Z., **Liu**, W. K., Efficient hyper-reduced order model for additive manufacturing thermal fluid analysis, USNCCM16, Chicago, IL, USA, 25-29 July, 2021.
24. Lu, Y., Cheng, L., **Liu**, W. K., CNN enhanced hyper-reduced order model for additive manufacturing thermal fluid analysis, MMLDT-CSET, San Diego, CA, USA, 26-29 Sep, 2021
25. S. Liao, S. Webster, K. Ehmann, J. **Cao**, “Simulation-guided Melt Pool Control in Directed Energy Deposition”, ASTM-ICAM 2021, November 1, 2021, California, USA

26. W. Tso, C. Liu, D. **Seidman**, and G. **Olson**, Computational Design of high-temperature, creep-resistant, printable, Co-based superalloys, 37th Steel Research Group Annual Meeting, October 5, 2021, Virtual
27. W. Tso, W. Wu, D. **Seidman**, O. **Heinonen**, Machine learning aided phase-field sensitivity analysis, CHiMaD Phase Field Methods XII, November 3, 2021, Virtual
28. A. Adekoya, W. Tso, H. Zhang, W. **Chen**, D. **Seidman**, J. **Snyder**, Predicting finite temperature formation energies of multicomponent phases using physics-informed data-driven modeling, PSED-510 course, December 10, 2021, Northwestern University, Evanston, IL
29. S. **Keten**, Ideas for Creating Impact Resistant Polymeric Materials by Tuning Molecular Topology, UCSD, 2021 (Invited Virtual Seminar)
30. S. **Keten**, Ideas for Creating Impact Resistant Polymeric Materials by Tuning Molecular Topology, Bogazici University, 2021 (Invited Virtual Seminar)
31. S. **Keten**, Ideas for Creating Impact Resistant Polymeric Materials by Tuning Molecular Topology, Stevens Institute of Technology, 2021 (Invited Virtual Seminar)
32. S. **Keten**, Ideas for Creating Impact Resistant Polymeric Materials by Tuning Molecular Topology, UT San Antonio, 2021 (Invited Virtual Seminar)
33. S. **Keten**, Ideas for Creating Impact Resistant Polymeric Materials by Tuning Molecular Topology, APS March Meeting, Virtual, 2021. (Invited Talk)
34. W. **Chen**, “Adaptive Discovery and Mixed-Variable Optimization of Next Generation Synthesizable Microelectronic Materials”, Conference Keynote, 5th Forum of Materials Genome Engineering, Zhen Zhou, China, Dec 14, 2021.
35. W. **Chen**, “Computational Design of Multifunctional Materials and Structures”, Panelist, National Academy Workshops on Convergent Manufacturing, Panel on Multifunctional Materials Design, November 15, 2021.
36. W. **Chen**, “Interdisciplinary Data-driven Design of Engineered Materials Systems”, Conference Keynote, 4th National Conference on Multidisciplinary Design, Analysis, & Optimization (NCMDAO), October 9th, 2021, India.
37. W. **Chen**, “Data-Driven Design of Engineered Materials Systems: From Nano- to Metamaterials”, Conference Plenary Speaker, International Conference of Mechanical Design & the 19th Mechanical Design Annual Conference (ICMD2021), August 12, 2021, Changsha, China.
38. W. **Chen**, “Data-Driven Design of Engineered Materials Systems: Challenges and Opportunities”, Conference Plenary Speaker, 16th U.S. National Congress on Computational Mechanics (USCCM), July 26, 2021, Chicago USA.
39. W. **Chen**, “Data-Driven Design of Engineered Materials Systems”, Keynote Speaker, KTH Solid Mechanics seminar series, May 20, 2021.
40. W. **Chen**, “Data-Driven Design of Microstructural Material Systems”, Invited Speaker, Data Science for Materials Discovery, I-AIM Seminar Series, Feb 19, 2021.
41. W. **Chen**, “Data-Centric Mixed Variable Bayesian Optimization for Materials Design”, Invited Speaker, American Physical Society March Meeting 2021.
42. W. **Chen**, “Multiscale and Multidimensional Quantification and Propagation of Manufacturing Induced Uncertainty”, Invited Keynote Speaker, 2021 AIAA Non-Deterministic Approaches (NDA) Conference, January 11, 2021.
43. W. **Chen**, “Data-Driven Design of Microstructural Materials Systems”, Department Seminar, Materials Science and Engineering, Carnegie Mellon University, November 12, 2021.



44. W. **Chen**, “Data-Driven Design of Engineered Materials Systems”, Distinguished Seminar, Engineering, co-sponsored by Engineering Design and Convergence Center for Living Multifunctional Material Systems, Penn State, November 8, 2021.
45. W. **Chen**, “Data-Driven Design of Engineered Materials Systems”, Department Seminar, Mechanical and Aerospace Engineering, Case Western University, May 4, 2021.
46. W. **Chen**, “Data-Driven Design of Engineered Materials Systems”, MAE Distinguished Scholar Lecture, Arizona State University, April 9, 2021.
47. D. Da., W. **Chen**, “Data-driven and Topological Design of Structural Metamaterials for Fracture Resistance”, the 16th U.S. National Congress on Computational Mechanics (USNCCM), a virtual conference held at Chicago, USA, 25 – 29 July 2021.
48. D. Da., W. **Chen**, “Tailoring fracture properties of brittle structural materials”, the 14th World Congress of Structural and Multidisciplinary Optimization (WCSMO-14), 13 – 18 June 2021.
49. D. Da., W. **Chen**, “Data-driven and Topological Design of Structural Metamaterials for Fracture Resistance”, WebCongress on Metamaterials organized by the International Association of Advanced Materials (IAAM), Invited Speaker, 25 – 26 February 2021.
50. A. van Beek, A. Giuntoli, N Hansogi, S. **Keten**, and W. **Chen**, (May-2021) Uncertainty Quantification in Functional Model Calibration: An Application in Coarse-Grained Epoxy Models. SIAM Conference on Mathematical Aspects of Materials Science. Virtual. Bilbao, Spain.
51. A. **Choudhary** (Invited), “AI for Science and Science of AI”, Nanocombinatorics Workshop on Science of AI, August 19, 2021, Virtual.
52. A. **Agrawal** (Invited), “Artificial Intelligence and High-Performance Data Mining for Accelerating Scientific Discovery”, US Army DEVCOM CBC Seminar on AI/ML Applications, November 10, 2021, Virtual.
53. A. **Agrawal** (Invited), “Introduction to Machine Learning and Deep Learning for Materials Science”, TMS Online Course: Artificial Intelligence in Materials Science and Engineering, November 02, 2021, Virtual.
54. A. **Agrawal** (Invited), “Artificial Intelligence and High-Performance Data Mining for Accelerating Scientific Discovery”, BiGmax Summer School on Harnessing Big Data in Materials Science from Theory to Experiment, September 15, 2021, Max Plank Institute, Germany (Virtual).
55. A. **Agrawal** (Invited), “AI for Accelerating Materials Discovery and Design”, Nanocombinatorics Workshop on Science of AI, August 19, 2021, Virtual.
56. A. **Agrawal** (Invited), “Artificial Intelligence and High-Performance Data Mining for Accelerating Scientific Discovery”, ULTRA DOE-EFRC Seminar, June 28, 2021, Virtual.
57. A. **Agrawal** (Invited), “Artificial Intelligence and High-Performance Data Mining for Accelerating Scientific Discovery”, NSF Workshop on Accelerating Materials Discovery, Design, and Synthesis: A Grand Challenge for Artificial Intelligence (AIMS): AI Panel, April 09, 2021, Virtual.
58. A. **Agrawal** (Invited), “Deep Materials Informatics: Illustrative Applications of Deep Learning in Materials Science”, TMS Webinar Series: Artificial Intelligence in Materials: Research, Design, and Manufacturing, February 04, 2021, Virtual.

59. A. **Agrawal** (Keynote), “Artificial Intelligence and High-Performance Data Mining for Accelerating Scientific Discovery”, 11th International Conference on Cloud Computing, Data Science & Engineering (CONFLUENCE) 2021, January 29, 2021, Virtual.
60. A. **Agrawal** (Invited), “AI and High-Performance Data Mining: Illustrative Applications in Materials Science”, Indian Symposium on Machine Learning (IndoML), December 16, 2020, Virtual.
61. D. Jha, K. V. L. V. Narayanachari, R. Zhang, D. T. Keane, W. Liao, A. **Choudhary**, Y.-W. Chung, M. J. Bedzyk, and A. **Agrawal**, “Enhancing Phase Mapping for High-throughput X-ray Diffraction Experiments using Fuzzy Clustering,” International Conference on Pattern Recognition Applications and Methods (ICPRAM), February 2021.
62. Z. Yang, T. Watari, D. Ichigozaki, A. Mitsutoshi, H. Takahashi, Y. Suga, W. Liao, A. **Choudhary**, and A. **Agrawal**, “Heterogeneous feature fusion based machine learning on shallow-wide and heterogeneous-sparse industrial datasets,” ICPR Workshop on Industrial Machine Learning (IML), January 2021.
63. W. Loo, H. Feng, R. Ruiz, P. **Nealey**, Fine Tuning the Interaction Parameter for Sub-10 nm Block Copolymer Directed Self-Assembly, American Institute of Chemical Engineers Annual Meeting, Nov 2021, Boston MA.
64. H. Feng, Facile Control of block surface energy via clickable modification of polystyrene-block-polybutadiene enabling topcoat-free directed self-assembly with thermal annealing, American Chemical Society Fall Meeting, Aug 2021, Virtual Format.
65. W. Loo, C. Zhu, C. Wang, High Throughput and in-situ Scattering Experiments at the ALS, Advanced Light Source User Meeting, Aug 2021, Virtual Format.
66. W. Loo, H. Feng, D. **Sunday**, P. **Nealey**, Determining Lamellar Structure with Soft X-ray Reflectivity, American Physical Society March Meeting, March 2021, Virtual Format.
67. D. **Sunday**, J. Thelen, C. Zhou, J. Ren, R.J. **Kline**, P. **Nealey**, Probing Buried Interfaces in Polymers with Soft X-ray reflectivity, American Physical Society March Meeting, Mar 2021, Virtual Format.
68. Y. Dahal, H. Feng, J. **de Pablo**, P. **Nealey**, R.J. **Kline**, D. **Audus**, Designing A-b-(B-r-C) copolymers for lithographic applications, American Physical Society March Meeting, Mar 2021, Virtual Format.
69. N.D. Dolinski, K.M. Herbert, S.J. **Rowan** "Highly tunable, catalyst-free dynamic covalent bonds and their incorporation into networks" ACS National Meeting, Atlanta, GA August, 2021.
70. C. Chen, M. van de Naald, A. Singh, J. Jureller, S. **Rowan** "Impact of glass transition temperature on the shear jamming of polymeric particle suspensions" ACS National Meeting, Atlanta, GA August, 2021.
71. G.L. Jackson, J.M. Dennis, N. Dolinski, C. Eom, S. **Rowan**, H. **Jaeger**; “Designing Stress-adaptive Dense Suspensions using Dynamic Covalent Chemistry.” 2021 APS National March Meeting (Abstract J04.00009), March 16, 2021, virtual
72. G.L. Jackson, J.M. Dennis, N. Dolinski, C. Eom, S. **Rowan**, H. **Jaeger**; “Designing Stress-adaptive Dense Suspensions using Dynamic Covalent Chemistry.”, Pfizer Chemistry Connect, November 9, 2021, virtual
73. A. Singh; “Shear Thickening in Dense Suspensions: The Constraints and a Master Curve” UIC Chemical Engineering Seminar, UIC, IL, USA (virtual) January 2021. (Invited)

74. A. Singh; “Macroscopic response as a lens to particle properties in dense suspensions” STMS Virtual Seminar Series 2022. (Invited)
75. A. Singh; “Dynamics of Complex Fluids and Soft Materials” AIChE Annual Meeting, Boston (MA) November 2021.
76. A. Singh, J.J. **de Pablo**, H.M. **Jaeger**; “Shear thickening: A transition from unconstrained to the constrained state” SOR Meeting, Bangor (ME) October 2021.
77. A. Singh, G.L. Jackson, M. Van der Naald, J.J. **de Pablo**, H.M. **Jaeger**; “Quantifying the influence of rolling friction on force networks and rheology in sheared suspensions” APS March Meeting, (Virtual) March 2021.
78. P. **Voorhees**, The Materials Genome Initiative and Additively Manufactured Metals: New Computational Tools and the Central Role of Materials, SOLID research group, Danish Technical University, virtual, 2/21.
79. P. **Voorhees**, Towards Rapid Throughout Measurement of Grain Boundary Properties, Institute for Mathematical and Statistical Innovation, University of Chicago, virtual, 2/21.
80. P. **Voorhees**, Grain Growth in Polycrystals, Metallurgy and Materials Society of the Canadian Institute of Metals. Virtual 6/21.
81. R. Gurunathan et al. Modeling Thermoelectric Properties in a Multicomponent Alloy Space. Virtual Conference on Thermoelectrics 2021.
82. J. Male et al. Thermal Evolution of Internal Strain in Doped PbTe. Virtual Conference on Thermoelectrics 2021.
83. R. Gurunathan et al. Modeling Thermoelectric Properties in a Multicomponent Alloy Space. MRS Fall Meeting 2021.
84. R. Gurunathan et al. Engineering Thermal Conductivity in Thermoelectric Materials. MRS Fall Meeting 2021.
85. J. Male et al. Dislocations Stabilized by Point Defects Increase Brittleness in PbTe. MRS Fall Meeting 2021.
86. M. C. **Hersam** (Keynote), “Mixed-dimensional heterostructures for electronic and energy technologies,” presented orally by M. C. Hersam at the University of Chicago Materials Research Science and Engineering Center Annual Symposium, Chicago, Illinois (12/7/21).
87. M. C. **Hersam** (Invited), “Mixed-dimensional heterostructures for electronic and energy technologies,” presented orally by M. C. Hersam at the Boston College Physics Colloquium, Boston, Massachusetts (12/1/21).
88. M. C. **Hersam** (Invited), “Design and applications of printable two-dimensional material inks,” presented orally by M. C. Hersam at the Materials Research Society Fall Meeting, Boston, Massachusetts (12/1/21).
89. M. C. **Hersam** (Invited), “Realizing biomimetic neuromorphic functionality with two-dimensional material electronic devices,” presented orally by M. C. Hersam at the Materials Research Society Fall Meeting, Boston, Massachusetts (11/30/21).
90. M. C. **Hersam** (Invited), “Two-dimensional neuromorphic computing materials and devices,” presented orally and virtually by M. C. Hersam at the 11th International Symposium of the Gunma University Initiative for Advanced Research, hosted in Gunma, Japan (11/23/21).
91. M. C. **Hersam** (Invited), “Chemically tailored two-dimensional materials for electronic and energy technologies,” presented orally and virtually by M. C. Hersam at the Imperial College London Department of Chemistry Seminar Series, hosted in London, England (11/18/21).

92. M. C. **Hersam** (Invited), “Chemically tailored two-dimensional materials for electronic and energy technologies,” presented orally and virtually by M. C. Hersam at the 2nd KAIST Emerging Materials e-Symposium, hosted in Daejeon, Korea (11/18/21).
93. M. C. **Hersam** (Invited), “Chemically tailoring interfaces in two-dimensional heterostructures,” presented orally and virtually by M. C. Hersam at the AVS 67th International Symposium, hosted in Charlotte, North Carolina (10/25/21).
94. M. C. **Hersam** (Keynote), “Chemically tailored two-dimensional materials for electronic and energy technologies,” presented orally and virtually by M. C. Hersam at the Beijing Graphene Forum, hosted in Beijing, China (10/24/21).
95. M. C. **Hersam** (Invited), “Chemically tailored two-dimensional materials for electronic and energy technologies,” presented orally and virtually by M. C. Hersam at the King Fahad University Materials Science and Engineering Colloquium, hosted in Dhahran, Saudi Arabia (10/7/21).
96. M. C. **Hersam**, “Mixed-dimensional heterostructures for electronic and energy technologies,” presented orally and virtually by M. C. Hersam at the Center for Integrated Nanotechnologies Annual Meeting, hosted in Los Alamos, New Mexico (9/22/21).
97. M. C. **Hersam** (Plenary), “Two-dimensional materials as a platform for mixed-dimensional heterostructures,” presented orally and virtually by M. C. Hersam at the Global Summit on Graphene and 2D Materials: 2DMAT2021, hosted in Paris, France (8/25/21).
98. M. C. **Hersam** (Invited, AAAFM STODDART Award) M. C. Hersam, “Chemically tailored 2D materials for electronic and energy technologies,” presented orally and virtually by M. C. Hersam at the AAAFM-UCLA International Conference on Advances in Functional Materials, hosted in Los Angeles, California (8/19/21).
99. M. C. **Hersam** (Invited), “Mixed-dimensional heterostructures for electronic and energy technologies,” presented orally and virtually by M. C. Hersam at the Tsinghua University Xuetao Lecture Series, hosted in Beijing, China (7/14/21).
100. M. C. **Hersam** (Plenary), “Mixed-dimensional heterostructures for electronic and energy technologies,” presented orally and virtually by M. C. Hersam at the International Conference on Advanced Materials for Better Tomorrow, hosted in Varanasi, India (7/13/21).
101. M. C. **Hersam** (Invited), “Chemically tailored two-dimensional materials for electronic and energy technologies,” presented orally and virtually by M. C. Hersam at the Hybrid Inorganic/Organic Systems Collaborative Research Centre Colloquium, hosted in Berlin, Germany (6/17/21).
102. M. C. **Hersam** (Invited), “Fundamentals and applications of hexagonal boron nitride ionogels,” presented orally and virtually by M. C. Hersam at the 239th Electrochemical Society Meeting, hosted in Chicago, Illinois (6/3/21).
103. M. C. **Hersam** (Keynote), “Chemically tailored two-dimensional materials for electronic and energy technologies,” presented orally and virtually by M. C. Hersam at the Sigma-Aldrich Materials Science Midwest Symposium, hosted in St. Louis, Missouri (5/13/21).
104. M. C. **Hersam** (Invited), “Chemically tailoring interfaces in two-dimensional heterostructures,” presented orally and virtually by M. C. Hersam at the Materials Research Society Spring Meeting 2021, hosted in Phoenix, Arizona (4/18/21).

105. M. C. **Hersam** (Invited), “Gate-tunable neuromorphic devices enabled by low-dimensional materials,” presented orally and virtually by M. C. Hersam at the TMS Annual Meeting, hosted in Orlando, Florida (3/16/21).
106. M. C. **Hersam** (Invited), “Fundamentals and applications of mixed-dimensional heterostructures,” presented orally and virtually by M. C. Hersam at the New York University Chemical and Biomolecular Engineering Colloquium Series, hosted in New York, New York (3/5/21).
107. M. C. **Hersam** (Keynote), “Chemically tailored two-dimensional materials for electronic and energy technologies,” presented orally and virtually by M. C. Hersam at the International Conference on Recent Trends in 2D Nanomaterials, hosted in Mumbai, India (2/24/21).
108. M. C. **Hersam** (Invited), “Fundamentals and applications of mixed-dimensional heterostructures,” presented orally and virtually by M. C. Hersam at the University of Illinois Materials Science and Engineering Colloquium Series, hosted in Urbana, Illinois (2/8/21).
109. Z. Zhu, J-S. Kim, M. Moody, and L. J. Lauhon, Towards the rational design of printed 2D materials, 63rd EMC Meeting, June 2021, Virtual Oral Presentation
110. N. **Paulson**, C. E. **Campbell**, B. **Gulsoy** Uncertainty Quantification of Phase Equilibria and Thermodynamics Workshop (Intro)”, 2nd Annual UQPET Workshop, 10/27/2021, Lemont, IL (virtual)
111. N. **Paulson**, J. Gabriel, T. Duong, M. **Stan**, “Uncertainty Quantification in Computational Thermodynamics – From the Atomistic to the Continuum Scale,” The 150th TMS Annual Meeting and Exhibition, March 14-18, 2021, Orlando, FL (virtual)
112. J. Gabriel, N. **Paulson**, T. Duong, M. **Stan**, “Uncertainty Quantification for Computational Thermodynamics” CHiMaD 2021 Annual meeting, January 24th-25th 2022 (virtual)
113. Z. Hong, “Gold Panning: Automatic Extraction of Scientific Information from Publications”, September 20-23, 2021, eScience 2021 (poster).
114. T.Skluzacek, “Automated metadata extraction to make data swamps more navigable.” (Sandia Labs, Invited Talk)
115. T.Skluzacek, “Enabling Data Utility Across the Sciences”, UChicago Rising Stars Summit.
116. L.C. Brinson, D. Elbert, P. **Voorhees**, L. **Bartolo**, B. **Blaiszik**, E. De Guire, V. Doan-Nguyen, I. **Foster**, S. Kalinin, B. Kozinsky, A. Mehta, A. Strachan. “Day 1 Workshop - Driving Infrastructure Forward – Materials in the Era of FAIR Data”. 2021 MaRDA Annual Meeting, Feb. 23, online.
117. L.C. Brinson, D. Elbert, P. **Voorhees**, L. **Bartolo**, B. **Blaiszik**, E. De Guire, V. Doan-Nguyen, I. **Foster**, S. Kalinin, B. Kozinsky, A. Mehta, A. Strachan. “Day 1 Workshop - Driving Infrastructure Forward – Materials in the Era of FAIR Data”. 2021 MaRDA Annual Meeting, Feb. 23, online.
118. L.C. Brinson, D. Elbert, P. **Voorhees**, L. **Bartolo**, B. **Blaiszik**, E. De Guire, V. Doan-Nguyen, I. **Foster**, S. Kalinin, B. Kozinsky, A. Mehta, A. Strachan. “Connecting Materials Infrastructure – Growing the State of the Art”. 2021 MaRDA Annual Meeting, Feb. 24, online.
119. L.C. Brinson, D. Elbert, P. **Voorhees**, L. **Bartolo**, B. **Blaiszik**, E. De Guire, V. Doan-Nguyen, I. **Foster**, S. Kalinin, B. Kozinsky, A. Mehta, A. Strachan. “Education and Workforce Development – Integrating Curricula and Research”. 2021 MaRDA Annual Meeting, Feb. 25, online.

120. **B. Blaiszik, I. Foster.** “A FAIR Approach Towards Fully Realizing the Impact of AI and Machine Learning Materials Science”. NIST Office of Data Informatics Seminar. Dec 14, 2021.
121. **B. Blaiszik, I. Foster,** “Advanced Robotics and Software Defined Automation to Speed Materials Discovery” AI/ML for Particle Accelerator, X-Ray Beamlines and Electron Microscopy. Nov. 3, 2021.
122. **B. Blaiszik, I. Foster,** “A FAIR Approach Towards Fully Realizing the Impact of AI and Machine Learning Materials Science”. University of Illinois at Urbana-Champaign Pathways Seminar. Jul 07, 2021.
123. L. Ward. "Introduction to ML and Effective Data Practices in Materials Science", CHiMaD Annual Meeting June 21, 2021.
124. A. Scourtas, KJ Schmidt, **B. Blaiszik.** "Publishing, Discovering, and Using Data with the Materials Data Facility, DLHub, and Foundry", CHiMaD Annual Meeting June 21, 2021.
125. Z. Hong, "Update on MDF Natural Language Processing Applications", CHiMaD Annual Meeting June 21, 2021.
126. **B. Blaiszik, I. Foster.** “A FAIR Approach Towards Fully Realizing the Impact of AI and Machine Learning Materials Science”. University of Illinois at Urbana-Champaign DigiMat Seminar. April 16, 2021.

### 16.3 Technologies and Techniques

In 2021, CHiMaD principle investigators and researchers have published 12 software technologies. For the list below, the primary affiliation of the work published with the CHiMaD Groups is as follows:

*AI: Softwares 1-5*

*MDF: Softwares 6-11*

*Outreach: 12*

1. **Type:** Open-Source Software

**Name of Technology:** LVGP: Latent Variable Gaussian Process Modeling with Qualitative and Quantitative Input Variables

**Authors:** S. Tao, Y. Zhang, D.W. Apley, W. Chen

**Date:** 1/11/2019

**Access Link:** [:https://cran.r-project.org/web/packages/LVGP/index.html](https://cran.r-project.org/web/packages/LVGP/index.html)

**Description:** code for implementing Latent Variable Approach to Gaussian Process Modeling with Qualitative and Quantitative.

Our original LVGP code (in R) was made available to the general public through <https://cran.r-project.org/web/packages/LVGP/index.html>. The code has attracted a lot of interest during the past two years. We extracted the number of LVGP package downloads from Jan 1, 2020 to Jan 23, 2022, Figure 16.1. The total downloads of LVGP R code from Jan 2020 are 10,764. The average daily downloads are about 30 times, and the monthly downloads range from 265 to 646 times.

2. **Type:** Software

**Name of Technology:** Cross-property deep transfer learning framework for enhanced predictive analytics on small materials data

**Authors:** V. Gupta, K. Choudhary, F. Tavazza, C. Campbell, W.-k. Liao, A.

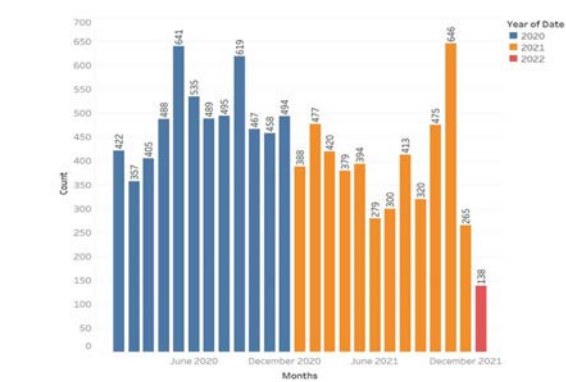


Figure 16.1: The number of LVGP Package downloads from Jan 1, 2020 to Jan 23, 2022.

**Choudhary, and A. Agrawal**

**Date:** November 2021

**Distribution:** Public

**Access Link:** <https://github.com/NU-CUCIS/CrossPropertyTL>

**Description:** This GitHub repository contains the code for performing cross-property deep transfer learning. It can be used to train predictive models for target properties with limited data, using transfer learning from pre-trained source models on big data, even if the source property is different from the target property.

3. **Type:** Software

**Name of Technology:** Learning to Predict Crystal Plasticity at the Nanoscale: Deep Residual Networks and Size Effects in Uniaxial Compression Discrete Dislocation Simulations

**Authors:** Z. Yang, S. Papanikolaou, A. **Reid**, W.-k. Liao, A N. **Choudhary**, C. **Campbell**, and A. **Agrawal**

**Date:** February 2021

**Distribution:** Public

**Access Link:** <https://github.com/NU-CUCIS/PlasticityDL>

**Description:** This GitHub repository contains code to apply deep residual networks for predicting crystal plasticity at nanoscale. The efficacy of the proposed approach is tested on a dataset of strain profiles to identify prior deformation history of the material.

4. **Type:** Software

**Name of Technology:** Deep learning based domain knowledge integration for small datasets: Illustrative applications in materials informatics

**Authors:** Z. Yang, R. Al-Bahrani, A. Reid, S. Papanikolaou, S. Kalidindi, W.-k. Liao, A N. **Choudhary**, and A. **Agrawal**

**Date:** February 2021

**Distribution:** Public

**Access Link:** <https://github.com/NU-CUCIS/DKACNN>

**Description:** This GitHub repository contains code to apply domain knowledge-aware convolutional neural networks (DKACNN) on small dataset. The efficacy of the proposed approach is tested on two materials science datasets with different types of inputs and outputs, for which domain knowledge-aware convolutional neural networks are developed.

5. **Type:** Software  
**Name of Technology:** Microstructural Materials Design via Deep Adversarial Learning Methodology  
**Authors:** Z. Yang, X. Li, L.C. Brinson, A. N. Choudhary, W. Chen, and A. Agrawal  
**Date:** February 2021  
**Distribution:** Public  
**Access Link:** <https://github.com/NU-CUCIS/MDGAN>  
**Description:** MDGAN is a generative adversarial network to generate materials microstructure images for materials discovery. It is trained on synthetic 2D microstructure images and can rapidly generate new microstructure images that are statistically similar to the training images.
6. **Type:** Software  
**Authors:** J. Gaff, B. Blaiszik, L. Ward, Ian Foster  
**Distribution:** Public  
**Access Link:** [https://github.com/materials-data-facility/connect\\_client](https://github.com/materials-data-facility/connect_client)  
**Description:** MDF Connect Client. Python client to manage submissions to the MDF Connect service.
7. **Type:** Software  
**Authors:** J. Gaff, B. Blaiszik, L. Ward, Ian Foster  
**Distribution:** Public  
**Access Link:** [https://github.com/materials-data-facility/connect\\_server](https://github.com/materials-data-facility/connect_server)  
**Description:** MDF Connect Server. Code that is used to operate the MDF Connect service
8. **Type:** Software  
**Authors:** L. Ward, J. Gaff, B. Blaiszik, I. Foster  
**Distribution:** Public  
**Access Link:** <https://github.com/materials-data-facility/MaterialsIO>  
**Description:** MaterialsIO. MaterialsIO is a repository of materials-specific metadata extraction tools written in Python with a consistent API. These extractors form the basis of automated extractions performed by MDF Connect.
9. **Type:** Software  
**Authors:** J. Gaff, B. Blaiszik, L. Ward, Ian Foster  
**Distribution:** Public  
**Access Link:** <https://github.com/materials-data-facility/forge>  
**Description:** MDF Forge
10. **Type:** Software  
**Authors:** J. Gaff, B. Blaiszik, L. Ward, Ian Foster  
**Distribution:** Public  
**Access Link:** <https://github.com/materials-data-facility/toolbox>  
**Description:** MDF Toolbox. MDF Toolbox is a collection of authentication and data transfer tools that may be useful across MDF projects and other community projects
11. Since MDF focuses on delivering data services to the community, the developed codes are critical to disseminate to the community. The code being developed in this project is made available freely and publicly to the community through repositories on Github. Where appropriate, Python packages are automatically built and



available through the Python Packing Index (PyPI) and may be installed on any Python-supported system by running the command `pip install <package>`. *Select*

*Supported Codes, Services, and Repositories*

**Authors:** J. Gaff, L. Ward, I. Foster, B. Blaiszik et al.

MDF Github Organization: <https://github.com/materials-data-facility>

MDF Connect Client: [https://github.com/materials-data-facility/connect\\_client](https://github.com/materials-data-facility/connect_client)

MDF Connect Server: [https://github.com/materials-data-facility/connect\\_server](https://github.com/materials-data-facility/connect_server)

MaterialsIO: <https://github.com/materials-data-facility/MaterialsIO>

MDF Forge: <https://github.com/materials-data-facility/forge>

MDF Toolbox: <https://github.com/materials-data-facility/toolbox>

Globus Flows: <https://www.globus.org/platform/services/flows>

12. **Type:** Software

**Authors:** B. Gulsoy, J. Emery, C. Houser, A. Geller

**Distribution:** Public

**Access Link:** <http://chimad-trainings.rcs.northwestern.edu>

**Description:** The CHiMaD System Design Toolbox is a web-based training and collaboration tool which allows users to build and customize system design charts.

## 16.4 Inventions, Patent Applications and/or Licenses

In 2020, CHiMaD principle investigators and researchers have contributed and patented 5 technologies with the one from Impact group being a NIST-CHiMaD co-patent. For the list below, the primary affiliation of the work published with the CHiMaD Groups is as follows:

*2D Inks: Inventions & Patents 1,2*

*Additive: Inventions & Patents 3*

*Cobalt: Inventions & Patents 4*

1. **Type:** Invention

**Name of Technology:** Aerosol jet printed flexible graphene circuits for electrochemical sensing and biosensing

**Authors:** K. Parate, S. V. Rangnekar, M. C. Hersam, and J. C. Claussen **Date:** January 14, 2021

**Patent Number:** 17/248,211 (US patent application) and PCT/US2021/013442 (PCT international patent application)

**Description:** An aerosol jet graphene ink has been developed and used to print interdigitated electrodes for flexible electrochemical sensors.

2. **Type:** Invention

**Name of Technology:** Printable ionogel inks and forming methods and applications of same

**Authors:** W. J. Hyun and M. C. Hersam

**Date:** January 28, 2021

**Patent Number:** PCT/US2021/015375 (PCT international patent application)

**Description:** An aerosol jet printable hexagonal boron nitride ionogel ink has been developed and utilized for electrolyte gated thin-film transistors.

3. **Type:** Software IP disclosure  
**Name of Technology:** LVGP: Latent Variable Gaussian Process Modeling with Qualitative and Quantitative Input Variables  
**Authors:** W. Chen, D. Apley, S. Yerramilli, and R. Bostanabad.  
**Date:** 11/1/2021  
**Distribution:** Disc-ID-21-11-16-002  
**Access Link:** not available yet  
**Description:** Python code for enhanced Latent Variable GP (LVGP) Approach to Gaussian Process Modeling with Qualitative and Quantitative Variables
  
4. **Type:** Invention  
**Name of Technology:** Cobalt-based superalloys with stable gamma-prime precipitates, method of producing same  
**Authors:** D.C. Dunand, F. Tirado  
**Date:** 2021-07-08 : Publication of US20210207255A1  
**Patent Number:** US Patent App. 17/056,519  
**Distribution:** public  
**Access Link:** <https://patents.google.com/patent/US20210207255A1/en>  
**Description:** A cobalt-based superalloy and a method of producing the same. The superalloy includes a nominal composition comprising at least cobalt, aluminum, Z and vanadium, Z being at least one of tantalum and niobium, processed such that the superalloy comprises gamma and gamma-prime phases with stable gamma+gamma-prime microstructures.

## 16.5 Data

For the list below, the primary affiliation of the work published with the CHiMaD Groups is as follows:

*2D Inks: Data 1-5*

*Thermoelectrics: Data 6-7*

*Impact: Data 8*

*AI: Data 9-13*

*UQ: Data 13*

1. **Accelerated decomposition kinetics of ammonium perchlorate via conformal graphene coating**  
M. D. Garrison, S. G. Wallace, L. C. Baldwin, Z. Guo, L. Kuo, J. E. Estevez, A. L. Briseno, M. C. **Hersam**, and A. J. Baca  
Access: Materials Data Facility (<https://doi.org/10.18126/2rpo-t1rn>)
2. **Thermoreflectance imaging of (ultra)wide band-gap devices with MoS<sub>2</sub> enhancement coatings**  
R. Hanus, S. V. Rangnekar, S. Mollah, K. Hussain, N. Hines, E. Heller, M. C. **Hersam**, A. Khan, and S. Graham  
(<https://doi.org/10.18126/emun-4lr3>)
3. **Ultrasensitive Molecular Sensors Based on Real-Time Impedance Spectroscopy in Solution-Processed 2D Materials**  
D. Moore, A. Jawaid, R. Busch, M. Brothers, P. Look, A. Miesle, R. Rao, J. Lee, L. Beagle, M. Motala, S. G. Wallace, J. R. Downing, A. Roy, C. Muratore, M. C.

- Hersam, R. Vaia, S. Kim, and N. R. Glavin  
Access: Materials Data Facility (<https://doi.org/10.18126/FIPX-0X7U>)
4. **Visualizing thermally activated memristive switching in percolating networks of solution-processed 2D semiconductors**  
V. K. Sangwan, S. V. Rangnekar, J. Kang, J. Shen, H.-S. Lee, D. Lam, J. Shen, X. Liu, A. C. M. de Moraes, L. Kuo, J. Gu, H. Wang, and M. C. **Hersam**  
Access: Materials Data Facility (<https://doi.org/10.18126/V4TM-NW3I>)
  5. **Intrinsic carrier multiplication in layered Bi<sub>2</sub>O<sub>2</sub>Se avalanche photodiodes with gain bandwidth product exceeding 1 GHz**  
V. K. Sangwan, J. Kang, D. Lam, J. T. Gish, S. A. Wells, J. Luxa, J. P. Male, G. J. **Snyder**, Z. Sofer, and M. C. **Hersam**  
Access: Materials Data Facility (<https://doi.org/10.18126/NE02-LZPS>)
  6. **Extracted Hall Data**  
A. Peyrera, J. Tran, M. Toriyama, R. Gurunathan, G.J. **Snyder**  
Access: StarryData2
  7. **Heat Capacity of undoped PbTe**  
R. Hanus, M. Agne, A. Rettie, D. Y. Chung, M. Kanatzidis, P. **Voorhees**, G.J. **Snyder**  
Access: Materials Data Facility (<https://doi.org/110.18126/1obf-bje9>)
  8. **Shear thickening and jamming of dense suspensions: The roll of friction**  
A. Singh; C. Ness; R. Seto; J.J. **de Pablo**; H.M. **Jaeger**  
Access: Materials Data Facility (<https://doi.org/10.18126/oqop-2zxxk>)
  9. **2D Orthotropic Metamaterial Dataset**  
W. **Chen**  
Access: Northwestern (<https://ideal.mech.northwestern.edu/research/software/>)
  10. **2D Multi-Class Unit Cell Library**  
A. van Beek, D. Da, W. **Chen**  
Access: Northwestern (<https://ideal.mech.northwestern.edu/research/software/>)
  11. **2D Unit Cell Dataset**  
D. Da, W. **Chen**  
Access: GitHub (<https://github.com/Daicong-Da/2D-Orthotropic-Unit-Cell-Dataset.git>)
  12. **Heat Capacity of undoped PbTe**  
R. Hanus, M. Agne, A. Rettie, D. Y. Chung, M. Kanatzidis, P. **Voorhees**, G.J. **Snyder**  
Access: Materials Data Facility (<https://doi.org/110.18126/1obf-bje9>)
  13. **Cross-property deep transfer learning framework for enhanced predictive analytics on small materials data**  
V. Gupta, K. **Choudhary**, F. **Tavazza**, C. **Campbell**, W.-k. Liao, A. **Choudhary**, A. **Agrawal**  
Access: (<https://doi.org/10.5281/zenodo.5533023>)
  14. **Aluminum Bayesian weighted DFT MD Experiments Cp and H data**  
J. Gabriel, N. **Paulson**, T. Duong, C. **Becker**, F. **Tavazza**, U. **Kattner**, M. **Stan**  
Access: Materials Data Facility (<https://doi.org/10.18126/to2p-lmot>)

## 16.6 CHiMaD Databases

Below are the four main CHiMaD databases and data resources funded through the efforts.

### Open Quantum Materials Database

*Authors:* Wolverton Group, Northwestern

*Distribution:* Public

*Access Link:* <http://oqmd.org>

*Description:* The OQMD is a database of DFT calculated thermodynamic and structural properties. In 2020, the Open Quantum Materials Database has broken a significant barrier reaching quantum mechanical calculations of over 800,000 compounds.

### Curation and Exploration of Reproducible Scientific Papers (Qresp)

*Authors:* Galli Group, University of Chicago

*Distribution:* Public

*Access Link:* <http://qresp.org>

*Description:* Qresp is an open source software to facilitate the organization, annotation and exploration of data presented in scientific papers, addressing data accessibility and reproducibility. In particular, in 2020, Qresp team improved two tools: (1) Curator: This tool guides users in the creation of metadata for the data that accompanies a publishable scientific work; improvements were made towards ease of use and automation of this process; (2) Explorer: This tool provides a portal for the scientific community to access datasets, explore workflows and download curated data, published in scientific papers; improvements were made to be able to access it tool through a GUI, making it more user-friendly.

### Polymer Property Predictor and Database

*Authors:* Tchoua, R.; Hong, Z.; Audus, D.; Patel, S.; Ward, L.; Chard, K.; De Pablo, J.; Foster, I.

*Distribution:* Public

*Access Link:* <https://pppdb.uchicago.edu>

*Description:* Polymer Property Predictor and Database (3PDB). 3PDB is a database of curated polymer properties (e.g., Flory-Huggins parameters and T<sub>g</sub>) extracted from the literature using natural language processing (NLP) and hybrid human-NLP pipelines. 3PDB also includes a number of applications to allow users to generate phase diagrams given input polymer properties and more.

### Materials Data Facility

*Authors:* Blaiszik, B.; Chard, K.; Pruyne, J.; Ananthakrishnan, R.; Tuecke, S.; Foster, I.

*Distribution:* Public

*Access Link:* <https://materialsdatafacility.org>

*Description:* A simple way to publish, discover and access materials databases. More information can be found in Chapter 14.

### Other Databases

Below are the additional community databases built through collaborations of MDF teams and using MDF services and framework.

#### Solvation energy database

*Authors:* Ward, Logan; Dandu, Naveen; Blaiszik, Ben; Narayanan, Badri; Assary, Rajeev S.; Redfern, Paul C.; Foster, Ian; Curtiss, Larry A.

*Distribution:* Public

*Access Link:* <https://doi.org/10.18126/jos5-wj65>

*Description:* This database, hosted on Materials Data Facility, is a collection of >600,000 calculated molecular solvation energies in various solvents.

#### **G4MP2-GDB9 Database**

*Authors:* Narayanan, Badri; Redfern, Paul; Ward, Logan; Blaiszik, Ben; Foster, Ian;

*Distribution:* Public

*Access Link:* <https://doi.org/10.18126/M23P9G>

*Description:* This database is the largest collection of simulation of molecules at the G4MP2 level of accuracy. This database was created in collaboration with JCESR, and is hosted via MDF.

#### **Virtual Excited State Reference for the Discovery of Electronic Materials Database (VERDE)**

*Authors:* Biruk Abreha, Snigdha Agarwal, Ian Foster, Ben Blaiszik, Steven Lopez *Distribution:* Public

*Access Link:* <https://doi.org/10.18126/1m40-u86g> and <https://verdedb.org>

*Description:* Virtual Excited State Reference for the Discovery of Electronic Materials Database (VERDE). The VERDE Materials database is the first database to include downloadable excited-state structures (S0, S1, T1) and photophysical properties of molecules. This database was created by the group of Steven Lopez at Northeastern University, and is hosted via MDF.

CHMaD

